

**Synthesis, Electrochemistry and Solid-Solution Behaviour of Energy
Storage Materials Based on Natural Minerals**

by

Brian Ellis

A thesis

presented to the University of Waterloo

in fulfillment of the

thesis requirement for the degree of

Doctor of Philosophy

in

Chemistry

Waterloo, Ontario, Canada, 2013
© Brian Ellis 2013

I hereby declare that I am the sole author of this thesis. This is a true copy of the thesis, including any required final revisions, as accepted by my examiners.

I understand that my thesis may be made electronically available to the public.

Brian Ellis

Abstract

Polyanionic compounds have been heavily investigated as possible electrode materials in lithium- and sodium-ion batteries. Chief among these is lithium iron phosphate (LiFePO_4) which adopts the olivine structure and has a potential of 3.5 V vs. Li/Li^+ . Many aspects of ion transport, solid-solution behaviour and their relation to particle size in olivine systems are not entirely understood. Morphology, unit cell parameters, purity and electrochemical performance of prepared LiFePO_4 powders were greatly affected by the synthetic conditions. Partially delithiated olivines were heated and studied by Mössbauer spectroscopy and solid-solution behaviour by electron delocalization was observed. The onset of this phenomenon was around 470-500 K in bulk material but in nanocrystalline powders, the onset of a solid solution was observed around 420 K. The isostructural manganese member of this family (LiMnPO_4) was also prepared hydrothermally. Owing to the thermal instability of MnPO_4 , partially delithiated LiMnPO_4 did not display any solid-solution behaviour.

Phosphates based on the tavorite (LiFePO_4OH) structure include LiVPO_4F and $\text{LiFePO}_4(\text{OH})_{1-x}\text{F}_x$ which may be prepared hydrothermally or by solid state routes. LiVPO_4F is a high capacity (2 electrons/transition metal) electrode material and the structures of the fully reduced $\text{Li}_2\text{VPO}_4\text{F}$ and fully oxidized VPO_4F were ascertained. Owing to structural nuances, the potential of the iron tavorites are much lower than that of the olivines. The structure of $\text{Li}_2\text{FePO}_4\text{F}$ was determined by a combined X-ray and neutron diffraction analysis.

The electrochemical properties of very few phosphates based on sodium are known. A novel fluorophosphate, $\text{Na}_2\text{FePO}_4\text{F}$, was prepared by both solid state and hydrothermal

methods. This material exhibited two two-phase plateau regions on cycling in a half cell *versus* sodium but displayed solid-solution behaviour when cycled *versus* lithium, where the average potential was 3.3 V. On successive cycling *versus* Li a decrease in the sodium content of the active material was observed, which implied an ion-exchange reaction occurred between the material and the lithium electrolyte.

Studies of polyanionic materials as positive electrode materials in alkali metal-ion batteries show that some of these materials, namely those which contain iron, hold the most promise in replacing battery technologies currently available.

Acknowledgements

This thesis arose out of years of research that has been done since I came to the Nazar group. Over this time, a great number of people have shared in this scientific expedition.

First and foremost, I would like to send my sincere gratitude to my supervisor, Dr. Linda Nazar, for her guidance, critical judgment and commitment to research. I would also like to thank my supervisory committee: Dr. Holger Kleinke, Dr. Sonny Lee and Dr. Peter Tremaine (University of Guelph) for their participation and guidance as well. Thanks to Dr. Zhongwei Chen (Waterloo) and to my external examiner Dr. Karim Zaghbi (Hydro Quebec) for taking the time to come to Waterloo and participate in my thesis defense.

I have also been very privileged to have been part of many successful collaborations with talented researchers and students from around the world including Dr. Gillian Goward (McMaster University), Dr. Marnix Wagemaker (TU Delft), Dr. Dominic Ryan (McGill University), Dr. Brent Fultz (California Institute of Technology), Dr. Doron Aurbach (Bar-Ilan University), Dr. Ashfia Huq (Oak Ridge National Labs). I wish everyone the best in their future scientific endeavours.

But I have been extremely fortunate to have the opportunity to come into a chemistry lab each day and be greeted by friendly, charismatic and insightful group of people who provide support, enthusiasm and fresh perspective over the many years I have been here. I have enjoyed our (sometimes passionate) discussions immensely. Hearty thanks to all of the members of the Nazar group, past and present. Thanks also to the late Dr. Nick Taylor for providing a spot of wit and wisdom.

Finally, I would like to thank my family (especially my parents) and friends who have been wonderfully supportive.

Table of Contents

List of Figures.....	viii
List of Tables.....	xv
List of Abbreviations.....	xvii
1 Introduction to Lithium Ion Batteries	1
1.1 Overview	1
1.2 Rechargeable Energy Storage Systems	2
1.3 Lithium-Ion Batteries	4
1.4 Positive Electrode Materials for Lithium-Ion Batteries	8
1.5 Use of Iron and Manganese Compounds as Positive Electrode Materials.....	12
1.6 Sodium and Hybrid Sodium-Lithium-Ion Cells.....	15
1.7 Solid Solutions and Li batteries	17
1.8 Scope of Thesis	20
2 Instruments and Techniques	23
2.1 Overview	23
2.2 Powder X-ray Diffraction and Bragg's Law	24
2.3 Rietveld Refinement.....	25
2.4 Scanning and Transmission Electron Microscopy	28
2.5 Mössbauer Spectroscopy.....	30
2.6 Thermal Analysis	33
2.7 Electronic Conductivity.....	34
2.8 Electrochemical Cycling Techniques.....	35
3 Hydrothermal Synthesis and Thermally Driven Solid Solutions in the Olivine LiFePO₄ and LiMnPO₄ Systems.....	39
3.1 Introduction to Olivines	39
3.2 Synthesis of Olivine Compounds.....	45
3.3 Hydrothermal Synthesis of LiFePO ₄ : Mechanism and Effect of Conditions.....	47
3.4 Modified Hydrothermal Synthesis: Use of Carbonaceous Additives	57
3.5 High Temperature Mössbauer Studies on LiFePO ₄	62
3.6 Synthesis and High Temperature Mössbauer Studies on Nano-LiFePO ₄	74
3.7 Hydrothermal Synthesis and High Temperature Studies of LiMnPO ₄	78
3.8 Conclusions	82
4 Preparation, Electrochemistry and Anion-Induced Solid Solutions in Hydroxyphosphates and Fluorophosphates based on the Tavorite Structure.....	84
4.1 Overview of Tavorite-type Compounds.....	84
4.2 Synthesis of Tavorite Compounds	86
4.3 Diffraction and Electrochemical Studies of LiVPO ₄ F	88
4.4 Synthesis & Electrochemical and <i>Ex-Situ</i> X-ray Studies of the Novel Lithium Iron Fluorophosphate LiFePO ₄ F.....	99

4.5	The Mechanism of Lithium Insertion into LiFePO_4OH : Preparation of Amorphous $\text{Li}_2\text{FePO}_4\text{OH}$	113
4.6	Anion Disorder Induced Solid Solution Behaviour in $\text{LiFePO}_4(\text{OH})_{0.4}\text{F}_{0.6}$	120
4.7	Synthesis and Electrochemistry of Manganese Phosphate Tavorite.....	127
4.8	Conclusions	134
5	Fluorophosphates of the Composition $\text{A}_2\text{MPO}_4\text{F}$.....	135
5.1	Background	135
5.2	Synthesis of $\text{Li}_2\text{MPO}_4\text{F}$ Materials.....	137
5.3	$\text{Li}_2\text{MPO}_4\text{F}$ Results.....	137
5.4	Sodium-ion and Hybrid Na/Li-ion Cells for Energy Storage	143
5.5	Synthesis of $\text{Na}_2\text{MPO}_4\text{F}$ Compounds.....	144
5.6	Synthesis and Structure of $\text{Na}_2\text{FePO}_4\text{F}$	145
5.7	Sodium Electrochemistry and <i>Ex-situ</i> Diffraction Study.....	151
5.8	Electrochemistry and Ion Exchange of $\text{Na}_2\text{FePO}_4\text{F}$ with Lithium.....	155
5.9	Mössbauer studies of small polaron hopping in $\text{Na}_{1.5}\text{FePO}_4\text{F}$	162
5.10	Synthesis and Electrochemistry of Other $\text{Na}_2\text{MPO}_4\text{F}$ Phases.....	165
5.11	Conclusions	171
6	Final Conclusions and Future Directions.....	172
	Permissions.....	175
	References.....	175

List of Figures

Figure 1.1: Large-scale energy production from windmills at a wind farm and solar energy farms.	2
Figure 1.2: Schematic diagram of the electrochemical processes in a lithium-ion battery	5
Figure 1.3: Structures of oxide materials for lithium-ion batteries.....	9
Figure 1.4: Sample of natural triphylite (LiFePO_4)	13
Figure 1.5: a) the olivine structure of LiFePO_4 ; b) the tetrahedrally-coordinated structure of $\text{Li}_2\text{FeSiO}_4$; c) the tavorite (LiFePO_4OH) structure; d) the layered fluorophosphate structure of $\text{Na}_2\text{FePO}_4\text{F}$	13
Figure 1.6: A comparison of solid solutions and two-phase materials with sample phase diagram and an example of the differing voltage profiles and intermediate particle compositions for LiCoO_2 and LiFePO_4	18
Figure 2.1: a) Representation of Bragg's law for a given set of crystal planes. b) Schematic diagram of a powder X-ray diffraction experiment.	24
Figure 2.2: a) Schematic representation of Mössbauer experimental setup. b) Approximate Mössbauer isomer shifts for Fe compounds in various co-ordinations.	32
Figure 2.3: View of Swagelok cell and the internal components.	38
Figure 3.1: Polyhedral representation of the structure of LiFePO_4	40
Figure 3.2: a) TEM image and b) carbon map from a sample of $\text{Li}_{0.90}\text{Zr}_{0.01}\text{FePO}_4$	41
Figure 3.3: Powder X-ray diffraction patterns and corresponding SEM micrographs of hydrothermal LiFePO_4 after various reaction times	50

Figure 3.4: a) The olivine structure, adopted by several minerals including LiFePO_4 , in the space group Pnma; b) structure of $\text{NH}_4\text{FePO}_4 \cdot \text{H}_2\text{O}$ in the space group Pmn2 ₁	51
Figure 3.5: Rietveld refinement of hydrothermally-prepared LiFePO_4 at 190°C.....	53
Figure 3.6: Raman spectra of LiFePO_4	54
Figure 3.7: SEM micrographs of carbon-free LiFePO_4 crystallized at different concentrations and temperatures.....	55
Figure 3.8: Typical electrochemical profile of hydrothermal LiFePO_4	57
Figure 3.9: SEM images of hydrothermal LiFePO_4 treated with citric acid and ascorbic acid in the reactor	58
Figure 3.10: XRD pattern and LeBail refinement (a) and SEM micrograph (b) of LiFePO_4 synthesized hydrothermally in the presence of polyacrylic acid	60
Figure 3.11: X-ray diffraction patterns of $\text{Li}_{1-x}\text{FePO}_4$ prepared from oxidation of LiFePO_4 . A two-phase transition to FePO_4 is evident.	62
Figure 3.12: Room temperature Mössbauer spectra of Li_xFePO_4 compositions showing localized Fe^{2+} and Fe^{3+} components.	64
Figure 3.13: Mössbauer spectra at elevated temperatures illustrating the evolution from two-phase compositions to solid-solution $\text{Li}_x\text{Fe}^{2+/3+}\text{PO}_4$ as a function of temperature	64
Figure 3.14: Change in isomer shift of the Fe^{2+} , Fe^{3+} and solid-solution phases as a function of temperature	66
Figure 3.15: Relative areas of Fe^{2+} , Fe^{3+} and solid solution regime as a function of temperature.	67
Figure 3.16: Plot of isomer shift <i>versus</i> x in Li_xFePO_4	69

Figure 3.17: Mössbauer spectra of the solid-solution component of $\text{Li}_{0.55}\text{FePO}_4$ phase from 500-673 K showing growth of the solid-solution phase and motional narrowing.....	70
Figure 3.18: Schematic illustration of small polaron hopping within the bc plane of the olivine lattice.....	72
Figure 3.19: Two-point probe dc conductivity measurement for $\text{Li}_{0.5}\text{FePO}_4$	73
Figure 3.20: TEM micrograph of nano- LiFePO_4 prepared by the polyol route.	75
Figure 3.21: The relative areas and the change in isomer shift of the Fe^{2+} , Fe^{3+} and the solid solution phases as a function of temperature from the Mössbauer spectra for nanophased $\text{Li}_{0.5}\text{FePO}_4$ and bulk $\text{Li}_{0.5}\text{FePO}_4$	76
Figure 3.22: Rietveld refinement of hydrothermally-prepared LiMnPO_4 at 190 °C.	79
Figure 3.23: Electrochemistry of nano- LiMnPO_4	80
Figure 3.24: X-ray diffraction patterns of $\text{Li}_{0.5}\text{MnPO}_4$ prepared by chemical oxidation of LiMnPO_4	81
Figure 3.25: TGA of LiMnPO_4 and $\text{Li}_{0.5}\text{MnPO}_4$	82
Figure 4.1: Synchrotron X-ray diffraction pattern and Rietveld refinement of LiVPO_4F synthesized by a solid state method	89
Figure 4.2: Pictorial representation of the structure of LiVPO_4F with a close-up view of the split lithium position	90
Figure 4.3: Electrochemical curve of $\text{LiVPO}_4\text{F}/\text{C}$ composite cycled vs. Li/Li^+ starting in discharge	92
Figure 4.4: X-ray powder diffraction patterns of $\text{Li}_{1+x}\text{VPO}_4\text{F}$, synthesized by the chemical reduction of LiVPO_4F with LiAlH_4	93

Figure 4.5: X-ray diffraction pattern and neutron diffraction pattern for combined Rietveld refinement of $\text{Li}_2\text{VPO}_4\text{F}$ synthesized by chemical reduction of LiVPO_4F with LiAlH_4	94
Figure 4.6: Pictorial representation of the structures of VPO_4F , LiVPO_4F and $\text{Li}_2\text{VPO}_4\text{F}$...	96
Figure 4.7: X-ray powder diffraction patterns of $\text{Li}_{1-x}\text{VPO}_4\text{F}$, synthesized by the chemical oxidation of LiVPO_4F with NOBF_4	97
Figure 4.8: X-ray diffraction pattern and Rietveld refinement of VPO_4F synthesized by chemical oxidation of LiVPO_4F	98
Figure 4.9: a) X-ray diffraction patterns, and SEM micrographs of b) LiFePO_4F prepared by our solvothermal method and c) LiFePO_4F prepared by our solid-state method	100
Figure 4.10: Graphical comparison of the KFePO_4F and tavorite (LiFePO_4F) structures ..	101
Figure 4.11: Thermal gravimetric analysis of iron tavorites heated in nitrogen.	102
Figure 4.12: Electrochemical data for LiFePO_4F vs. Li/Li^+ for a) as-synthesized solid-state LiFePO_4F and b) LiFePO_4F ground in a ball mill for 3 hours. SEM images of prepared electrodes for each material are shown in the insets.	103
Figure 4.13: XRD patterns of $\text{Li}_{1+x}\text{FePO}_4\text{F}$ compositions prepared by chemical reduction with stoichiometric amounts of LiAlH_4	105
Figure 4.14: Room temperature Mössbauer spectra of a) LiFePO_4F and b) $\text{Li}_2\text{FePO}_4\text{F}$	106
Figure 4.15: Combined Rietveld refinement of X-ray and neutron powder diffraction data from a sample of $\text{Li}_2\text{FePO}_4\text{F}$	108
Figure 4.16: Comparison of the Li1 environments in LiFePO_4F and $\text{Li}_2\text{FePO}_4\text{F}$	110
Figure 4.17: Graphical representation of the $\text{Li}_2\text{FePO}_4\text{F}$ structure with the Fe environments in $\text{Li}_2\text{FePO}_4\text{F}$	111

Figure 4.18: Rietveld refinement of X-ray diffraction data from a polycrystalline sample of LiFePO ₄ OH. Inset: Scanning electron microscope image of the LiFePO ₄ OH powder.	114
Figure 4.19: Infrared spectroscopy data for LiFePO ₄ F, LiFePO ₄ (OH) _{0.4} F _{0.6} and LiFePO ₄ OH	116
Figure 4.20: Electrochemical data for LiFePO ₄ (OH) vs. Li/Li ⁺	118
Figure 4.21: X-ray diffraction patterns of chemical oxidation and reduction products of LiFePO ₄ OH.....	119
Figure 4.22: Rietveld refinement of XRD data from a sample of hydrothermally prepared LiFePO ₄ F _{0.6} (OH) _{0.4}	121
Figure 4.23: a) Voltage profile on first discharge of LiFePO ₄ F, LiFePO ₄ OH and LiFePO ₄ F _{0.6} (OH) _{0.4} b) Electrochemical cycling of cells comprised of LiFePO ₄ F _{0.6} (OH) _{0.4} cycled at a rate of C/10	123
Figure 4.24: PITT measurement of the first discharge of LiFePO ₄ F _{0.6} (OH) _{0.4}	124
Figure 4.25: X-ray diffraction patterns of LiFePO ₄ (OH) _{0.6} F _{0.4} chemically reduced with LiAlH ₄ to produce Li _{1.5} FePO ₄ (OH) _{0.6} F _{0.4} , and Li ₂ FePO ₄ (OH) _{0.6} F _{0.4}	126
Figure 4.26: a) X-ray diffraction pattern and SEM micrograph of MnPO ₄ •H ₂ O precipitated from solution. b) TGA data for MnPO ₄ •H ₂ O heated under nitrogen.....	128
Figure 4.27: Electrochemical data for MnPO ₄ •H ₂ O cycled at a rate of C/50.....	129
Figure 4.28: Rietveld refinement of XRD data from a sample of LiMnPO ₄ OH.	130
Figure 4.29: Electrochemical results for cycling of LiMnPO ₄ OH versus Li at a rate of C/50	132

Figure 5.1: The crystal structure of a) $\text{Na}_2\text{FePO}_4\text{F}$, view down the b-axis and a-axis, b) $\text{Li}_2\text{CoPO}_4\text{F}$ and c) $\text{Na}_2\text{MnPO}_4\text{F}$.	136
Figure 5.2: Powder X-ray diffraction patterns of a) $\text{Li}_2\text{NiPO}_4\text{F}$ and b) $\text{Li}_2\text{CoPO}_4\text{F}$	138
Figure 5.3: X-ray diffraction pattern after treatment of LiMnPO_4 and LiF at $800\text{ }^\circ\text{C}$.	138
Figure 5.4: X-ray diffraction pattern after treatment of LiFePO_4 and LiF at $750\text{ }^\circ\text{C}$	139
Figure 5.5: X-ray diffraction pattern of the reaction of FeF_2 , LiH_2PO_4 and LiOAc	140
Figure 5.6: Schematic representation of a) the M1-M1 edge-sharing sites and b) the M2-M2 edge-sharing sites in $\text{Li}_2\text{MPO}_4\text{F}$.	141
Figure 5.7: Powder diffraction patterns and corresponding SEM micrographs of $\text{Na}_2\text{FePO}_4\text{F}$ prepared hydrothermally and prepared by a solid-state route.	146
Figure 5.8: TGA curve showing the decomposition point of $\text{Na}_2\text{FePO}_4\text{F}$.	147
Figure 5.9: The first two cycles of a $\text{Na}_2\text{FePO}_4\text{F}$ composite electrode cycled versus sodium at a rate of $\text{C}/20$.	152
Figure 5.10: X-ray diffraction patterns of $\text{Na}_x\text{FePO}_4\text{F}$ illustrating the solid-solution behavior of the system in the range from $x = 2 \rightarrow 1$.	153
Figure 5.11: LeBail XRD refinement of $\text{Na}_{1.5}\text{FePO}_4\text{F}$ in P2/c	154
Figure 5.12: Electrochemical curve of $\text{Na}_2\text{FePO}_4\text{F}$ cycled versus Li prepared by a carbon-free hydrothermal technique and by a hydrothermal route containing 2% C.	156
Figure 5.13: Rate performance of carbon-containing hydrothermally prepared $\text{Na}_2\text{FePO}_4\text{F}$ at various discharge rates after charging at a rate of $\text{C}/10$.	156
Figure 5.14: Na:P ratios determined by EDX analysis of crystallites in the SEM. a) $\text{Na}_2\text{FePO}_4\text{F}$ material taken from electrochemical cells cycled versus Li as a function of cycle number; b) $\text{Na}_2\text{FePO}_4\text{F}$ after ion exchange with LiBr .	158

Figure 5.15: Rietveld refinement of $\text{Li}_{1.23}\text{Na}_{0.77}\text{FePO}_4\text{F}$, synthesized from NaFePO_4F reduced with excess LiI	161
Figure 5.16: Room temperature Mössbauer data of $\text{Na}_2\text{FePO}_4\text{F}$, $\text{Na}_{1.75}\text{FePO}_4\text{F}$, $\text{Na}_{1.5}\text{FePO}_4\text{F}$, $\text{Na}_{1.25}\text{FePO}_4\text{F}$ and NaFePO_4F , prepared by chemical oxidation of $\text{Na}_2\text{FePO}_4\text{F}$	163
Figure 5.17: Variable temperature Mössbauer data of $\text{Na}_{1.5}\text{FePO}_4\text{F}$ summarizing a) area fraction of each Fe valence in the spectrum and b) isomer shifts at various temperatures... ..	164
Figure 5.18: Powder diffraction patterns and corresponding SEM micrographs of $\text{Na}_2\text{CoPO}_4\text{F}$ a) & b) prepared by a carbon-free solid-state route c) & d) ion-exchanged for 7 hours. Inset: First electrochemical profile of $\text{Na}_2\text{CoPO}_4\text{F}$ cycled at a rate of C/10.	166
Figure 5.19: Lattice parameters for single-phase solid solution compounds $\text{Na}_2(\text{Fe}_{1-x}\text{Co}_x)\text{PO}_4\text{F}$	167
Figure 5.20: X-ray powder diffraction pattern of $\text{Na}_2\text{NiPO}_4\text{F}$	169

List of Tables

Table 3.1: Dopant concentrations resulting from simultaneous refinement of the X-ray and neutron data for the samples with composition $\text{Li}_{1-x}\text{D}_x^{\text{y+}}\text{FePO}_4$, D = Zr and Cr, and the Fe valence derived from the refined atomic occupancies.....	43
Table 3.2: Lattice constants and atomic parameters for hydrothermal LiFePO_4 refined from X-ray diffraction powder data.....	53
Table 3.3: Typical lattice parameters for olivines prepared by different synthetic routes with varying particle size.....	61
Table 3.4: Lattice constants and atomic parameters for hydrothermal LiFePO_4 refined from X-ray diffraction powder data.....	79
Table 4.1: Lattice constants and atomic parameters of LiVPO_4F refined from powder XRD data.....	89
Table 4.2: Summary of bond distances for Li environment in LiVPO_4F	91
Table 4.3: Lattice constants and atomic parameters for $\text{Li}_2\text{VPO}_4\text{F}$ refined from combined X-ray and neutron diffraction powder data.....	95
Table 4.4: Lattice constants and atomic parameters of VPO_4F refined from powder XRD data.....	98
Table 4.5: Lattice parameters for solid-state and solvothermally prepared iron tavorite phosphates.....	101
Table 4.6: Lattice constants and atomic parameters of $\text{Li}_2\text{FePO}_4\text{F}$ determined by a combined refinement of X-ray and neutron powder diffraction data.....	109
Table 4.7: Summary of Bond Distances for Each Iron Environment in $\text{Li}_2\text{FePO}_4\text{F}$	111

Table 4.8: Results from the refinement of LiFePO_4OH	115
Table 4.9: Lattice constants and atomic parameters of $\text{LiFePO}_4(\text{OH})_{0.4}\text{F}_{0.6}$ refined from powder XRD data.	122
Table 4.10: Lattice constants and atomic parameters of LiMnPO_4OH refined from powder XRD data.	131
Table 5.1: Bond lengths for transition metal sites in $\text{Li}_2\text{MPO}_4\text{F}$, $\text{M} = \text{Co}, \text{Ni}$	142
Table 5.2: Lattice parameters for $\text{Li}_2\text{CoPO}_4\text{F}$ and $\text{Li}_2\text{NiPO}_4\text{F}$	142
Table 5.3: Atomic parameters and unit cell constants for $\text{Na}_2\text{FePO}_4\text{F}$	148
Table 5.4: Selected bond distances in $\text{Na}_2\text{FePO}_4\text{F}$	149
Table 5.5: Lattice parameters for sol-gel $\text{Na}_{2-x}\text{FePO}_4\text{F}$ prepared by chemical oxidation of $\text{Na}_2\text{FePO}_4\text{F}$	153
Table 5.6: Rietveld refinement results and atomic positions for $\text{Li}_{1.23}\text{Na}_{0.77}\text{FePO}_4\text{F}$ synthesized from NaFePO_4F reduced with excess LiI	162

List of Abbreviations

NaSICON	Sodium Super Ionic Conductor
SEM	Scanning Electron Microscope
EDX	Elemental Dispersive X-ray
TEM	Transmission Electron Microscope
TGA	Thermal Gravimetric Analysis
DTA	Differential Thermal Analysis
IR	Infrared
XRD	(Powder) X-ray Diffraction
PND	Powder Neutron Diffraction
v	Velocity
IS	Isomer Shift
QS	Quadrupole Splitting
σ	Conductivity
E_a	Activation Energy
Q	Specific Capacity
PITT	Potentiostatic Intermittent Titration Technique
NaSICON	Sodium Super Ionic Conductor

1 Introduction to Lithium Ion Batteries

1.1 Overview

Energy storage has become a growing global concern over the past decade as a result of increased energy demand globally, combined with drastic increases in the price of refined fossil fuels and the environmental consequences of their use. This has increased demand for environmentally responsible alternative energy sources for both energy generation and storage. Although wind and solar generated electricity (see Figure 1.1) is becoming increasingly popular in several industrialized countries, these sources provide intermittent energy, thus energy storage systems are required for load-leveling, storage of energy until needed by the electrical grid. Furthermore, portable energy solutions which would realize the practical use of hybrid electric vehicles (HEV), plug-in hybrid electric vehicles (PHEV) and purely electric vehicles (EV) would reduce dependence on fossil fuels.

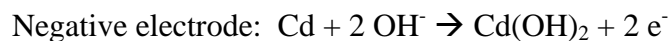
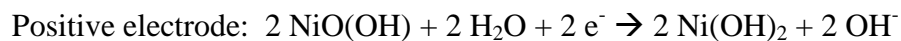
Lithium-ion batteries, the most common type of secondary (rechargeable) cells found in everything from MP3 players to laptop computers, are a possible solution to these larger global concerns.¹ Typically, these batteries feature high energy density, owing primarily to their high electrochemical potential, which is stable over the course of several hundred cycles. Lithium-ion batteries also exhibit low self-discharge, especially when compared to other secondary battery systems such as nickel-cadmium or nickel-metal hydride, although each of these systems has its own advantages as discussed below.



Figure 1.1: Large-scale energy production from windmills at a wind farm in Port Burwell, ON (left) and solar energy farms such as the one operated by the local utility commission in Peterborough ON, are becoming common landscape features in developed countries.

1.2 Rechargeable Energy Storage Systems

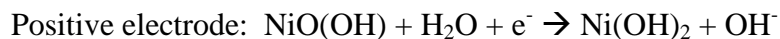
There are many types of secondary batteries available in the marketplace today, each with its own specific characteristics. Nickel-cadmium (NiCd) rechargeable batteries have been available since the mid-1970's.² They provide a relatively low energy density of about 30 Wh/kg, thus limiting their applications to small electronic devices such as video cameras and radios.³ The reactions at each electrode during discharge of the cells are shown below:



The above reactions generate a potential of 1.2 V. NiCd cells provide long cycling life as the batteries can typically be recharged up to about 700 cycles.

Nickel-metal hydride (NiMH) batteries are related to NiCd cells as they employ the same positive electrode composition. NiMH cells have higher energy density of about 50

Wh/kg³ and, compared to NiCd batteries are less toxic, due to the absence of cadmium. NiMH cells produce a voltage of about 1.2 V and the discharge reactions at each electrode are shown below:



where M is an alloy of a rare earth metal with nickel, cobalt or manganese.⁴ These cells have a shorter cycling life: they are typically limited to 500 charges and are prone to slow discharging when not in use.³ They can be found in some cell phones and laptop computers, as well many hybrid electric vehicles (HEV's) currently in production.

The advent of lithium batteries came in the 1970's, with intensive work done in the field of intercalation chemistry. The lithium battery was first demonstrated in a patent from M. S. Whittingham.⁵ These rechargeable lithium cells were configured with metallic lithium or a lithium-aluminum alloy as the negative electrode and a variety of chalcogenides including TiS₂^{6,7} were used the positive electrode in several prototypes. These chalcogenides are layered and are isostructural with CdI₂ and lithium were found to intercalate between the layers. The use of lithium as the negative electrode in these systems allowed for high energy density since lithium is the most electropositive (-3.04 V *versus* the standard hydrogen electrode) and lightest metal (atomic mass of 6.941 g/mol).

In the early 1980's, various oxides of vanadium and molybdenum were also found to intercalate lithium, including MoO₃,⁸ V₆O₁₃,⁹ LiV₃O₈^{10,11} and V₂O₅.⁷ These compounds may be described as also having layered structures and owing to the nature of the transition metals present, these compounds were found to intercalate >1 Li per transition metal. For example, the intercalation of lithium into V₂O₅ is very complex and involves several structural

rearrangements, but up to three moles of lithium were found to reversibly intercalate into one mole of V_2O_5 . These electrodes were paired with either elemental lithium or metals which alloy with lithium such as aluminum or tin, which were later found to be problematic as electrode materials: lithium metal was eventually rejected as an anode material in rechargeable batteries due to safety concerns, owing to dendrite growth on the surface of the lithium metal which could cause internal short circuits and lead to overheating or fire.¹² Lithium metal alloys were also rejected as a result of their large expansion upon Li intercalation, which results in fragmentation of the electrode particles and loss of contact with the electrode, thus resulting in poor reversibility.¹³

1.3 Lithium-Ion Batteries

Further studies of layered oxides led to the study of lithium-containing layered metal oxides of the form $LiMO_2$. The first of these researched was $LiCoO_2$ by Goodenough and co-workers in 1980.¹⁴ They discovered that the lithium could be removed from the structure electrochemically and that this reaction was reversible, thus making $LiCoO_2$ suitable as a positive electrode material in a secondary (rechargeable) battery. Further, Sony combined the $LiCoO_2$ electrode with graphite,¹⁵ a material shown to intercalate lithium at a very low potential (about 0.3 V vs. Li)¹⁶ to create the first successful Li-ion battery, so called because of its lack of elemental lithium.

Insertion materials serve as electrodes for many ambient temperature rechargeable battery systems. Electroinsertion refers to a host/guest redox reaction where charge transfer occurs during the insertion of mobile guest ions into a solid host. These electrode types are common, due to their reversibility and mechanistic simplicity. In lithium ion batteries, lithium ions are the mobile species and are typically present in the positive electrode material

(e.g LiCoO_2). A cell such as this is in the discharged state, as the positive electrode is in its thermodynamically stable form. Thus, an external electromotive force must be applied to charge the cell; a representation of this process is shown in Figure 1.2.

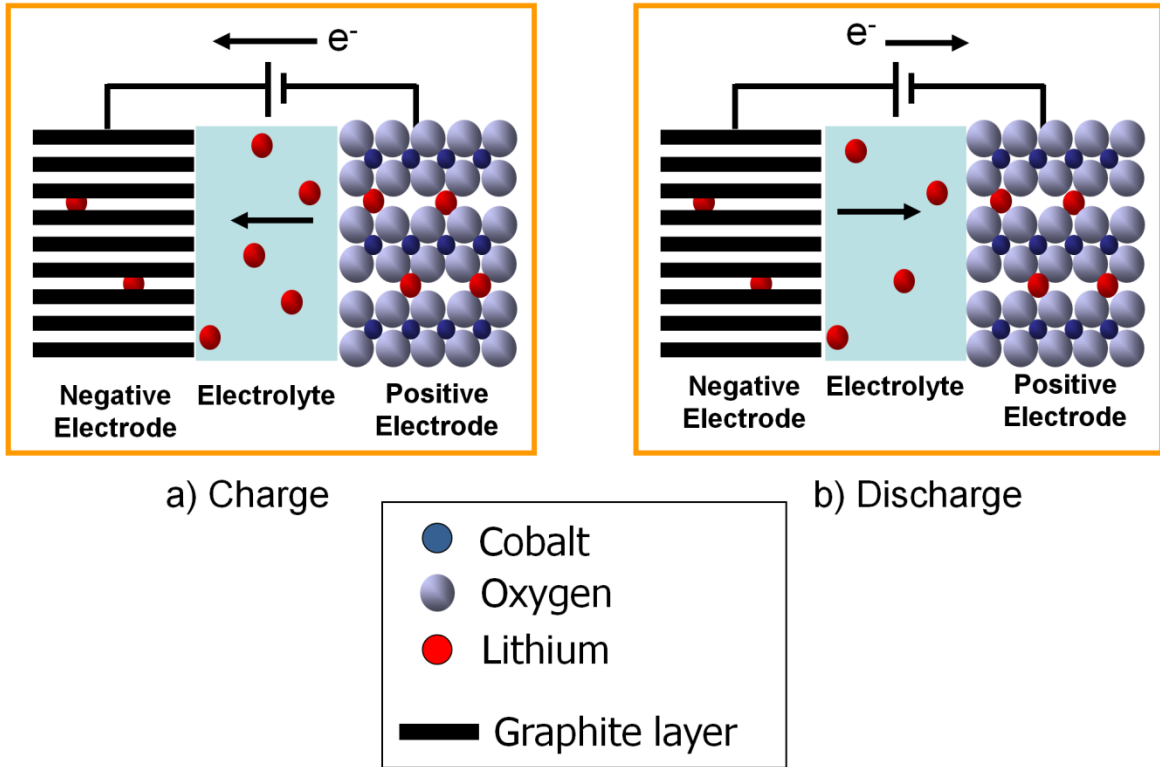
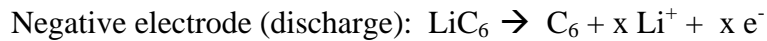
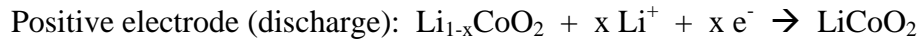
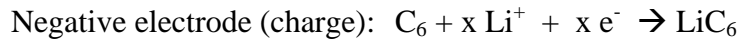


Figure 1.2: Schematic diagram of the electrochemical processes inside a lithium-ion battery.

On charging, an external voltage applied to the cell drives electrons through an external circuit while lithium ions shuttle out of the positive electrode, through the electrolyte, to the negative electrode (one Li^+ ion per electron). The electrolyte allows the diffusion of ions, but is electronically insulating. The positive electrode compensates charge for the removal of lithium *via* oxidation of the transition metal present in the lattice. Upon reaching the negative electrode (usually graphite), the lithium ions intercalate into the electrode and recombine with the electrons, resulting in the reduction at the negative electrode.

During discharge in a lithium ion cell, the process is reversed, as depicted in Figure 1.2. Lithium ions shuttle from the negative electrode, through the electrolyte, back to the positive electrode while electrons spontaneously flow from the negative electrode to the positive electrode through the external system. The lithium ions re-intercalate into the lattice of the positive electrode and recombine with the electrons. The electrode compensates charge by reducing the transition metal ion present to its original oxidation state. In summary for a LiCoO₂/graphite cell:



LiCoO₂ balances lithium insertion/deinsertion from the lattice with the Co³⁺/Co⁴⁺ redox reaction which provides a high potential above 4 V (*versus* Li) and a practical reversible capacity of about 130 mAh/g.¹⁷ Since lithium ions are “rocked” back and forth between the insertion materials present in the two electrodes, this system is referred to as “rocking-chair technology”. As both electrons and lithium ions are transported into and out of the electrodes, the electrodes in the system must be comprised of compounds which allow for the conductivity of both lithium ions and electrons. This requires careful selection of electrode pairs to maintain a useful voltage (at least 2 V) over the discharge.

A typical electrochemical charge and discharge curve for LiCoO₂ cycled *versus* lithium metal is shown later in this chapter in Figure 1.6. As one electron and one Li ion are concerned with the oxidation and reduction of each cobalt in the LiCoO₂ structure, the state of charge for a cell may be represented by the total electrochemical capacity, but most often

it is represented by the quantity of lithium (per mole of transition metal) present in the structure of the positive electrode. As a result, the stoichiometry of the phase(s) at the positive electrode denotes a particular state of charge of the battery: LiCoO_2 indicates the electrode is in its fully discharged state, while $\text{Li}_{0.5}\text{CoO}_2$ implies half a charge cycle has occurred, as half of the cobalt ions have oxidized and half of the lithium has been deintercalated from the structure.

The rate of lithium transfer between electrodes depends mainly on the dimensional stability of the host material during insertion and deinsertion of Li^+ and on the kinetics of the lithium ion and electron transport in the host. Mechanical stresses occur in electrode particles of active material, owing to the expansion and contraction of the structure based on intercalation and deintercalation of lithium during charge and discharge cycles. This may result in cracks in the particles, which can eventually crumble, as in the case of lithium alloys for negative electrodes which were previously discussed where expansion of up to 200% was found to occur.¹³ This lack of structural integrity reduces, and can eliminate the electronic connectivity of the system, thus limiting the cycle life of the cell. It is preferable to discover and employ electrode materials stable upon lithium insertion and removal which have unit cell volume changes $< 10\%$ between the fully lithiated and delithiated forms. Key requirements for an intercalation material to be suitable for use as an electrode in a lithium battery include:

- Contains a readily reducible/oxidizable ion, usually a transition metal
- Framework of structure does not change when lithium is intercalated or removed; and when it is over-charged or discharged
- High capacity for lithium

- Structure can intercalate lithium quickly
- Good electronic conductor (easy addition/removal of electrons during cycling which minimizes the need for conductive additives)

In terms of commercialization, the electrode materials should also be cost-efficient to produce and environmentally friendly. Carbon and various transition metal oxide/oxoanion systems fit several of these criteria.

1.4 Positive Electrode Materials for Lithium-Ion Batteries

The realization of LiCoO_2 as a positive electrode material was key in that the electrode material itself was a source of lithium, thus eliminating the need to use metallic lithium in cells and improving safety. This discovery triggered a mass of new research on lithium and transition metal-containing compounds for Li-ion batteries. LiCoO_2 has been used in extensive commercial applications for lithium batteries; it was commercialized in 1991 and it is currently the standard positive electrode material in the lithium ion battery market. This compound has many features that make it suitable for use in this application. The structure of LiCoO_2 is ideally a superstructure of the rock-salt type in which the lithium and cobalt ions alternate layers (as shown in Figure 1.3a).¹⁸ The layered structure allows two dimensional lithium diffusion through the solid. Furthermore, electronic conductivity in this compound is also high ($5 \times 10^{-3} \text{ S/cm}$).¹⁹ The cell, with lithium as a positive electrode, operates at a high voltage (4 V *versus* Li).²⁰⁻²²

Although the majority of lithium ion batteries produced since 1991 have been LiCoO_2/C cells, there are limitations to current lithium ion battery technology. Although almost all of the Li can be extracted from LiCoO_2 to give theoretical capacity of over 270 mAh/g, only a little over half of the capacity is reversible in a practical sense. Capacity

fading is severe upon extraction of > 0.7 Li from the lattice as oxygen is also removed from the lattice lost from the lattice at such high states of charge, which is a major safety concern.²³ Capacity fading may also result from electrolyte decomposition and from cobalt dissolution in typical electrolytes.²⁴ As such, alternatives to LiCoO_2 are necessary because of its high cost, toxicity, and poor safety that make it unsuitable for large-scale energy-storage applications.

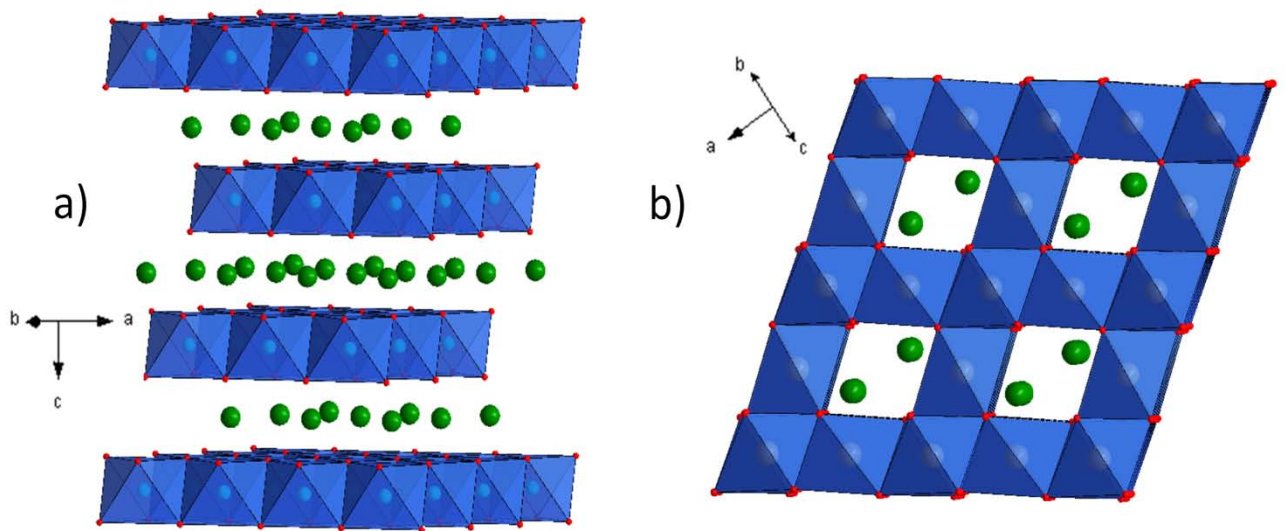


Figure 1.3: Structures of oxide materials for lithium-ion batteries. a) The layered structure of LiCoO_2 and b) the spinel structure of LiMn_2O_4 . For each structure, the transition metal polyhedra are shown in blue and lithium ions in green.

In addition, cobalt is toxic, making disposal of these batteries hazardous to the environment and cobalt has a limited natural abundance compared to many other transition metals: as a result, cobalt-based precursors tend to be expensive. Combined, these factors limit the use of these batteries to small devices such as cameras, cell phones and computers. Replacement of rare metals (namely cobalt in the positive electrode material) and improving manufacturing techniques will make these batteries more economical. As a result, new positive electrode materials must be found if lithium batteries are to have an impact with

larger devices, namely electric vehicles, the realization of which has led to feverish research in the battery community in the past decade.

Among the compounds which have been the focus of intense research as potential replacements for LiCoO_2 are other lithium transition metal oxides which are isostructural with LiCoO_2 , where the cobalt is substituted either partially or entirely with manganese and nickel. The first of these reported was $\text{LiMn}_{0.5}\text{Ni}_{0.5}\text{O}_2$ in 1992, but it was not until later that substantial improvements in electrochemistry were found.^{25,26} One of the drawbacks with this material is cation disorder. Unlike the strict ordering of cations found in LiCoO_2 , on average, 10% of the nickel in $\text{LiMn}_{0.5}\text{Ni}_{0.5}\text{O}_2$ is found in the lithium sites, which in turn implies that 10% of the lithium resides in the transition metal layer, leading to reduced capability of cell made from this material.^{27,28} The disorder arises from the similarity in cation size between nickel, determined to be Ni^{2+} (with manganese as Mn^{4+}), and lithium.²⁹ Following a study by Ohzuku *et al.* where a capacity of 150 mAh/g was obtained, substantial work on this compound as well as cobalt substituted compounds $\text{LiNi}_y\text{Mn}_y\text{Co}_{1-2y}\text{O}_2$, $0.5 \leq y \leq 0.33$ ensued.³⁰⁻³² The most studied of these is the $y = 0.33$ composition, for which capacities between 150-220 mAh/g have been reported, however some reduction of this capacity occurs after several charges. When cobalt is present in most $\text{LiNi}_y\text{Mn}_y\text{Co}_{1-2y}\text{O}_2$ compositions, the lithium/nickel site mixing is $< 5\%$, which typically results in higher reported rate capacity compared to $\text{LiMn}_{0.5}\text{Ni}_{0.5}\text{O}_2$.³²⁻³⁴

Besides the layered oxides, LiMn_2O_4 with the spinel structure has also been studied as a positive electrode material, an appealing candidate as the chemically stable $\text{Mn}^{3+}/\text{Mn}^{4+}$ redox couple operates at 4.1 V vs. Li.³⁵⁻³⁷ A graphical view of the structure of the structure of LiMn_2O_4 is shown in Figure 1.3b. Although this material is inexpensive and

environmentally benign, problems with capacity fading are also prominent for this compound, especially at high temperatures ($> 50\text{ }^{\circ}\text{C}$). Dissolution of LiMn_2O_4 is considered to be the predominant cause,³⁸ although aliovalent lattice substitutions have been found which mitigate the dissolution of manganese into the electrolyte.³⁹

In order to overcome problems of safety and electrode decomposition, several series of compounds have been explored as possible alternatives, including those obtained by introducing large polyanions of the form $(\text{XO}_4)^{y-}$ ($\text{X} = \text{S}, \text{P}, \text{As}, \text{Mo}, \text{W}; y = 2 \text{ or } 3$) into the lattice. Goodenough's group determined that the $(\text{PO}_4)^{3-}$ and $(\text{SO}_4)^{2-}$ ions stabilize the structure and raise the redox energy of the transition metal compared to potentials of the respective oxides.⁴⁰ The presence of the polyanion $(\text{XO}_4)^{y-}$ with strong X-O covalent bonds increases the potential as a result of the strong polarization of oxygen ions toward the X cation which lowers the covalency of the M-O bond. This is referred to as the M-O-X inductive effect which has been thoroughly studied for many transition metal phosphates including vanadium and iron. $\alpha\text{-LiVOPO}_4$ was found to intercalate lithium through a two-phase process at a potential of 3.95 V.⁴¹ Ball-milling the material with conductive carbon reduces the particle size and produces reversibility of over 100 mAh/g. $\beta\text{-LiVOPO}_4$ has been shown to have a reversible capacity of 110 mAh/g at a potential also close to 4 V.⁴² Phosphates such as $\text{Li}_3\text{V}_2(\text{PO}_4)_3$ which are based on the NaSICON structure are intriguing due to their high ionic conductivity. It is possible to extract two moles of lithium from this compound, however upon discharge, only 1.3 lithium are reinserted (corresponding to a capacity of 90 mAh/g) which may be due to structural changes incurred during charge.⁴³ The fluorophosphate LiVPO_4F enhances the inductive effect by the introduction of electronegative fluorine into the lattice. This structural modification raises the $\text{V}^{3+}/\text{V}^{4+}$ redox

potential to a higher voltage compared to the vanadium phosphates: LiVPO_4F has a potential of 4.19 V *versus* Li and can reversibly accommodate 114 mAh/g at a C/5 rate.⁴⁴

1.5 Use of Iron and Manganese Compounds as Positive Electrode Materials

Research has moved toward finding iron compounds which could be used as materials for positive electrodes. The advantage in using iron-based compounds is that, in addition to being naturally abundant and inexpensive, they are typically less toxic than vanadium, cobalt, manganese and nickel compounds. A logical initial strategy was to prepare LiFeO_2 , the oxide which is isostructural with LiCoO_2 , although materials related to LiFeO_2 have shown little ability for lithium extraction due to the instability of the redox couple ($\text{Fe}^{+4}/\text{Fe}^{+3}$).⁴⁵

Research on polyanion compounds of iron revealed most iron phosphate and sulfate compounds containing FeO_6 octahedra had potentials in the range of 2.8-3.6 V *versus* Li^+ . One such compound is rhombohedral $\text{Li}_3\text{Fe}_2(\text{PO}_4)_3$, a NaSICON-related iron phosphate.^{46,47} Ball-milling of the material with carbon produced a reversible capacity of 95 mAh/g when cycled at a rate of C/2.⁴⁶ Other iron(III) phosphates including several crystalline and amorphous phases of $\text{FePO}_4 \cdot x\text{H}_2\text{O}$; $x \leq 2$ have also been studied.^{48,49}

The focus of the lithium battery community changed radically in 1997 with the discovery of the electrochemical properties of LiFePO_4 by Padhi *et al.*⁵⁰ This was the first iron-phosphate based positive electrode material which exhibited a high potential for the $\text{Fe}^{2+}/\text{Fe}^{3+}$ redox couple (3.5 V) *versus* Li with a high theoretical capacity of 170 mAh/g. In addition, the compound is found in nature as the mineral triphylite (see Figure 1.4),

confirming the compound may be classified as environmentally friendly and it is made from plentiful elements, so as to reduce the potential cost of production of this compound. LiFePO_4 adopts the olivine structure, shown in Figure 1.5a and discussed in more detail in Chapter 3.



Figure 1.4: Sample of natural triphylite (LiFePO_4) from the Cornelia Mine in Hagendorf, Germany. From the author's collection.

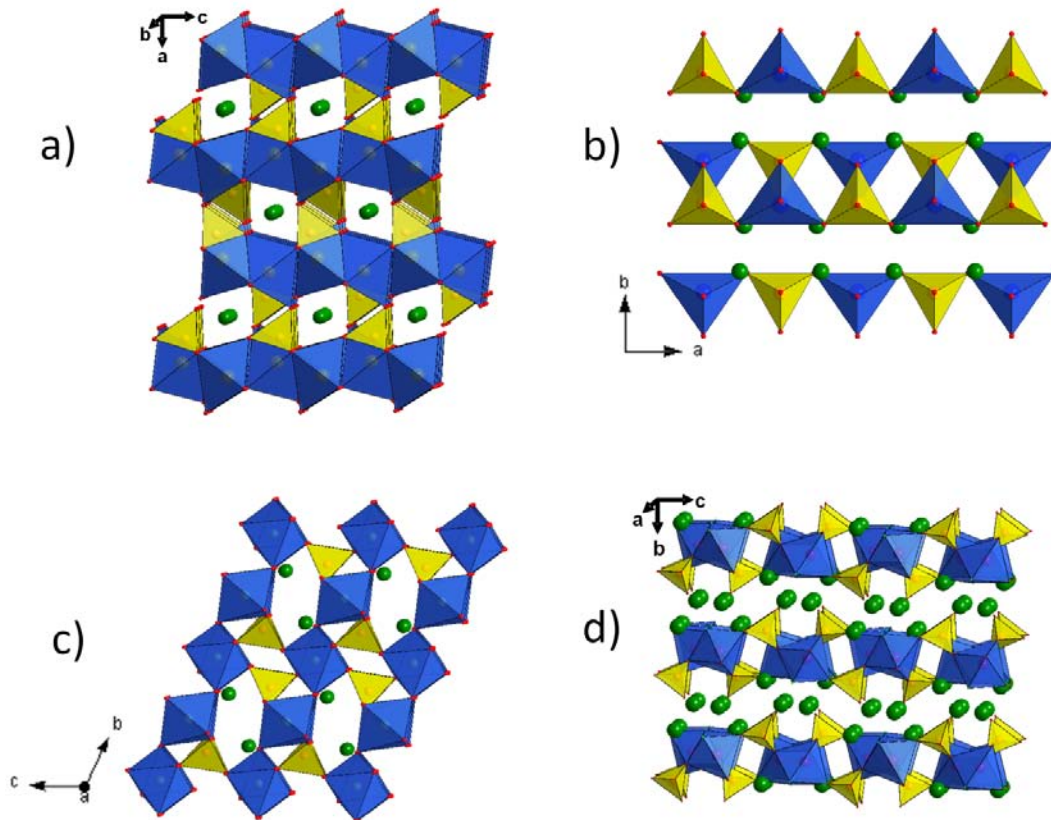


Figure 1.5: a) the olivine structure of LiFePO_4 ; b) the tetrahedrally-coordinated structure of $\text{Li}_2\text{FeSiO}_4$; c) the tavorite (LiFePO_4OH) structure; d) the layered fluorophosphate structure of $\text{Na}_2\text{FePO}_4\text{F}$. In each, polyanion tetrahedra are shown in yellow, transition metal polyhedra are shown in blue and alkali metal ions in green.

Replacing the Fe with Mn and Co in the olivine structure raises the potential: LiMnPO_4 (4.1 V)⁵⁰⁻⁵³ and LiCoPO_4 (4.8 V)^{54,55} have also been studied in great detail, although the reversibility of LiCoPO_4 is quite poor, likely as a result of the poor stability of the delithiated cobalt phase (CoPO_4).⁵⁶ LiMnPO_4 suffers from very low electronic conductivity, necessitating the synthesis of nanosized particles in order to attain reasonable performance in a lithium ion cell.

Lithium transition metal silicates of the form Li_2MSiO_4 (M = Mn, Fe, Co) have also emerged as positive electrode materials.⁵⁷⁻⁶¹ As silicon is one of the most abundant elements in the Earth's crust, silicates offer enormous potential for cost-effective positive electrode materials for Li-ion batteries. These compounds are all related to the various forms of Li_3PO_4 : all the transition metal and lithium sites are tetrahedrally coordinated; a graphical representation is shown in Figure 1.5b. As with most silicates, these compounds exhibit very low electronic conductivity: 2×10^{-12} S/cm for $\text{Li}_2\text{FeSiO}_4$ and 3×10^{-14} S/cm for $\text{Li}_2\text{MnSiO}_4$.⁶² As such, one of the primary challenges with these materials is effective carbon coating to increase conductivity. Silicates have lower potentials compared to the corresponding transition metal olivines: the electrochemistry of $\text{Li}_2\text{FeSiO}_4$ prepared at 750 °C shows a plateau on the initial charge of 3.10 V vs. Li/Li^+ , while on subsequent cycles this plateau shifts to 2.80 V.^{57,63,64} This change in potential is indicative of a structural change during the first cycle. The capacity of $\text{Li}_2\text{FeSiO}_4$ is 166 mAh/g (extraction of only 1 Li), although a recent report from Manthiram and co-workers has shown that the $\text{Fe}^{3+}/\text{Fe}^{4+}$ plateau, calculated to be at 4.8 V,⁶⁵ may be reached electrochemically in cells cycled at 55 °C,⁶⁶ which would double the theoretical capacity of $\text{Li}_2\text{FeSiO}_4$ to 332 mAh/g.

Although it has a lower conductivity, $\text{Li}_2\text{MnSiO}_4$ has been studied intently as a high capacity material with the expectation that the $\text{Mn}^{3+}/\text{Mn}^{4+}$ plateau would be at a lower potential than that for the iron silicate.⁶⁵ Upon deintercalation of Li, $\text{Li}_2\text{MnSiO}_4$ has been found to be amorphous⁶² and in this state, quick fading of the electrochemical capacity was observed.^{59,60,62} In spite of these drawbacks, the field of silicates is growing in popularity due chiefly to the large theoretical capacity of these materials.

Fluorophosphates are another class of electrode materials which have been investigated as positive electrode materials for lithium-ion batteries. Depending on the connectivity of the ionic framework, these compounds may be expected to exhibit a high cell potential as a result of both the inductive effect of PO_4^{3-} group and the electron-withdrawing character of the F^- ion. One of the first successful fluorophosphate materials was LiVPO_4F , reported by Barker *et al.* in 2003,⁴⁴ isostructural with the natural minerals tavorite (LiFePO_4OH)⁶⁷ and amblygonite (LiAlPO_4F).⁶⁸ The tavorite structure is shown in Figure 1.5c.

1.6 Sodium and Hybrid Sodium-Lithium-Ion Cells

The demand for lithium-ion batteries as a major power source in portable electronic devices and vehicles is rapidly increasing: lithium-ion batteries are regarded as the battery of choice for powering future generations of hybrid and plug-in hybrid electric vehicles (HEVs and PHEVs).² With the potential of enormous demands on available global lithium resources, concerns over lithium supply have arisen. Many global lithium reserves are located in remote or in politically sensitive areas.^{69,70} Even if extensive battery recycling programs were established, it is possible recycling could not prevent this resource depletion

over time. Furthermore, the increasing lithium scarcity could increase the price of lithium compounds, thereby making devices or vehicles with large cells prohibitively expensive.

With its abundant resources and low cost, along with its low redox potential ($E^\circ_{(\text{Na}^+/\text{Na})} = -2.71 \text{ V}$ vs. standard hydrogen electrode), rechargeable electrochemical cells based on sodium also hold promise for energy storage applications. The report of a high-temperature solid-state sodium ion conductor sodium β'' -alumina ($\text{NaAl}_{11}\text{O}_{17}$) almost 50 years ago spawned interest in the field of sodium electrochemistry.⁷¹ Two commercial cells currently available are sodium/sulfur (Na/S)⁷²⁻⁷⁴ and ZEBRA (Zero-Emission Battery Research Activities) cells based on Na/NiCl₂.^{75,76} Both technologies operate at high temperature (near 300°C) where sodium and the positive electrodes are molten (thus removing concerns over internal short circuits as a result of dendrite formation) and the sodium β'' -alumina exhibits high ionic conductivity. More recently, room temperature sodium-ion cells based on intercalation materials with non-aqueous electrolytes, akin to lithium-ion batteries, have been explored.⁷⁷⁻⁸²

In 2007, a new sodium-based iron fluorophosphate was introduced: $\text{Na}_2\text{FePO}_4\text{F}$ which had a layered structure (see Figure 1.5d).⁸³ This new material functions very well as a positive electrode material in a coin cell using a lithium salt electrolyte and lithium as the negative electrode where the electrochemical profile displayed a voltage of about 3.5 V, as outlined in Chapter 5 of this thesis. In a lithium-ion cell, mobile Na contained within the structure of the positive electrode material was rapidly exchanged for Li.⁸⁴ $\text{Na}_2\text{FePO}_4\text{F}$ may be a low-cost alternative to lithium-containing iron phosphates with a theoretical capacity of 135 mAh/g in the form $(\text{Na},\text{Li})\text{FePO}_4\text{F}$.

1.7 Solid Solutions and Li batteries

The shape of the voltage profile for a lithium battery may be rationalized in part by employment of the Gibbs Phase Rule:

$$F = C - P + 2$$

where C is the number of chemical components present, P is the number of phases present in the system and F is the number of degrees of freedom or thermodynamic parameters which define the state of the system such as temperature, pressure and electrochemical potential. Though unsuitable for practical use in large-scale applications, lithium metal is often used as a negative electrode for electrochemical testing for research purposes. Lithium is a single phase of constant composition, thus $P = 1$ and $C = 1$. So according to the Gibbs Phase Rule, when lithium metal is used as a negative electrode, F would equal 2. This implies that if two thermodynamic parameters (such as temperature and pressure) are specified, there are no degrees of freedom remaining. As a result, the intensive properties of the lithium metal electrode, such as chemical potential, have fixed values. This makes the lithium metal electrode ideal for electrochemical testing of batteries: under ambient conditions where temperature and pressure are relatively constant, the electrochemical potential of the lithium electrode will not change, regardless of the state of charge of the battery. This allows the lithium electrode to not only function as the working negative electrode but also as a reference electrode.

Most positive electrode materials cycled versus lithium may be separated into one of two categories: those which do not change composition over the course of cycling and those which display solid-solution behaviour. Schematic representations of the phase diagrams for both systems are shown in Figure 1.6. Many polyanionic materials (including LiFePO_4) have

been found to exhibit two-phase behaviour.⁵⁰ For these compounds, the positive electrode contains one electrochemically active composition: in the case of LiFePO_4 , intermediate compositions between the two end-member phases FePO_4 and LiFePO_4 are simply mixtures of those end-member compositions, so in the Gibbs Phase Rule, $C = 2$ and $P = 2$, therefore $F = 2$. Again, if temperature and pressure are fixed, the electrical potential of LiFePO_4 can be determined and will not vary with state of charge. A typical charge/discharge profile for LiFePO_4 is shown in Figure 1.6, where it can be seen that the electrochemical charge and discharge of the cell both occur at constant voltages, both around 3.5 V versus Li.

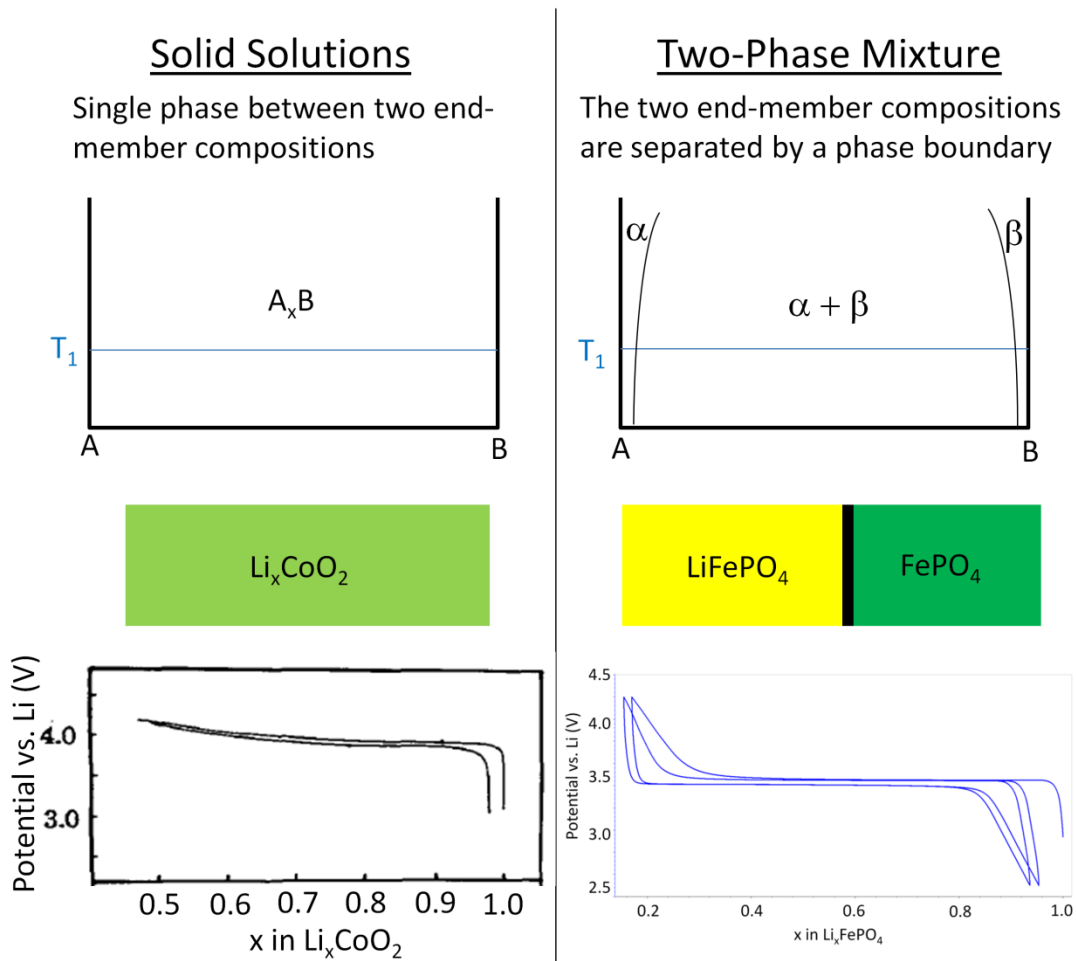


Figure 1.6: A comparison of solid solutions and two-phase materials with sample phase diagram (top) and an example of the differing voltage profiles and intermediate particle compositions for LiCoO_2 ⁸⁵ and LiFePO_4 .

The slight difference of potential on charge and discharge, known as polarity, is the result of internal resistance inside the cell. On a charge cycle, the removal of lithium from LiFePO_4 nucleates a lithium-poor phase (FePO_4). The two phases are separated by an interface (phase boundary) which moves through the particle, depending on the state of charge; a schematic of this phenomenon is shown in Figure 1.6.

Several oxide-based positive electrode materials, $\text{Li}_{1-x}\text{MO}_2$, display solid-solution character, wherein subtle changes in lithium stoichiometry at the surface of the active particles are mitigated over the entire crystal, when the cell is allowed to reach equilibrium. A schematic is shown in Figure 1.6. In this case, phases between the two end-member compositions CoO_2 and LiCoO_2 are single phases.¹⁷ $C = 2$, $P = 1$ and $F = 3$. If temperature and pressure are fixed, this leaves a residual value of F equal to one, thus the electrochemical potential of these compounds is not fixed and varies depending on the state of charge of the cell. This is seen for layered oxides such as LiCoO_2 , among others. A typical example of the electrochemical curve for LiCoO_2 is shown in Figure 1.6, where the voltage varies between 3.8-4.2 V.⁸⁵ Cathode materials for lithium ion batteries which exhibit solid solution properties over a wide lithium compositional range have been sought after for decades. Solid solution behavior is exhibited in where it is typically attributed to delocalized and/or weakly correlated ion and electron transport, coupled with a small volume difference between the redox end members. Its existence implies an absence of any phase boundary impediment during redox cycling, and is associated with good carrier mobility.

Apart from observation of the electrochemical profile, the presence of solid solutions in electrode materials may be ascertained by collection of X-ray powder diffraction patterns of electrode materials cell after partial charge or discharge has occurred, either by removal of

the material from the cell or by examination of the electrode material while still inside the cell (*in situ*). As the quantity of material contained in an electrochemical cell is typically small (5-10 mg), chemical methods of lithium removal and insertion also exist to treat large-scale quantities of powders: common oxidizing agents include NOBF_4 , NO_2BF_4 and $\text{K}_2\text{S}_2\text{O}_8$; common lithium-containing reducing agents include LiAlH_4 and $\text{C}_4\text{H}_9\text{Li}$.

In addition to signifying good ionic transport through the lattice, the existence of a single phase extraction/insertion mechanism allows for additional practical benefits. Chiefly, the resultant sloping voltage curve permits facile monitoring of the state of charge of the battery, as compared with two- phase materials which display a constant voltage over a range of compositions.

1.8 Scope of Thesis

Positive electrode (or cathode) materials containing iron and/or manganese with high potential, high capacity for lithium insertion and solid-solution character are desirable for practical applications of lithium-ion batteries. The most popular of these compounds are those based on the olivine structure: LiFePO_4 and LiMnPO_4 . Room-temperature $\text{Fe}^{2+}/\text{Fe}^{3+}$ solid solutions of LiFePO_4 derived from aliovalent doping with high-valent transition metals such as Zr^{4+} and Nb^{5+} were reported in 2002, although some of the characteristics of these compounds, chiefly increased electronic conductivity,⁸⁶ were later explained shortly thereafter by the Nazar group who discovered the presence of reduced metal phosphide/phosphocarbide phases at the particle grain boundaries.⁸⁷ Later, in 2005, Masquelier et al. found diffraction evidence of high temperature coalescence of $\text{LiFePO}_4/\text{FePO}_4$ two-phase mixtures.⁸⁸ These phases could be quenched and the metastable compounds that result could be stabilized for several weeks.^{89,90} In 2005, Yamada et al.

observed deviations from the stoichiometric end-members: they reported the presence of $\text{Li}_{1-x}\text{FePO}_4$ and Li_yFePO_4 compositions at room temperature.⁹¹ It was later found that the solid-solution regimes were particle-size dependent.⁹² These findings raised questions about the origin of solid-solution behaviour, electron dynamics and thermal stability in LiFePO_4 and other olivines.

In this thesis, high-temperature solid solutions in the LiFePO_4 system were probed with Mössbauer spectroscopy⁹³ and 2-point DC conductivity measurements for both bulk materials produced by a novel hydrothermal method⁹⁴ and nanoparticles synthesized by a low-temperature precipitation route⁹⁵ to determine the onset temperature of solid-solution behaviour in delithiated LiFePO_4 . In the case of LiMnPO_4 , *ex-situ* X-ray diffraction, thermal gravimetric analysis and electrochemical measurements were used to probe the existence of solid-solutions. The results of these studies are presented in Chapter 3.

The other focus of this work involved the preparation of other iron, manganese-based phosphate materials of the general formula $(\text{Li,Na})_x\text{MPO}_4(\text{OH,F})$ where $\text{M} = \text{Fe, Mn}$, whose electrochemical properties were not known and ascertain their suitability as positive electrodes in lithium-ion batteries. Few reports of the synthesis of some of these materials could be found in the literature. As such, a primary focus was to find a suitable preparation method to synthesize pure crystalline powders, typically either by solid-state or hydrothermal routes. One group of compounds targeted were those with the tavorite structure, which have been known as good ionic conductors at high temperatures.^{96,97} We also synthesized a series of isostructural iron compounds: $\text{LiFePO}_4(\text{OH})_x\text{F}_{1-x}$ ($0 \leq x \leq 1$). Although polycrystalline LiFePO_4OH had been synthesized previously,^{98,99} we found a new hydrothermal method for its synthesis as well as methods for preparing mixed hydroxy/fluorophosphates¹⁰⁰ and the

pure fluorophosphate.¹⁰¹ Electrochemical measurements and X-ray diffraction studies on chemically reduced powders confirmed the mechanism for lithium intercalation in these compounds is different for each of LiFePO_4OH , $\text{LiFePO}_4(\text{OH})_{0.4}\text{F}_{0.6}$ and LiFePO_4F and the structure of $\text{Li}_2\text{FePO}_4\text{F}$ was solved by combined X-ray and neutron refinement.¹⁰¹ With an electrochemical potential of 4.1 V vs. Li, LiVPO_4F has been the best studied material in this category of compounds.^{44,102} We explored the electrochemistry of this compound as well as ex-situ chemical oxidation and reduction to verify the mechanism of lithium (de)insertion.¹⁰³ The results of our synthetic, structural and electrochemical studies on the variousavorite systems are detailed in Chapter 4.

Other fluorophosphates we studied as positive electrode materials in Li-ion batteries include those based on sodium, namely a previously unreported compound, $\text{Na}_2\text{FePO}_4\text{F}$. Structural and electrochemical characterization of this compound was carried out. $\text{Na}_2\text{FePO}_4\text{F}$ was found to crystallize in a layered structure⁸³ and the unit cell was subject to a small (4%) volume contraction on extraction of 1 Na and was shown to demonstrate solid-solution behaviour when cycled versus Li. The products of partial Na/Li ion-exchange were examined by X-ray and neutron diffraction to ascertain the presence of each ion on the two crystallographically unique alkali metal sites and the kinetics of ion-exchange on electrochemical cycling were probed.⁸⁴ The structure of $\text{Na}_2\text{FePO}_4\text{F}$ differs from that of previously reported lithium and sodium compounds with similar stoichiometries (such as $\text{Li}_2\text{NiPO}_4\text{F}$ ¹⁰⁴ or $\text{Na}_2\text{MnPO}_4\text{F}$).¹⁰⁵ Other previously unknown compounds of similar stiochiometry, namely $\text{Li}_2\text{FePO}_4\text{F}$ and $\text{Li}_2\text{MnPO}_4\text{F}$ were not synthesized successfully. A summary of the synthesis conditions for $\text{A}_2\text{MPO}_4\text{F}$ (A = Li, Na; M = Mn, Fe, Co, Ni), along with structural and electrochemical characterization is presented in Chapter 5.

2 Instruments and Techniques

2.1 Overview

Upon the completion of a chemical reaction, the challenge therein is to characterize the product (or products) of the reaction. In most cases this involves the identification of the products formed including any impurities, determination of the structure and lattice parameters of the principle phase, and the determination of the particle morphology. In our work, this was principally accomplished using diffraction, microscopy and spectroscopic techniques. Powder X-ray diffraction (XRD) and neutron diffraction (PND) were used in conjunction with Rietveld refinement to identify phases and obtain information about crystal structure and composition. Microscopy methods such as scanning electron microscopy (SEM) and transmission electron microscopy (TEM) were used to generate images in order to probe information on particle size and morphology of a material as well as determine atomic composition on small regions of the sample. Infrared and Raman spectra were collected to identify functional groups within a compound. Mössbauer spectroscopy was used to probe the valence state and co-ordination environment of iron in the lattice of Fe-containing compounds. This was useful when studying compounds where iron could be present in multiple valence states.

In addition to characterization of the structure, physical properties of these compounds were also surveyed. Electrochemical properties were determined by galvanostatic cycling and the potentiostatic intermittent titration technique (PITT). Thermal gravimetric analysis (TGA) was used to determine thermal stability of various materials and to determine the amount of carbon present in various nanoparticle/carbon composites.

2.2 Powder X-ray Diffraction and Bragg's Law

The atoms and ions which occur in regular repeating intervals in a crystalline compound can be regarded as planes that act as semi-transparent mirrors when compounds (powders or single crystals) interact with X-rays. When the angle of incidence equals the angle of reflection for a given plane, X-ray beams can be diffracted from adjacent planes. This is seen in Figure 2.1a. Two X-ray beams with a wavelength λ strike adjacent planes in a crystal with an angle of incidence θ . Using relations of right triangles, the path length between the two beams is related to the angle of incidence and the distance between the two planes (d) by two equal distances of $d\sin\theta$ (between points A and B and between points B and C in Figure 2-1).

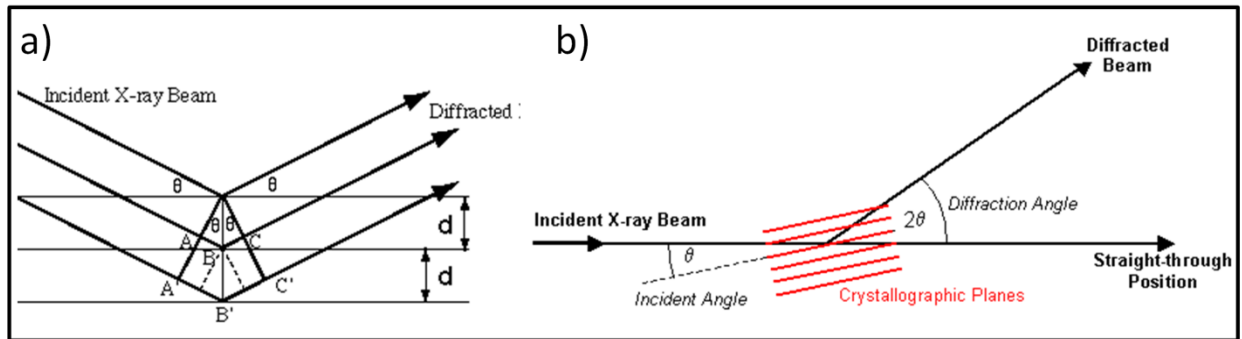


Figure 2.1: a) Representation of Bragg's law for a given set of crystal planes. b) Schematic diagram of a powder X-ray diffraction experiment.

In order to have constructive overlap of the X-ray radiation, this distance must be an integer multiple of the X-ray wavelength. This relation is known as Bragg's law:

$$n\lambda = 2d\sin\theta \quad (2.1)$$

When Bragg's law is satisfied, the reflected beams interfere constructively and give rise to a diffraction peak. When the sample angle does not correspond to crystal plane spacing, there is destructive interference of the X-rays. The peaks in a diffraction pattern are not a set of

lines however; slight broadening occurs as a result of crystallite sizes and micro-stress within the crystallites.

Figure 2-1b depicts a typical powder diffraction experiment with the Bragg-Bretano setup. A monochromatic beam of X-rays strikes a finely ground sample. The powder is a conglomeration of many randomly oriented tiny crystals. Thus, for each set of crystal planes, there will be a number of crystals oriented correctly for Bragg diffraction to take place. The diffracted beams are collected with a moving detector. Plotting the angular positions and intensities of the resultant diffracted peaks of radiation produces a pattern which is characteristic of the sample. Where a mixture of different phases is present, the resultant diffractogram is a combination of the individual patterns.

Unless otherwise stated, all X-ray diffraction patterns presented here were obtained from a Bruker D8 Advance powder X-ray diffractometer equipped with a Sol-X or a Vântec-1 detector operating at 40 kV and 30 mA.

2.3 Rietveld Refinement

In the Rietveld method, successive least-squared refinements are carried out to obtain a fit between a calculated powder X-ray diffraction pattern and a measured pattern. Characteristics such as crystal structure, lattice parameters, atomic positions, occupancy and thermal parameters are refined to achieve a model for a measured powder diffractogram.

The calculation of a theoretical diffraction pattern relies on more than just Bragg's law, which simply determines the position of the peak: the intensity of these peaks must also be calculated. Atoms diffract X-rays (electromagnetic waves) as a result of an incident X-ray which causes each electron of an atom to vibrate. In order for the atom to return to the ground energy state, the atom emits radiation of the same wavelength and coherent to the

absorbed X-ray, making the atom a secondary point source of X-rays. Each atom in a crystal scatters X-rays in an amount related to the number of electrons in the atom; this quantity is known as the atomic scattering factor (f). However, since each electron in the atom scatters X-rays, the phase difference between the beams emitted from the individual electrons will cause a destructive interference effect. The net effect of interference from the beams scattered by all the electrons in an atom causes a decrease in intensity with increasing diffraction angle (2θ), meaning powder patterns have weak lines at higher angles ($2\theta > 70^\circ$). As a result, f for an atom at $2\theta = 0^\circ$ is proportional to the number of electrons possessed by the atom, thus lighter atoms may be difficult to locate. The structure factor (F) of a reflection from a given Miller plane (hkl) is dependent upon the atomic scattering factors for all the individual atoms within the lattice and their position relative to the origin of the unit cell (xyz):

$$F_{hkl} = \sum f_j [\cos 2\pi(hx + ky + lz)] + i[\sin 2\pi(hx + ky + lz)] \quad (2.2)$$

The intensity of the diffracted beam is proportional to FF^* :

$$I \propto \sum [f_j \cos 2\pi(hx + ky + lz)]^2 + \sum [f_j \sin 2\pi(hx + ky + lz)]^2 \quad (2.3)$$

Other factors such as temperature also affect the intensity of diffraction peaks. Using the lattice parameters and Bragg's law to determine the angle of the allowed reflections, the structure factors to determine intensity, and profile coefficients to model the peak shape, a diffraction pattern can be calculated by the program.

The first step is to collect a powder X-ray diffraction pattern with minimal baseline noise. This is done by limiting the step size of the detector on the diffractometer to 0.01 to 0.02° in 2θ for constant wavelength data. This usually gives thousands of data points y_i (2θ , intensity). The space group, lattice parameters and atom positions are input into the Rietveld

program. In this study, the program EXPGUI¹⁰⁶ was utilized as an interface to GSAS, Generalized Structure Analysis Software.¹⁰⁷ The background function, peak shape and symmetry and crystal parameters are then refined using an iterative least-squares routine until the differences between the calculated and observed patterns are minimized.

Rietveld is a method of structural refinement, rather than outright structural determination. As such, before commencing the process of refinement, a structural model containing information regarding the space group, lattice parameters and atomic positions similar to the compound being refined is needed. These data may be obtained from known compounds of similar structure or composition, where available. Modeling typically begins with the fitting of a background function: a long polynomial to fit the any sloping features of the background. The peak shape is then modified. Although many factors contribute to the peak shape, most powder X-ray patterns have Gaussian shapes but may have other features such as long tails or asymmetry which must also be taken into account when modeling an experimental pattern. At this point, the lattice parameters, atom positions, site occupancy and thermal parameters can be refined from the original inputted parameters to give a more precise model of the lattice.

Least-squared refinements proceed to reduce the residual (S_y) over all the data points:

$$S_y = \sum_i 1/y_i (y_i - y_{ci})^2 \quad (2.4)$$

where y_i is the observed intensity at the i th step and y_{ci} is the calculated intensity at the i th step. However, the model must contain parameters to adequately match the structure and diffraction conditions. There must also be indications at each step of the refinement to judge whether the refinement is proceeding properly. There are several estimates of uncertainty

which are used in the Rietveld method. The most mathematically meaningful of these is R_{wp} where the residual being minimized is in the numerator of the fraction:

$$R_{wp} = \{[\sum 1/y_i (y_i - y_{ci})^2]/[\sum 1/y_i (y_i)^2]\}^{1/2} \quad (2.5)$$

Another useful measure of the model is the goodness of fit (χ). It is calculated by the following expression:

$$\chi = [S_y/(N-P)]^{1/2} \quad (2.6)$$

where N-P is the sum of the squared residuals. The final fit is the best least-squares fit to all of the experimental points (y_i) simultaneously which corresponds to the best description of the lattice parameters and atomic information for that sample.

Rietveld refinement can also be used for quantification when two or more phases are present in the diffraction pattern. Once refined, the scale factors (S_{ph}) for each phase are proportional to the stoichiometry of the sample.

A refinement may be considered to be satisfactory when the residual difference between the model and the experimental diffraction patterns reaches a minimum value (there are many statistics which measure the discrepancy but there is no one statistic which can be used as an unconditional gauge of refinement quality) and the model makes sense in terms of atomic co-ordination, bond lengths and bond angles.¹⁰⁸

2.4 Scanning and Transmission Electron Microscopy

A scanning electron microscope (SEM) is a valuable tool for surveying materials at high magnifications and providing structural information such as texture, morphology and particle size. The SEM microscope is an instrument that produces a magnified image by using electrons instead of light to form the image. A beam of electrons is produced at the top of the microscope by an electron gun. The electron beam follows a vertical path through the

microscope, which is held under vacuum. The beam travels through electromagnetic fields and lenses, which focus the beam down toward the sample. The beam is scanned over the specimen in a series of lines and frames. The raster movement is accomplished by means of small coils of wire carrying the controlling current (the scan coils).

At any given moment, the sample is bombarded with electrons over a very small area. Several things may happen to these electrons: they may be elastically reflected from the specimen, with no loss of energy (elastically scattered electrons), or reflected with a slightly reduced energy (backscattered electrons). They may also be absorbed by the specimen and give rise to secondary electrons of very low energy. They may be absorbed and give rise to the emission of visible light (cathodoluminescence) or the emission of X-rays. All these effects can be used to produce an image, though the most common techniques are imaging by detectors which collect signals from backscattered electrons and secondary electrons.

SEM instruments typically have detectors which also provide elemental analysis for a given sample. Bombarding a specimen with electrons causes X-rays, specific to the elements present, to be emitted from the spot where the beam strikes the specimen. By scanning the energy of these X-rays, it is possible to identify and, if the instrument is calibrated, quantify the elements present in the sample. This method is referred to as elemental dispersive X-ray analysis (EDX). However, lighter elements such as lithium do not produce suitable X-ray spectra for this technique.

A transmission electron microscope (TEM) uses electrons to view a very small slice of a sample. As with the SEM, electrons are generated by an electron gun located at the top of the microscope. These electrons are then accelerated towards an anode, which is positively charged, causing the negatively charged electrons to accelerate toward it. As the

electrons are accelerated towards the anode, the stream of electrons are confined and focused by using a series of electromagnets and two condenser lenses. The first condenser lens focuses the general size range of the electron stream, and the second lens changes the size of the actual spot where the electrons hit the specimen. The electrons reach and pass through the sample. After they have passed through the sample, they are focussed by an objective lens, and then pass through a column of lenses, each enlarging the image further. Once the beam of electrons has passed through the column of enlarging lenses, it hits a phosphor image screen, where light is generated. Since electrons have little penetrating power, the sample must be very thin to allow electrons to pass through, and thus dense sections of the specimen which transmit fewer electrons produce darker sections of the image. A camera is placed beneath this screen, and takes the images and displays them on a screen for the user to view.

Similar to the SEM, the specimen produces X-rays specific to the elements present to be emitted from the area where the beam strikes the specimen. Scanning the energy of these X-rays allows for the quantification and location of the elements present in the sample.

2.5 Mössbauer Spectroscopy

Mössbauer spectroscopy is a technique which probes the nuclei of certain elements. The radiation that is used is a highly monochromatic beam of γ -rays, the energy of which can be varied by use of the Doppler effect. This radiation may then be absorbed by a sample containing similar atoms as those responsible for emission. The most widely used γ -radiation sources for Mössbauer spectroscopy are ^{57}Fe and ^{119}Sn ; as a result, this technique is used primarily on compounds containing iron or tin. The absorption of γ -rays by the sample is

monitored with respect to the energy of the incident radiation, which gives information about the local environment of these atoms.

The γ -radiation is associated with a change in population of energy levels in the nuclei of the source. Under conditions of recoilless emission, monochromatic γ -rays are emitted as the nucleus goes from an excited state to the ground state. The energy of the radiation can be varied by use of the Doppler effect; the sample remains in a fixed position and the γ -source is moved at a constant velocity, either toward or away from the sample (Figure 2.2a). When a γ -ray is emitted from a nucleus with a velocity (v) along a straight line toward the sample, the energy of the γ -rays (E_γ) is shifted to a new value (E_D) as a result of the Doppler effect:

$$E_D = (v/c) E_\gamma \quad (2.7)$$

Thus a spectrum of absorbance as a function of energy may be determined for a given sample and this spectrum contains information regarding the local environment (such as coordination number and oxidation state) which can be determined by the isomer shift and quadrupole shift in the spectrum.

The isomer shift, IS (or center shift, CS) arises from the fact that atomic nuclei occupy a finite volume and that s-electrons have the ability to penetrate the nucleus (unlike p, d or f electrons). As a result, the nuclear charge interacts electrostatically with the s-electron cloud inside the nuclear region. This causes a shift in the level of the energy in the nucleus (δE). Since the nuclear volume will typically be different in each excitation state, the shift will be different in each nuclear state. Therefore, in a transition from ground state (g) to excited state (e), the energy change of the ray due to this effect (with respect to a point-charge nucleus) can be described as:

$$\Delta E = (\delta E)_e - (\delta E)_g \quad (2.8)$$

In a Mössbauer experiment, where an appropriate Doppler velocity is applied to either the source (S) or the absorber (A), the difference in electrostatic shift (δ) is observed:

$$\delta = E_S - E_A \quad (2.9)$$

Thus when the emitter and absorber are the same, the isomer shift is zero; if the materials are physically or chemically different, the electron density at the nucleus of the source and absorber will also differ, thus the absorption peak will be shifted. Isomer shifts are principally determined by oxidation state, co-ordination number and type of bonding. Figure 2.2b shows a summary of approximate chemical shifts in various iron-containing ionic compounds.

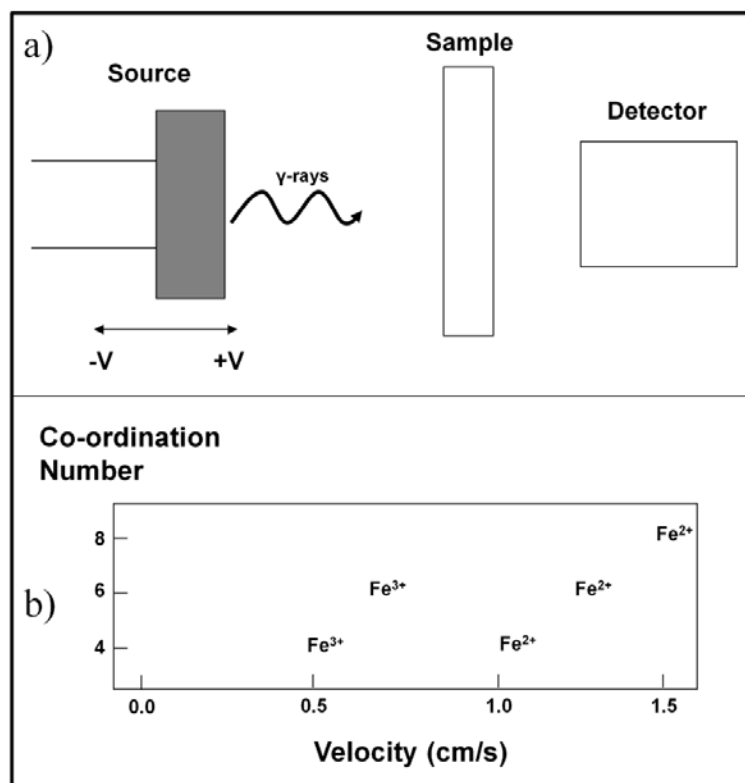


Figure 2.2: a) Schematic representation of Mössbauer experimental setup. b) Approximate Mössbauer isomer shifts for Fe compounds in various co-ordinations.

For nuclei that have a nuclear spin quantum number $I > 1/2$, the allocation of positive charge inside the nucleus is non-spherical, resulting in a non-zero quadrupole moment. This causes a splitting of the peaks at a given isomer shift in the Mössbauer spectrum. For ^{57}Fe and ^{119}Sn , this results in the presence of doublets in the spectrum; the distance separating the two peaks referred to as the quadrupole splitting which is also sensitive to oxidation state and local co-ordination.

In a typical Mössbauer experiment, the γ -source is moved at a constant velocity either toward (+V) or away (-V) from the sample. The absorption of γ -rays by the sample is plotted as a function of the velocity (and thus energy) of the source.

2.6 Thermal Analysis

Thermal analysis is often performed to determine physical properties and thermal stability of compounds. Thermal gravimetric analysis (TGA) measures weight changes as a function of temperature, allowing for the quantification of volatile or combustible constituents in a sample. The differential thermal analysis instrument (DTA) measures energy absorbed (endothermic reaction) or released (exothermic) by the sample as it is heated to induce transformations in the material. These transformations can involve the gain or loss of mass (detected by the TGA), or they can be mass-less events involving structural transitions (not observable by TGA). TGA/DTA measurements were performed using a SDT 6000 instrument. Typical experiments involve loading about 15mg of sample into an alumina crucible and subsequent heating in oxygen to oxidize carbon.

2.7 Electronic Conductivity

Conductivity (σ) can be expressed as:

$$\sigma = ne\mu \quad (2.10)$$

Where n is the number of carrier species (electrons or ions), μ is their mobility and e is the charge on the carrier. The electronic conductivity of various classes of materials varies greatly with temperature: as temperature decreases, metallic compounds show an increase in conductivity (as a result of reduced electron collisions within the lattice) while semi-conducting and insulating compounds experience a decrease in electronic conductivity (resulting from less thermal energy to promote electrons into empty energy bands). Conductivity and temperature for a semiconductor are related by an Arrhenius expression:

$$\sigma = A \exp(-E_a/RT) \quad (2.11)$$

where A is the pre-exponential factor, E_a is the activation energy for conductivity, R is the ideal gas constant and T is temperature in degrees Kelvin. Thus after a graph of $\ln \sigma$ versus $1/T$ has been plotted, the graph has a slope of $-E_a/R$.

Although there are many ways to measure conductivity, the two probe method was used in this study. For this technique, a finely ground powders were pressed into pellets 12 mm in diameter using a die press. The faces of the pellets were coated with silver paint and dried. The pellets were affixed between two flat steel plates (also 12 mm in diameter) which acted as electrical contacts. An external voltage was applied to the sample through the contacts, which created a circuit where the pellet acted as the only resistor. The current passed through the sample was measured while the voltage was applied and using Ohm's law, the sheet resistance could be calculated. Errors due to contact resistance of attaching

leads on to the sample can not easily be eliminated. Once the resistance has been calculated, the specific conductivity (σ_s) is found by the following expression:

$$\sigma_s = l/RA \quad (2.13)$$

where A is the cross-sectional area of the length and l is the thickness of the pelletized sample (measured in centimeters) and R is the sheet resistance. Thus, the final unit for conductivity is: $\Omega^{-1}\text{cm}^{-1}$ (S/cm).

2.8 Electrochemical Cycling Techniques

Galvanostatic charge and discharge of a battery by applying a constant current is the standard method in determining the electrochemical characteristics of a battery, such as specific capacity, rate capability and cycling stability. As the number of electrons is equal to the number of lithium intercalated or de-intercalated from a compound, the overall composition changes linearly as a function of time and typically, the cell voltage is plotted as a function of composition.

The specific capacity (Q) of the material at a specified current flow is related to the molar mass (M_w) of the compound and calculated by:

$$Q = nF/3.6M_w \quad (\text{mAh/g}) \quad (2.14)$$

where F is Faraday's constant (96485 C/mol) and the constant arises as a result of unit conversions. Rate capability refers to the ability to maintain the specific capacity as the current is varied; minimizing the loss of capacity as current increases is critical for battery applications requiring high power (such as electric or hybrid vehicles). Galvanostatic cycling rates are often quoted as fractions of C: the insertion or extraction of one mole of lithium in one hour. A common cycling rate for positive electrode materials is C/5 (one lithium removed/inserted per mole of active material every 5 hours). Cycling stability is presented

by graphing the specific capacity after several cycles. Practical electrode materials will exhibit minimal or no capacity decrease after several hundred cycles, indicating that a battery may be charged and discharged several times while maintaining the original capacity.

When the cell is cycled at a very slow rate (C/50 for example), it is assumed that the cell is operating under equilibrium conditions. Under these conditions, electrode materials experience the maximum lithium removal and insertion, and most achieve a reversible capacity close to the theoretical value. The shape of the curve yields information about the mechanism of insertion. A single-phase reaction (one that sustains a lithium solid solution) exhibits a smooth continuous S-shaped voltage curve. A two-phase reaction involves the formation of a phase boundary upon removal of lithium, rather than mixing. As a result, the voltage curve has zero slope as a function of composition. Increasing the rate of cycling in these systems to rates greater than 1C changes the shape of the curve. The increase in charge increases the polarization of individual grains, resulting in a higher voltage upon extraction compared to equilibrium which causes the cell to reach the maximum potential faster, leaving large particles partially lithiated and reducing the reversible capacity. The increased polarity causes the voltage curve to display a more sloped profile.

In potentiodynamic mode, a voltage is applied to the system and the current response is measured. The voltage is applied in small steps (usually 0.01 V), after which the system relaxes for a given amount of time or until the current decays to a specific amount. This slow cycling usually corresponds to a cycling rate of C/500 or lower, so again, equilibrium conditions are assumed.

As in galvanostatic cycling, the difference between single-phase and two-phase cycling processes are distinguishable. For a single-phase transition, the current decays

exponentially after a step in voltage and follows simple diffusion behaviour. In two-phase materials, a constant current is observed, which depends linearly on the difference between the applied voltage and the potential at the phase boundary. The constant current is a result of the inability of lithium to diffuse across the phase boundary. PITT measurements may be used to study potential dependent cell kinetics as well as provide information on the nature of the phase diagrams with regard to lithium content of the electrode materials.

Electrochemical tests in this thesis were performed using a VMP3 electrochemical cycler, an instrument which supplies either constant current with high accuracy (galvanostatic mode) or constant potential which is swept over a voltage range (potentiostatic mode). The measurements made for testing the electrodes in this study were carried out in galvanostatic mode. All parameters, such as voltage window, mass of active material and reaction cycling rate, are input into the system. Battery cycling involves two steps: charge, where Li is removed from the lattice of the positive electrode material and compensated by oxidation of a transition metal, and discharge, which involves reinsertion of lithium into the structure and reduction of the positive electrode.

The positive electrode of the cell consists of a powder mixture of the active positive electrode material, carbon black and poly-vinylidene fluoride (PVDF) as a binder in a 80:10:10 mass ratio. This mixture is mixed in N-methylpyrrolidinone (NMP), and the suspension is spread on aluminum foil. After evaporation of the NMP solvent, circular electrodes are punched out of the foil and approximately five milligrams of dry material (active material, carbon and PVDF) remains on the disc.

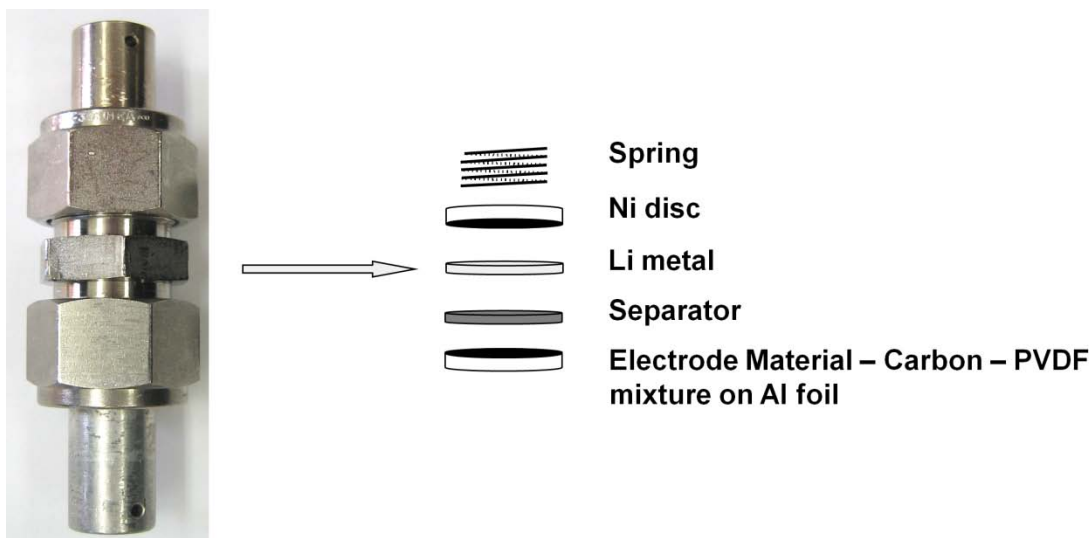


Figure 2.3: View of Swagelok cell and the internal components.

The carbon is added to increase the conductivity of the mixture. PVDF is added to improve the cohesion between particles and the surface of the aluminum disc. This allows the active materials to be housed in an electronically conductive environment. A schematic diagram for the assembly of a cell is shown in Figure 2-9. The aluminum disc with the dried test material is placed in the bottom of a Swagelok cell assembly, followed by two electronically insulating glass fibre separators which are then saturated with an electrolyte solution (1M LiPF_6 in a 1:1 solvent mix of ethylene carbonate and dimethyl carbonate for lithium cells).

Lithium or sodium metal was used as a negative electrode, as described in the text. Since the alkali metals are air, water (and in the case of lithium, nitrogen) sensitive, the cell must be assembled in an argon-filled glove box or dry room. The alkali metal anode is then placed on the separators followed by a stainless steel disc. A spring is placed in the cell to ensure all components have good contact and the cell is locked in place. A polyamide sleeve was used inside the cell to electrically insulate the reaction from the stainless steel housing.

3 Hydrothermal Synthesis and Thermally Driven Solid Solutions in the Olivine LiFePO_4 and LiMnPO_4 Systems

3.1 Introduction to Olivines

The focus of the lithium battery community intensified on polyanionic materials with Pahdi *et. al.* report on the electrochemical properties of LiFePO_4 .^{40,50} LiFePO_4 satisfies many of the criteria for an electrode material in a Li-ion battery: it can reversibly intercalate Li at a high voltage (3.5 V) and has a gravimetric capacity (170 mAh/g) which gives a cell made of the material a high energy density. The material is stable against overcharge or discharge and compatible with most electrolyte systems.¹⁰⁹ The structure of LiFePO_4 is shown in Figure 3.1 and falls into the category of olivines, consisting of a distorted hexagonal close-packed (hcp) oxygen framework with 1/8 of the tetrahedral holes occupied by P, and 1/2 of the octahedral holes occupied by various metal atoms (in this case Li and Fe). The two octahedral sites are crystallographically unique and have been designated M1 and M2 for Li and Fe respectively in LiFePO_4 . Although some mixing of cations between the two sites has been found to occur in olivine silicates such as $(\text{Mg,Fe})\text{SiO}_4$,¹¹⁰ in the case of the phosphates, cations are ordered in the sites: in LiFePO_4 , Li^+ reside in the M1 site and Fe^{2+} ions reside in the M2 site owing to size and charge considerations, though this is not strictly the case, as discussed later. LiFePO_4 crystallizes in space group #62 (Pnma). Layers of FeO_6 octahedra are corner-shared in the *bc* plane and linear chains of LiO_6 octahedra are edge-shared in a direction parallel to the *b*-axis. These chains are bridged by edge and corner shared phosphate tetrahedra, creating a stable three-dimensional structure. The promise of LiFePO_4 as an electrode material has prompted many reports and debates on physical properties of the

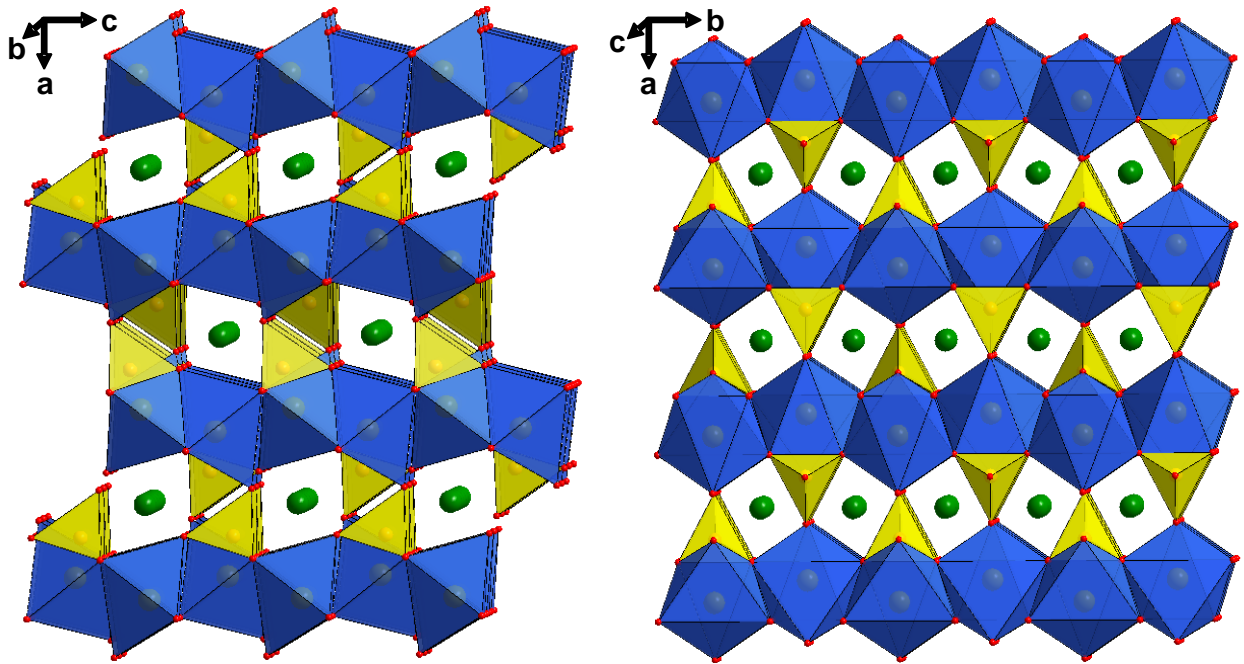


Figure 3.1: Polyhedral representation of the structure of LiFePO₄ (space group Pnma) viewed a) along the *b*-axis and b) along the *c*-axis. The iron octahedra are shown in blue, the phosphate tetrahedral in yellow and the lithium ions in green.

materials such as the nature of ionic and electronic conductivity,^{111–115} aliovalent cation doping,^{86,87,116–119} solid solution behavior,^{88,120,121} particle size effects^{122–124} and surface coatings.^{125–133}

Initial reports on LiFePO₄ focused on carbon coating to both increase the poor electronic conductivity and to produce small particles in order to decrease the path length of lithium transport through the electrode particles. In 2002, a report from Chung *et al.* on aliovalent doping further concentrated research efforts on LiFePO₄.⁸⁶ This study brought the study of vacancies, lithium mobility, conductivity and the possibility of solid solutions to forefront. Compounds of the type Li_{1-x}M^{z+}_xFePO₄ ($z \geq 2$), sintered at 800 °C, were found to have exceptional electronic conductivity, more than 10⁸ times higher than in pure LiFePO₄. While this stoichiometry strictly implied the iron valence would be less than Fe⁺², charge

compensation by Fe^{+3} was postulated as the basis of the dramatic conductivity increase. Although the dopant was thought to reside on the lithium (M1) site and create additional lithium vacancies, no crystallographic evidence of the presence of dopants in the lattice was presented. This sparked debates over the source of the increased conductivity, the presence of dopants in the lattice and the sustainability of lithium vacancies in the structure.

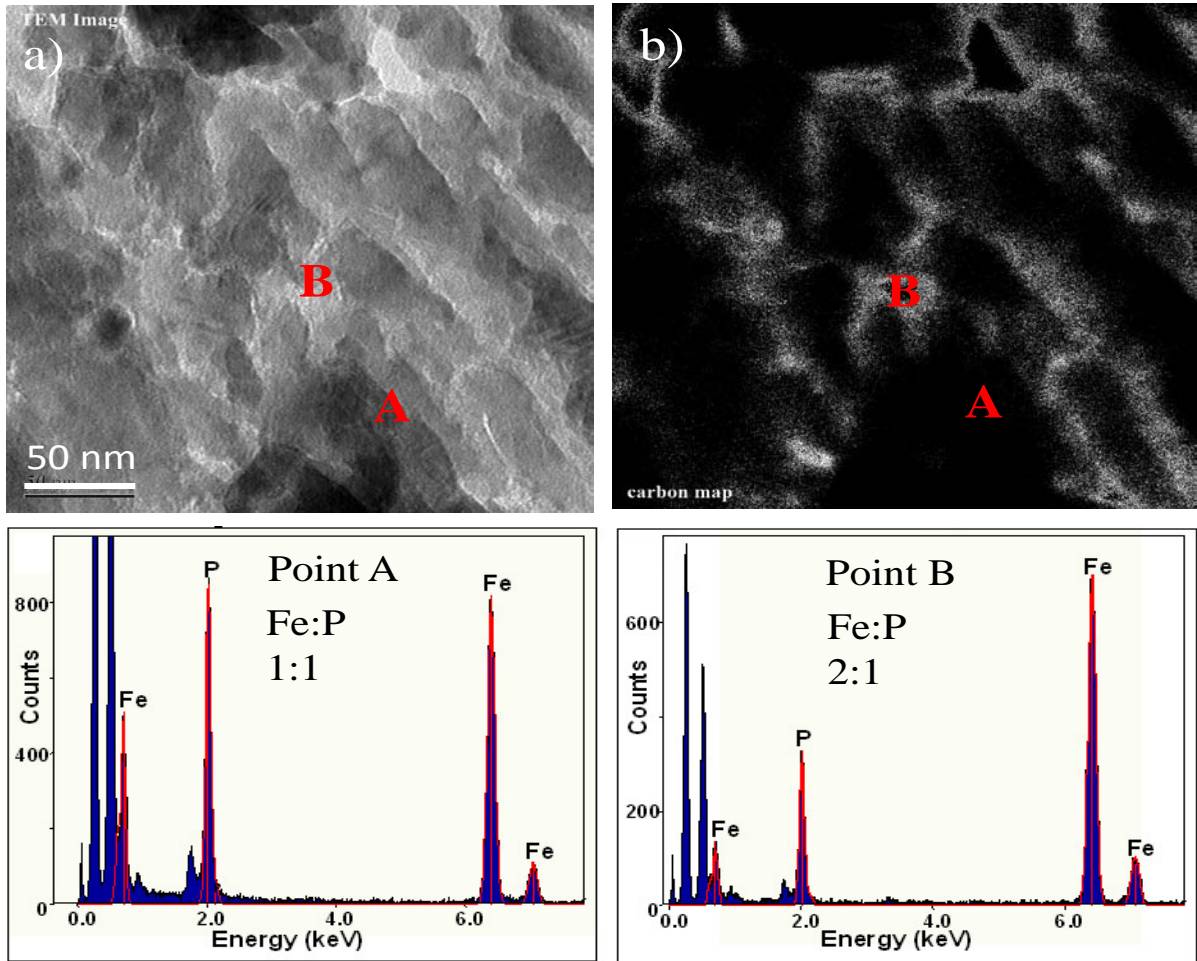


Figure 3.2: a) TEM image and b) carbon map from a sample of $\text{Li}_{0.90}\text{Zr}_{0.01}\text{FePO}_4$, along with TEM-EELS data from two points on the sample. Point A (LiFePO_4 particle) exhibited a 1:1 Fe:P ratio, corresponding to LiFePO_4 . Point B (grain boundary) exhibited a 2:1 Fe:P ratio, corresponding to the formation of metallic Fe_2P . Regions of Fe_2P are connected by the carbon, creating a conductive “nano-network”.

A subsequent study revealed poor conductivity of Zr^{4+} and Nb^{5+} doped $LiFePO_4$.⁸⁷ The conductivity was increased only when additional carbon was added. Carbon-containing precursors, as carbon or which decomposed to produce metallic species, were thus deemed to be the source of high conductivity in the Chung material. Other studies of high-temperature lithium-deficient doped and undoped $LiFePO_4$ that followed found highly conductive compounds, similar to Chung *et. al.* Electron energy loss spectroscopy revealed a high Fe:P ratio in the grain boundaries in addition to carbon (see Figure 3.2), indicative of metallic iron phosphides or iron phosphocarbides. The phosphides were produced by carbothermal reduction of $Fe_2P_2O_7$ or $LiFePO_4$. Carbon made a percolating conductive network through the sample with the phosphides which accounted for the increase in conductivity. X-ray diffraction analysis probing the presence of small dopant quantities in the $LiFePO_4$ lattice was inconclusive. In the presence of small quantities of carbon, pure $LiFePO_4$ could also be made conductive; carbon-free doped and undoped materials exhibited no increase in conductivity. A further study by Delacourt *et. al.* on Nb-doped $LiFePO_4$ revealed only samples prepared with high carbon content were found to be highly conductive.¹³⁴ Furthermore, crystalline β - $NbOPO_4$ was detected on the surface of the olivine particles, further questioning the validity of doping claims. Calculations by Islam *et. al.* also demonstrated the accommodation of an aliovalent dopant on either the M1 or M2 site is highly unfavorable.¹¹⁹

In contrast, X-ray diffraction studies on doped olivines with lithium substoichiometry properly charge compensated by dopant concentration, $Li_{1-3x}Fe^{+3}_xMgPO_4$ and $Li_{1-3x}Fe^{+3}_xNiPO_4$, revealed that substantial doping ($x < 0.15$) could be sustained in the magnesium and nickel olivines.^{135,136} This prompted us to revisit the possibility of dopants in

Table 3.1: Dopant concentrations resulting from simultaneous refinement of the X-ray and neutron data for the samples with composition $\text{Li}_{1-x}\text{D}_x^y\text{FePO}_4$, $\text{D} = \text{Zr}$ and Cr , and the Fe valence derived from the refined atomic occupancies.

sample	Refined stoichiometry	Dopant M1 Occupancy	Dopant M2 Occupancy	Fe M2 Valence
$\text{Li}_{0.96}\text{Zr}_{0.01}\text{FePO}_4$	$[\text{Li}_{0.976}\text{Zr}_{0.008}][\text{Li}_{0.004}\text{Fe}_{0.996}]\text{PO}_4$	0.008	0.000	1.996
$\text{Li}_{0.88}\text{Zr}_{0.03}\text{FePO}_4$	$[\text{Li}_{0.892}\text{Zr}_{0.023}][\text{Li}_{0.004}\text{Zr}_{0.008}\text{Fe}_{0.988}]\text{PO}_4$	0.023	0.008	2.004
$\text{Li}_{0.91}\text{Cr}_{0.03}\text{FePO}_4$	$[\text{Li}_{0.924}\text{Cr}_{0.021}][\text{Cr}_{0.008}\text{Fe}_{0.992}]\text{PO}_4$	0.021	0.008	2.004

the LiFePO_4 lattice in collaboration with M. Wagemaker *et. al.*¹¹⁶ Combined refinement of X-ray and neutron diffraction data was carried out on compounds with various dopant stoichiometries and the results are summarized in Table 3.1. Refinements of target compounds similar to those reported by Chung *et. al.* (ie. $\text{Li}_{1-x}\text{M}^{z+}_x\text{FePO}_4$) show a preference of the dopant to occupy the M1 site, although the quantity of dopant in the lattice is much less than targeted. In contrast, target compounds with charge-compensated stoichiometries (ie. $\text{Li}_{1-zx}\text{M}^{z+}_x\text{FePO}_4$, $x \leq 0.03$) were found to incorporate roughly all of the dopant, again with a preference for doping on the M1 site. At higher dopant concentrations, impurities are clearly detected by diffraction. Most importantly, the refinements showed the incorporation of the aliovalent dopant was balanced by lithium vacancies, which resulted in the charge of the iron ion in the lattice to remain at +2.00, ruling out the presence of Fe^{+3} holes. The resultant vacancies (9% for $\text{Li}_{0.88}\text{Zr}_{0.03}\text{FePO}_4$) were determined to be entirely localized on the M1 sites. Compositions which stabilized a high concentration of vacancies exhibited a larger unit cell volume as a result of oxygen-oxygen repulsion at the vacant M1 sites.

Although initial reports of LiFePO_4 described the electrochemical behavior as strictly two-phase in nature, solid solution behavior has been observed at room temperature in the $\text{Fe}^{+2}/\text{Fe}^{+3}$ region of $\text{Li}_x(\text{Mn}_y\text{Fe}_{1-y})\text{PO}_4$, $y < x$.^{137,138} The presence of manganese was thought

to disrupt a weak transition metal association which stabilizes the $\text{LiFePO}_4/\text{FePO}_4$ phase boundary.

An early model predicted the existence of two single compositional regimes, $\text{Li}_{1-y}\text{FePO}_4$ and Li_xFePO_4 , close in composition to the end-members LiFePO_4 and FePO_4 .¹³⁹ This was first confirmed experimentally by Yamada *et. al.*⁹¹ X-ray diffraction studies on bulk particles of various compositions of the chemically oxidized olivine confirmed the presence of two phases: a Li-rich phase with a unit cell volume less than that of pure LiFePO_4 and a Li-deficient phase with a unit cell volume greater than that of pure FePO_4 . Using Vegard's law, the limits of the solid solution were determined to be $\text{Li}_{1-y}\text{FePO}_4$, $y = 0.038$ and Li_xFePO_4 , $x = 0.032$. A further study using neutron diffraction to determine lithium content showed the miscibility gap to be narrower, where $y = 0.11$ and $x = 0.05$.¹⁴⁰ These monophasic regions of the electrochemical curve were also found to stray from the constant value of 3.42 V seen for the two-phase transition. This miscibility gap was found to be reduced upon decreasing particle size: values of $y = 0.12$ and $x = 0.06$ were obtained for 40 nm particles while values of $y = 0.17$ and $x = 0.12$ were obtained for 34 nm particles.⁹² Oxidation of LiFePO_4 upon exposure to air also results in the formation of $\text{Li}_{1-y}\text{FePO}_4$ solid solutions.^{141,142}

The discovery of thermally activated solid solution behavior over the entire compositional range of Li_xFePO_4 was made by Delacourt *et. al.*, based on temperature-dependant X-ray diffraction studies.^{88,143} Peaks from the $\text{Li}_{1-y}\text{FePO}_4$ and Li_xFePO_4 phases present at room temperature begin to broaden near 210 °C and completely coalesce near 300 °C for most compositions, giving rise to a set of sharp reflections characteristic of new Li_xFePO_4 phases. Upon cooling, these newly formed high-temperature phases demix into

FePO₄, LiFePO₄ and other metastable Li_xFePO₄ phases, later determined to include Li_{0.6}FePO₄.⁸⁹ Examination of the X-ray diffraction data at 350 °C revealed the presence of a single olivine phase for all compositions. The unit cell parameters at this temperature for each stoichiometry roughly followed Vegard's law.

This prompted us to study the dynamics of electron transport in these high temperature solid solutions using Mössbauer spectroscopy, using partially oxidized powders of bulk LiFePO₄ prepared by hydrothermal, sol-gel routes and nano-LiFePO₄ synthesized by a low-temperature precipitation route. We also studied the high-temperature characteristics of partially oxidized LiMnPO₄. Control of the morphology of the hydrothermally produced LiFePO₄ and LiMnPO₄ may be achieved through precise manipulation of the synthetic conditions as discussed below. The electrochemical performance of these compounds was also evaluated.

3.2 Synthesis of Olivine Compounds

Hydrothermal LiFePO₄: Carbon-free triphylite samples were prepared from (NH₄)₂Fe(SO₄)₂•6H₂O, H₃PO₄ and LiOH•H₂O in a 1:1:3 molar ratio. Carbon-containing samples were prepared from the same quantities and reagents as carbon-free materials with the addition of various organic additives (as described in the text), in the ratio of 1:1:3:0.25. For all syntheses, the reactants were stirred in a sealed 45 ml Parr autoclave at 140-220 °C for 0.5-24 hours. Subsequent sintering of the products took place at 600-800 °C under flowing argon.

Polyol LiFePO₄: prepared by a method similar to that reported by Kim et al. in 2006.¹⁴⁴ 2.175 g anhydrous iron acetate [Fe(CH₃COO)₂], 1.430 g ammonium dihydrogen phosphate (NH₄H₂PO₄) and 0.825 g anhydrous lithium acetate (LiCH₃COO) were added to 50 ml

tetraethylene glycol (TEG). The solution was slowly heated to 320 °C in a round-bottomed flask equipped with a reflux condenser and maintained at this temperature for 20 hours. The product was filtered, washed with acetone to remove TEG and dried in a vacuum oven at 150 °C for 24 hours.

Solid state LiFePO₄: prepared by ball milling stoichiometric amounts of FeC₂O₄•2H₂O, Li₂CO₃ and NH₄H₂PO₄ for 6-18 hours in a planetary ball mill. The powder was heated to 350 °C under argon to decompose the precursors. The mixture was then milled again for one hour, followed by a final heat treatment at 600-700 °C where LiFePO₄ formed.

Sol-gel LiFePO₄: prepared by dissolving stoichiometric quantities of Fe(NO₃)₃•9H₂O and LiH₂PO₄ in water. The solution was stirred and evaporated to dryness. The gel was fired at 500 °C under a reducing atmosphere (7% H₂, bulk N₂) to produce LiFePO₄.

Solid state LiMnPO₄: stoichiometric quantities of Mn(CH₃COO)₂, Li(CH₃COO) and NH₄H₂PO₄ were ground for 6-18 hours in a planetary ball mill. The mixture was heated to 350 °C under argon. The mixture was then milled again for one hour, followed by a final heat treatment at 600-700 °C.

Hydrothermal LiMnPO₄: prepared by a method similar to that stated for the synthesis of LiFePO₄. In short, a 1:1:0.25:3 molar ratio of MnSO₄•H₂O, H₃PO₄, carbon-containing organic additive and LiOH•H₂O was used to produce 5-20 mmol of LiMnPO₄. The first three precursors were dissolved in 15 ml H₂O in a 45 ml Parr reactor, while the LiOH•H₂O was dissolved in 15 ml H₂O in a separate beaker. The solution of LiOH was added to the solution in the reactor with vigorous stirring. Some of the carbon-containing additives used included ascorbic acid, citric acid and polyacrylic acid.

3.3 Hydrothermal Synthesis of LiFePO_4 : Synthetic Mechanism and Effect of Synthetic Conditions

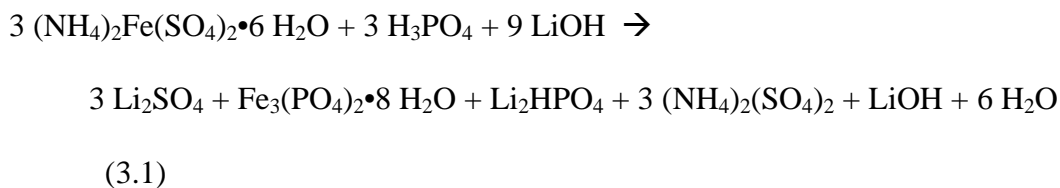
Powders of lithium metal phosphates and silicates can be easily prepared by a variety of synthetic routes. The most common are solid state methods in which precursors are ground or ball milled together and the resultant mixture is treated in a furnace.^{145–150} With iron compounds, inert gas or slightly reducing conditions are used to achieve an iron valence of Fe^{+2} . Carbon-coated particles result from the use of carbon-containing precursors or the addition of organic compounds which decompose to carbon during thermalisation. Sol-gel and solution deposition routes involve the mixing of appropriate precursors in solution, followed by drying and subsequent furnace treatment under inert or reducing atmosphere. When organic chelating agents are used to prepare the gel, a carbon coating is produced.

Low-temperature precipitation methods to prepare phosphates involve solution reflux. Crystalline olivine compounds can be precipitated from water,^{120,151} polyols^{144,152,153} and ionic liquids.^{154,155} Typically nanoparticles result as the solvent acts as a stabilizer and growth inhibitor for the particles. Hydrothermal and solvothermal methods have been reported for the preparation of LiFePO_4 at temperatures as low as $120\text{ }^\circ\text{C}$.^{98,99,156,157} These low-temperature synthesis routes may be preferred as they are not energy intensive.

Hydrothermal chemistry is one of the principal synthetic methods for the preparation of new inorganic materials. It is used to produce various nanomaterials such as zeolites, oxides and phosphates which are functional in catalysis, electrochemistry and separation science. These compounds may have intriguing morphologies such as nanospheres, nanowires and nanotubes. Morphology control of the products comes as a result of careful manipulation of concentration, pH and temperature.

The hydrothermal synthesis of LiFePO₄ was first published in 2001 by Yang *et al.*⁹⁸ In the reaction, a mixture of FeSO₄, H₃PO₄ and LiOH were combined in a 1:1:3 molar ratio. It was also reported that any water-soluble iron (II) salt, such as FeCl₂ and (NH₄)₂Fe(SO₄)₂ could also be used to produce LiFePO₄. Polycrystalline powders produced by these hydrothermal methods were carbon-free and thus did not exhibit good electrochemical capabilities. Furthermore, if the reaction temperature was kept relatively low (120-140 °C), site mixing, ie. Li on the M2 site and Fe on the M1 site, was found to occur which also adversely affected electrochemical performance.

Our study of the preparation of hydrothermal LiFePO₄ began with an investigation of the mechanism of its formation inside a hydrothermal container. The addition of lithium hydroxide to the mixture of ferrous ammonium sulfate and phosphoric acid resulted in the formation of a basic solution (pH = 8.3) and precipitation of an amorphous green solid which turned yellow when dried, which clearly indicated the product oxidized on drying. Lithium sulfate was detected in the filtrate after the water was evaporated. Ascorbic acid, a well-known reducing agent, was added to the mixture of ferrous ammonium sulfate and phosphoric acid to prevent iron oxidation. Addition of lithium hydroxide to this solution also produced a crystalline green precipitate: vivianite, (Fe₃(PO₄)₂•8H₂O). Lithium sulfate was again detected in the remaining solution. In general, we conclude the initial reaction in the hydrothermal vessel (before heating) is:



Pure LiFePO_4 may be produced when the reagents are heated to $190\text{ }^\circ\text{C}$ for as little as 5 hours; the bombs were exposed to shorter heating periods to try to isolate intermediates. A summary of the resultant X-ray diffraction patterns and SEM micrographs is shown in Figure 3.3. Hydrothermal treatment of the basic mixture at $190\text{ }^\circ\text{C}$ for 30 minutes produced an intermediate phase, formed as crystalline “nanoleaflets” detectable by X-ray diffraction (Figure 3.3a). It exhibited a relatively weak and disordered XRD pattern, albeit with one very strong, characteristic reflection at $2\theta = 9.8^\circ$. Elemental analysis of material extracted from the autoclave and filtered at this stage confirmed a Li:Fe ratio of approximately 1:5, indicative of partial reaction of the initial vivianite formed with the compounds present in the autoclave. Sintering of this intermediate at $600\text{ }^\circ\text{C}$ under Ar produced a mixture of triphylite and graffonite ($\text{Fe}_3(\text{PO}_4)_2$), again indicating partial reaction of the vivianite.

When the hydrothermal reaction was stopped after 90 minutes at the same temperature, a new morphology was evident in the SEM. The appearance of larger crystallites coincided with the detection of triphylite in the XRD pattern (Fig 3.3b). The reaction had not gone to completion at this point, as some leaflets remained in the hydrothermal product, and the pronounced intermediate peak remained in the diffraction pattern. After 5 hours, the leaflets fully reacted to produce larger crystallites (Figure 3.3f) which were determined to be LiFePO_4 , as seen by the pure olivine phase in the X-ray diffraction pattern (Figure 3.3c).

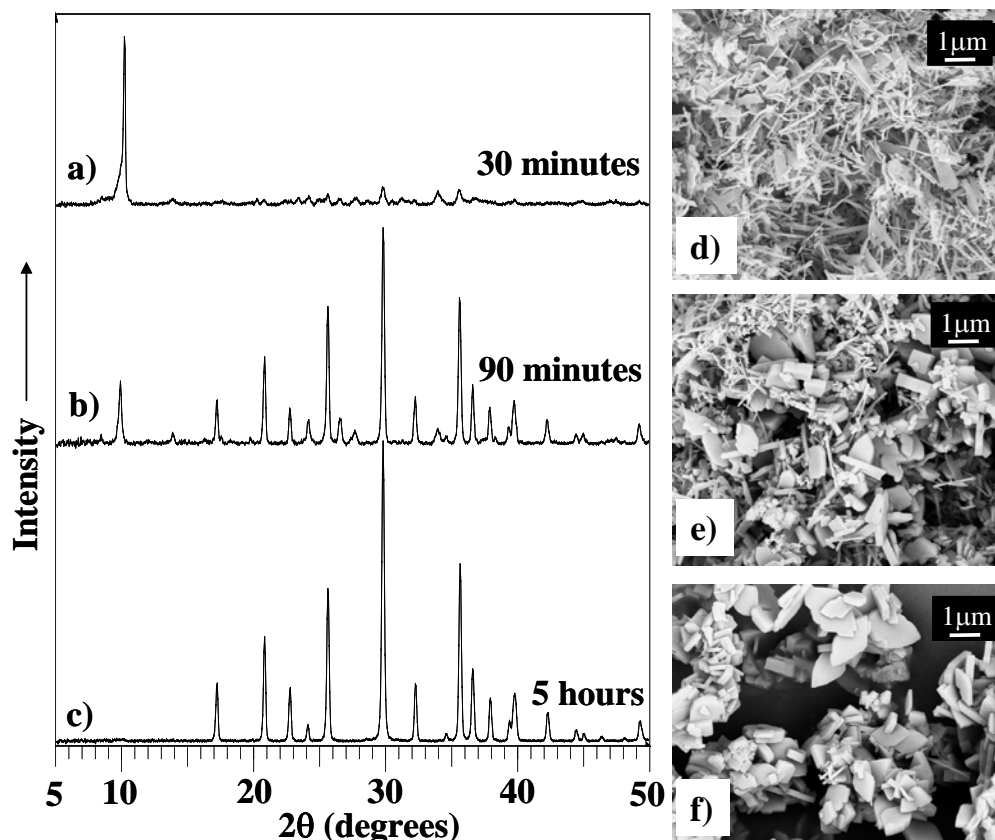


Figure 3.3: Powder X-ray diffraction patterns and corresponding SEM micrographs of hydrothermal LiFePO_4 after various reaction times, depicting the presence of an intermediate that reacts to form LiFePO_4 : 30 minutes (a, d), 90 minutes (b, e) and 5 hours (c, f). Reproduced from reference ⁹⁴ with permission from the Royal Society of Chemistry.

The XRD pattern of the intermediate, and its morphology (Figure 3.3d) suggested it may be related to $\text{NH}_4\text{FePO}_4 \cdot \text{H}_2\text{O}$, whose XRD pattern is also dominated by a very prominent high-intensity reflection at $2\theta = 9.8^\circ$ (JCPDS #45-0424), as shown in Figure 3.4. This peak corresponds to the (010) reflection in the $\text{Pmn}2_1$ space group, and the intensity is due to a high degree of preferred orientation arising from the thin plate morphology exhibited by this material. Comparison of the structures of LiFePO_4 (Figure 3.4a) and $\text{NH}_4\text{FePO}_4 \cdot \text{H}_2\text{O}$ (Figure 3.4b) indicates how they could be related by a simple transformation. The connectivity of the iron and phosphate polyhedra in the (100) plane of LiFePO_4 is identical to that in the corresponding (101) plane of $\text{NH}_4\text{FePO}_4 \cdot \text{H}_2\text{O}$ (note the difference in the space

groups switches the a and b axes); similarly, the d-spacing corresponding to the (020) reflection in LiFePO_4 is almost the same as the (200) reflection for $\text{NH}_4\text{FePO}_4\cdot\text{H}_2\text{O}$ since the repeating polyhedral motif is the same, as illustrated in Figure 3.4. We surmised the precursors which initially precipitated in the autoclave (ie. $\text{Fe}_3(\text{PO}_4)_2\cdot 8\text{H}_2\text{O}$ and other amorphous solids) reacted with excess NH_4^+ in solution when the vessel was first exposed to heat and pressure to first form the ammonium intercalated solid $\text{NH}_4\text{FePO}_4\cdot\text{H}_2\text{O}$ (Figure 3.4b). The next step in the reaction was the rapid subsequent exchange of NH_4^+ for Li^+ in the

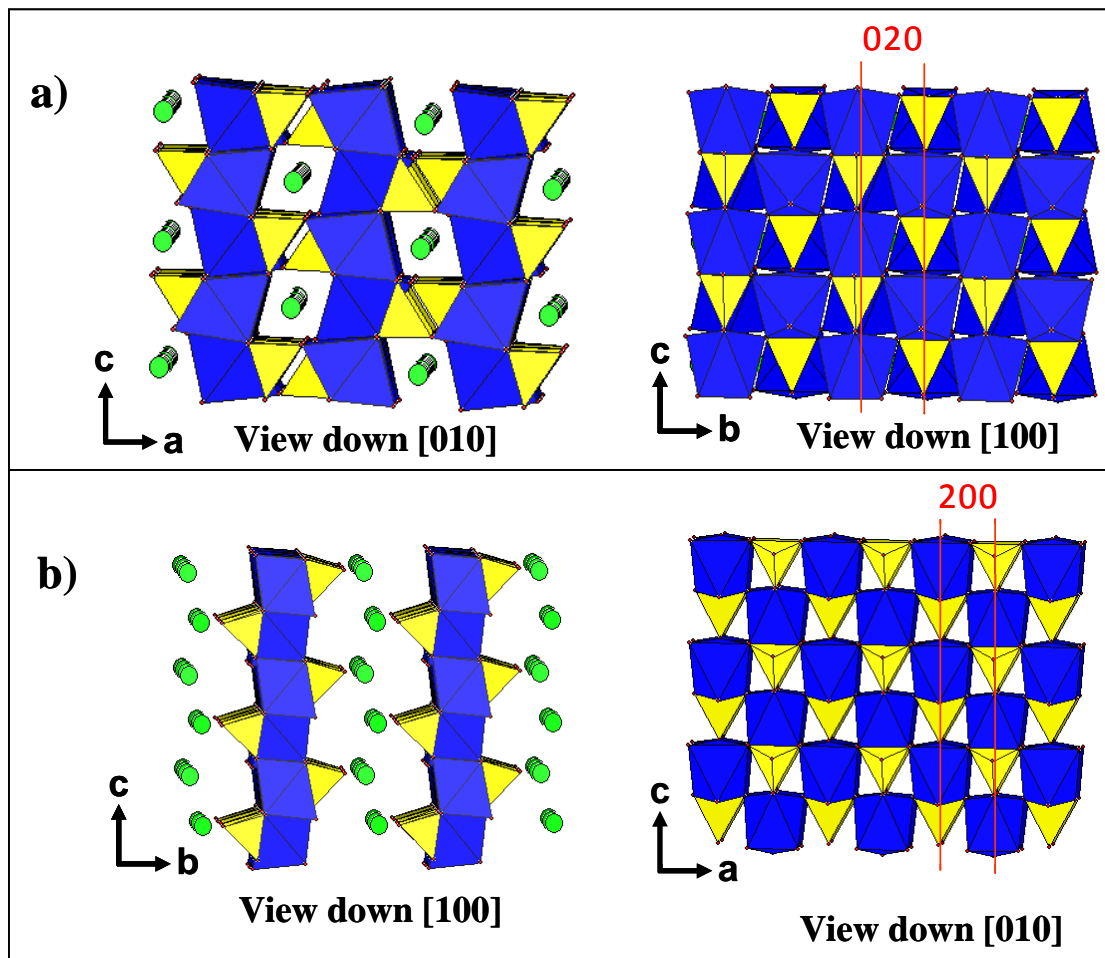


Figure 3.4: a) The olivine structure, adopted by several minerals including LiFePO_4 , in the space group Pnma ; b) structure of $\text{NH}_4\text{FePO}_4\cdot\text{H}_2\text{O}$ in the space group $\text{Pmn}2_1$ showing the comparison to the olivine structure. For each, iron octahedra are shown in blue, phosphate tetrahedra in yellow and $\text{Li}^+/\text{NH}_4^+$ ions in green. Reproduced from reference ⁹⁴ with permission from the Royal Society of Chemistry.

autoclave solution: the reaction intermediate seen after 30 minutes of reaction in the autoclave was not pure $\text{NH}_4\text{FePO}_4\cdot\text{H}_2\text{O}$, but a material that already underwent partial Li^+ exchange to give rise to a disordered material, evident from the X-ray diffraction pattern of the sintered intermediate. The mechanism of final step, the crystallization of olivine LiFePO_4 , is not precisely known. The lithium-substituted intermediate may have undergone a pressure-induced transformation to form the final product or a dissolution-reprecipitation step may have been involved.

An X-ray diffraction pattern and Rietveld refinement of a sample of hydrothermal LiFePO_4 prepared at 190 °C is shown in Figure 3.5. The full summary of the refinement result may be found in Table 3.2. The theoretical peaks of LiFePO_4 match very well with the pattern, although the intensities are slightly off. To ascertain any Fe-Li site mixing, as previously speculated, an additional Fe atom was placed on the lithium site and the total occupancy of the iron atoms was constrained to be one (a lithium atom was also placed on the iron site to account for valence compensation). This produced a much better fit: a minimum residual error value was reached when the value of iron on the M1 site was about 2.3%.

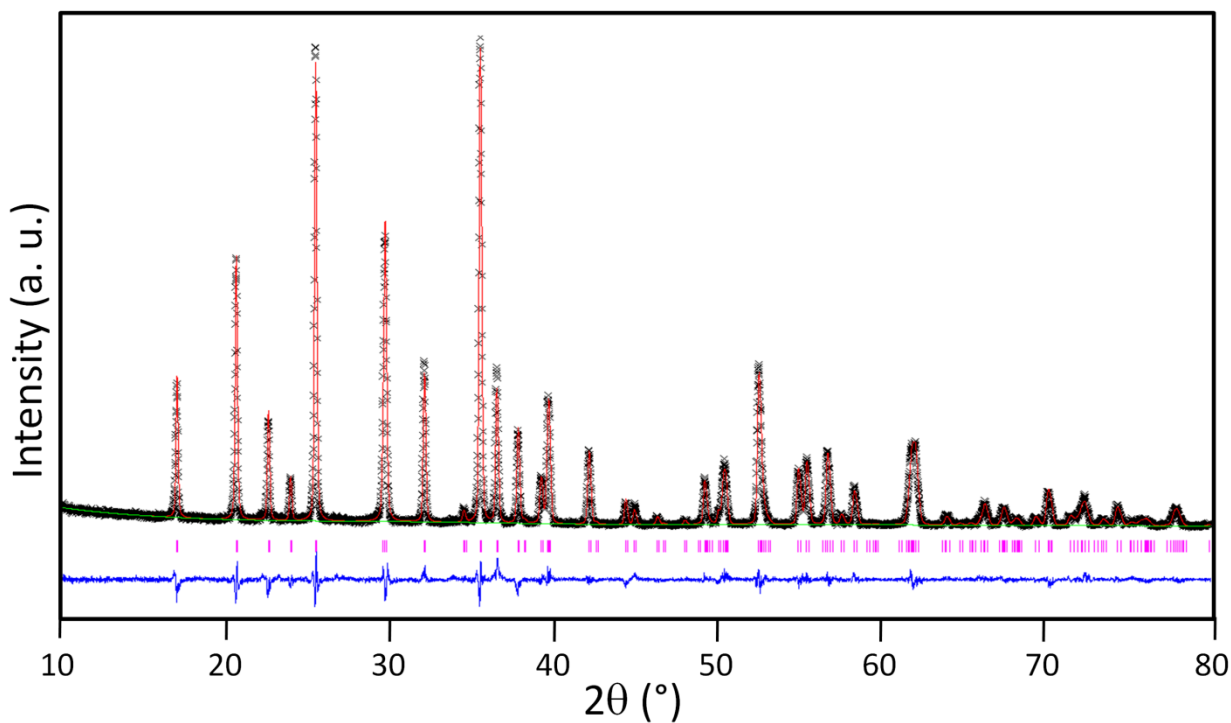


Figure 3.5: Rietveld refinement of hydrothermally-prepared LiFePO_4 at 190°C . The calculated pattern is shown in red, experimental data in black, phase lines for LiFePO_4 in magenta and difference map in blue. Details of the refinement are given in Table 3.2.

Table 3.2: Lattice constants and atomic parameters for hydrothermal LiFePO_4 refined from X-ray diffraction powder data. X-ray diffraction agreement factors: $R_{\text{wp}} = 9.88\%$, $R_p = 7.59\%$, $\chi^2 = 1.953$.

LiFePO_4					
Space group: Pnma (#62), Orthorhombic					
$M_w = 157.76 \text{ g/mol}$					
$a = 10.3361(1) \text{ \AA}$					
$b = 5.9902(1) \text{ \AA}$					
$c = 4.6993(1) \text{ \AA}$					
$V = 290.96(1) \text{ \AA}^3$					
Atom	x/a	y/b	z/c	Occ.	U_{iso}
Li(1)	0	0	0	0.977(1)	0.015
Fe(1)	0	0	0	0.023(1)	0.015
Li(2)	0.2816(2)	1/4	0.9753(3)	0.023(1)	0.006(1)
Fe(2)	0.2816(2)	1/4	0.9753(3)	0.977(1)	0.006(1)
P(1)	0.0956(1)	1/4	0.4169(4)	1.0	0.011(2)
O(1)	0.0931(4)	1/4	0.7516(5)	1.0	0.012(2)
O(2)	0.4521(4)	1/4	0.2207(5)	1.0	0.011(2)
O(3)	0.1613(4)	0.0423(5)	0.2775(6)	1.0	0.011(2)

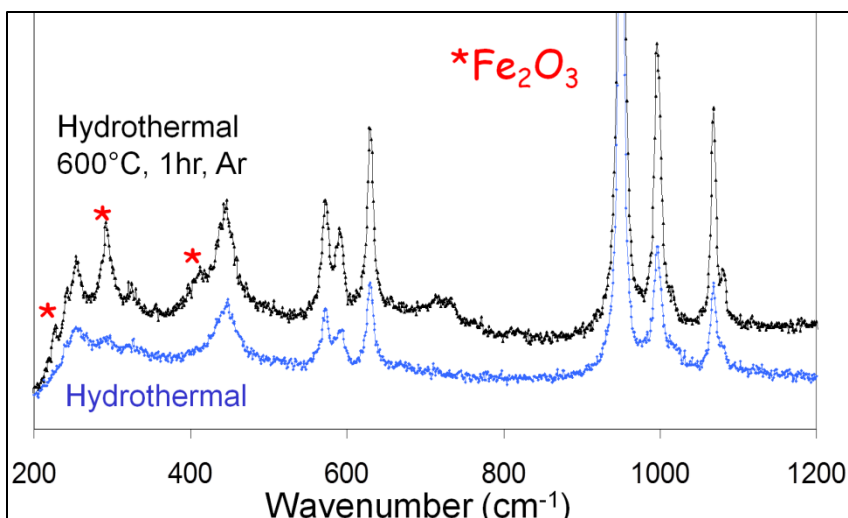


Figure 3.6: Raman spectra of LiFePO₄ collected straight after filtration (blue) and after being fired under Ar at 600 °C (black). Peaks of Fe₂O₃ are marked. Reproduced from reference ⁹⁴ with permission from the Royal Society of Chemistry.

The purity of the products depended predominantly on the oxygen content of the gaseous headspace in the autoclave, and the oxidizing power of the medium. Trace impurity phases containing Fe³⁺ such as tavorite (LiFePO₄OH), formed along with LiFePO₄ if the atmosphere was oxidizing. Tavorite is known to form under mild hydrothermal conditions and upon subsequent heat treatment in excess of (550 °C), tavorite decomposes to Li₃Fe₂(PO₄)₃ and Fe₂O₃.⁹⁹ Although these ferric compounds were formed in trace quantities in the reactor and were not readily detectable by X-ray diffraction, they could be detected by Raman spectroscopy. Figure 3.6 shows the Raman spectrum of LiFePO₄ directly after collection from the hydrothermal reactor which was loaded in ambient conditions. The spectrum looks much like that reported previously for LiFePO₄,^{158,159} highlighted by three prominent P-O stretching bands between 900 and 1100 cm⁻¹. Although not seen clearly in the diffraction pattern, Fe₂O₃ was clearly visible in a Raman spectrum of a sample fired at 600 °C under argon, as the surface Fe³⁺ impurities had crystallized. These impurities were detrimental to the electrochemical performance of LiFePO₄, and could be eliminated by purging oxygen

from the solution and the headspace by bubbling nitrogen into the solution. When hydrothermal LiFePO_4 prepared in this fashion was filtered, dried, and subjected to further heating at $600\text{ }^\circ\text{C}$ in argon, it was found to be free of Fe_2O_3 and any other Fe^{3+} impurities.

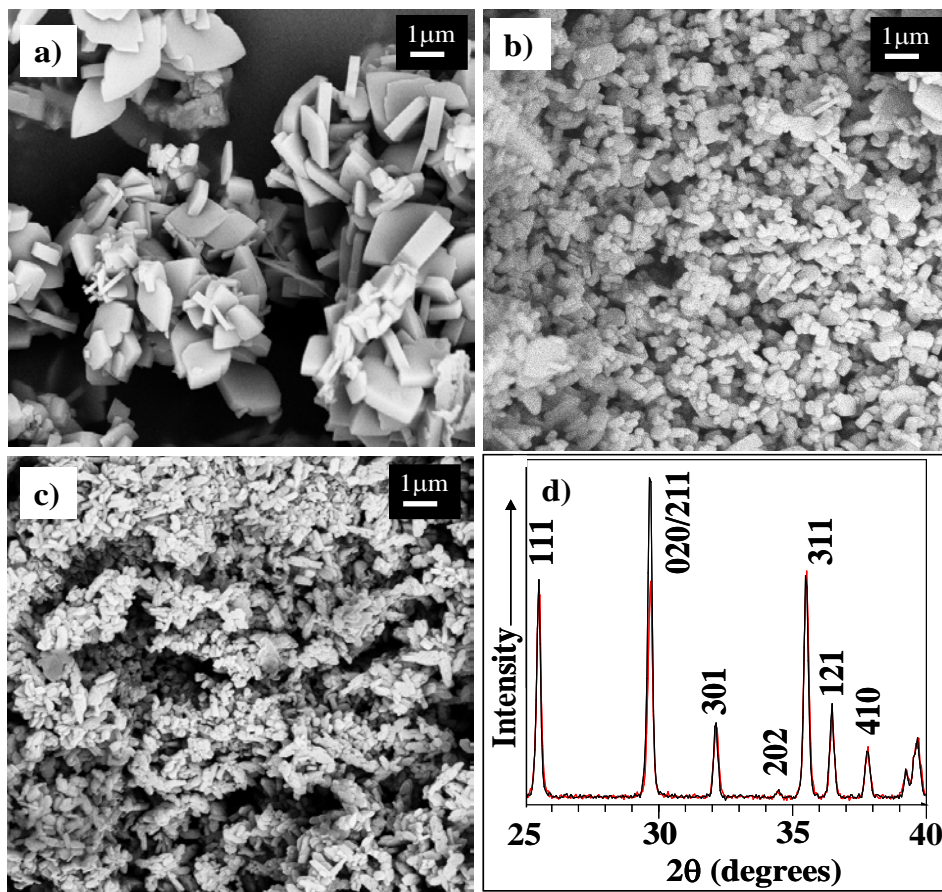


Figure 3.7: SEM micrographs of carbon-free LiFePO_4 crystallized at different concentrations and temperatures: a) 0.25M (Fe), 190°C ; b) 0.25M (Fe), 140°C ; c) 0.75M (Fe), 190°C . Figure 3d shows the XRD patterns of the compounds synthesized at 190°C (0.25M (Fe) in black, 0.75M (Fe) in red). Preferred orientation in the (020) direction is seen in the 0.25M sample.

The size of the crystallites in the absence of organic additives was controlled predominantly by the reaction temperature and concentration of the precursors in the autoclave. At $190\text{ }^\circ\text{C}$, typical low concentrations of precursors (7 mmol of $(\text{NH}_4)_2\text{Fe}(\text{SO}_4)_2 \cdot 6\text{H}_2\text{O}$ in 28 ml of water (0.25 M in Fe) along with stoichiometric amounts of H_3PO_4 $\text{LiOH} \cdot \text{H}_2\text{O}$) produced diamond-shaped platelets that were about 250 nm thick which had large basal dimensions in the range of 1-5 μm as seen in Figure 3.7a. Increasing the

reactant concentration by threefold created more nucleation sites and therefore produced much smaller particles whose basal size distribution peaks around 250 nm, as seen in Figure 3.7b. The corresponding X-ray diffraction patterns are shown in Figure 3.7d. The two patterns are normalized to the intensity of the most intense peak for triphylite, the (211) peak at 35.6°. While most of the peaks are of similar intensity, it was evident that the peak at 29.8° was much more intense for the materials prepared using the lower concentration. As shown by Chen, the large diamond-shaped surfaces of hydrothermally prepared LiFePO₄ correspond to the *ac* plane, which is perpendicular to the (020) direction.¹⁶⁰ Accordingly, the increased intensity of the peak at 29.8° we observed was the result of preferred orientation in the (020) direction. This is significant since this direction is the most facile pathway for lithium mobility in the material, as predicted by consideration of the structure, and as calculated previously.^{111,112} The large exposure of the electrochemically active crystal face represents approximately 80% of the surface area of each individual particle, and thus the thin profile of these particles reduces the lithium diffusion path length.

Although this prevailing morphology may show potential for improved electrochemistry, reducing the overall particle size of the electrode material is also important. As is the case with solid state or sol-gel techniques, this was accomplished with our hydrothermal route by synthesis at lower temperatures. Material synthesized at 140 °C using an autoclave concentration of 0.25 M (Fe) produced substantially smaller particles than crystallites synthesized at 190 °C, as clearly seen in the SEM micrograph (Figure 3.7c). The former temperature was found to be the minimum temperature the autoclave must reach in order to produce pure LiFePO₄. The heating period has little effect on the morphology of the hydrothermal product once the minimum reaction time (3 hours) was surpassed.

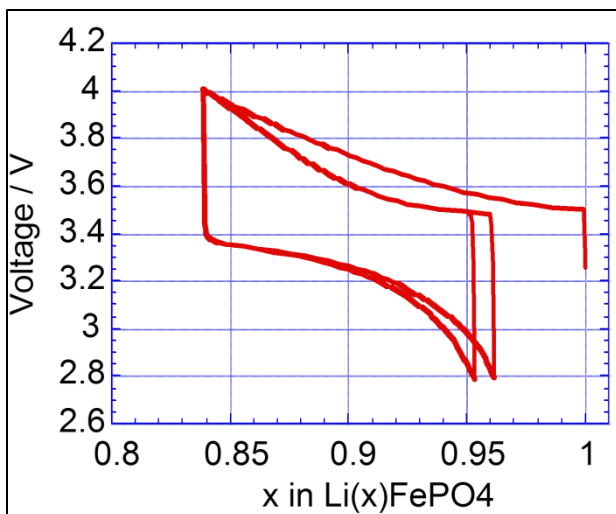


Figure 3.8: Typical electrochemical profile of hydrothermal LiFePO₄.

Despite the relatively small average particle size of the LiFePO₄ as well as the lack of Fe³⁺ impurities present in these samples, the electrochemical properties of these carbon-free samples was found to be poor. Figure 3.8 shows the electrochemical profile of a 0.25 M batch of hydrothermal LiFePO₄ prepared at 190 °C and cycled at a rate of C/10. The profile did not exhibit the usual plateau at 3.5 V but instead charged quickly to the upper voltage limit with only 15% of the lithium deintercalated from the structure. The electronically-insulating nature of the LiFePO₄ particles prevented any significant electrochemical performance and prompted us to explore hydrothermal synthesis of carbon-coated LiFePO₄ as discussed below.

3.4 Modified Hydrothermal Synthesis: Use of Carbonaceous Additives

While the headspace of the autoclave is critical to producing single phase materials, organic compounds were added to the bombs to act as internal reducing agents. Carbon-containing molecular compounds such as ascorbic acid, sucrose and citric acid have been utilized previously as carbon sources and reducing agents in various sol-gel and solid state

methods for making LiFePO_4 .^{125,148,161} Furthermore, subsequent heating of these organic compounds in inert atmospheres decomposed these compounds into carbonaceous films, depositing a thin conductive layer of carbon on the triphylite particles.

We prepared LiFePO_4/C composites by adding organic compounds into the hydrothermal reactor in a 0.25:1 mole ratio with iron. Products recovered from samples prepared at low concentration of precursors (0.25 M in Fe), containing ascorbic acid or citric acid heated at 190 °C and subsequently fired at 600 °C in flowing Ar, were all identified as pure LiFePO_4 by X-ray diffraction. SEM micrographs of the products are presented in Figures 3.9a and 3.9b. Comparing the morphologies of these two samples with that in Figure

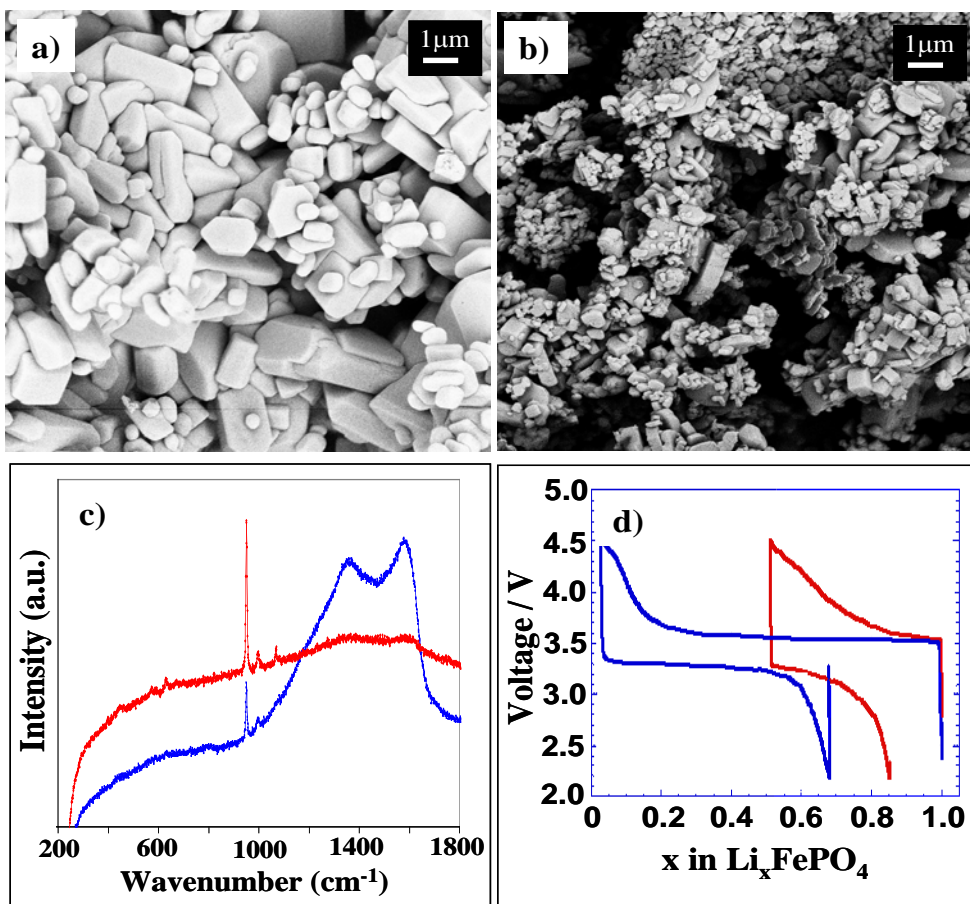


Figure 3.9: SEM images of hydrothermal LiFePO_4 treated with citric acid (a, red) and ascorbic acid (b, blue) in the reactor. The ascorbic acid decomposed, depositing carbon (Raman spectrum, 3c) and produces material with better electrochemical character at a rate of C/10 (3d). Reproduced from reference⁹⁴ with permission from the Royal Society of Chemistry.

3.7a confirmed that the presence of a decomposable reducing agent strongly affected the morphology: ascorbic acid decomposes near 200 °C when heated. The decomposed ascorbic acid was found to both affect morphology and deposit a carbonaceous coating on the particles. The particle size of the ascorbic acid sample was substantially smaller (250 - 1.5 μm) than that of LiFePO_4 prepared without any reducing agent.

Raman spectroscopy was used to study the carbon microstructure. The Raman spectra show two important frequencies for carbon: 1350 cm^{-1} corresponding to disorder in sp^2 -hybridized carbon (*D*-band) and 1590 cm^{-1} corresponding to tangential stretching in graphitic materials (*G*-band).^{162,163} The Raman spectra (Figure 3.9c) clearly show the presence of significant quantities of carbon, approximately 5% by mass as determined by TGA measurements in oxygen.

Conversely, LiFePO_4 prepared with citric acid, a more thermodynamically stable organic additive than ascorbic acid, resulted in a wide distribution of particle sizes (500 nm - 3 μm). Furthermore, the morphology of these samples did not exhibit the monolithic sponge appearance of samples made with citrates in the solid state.¹⁶⁴ Owing to the increased stability of citric acid, a minimal amount of carbon was detected on the surface of these particles, as seen by the very low intensity of the carbon peaks in the Raman spectrum.

These discrepancies in particle size and carbon content were clearly evident in a comparison of the electrochemistry of the two materials (Figure 3.9d). With substantially more carbon and smaller average particle size, almost 100% of the lithium could be extracted from and 70% of the lithium reinserted into LiFePO_4 prepared with ascorbic acid on the first cycle at a rate of C/10. In contrast, only 50% of the lithium could be extracted from the sample prepared with citric acid and 35% could be reintercalated when cycled at the same

rate of C/10. Clearly, the presence of carbon greatly affects the electrochemical performance of LiFePO_4 powders, however the presence of substantial amounts of carbon reduces the energy density of cells prepared with these materials as the carbon is not electrochemically active.

Nanoparticles of LiFePO_4 could be synthesized hydrothermally in the presence of water-soluble polymers, such as polyacrylic acid. Hydrothermal treatment with this additive produced 300 - 500 nm diameter agglomerated clusters which consisted of very small particles that were 75-100 nm in size (Figure 3.10). A diffraction pattern, together with a LeBail fit of the data is shown in Figure 3.10. The unit cell volume and the a lattice

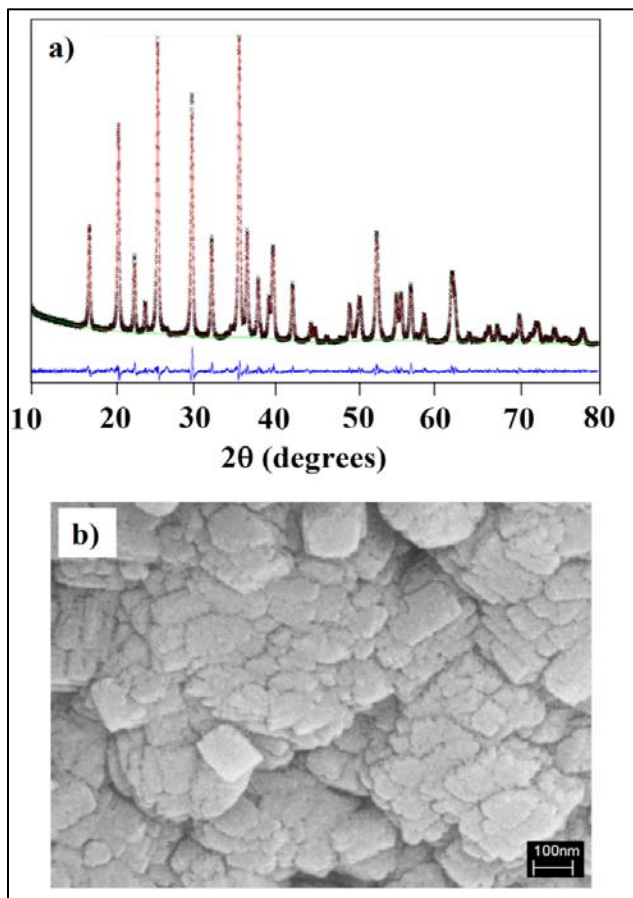


Figure 3.10: XRD pattern and LeBail (full pattern matching) refinement (a) and SEM micrograph (b) of LiFePO_4 synthesized hydrothermally in the presence of a water-soluble polymer, polyacrylic acid. The experimental (x) and calculated (-) diffraction patterns are shown, along with the difference curve (blue). Lattice parameters and the agreement factor are given in Table 3.3.

parameter are noticeably smaller than those for typical hydrothermal or solid state LiFePO₄, as summarized in Table 3.3. Decreased unit cell volumes for particles < 100 nm in size has been reported earlier.¹⁴² The likely cause is surface oxidation of iron to Fe³⁺ and subsequent removal of trace amounts of lithium (up to 7%) from the lattice as a result of air exposure of as little as a few hours.¹⁴¹ This surface oxidation was not prevalent for bulk particles of LiFePO₄ which were found to be stable in air for weeks. The increase or decrease of lattice parameters of nano-powders, as compared to bulk phases, is a phenomenon reported for other transition metal compounds: the decrease in the lattice parameters of triphylite particles < 100 nm is similar to that seen in other oxides of iron (γ -Fe₂O₃)¹⁶⁵ and cobalt (Co₃O₄).¹⁶⁶ In these cases, the decrease in lattice parameter was attributed to strain on the particles as a result of high surface tension. In contrast, cerium oxide, known to commonly undergo point defects in the bulk phase, undergoes an increase in lattice parameters.¹⁶⁷

Table 3.3: Typical lattice parameters for olivines prepared by different synthetic routes with varying particle size. Reproduced from reference⁹⁴ with permission from the Royal Society of Chemistry.

LiFePO ₄ Synthetic Route	Average Crystallite Size (nm)	<i>a</i> (Å)	<i>b</i> (Å)	<i>c</i> (Å)	V (Å ³)	wRp (%)
Solid State	280	10.3222(2)	6.00566(8)	4.6941(1)	290.99	5.25
Hydrothermal	700	10.3328(2)	6.00296(5)	4.6950(1)	291.22	7.94
Nanocrystalline Hydrothermal	100	10.3089(1)	5.9849(1)	4.6970(1)	289.79	6.65
LiMnPO ₄ Synthetic Route	Average Crystallite Size (nm)	<i>a</i> (Å)	<i>b</i> (Å)	<i>c</i> (Å)	V (Å ³)	wRp (%)
Solid State	300	10.4430(2)	6.1014(1)	4.7430(1)	302.22	6.12
Hydrothermal	550	10.4456(1)	6.09815(6)	4.7456(1)	302.29	5.61
Nanocrystalline Hydrothermal	80	10.4476(1)	6.10225(7)	4.7485(1)	302.74	5.20

3.5 High Temperature Mössbauer Studies on LiFePO_4

When lithium is partially extracted from the structure of LiFePO_4 , formation of a $\text{LiFePO}_4/\text{FePO}_4$ mixture is in part driven by the 6.6% volume change between the phases.⁵⁰ The solubility of the two phases at room temperature is not accurately known: some reports suggest a pure two-phase coexistence with no mutual solubility, whereas others give evidence for very narrow single-phase regimes $\text{Li}_\alpha\text{FePO}_4$ and $\text{Li}_{1-\beta}\text{FePO}_4$ at room temperature, with α and $1-\beta$ reported with values up to 0.05 and 0.89 respectively.¹⁴⁰ However, at elevated temperatures, the solubility increases to 100%: it was previously shown that a transition to a Li_xFePO_4 ($0 < x < 1$) solid solution phase occurs at about 485 K^{88,143} which could be quenched on rapid cooling.^{90,168} This was a solid solution with respect to lithium concentration, where lithium occupation was found to be random within the lattice.

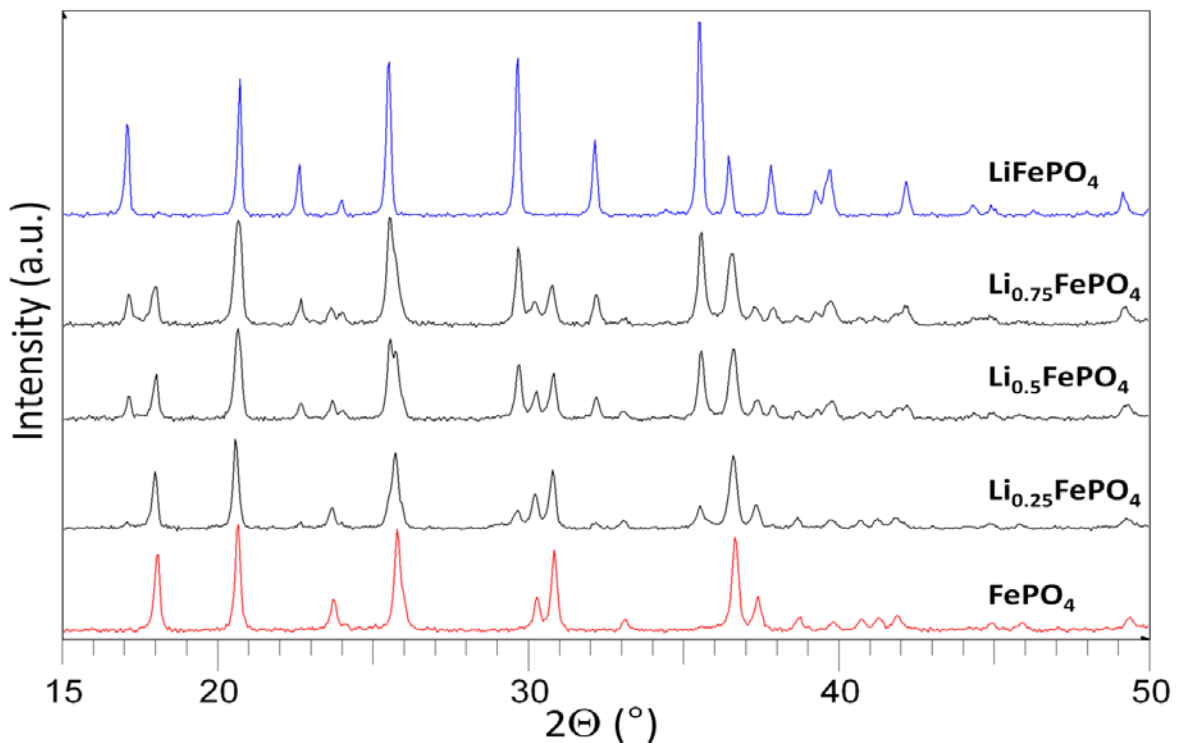


Figure 3.11: X-ray diffraction patterns of $\text{Li}_{1-x}\text{FePO}_4$ prepared from oxidation of LiFePO_4 . A two-phase transition to FePO_4 is evident.

We endeavoured to determine the onset temperature of electron delocalization and determine if there was a correlation to the state of lithium disorder. Three samples were prepared: $\text{Li}_{0.75}\text{FePO}_4$ and $\text{Li}_{0.55}\text{FePO}_4$ made by a carbon-free sol-gel method, and $\text{Li}_{0.25}\text{FePO}_4$ made by the solid state method. The stoichiometries were achieved by partial oxidation of LiFePO_4 with NOBF_4 as per the following reaction:



Partial oxidation resulted in intimate two-phase mixtures of LiFePO_4 and FePO_4 . X-ray diffraction patterns of the three samples collected at room temperature are shown in Figure 3.11, along with that of pure lithiated end-member LiFePO_4 and the delithiated end-member FePO_4 . Clearly, each intermediate stoichiometry was comprised of a mixture of LiFePO_4 and FePO_4 relative to the target stoichiometry.

The room temperature Mössbauer spectra of the two parent compositions, LiFePO_4 and FePO_4 , along with those of the two-phase mixtures of $\text{Li}_{0.75}\text{FePO}_4$, $\text{Li}_{0.55}\text{FePO}_4$ and $\text{Li}_{0.25}\text{FePO}_4$, are displayed in Figure 3.12. The contributions of the localized, static Fe^{2+} and Fe^{3+} components in the two phase mixtures were readily apparent and characterized by two doublets with Mössbauer parameters of $\text{IS} = 1.2 \text{ mm/s}$, $\text{QS} = 3.0 \text{ mm/s}$ and $\text{IS} = 0.42 \text{ mm/s}$, $\text{QS} = 1.5 \text{ mm/s}$, typical of Fe^{2+} and Fe^{3+} in these materials, respectively.¹⁴⁶ The relative areas of the two components confirmed that the target stoichiometries were achieved through chemical oxidation. The samples typically contained about 5% of impurity phases, which were apparent in the spectra shown in Figure 3.12 as additional lines: trace amounts of unreduced precursor were found in the spectrum of LiFePO_4 and unoxidized triphylite was found in the spectrum of FePO_4 , though these were not detectable by X-ray diffraction.

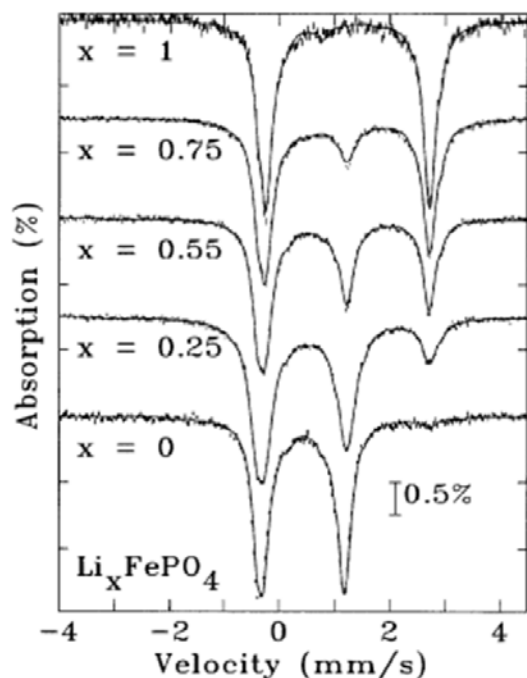


Figure 3.12: Room temperature Mössbauer spectra of Li_xFePO_4 compositions showing localized Fe^{2+} and Fe^{3+} components. Reprinted with permission from reference ⁹³, copyright 2006, American Chemical Society.

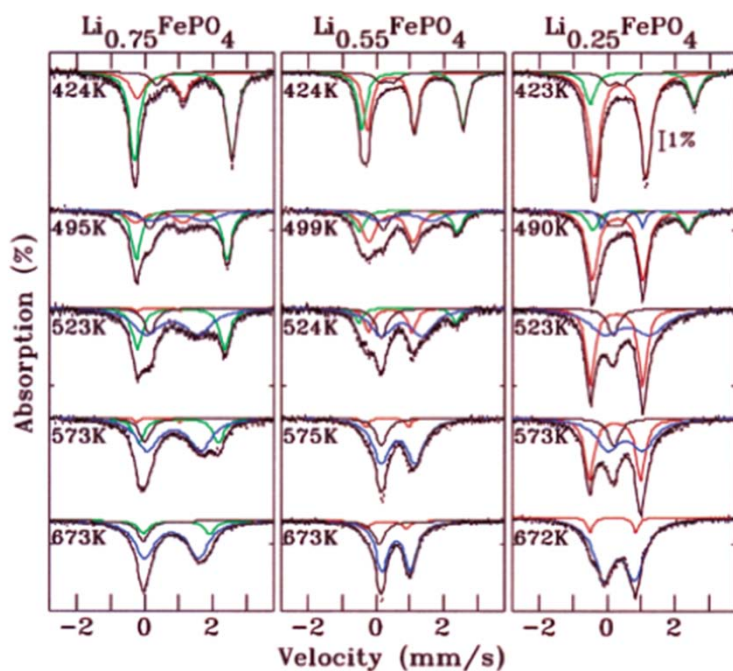


Figure 3.13: Mössbauer spectra at elevated temperatures illustrating the evolution from two-phase compositions to solid-solution $\text{Li}_x\text{Fe}^{2+/3+}\text{PO}_4$ as a function of temperature. Additional lines show the contributions of Fe^{2+} (green) Fe^{3+} (red) and solid solution (blue). Reprinted with permission from reference ⁹³, copyright 2006, American Chemical Society.

Mössbauer spectra recorded at temperatures above 400 and up to 700 K illustrate the evolution from the initial two phase composition to the solid solutions $\text{Li}_x\text{Fe}^{2+/3+}\text{PO}_4$ as a function of temperature (Figure 3.13). For each temperature point, the sample was maintained at said temperature for three hours, followed by a counting time of 20 h, which resulted in an overall time of 1 day per temperature. The time period was chosen on the basis of the XRD studies of solid solution behavior in this system that utilized a 12 h heating period to achieve “quasi-equilibrium” at any selected temperature.⁸⁸ At 650 K, it was reported that equilibrium was reached rapidly within 30 min, but below 500 K, the kinetics were more sluggish. Even in this regime, however, very little change was observed between 12 hours and 3-4 days.

As shown in Figure 3.13, the changes in the Mössbauer spectra as a function of temperature are clearly evident for each stoichiometry. On heating the samples to 425 K, each spectrum was dominated by the contributions of the parent phases, LiFePO_4 and FePO_4 . By 500 K, a new phase was visible that increases in fraction along with diminution of the parent phases on further heating. By 670 K, transformation to a single phase regime was essentially complete and the corresponding spectra were dominated by one doublet.

The quantitative changes in the spectra on heating are more clearly seen by examining the temperature dependence of the fitted parameters. Figure 3.14 shows the variation in the isomer shift of the Fe^{2+} and Fe^{3+} components along with that of the solid solutions for $\text{Li}_{0.75}\text{FePO}_4$, $\text{Li}_{0.55}\text{FePO}_4$ and $\text{Li}_{0.25}\text{FePO}_4$. Two important findings were evident from the plot. First, as mentioned above, a new phase signal in the Mössbauer spectra was evident for each stoichiometry around 495 ± 15 K. This is in good accord with the

temperature of Li disorder found by XRD measurements that place it about 473-493 K. Second, the value of the isomer shift of the new solid-solution phase (IS_{SS}) was between that of the parent Fe^{2+} and Fe^{3+} phases, which implied the iron valence of this phase was intermediate between Fe^{2+} and Fe^{3+} . Furthermore, the average oxidation state of the starting two-phase mixture dictated the precise value of the solid solution isomer shift: with increased Fe^{3+} , the average valence of the solid solution phase increased, and this was reflected in the lower IS_{SS} . Similar valence averaging has been reported in CoO and NiO at high temperatures.¹⁶⁹

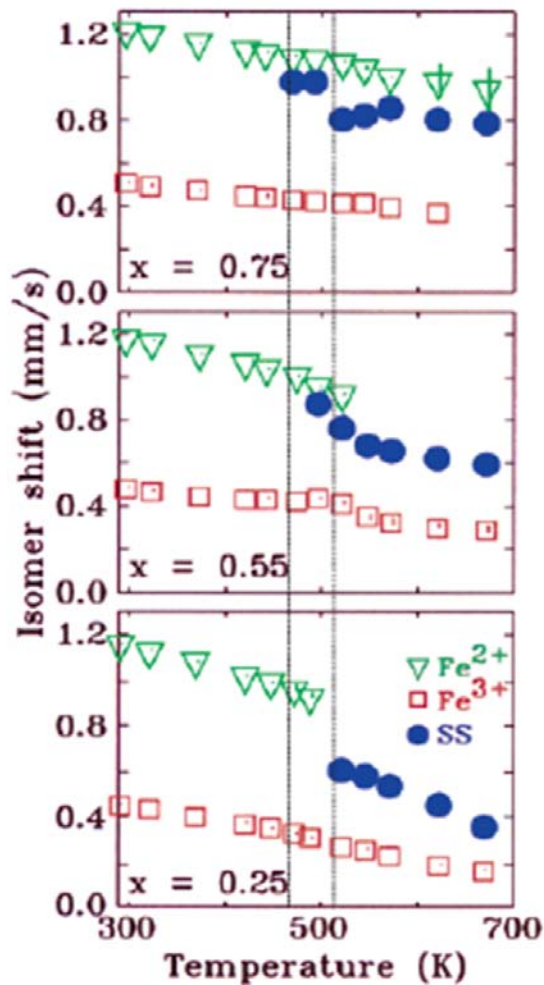


Figure 3.14: Change in isomer shift of the Fe^{2+} , Fe^{3+} and solid-solution phases as a function of temperature. The dotted lines denote the range of transition temperature. Reprinted with permission from reference ⁹³, copyright 2006, American Chemical Society.

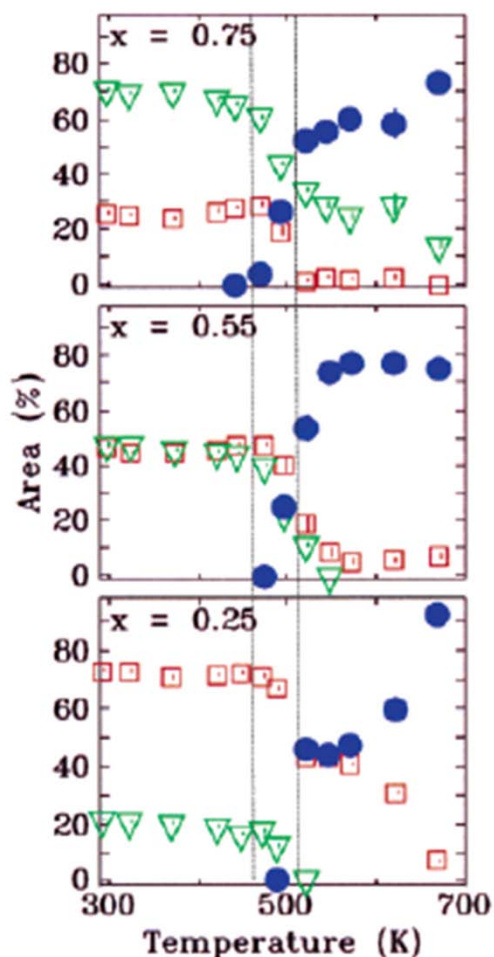


Figure 3.15: Relative areas of Fe²⁺, Fe³⁺ and solid solution regime as a function of temperature. Reprinted with permission from reference ⁹³, copyright 2006, American Chemical Society.

The temperature at which the parent phases are replaced by the solid solution phase is clearly seen in a plot of the relative phase fractions as a function of temperature, shown in Figure 3.15. The areas represent the close-to-equilibrium state of the samples as described above. The average onset temperature for appearance of the solid solution (495 K) was essentially the same as reported in XRD studies (475-495 K), as mentioned above. The latter reported the onset of the transformation of two-phase mixtures of LiFePO₄/FePO₄ into a solid solution Li_xFePO₄ as composition independent, however. Our Mössbauer studies showed that the temperature varied slightly with Li composition and, hence, Fe²⁺/Fe³⁺ content. At the

highest Fe^{2+} stoichiometry ($\text{Li}_{0.75}\text{FePO}_4$), the onset of the signal was at 470 K, whereas at the highest Fe^{3+} content ($\text{Li}_{0.25}\text{FePO}_4$), it was delayed until 510 K. This may reflect the difference in mobility between electron carriers that would predominate in the former case, as opposed to hole carriers that would predominate in the latter. These plots also indicated that the solubility of the Fe^{3+} phase within the mixture was less than that of the Fe^{2+} phase. Except for the sample $\text{Li}_{0.75}\text{FePO}_4$ where the Fe^{2+} component is the initial majority phase, the Fe^{2+} component was consumed first as the temperature increased. The Fe^{3+} phase persisted to high temperature in $\text{Li}_{0.55}\text{FePO}_4$ and $\text{Li}_{0.25}\text{FePO}_4$ even in the presence of substantial fractions of the solid solution phase. This suggests that there is a bias in solubility of the two phases in favour of Fe^{2+} dissolution. The persistence of some unconsumed majority phases in $\text{Li}_{0.75}\text{FePO}_4$ and $\text{Li}_{0.25}\text{FePO}_4$ probably indicated the presence of isolated regions of LiFePO_4 and FePO_4 that were unable to react. Alternatively, during preparation of the samples, oxidation of LiFePO_4 may have proceeded to completion in some very small crystallites to give particles composed entirely of FePO_4 , which were then unable to form a solid solution phase.

That the materials showed an average onset of rapid electron hopping behavior in the Mössbauer at effectively the same temperature as that reported from diffraction studies is highly significant. XRD studies showed that for compositions Li_xFePO_4 ($0.04 < x < 0.85$), the patterns for the two parent phases merged into one single phase that displayed intermediate lattice parameters. Neutron diffraction studies subsequently revealed that the lithium ions were fully disordered in the solid solution, which characterized it as a single phase from a structural perspective.¹⁴³ The Mössbauer data allow us to go further in interpretation of the nature of the solid solution. If the randomizing of the lithium on the M1

sites in the olivine structure simply led to a static random distribution of the Fe^{2+} and Fe^{3+} within the lattice, then the Mössbauer spectra would not have changed on entering the solid solution phase. However, the electrons were clearly dynamically delocalized on the Mössbauer time scale, and this correlated with the random lithium population within the solid solution lattice.

Analysis of the Mössbauer spectral evolution in the solid solution phases as a function of temperature can yield even more important information on the electron hopping rate owing to the time scale over which the dynamic process can be observed. The isomer shift of the solid solution phase at any specific temperature increased linearly with increasing Li content, as shown in Figure 3.16, in accord with the decrease in the mean valence. This revealed the development of rapid electron hopping in the solid solution phase that averaged the valence states on the time scale of the Mössbauer window.

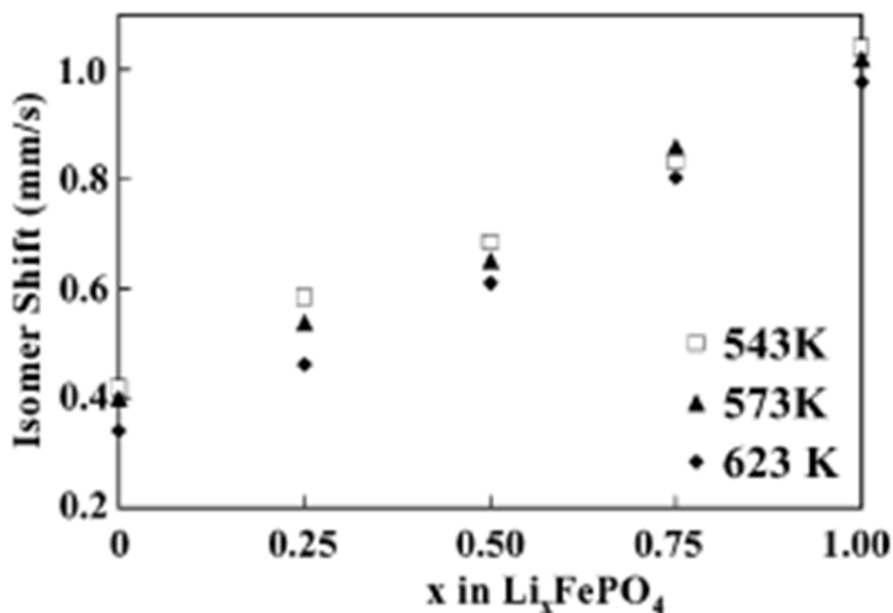


Figure 3.16: Plot of isomer shift *versus* x in Li_xFePO_4 . Reprinted with permission from reference ⁹³, copyright 2006, American Chemical Society.

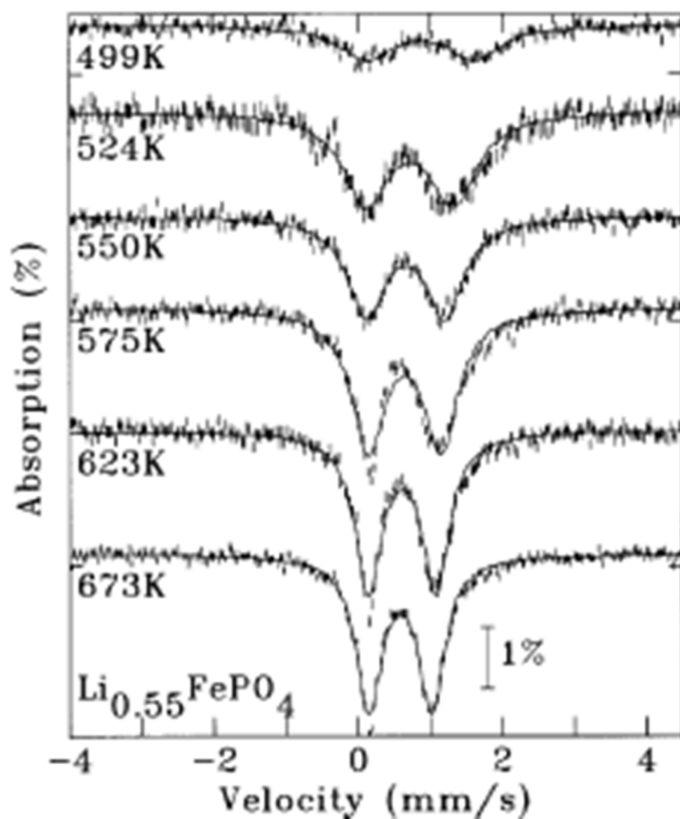


Figure 3.17: Mössbauer spectra of the solid-solution component of $\text{Li}_{0.55}\text{FePO}_4$ phase from 500-673 K showing growth of the solid-solution phase and motional narrowing. Reprinted with permission from reference ⁹³, copyright 2006, American Chemical Society.

For very slow fluctuations (events occurring on a time scale slower than the Mössbauer window of 10^{-6} - 10^{-10} s), a static pattern with sharp spectral features would be obtained which would provide no information on the dynamics. As initial electron hopping in the solid solution phase commenced, complex spectra developed with both the original static patterns coexist with a severely broadened solid-solution component as seen in Figure 3.13. As the temperature was increased, the rate of electron hopping averaged out over the entire particle and eventually a sharp, dynamically averaged pattern was regained. Figure 3.17 shows the motional narrowing of the solid solution contribution to the spectra on heating the $\text{Li}_{0.55}\text{FePO}_4$ phase. Two changes were readily apparent. Firstly, the area of the solid solution phase grows rapidly on heating, and secondly, the spectral lines become

progressively sharper as motional narrowing occurred. This latter change indicated that the small polaron transport became more rapid over the temperature window in which the Mössbauer experiment could detect the electron mobility. At temperatures lower than 500 K, the onset of electron mobility had barely commenced, whereas above 673 K, the mobility was too fast for the Mössbauer experiment to probe (ie. faster than 10^{-10} s). Detailed analysis of the line width yielded an electron hopping rate, and the temperature dependence of the line width allowed the calculation of an intrinsic activation energy (E_a) for the small polaron hopping of 775 ± 108 meV.

Several other measurements and calculations of activation energy in the olivine LiFePO_4 lattice have been reported. The most reliable value may be from ac impedance spectroscopy, of about 630 meV.¹⁵¹ In principle, this technique could allow grain boundary and inherent bulk contributions to be distinguished. Our dc conductivity measurements provided estimates of between 390 and 500 meV (see discussion below), but are not a true estimate of carrier activation energy in the lattice as measurements performed on pressed powders of LiFePO_4 would be subject to grain boundary effects. In contrast, Mössbauer should give a microscopic measure of the intrinsic barrier to transport within the lattice. The lower bound of the activation energy (670 meV) determined by Mössbauer was close to the ac conductivity result. All of the measured values of E_a were higher than that estimated by first-principle pseudopotential calculations of the “free” small polaron activation energy in LiFePO_4 (215 meV) or FePO_4 (175 meV).¹⁷⁰ It is important to note that strong binding of the polaron to the lithium-ion (calculated to be 370-500 meV by the same authors) would be expected to raise the activation energy substantially. Inclusion of this contribution to the free polaron E_a for LiFePO_4 raised the overall activation energy to a value of 585-715 meV,

similar to that measured experimentally, and fully consistent with the Mössbauer result. Thus, the activation energy for free polaron mobility is raised by strong interaction with the lithium ion, and the converse is also true: the activation energy for lithium ion transport is higher than predicted in the absence of coupling to the localized electrons. The high E_a calculated from the Mössbauer data compared to that predicted for unconstrained polaron migration implies strong interaction between hopping of the ion and electron carriers, by their concerted diffusion through the lattice.

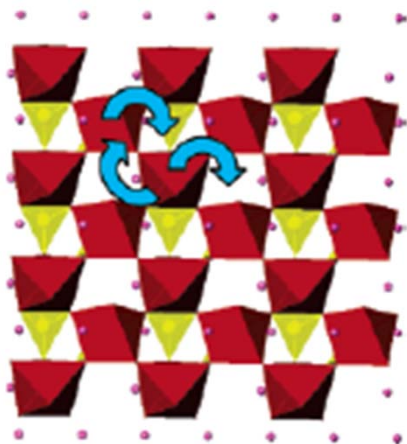


Figure 3.18: Schematic illustration of small polaron hopping within the bc plane of the olivine lattice.

The small polaron carrier mobility is expected to be two dimensional. This is depicted in Figure 3.18, which shows the connectivity within the (100) plane of the LiFePO_4 (Pnma) lattice. Transport perpendicular to the plane would have a very high activation energy because the FeO_6 octahedra are not directly connected along this direction, but are spanned by intervening PO_4^{3-} groups. The above considerations allow the explanation of temperature driven phase transition. For an electron to move to an adjacent Fe^{3+} site from an Fe^{2+} site, the Franck-Condon principle dictates that the iron nuclei must first assume a configuration that brings their two electronic energy levels into coincidence: a process accompanied by thermal fluctuations in the lattice. In this excited state, the Fe-O bond lengths in the Fe^{2+}O_6

and Fe^{3+}O_6 sites become transiently equivalent, permitting the electron hops to occur in a concerted manner that spans a large lattice domain. This can also be described by Marcus theory, which establishes that electron transfer between two redox sites takes place only after metal-ligand bond lengths have been altered enough to allow the transfer to occur adiabatically (i.e., without further change in energy).¹⁷¹

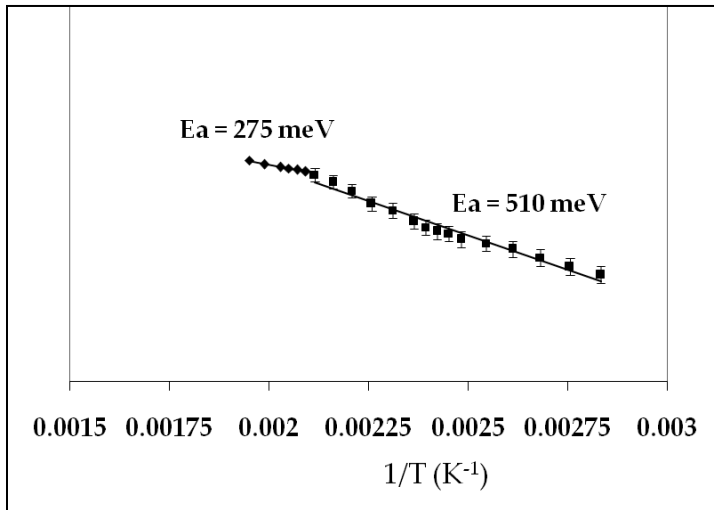


Figure 3.19: Two-point probe dc conductivity measurement for $\text{Li}_{0.5}\text{FePO}_4$.

The Mössbauer experiments are supported by two-probe variable temperature dc conductivity measurements of two phase mixtures, carried out between 300 K and 520 K for bulk crystalline $\text{Li}_{0.5}\text{FePO}_4$. The densified pellets of material were sealed in a Swagelok housing under inert atmosphere and remained at a given temperature for 24 hours, at which point the measurement for that temperature was collected. The results are shown in Figure 3.19. The $\log \sigma$ vs $1/T$ plot for the bulk $\text{Li}_{0.5}\text{FePO}_4$ material showed the expected linear relationship in the temperature range from 300 K-473 K with an average activation energy of $510 \pm 15 \text{ meV}$. Multiple data sets were collected from separate experiments on different pressed pellets and were remarkably consistent. Near 473 K, a distinct change in slope demarcates the transition to the solid solution regime with a significantly lower activation

energy of 275 ± 15 meV. Thus, the onset of the solid solution regime could be determined by temperature-dependent conductivity measurements.

The Mössbauer experiments pinpoint the temperature of formation of the solid solution on heating $\text{LiFePO}_4/\text{FePO}_4$ above 500 K and clearly showed that small polaron transport is responsible for electron transport. The isomer shift of the averaged $\text{Fe}^{2+/3+}$ environment is directly related to the averaged oxidation state in $\text{Li}_{1-x}\text{FePO}_4$. Mössbauer spectroscopy permits a precise measure of the phase transition temperature by the appearance of the solid solution signal in the spectra: the initial onset is present in small domains with short coherence lengths within the crystal, invisible to diffraction but detectable by Mössbauer because it is a local atomic probe.

3.6 Synthesis and High Temperature Mössbauer Studies on Nano- LiFePO_4

Solution precipitation is a common synthesis method for the production of both metallic and metal oxide nanoparticles and a similar approach was taken to produce nanoparticles of LiFePO_4 , precipitated from tetraethylene glycol in a method similar to that reported by Kim *et al.*¹⁴⁴ A TEM micrograph of the nanodimensional LiFePO_4 is displayed in Figure 3.20 which revealed crystallites with an average size distribution from 35-90 nm in length. Unlike the results of the structural refinements of hydrothermally-prepared LiFePO_4 , refinement of the nanomaterial prepared from the glycol led to the exact site occupancies predicted by stoichiometry: no M1/M2 site mixing was found.⁹⁵ This was likely a result of the higher synthesis temperature of the glycol synthesis (320 °C) where cation site preferences based on thermodynamics are prevalent, compared to that of the hydrothermal

method (140-200 °C). A sample of the nanoscale material was oxidized to a stoichiometry corresponding to $\text{Li}_{0.5}\text{FePO}_4$ with NOBF_4 .

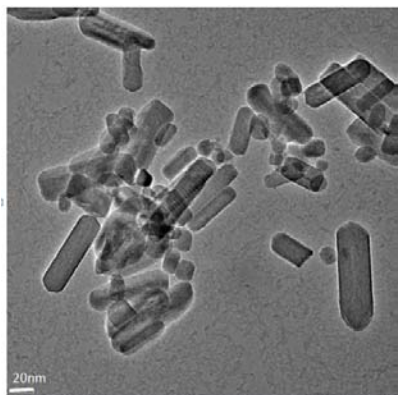


Figure 3.20: TEM micrograph of nano- LiFePO_4 prepared by the polyol route.

A comparison of the bulk and nano Li_xFePO_4 samples was undertaken to observe any effects of particle size on the high temperature solid solution regime found for bulk Li_xFePO_4 (as discussed in the previous section of this thesis). A summary of the isomer shifts and relative peak areas for the components found in nano $\text{Li}_{0.5}\text{FePO}_4$ and bulk $\text{Li}_{0.5}\text{FePO}_4$ is shown in Figure 3.21. Room temperature Mössbauer spectra for each sample displayed two doublets with Mössbauer parameters: $\text{IS} = 1.2 \text{ mm/s}$, $\text{QS} = 3.0 \text{ mm/s}$ and $\text{IS} = 0.42 \text{ mm/s}$, $\text{QS} = 1.5 \text{ mm/s}$, typical of Fe^{2+} and Fe^{3+} respectively in these materials. In addition, the relative areas of the two components confirmed the stoichiometry. Mössbauer spectra recorded at temperatures above 300 K up to 700 K tracked the evolution of the fitted parameters from the initial two-phase composition to the nano and bulk phase solid solutions $\text{Li}_{0.5}\text{Fe}^{2+/3+}\text{PO}_4$ as a function of temperature: Figure 3.21 shows the variation in the isomer shift (IS) of the Fe^{2+} and Fe^{3+} components, along with that of the solid solutions for the nano and bulk phases as the transition to the solid solution regime takes place. Formation of the solid solution was signaled by the appearance of a new spectral component with an isomer shift (IS_{SS}) that lies between that of the parent Fe^{2+} and Fe^{3+} phases, as discussed previously.

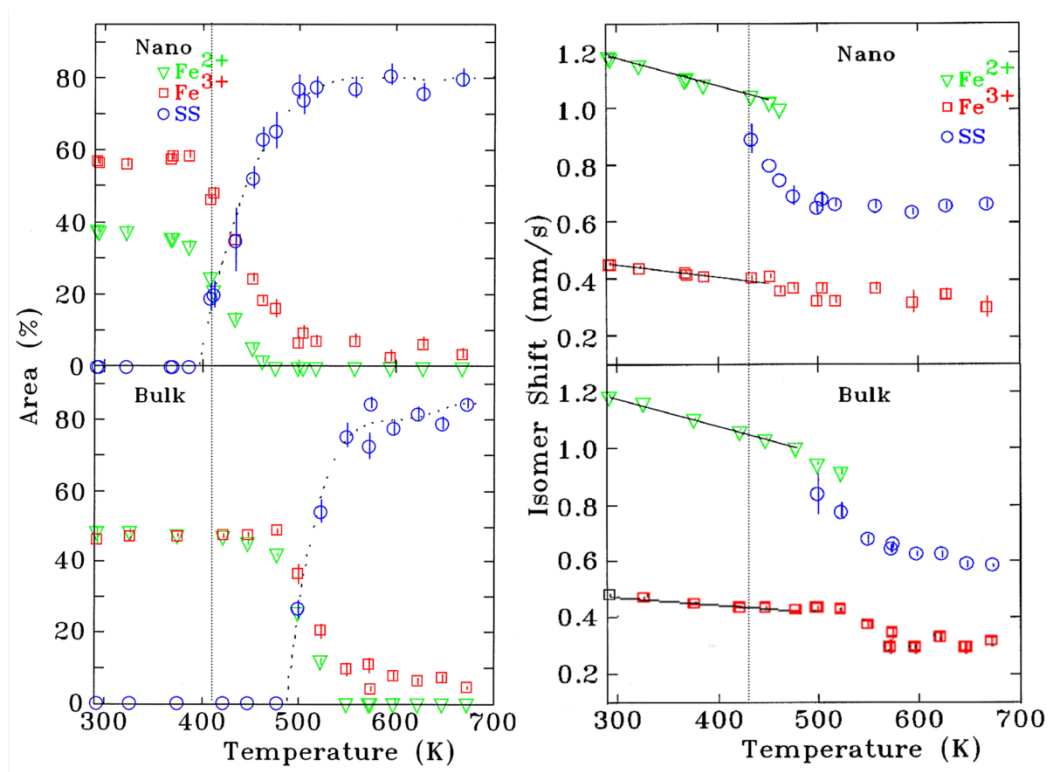


Figure 3.21: The relative areas and the change in isomer shift of the Fe^{2+} , Fe^{3+} and the solid solution phases as a function of temperature from the Mössbauer spectra for (a,c) nanophased $\text{Li}_{0.5}\text{FePO}_4$; (b,d) bulk $\text{Li}_{0.5}\text{FePO}_4$. Note that the isomer shift of the solid solution phase lies between those of the Fe^{2+} and Fe^{3+} phases in all cases and the dotted lines denotes the transition temperature of the nanomaterial.

This intermediate valence state was characterized by rapid polaron hopping on the Mössbauer time scale and allows us to pinpoint the exact temperature of the phase transition. As stated previously, the transition temperature for the bulk phase was determined to be 490 K. Most striking was that the onset transition temperature to the solid solution regime occurred about 80 K lower for the nano-phase material (at 410 K) as illustrated in Fig. 3.21. Transition to the solid solution regime was clearly facilitated by the restricted crystallite dimensions. The curves also indicated that the solubility of the Fe^{3+} phase within the mixture was less than that of the Fe^{2+} phase since the Fe^{2+} component was consumed first as the temperature increased, although the persistence of the Fe^{3+} component for both the bulk and nano $\text{Li}_{0.5}\text{FePO}_4$ samples could be due to the full oxidation of some particles.

Since the electron hopping rate between $\text{Fe}^{2+} \leftrightarrow \text{Fe}^{3+}$ increased upon heating, the activation energy of electron hopping could again be determined by analysis of the solid-solution phase line shapes in the spectra as a function of temperature. Within error, the activation energy for the nanocrystalline material, 420 ± 60 meV, was found to be much lower than that of the bulk material (775 ± 108 meV). The fitted activation energies, which provide a microscopic measure of the intrinsic barrier to transport within the lattice, compare well with values derived from ac and dc conductivity measurements of LiFePO_4 as previously discussed.

The onset temperature of the disordered phase and the activation energy for small polaron hopping are both clearly dependent upon the dimensions of the material. A greatly reduced crystallite size leads to a significant decrease of both parameters, possibly the result of the two end members having smaller differences in unit cell volume. Our data revealed a volume contraction of 6.4% upon going from LiFePO_4 to FePO_4 in the bulk material, compared to 5.6% in the nanocrystalline material.⁹⁵ As well, the overall energetic benefits of phase separation decrease for smaller particles. This arises from a change in the energy terms: contributions from the interface initially separating the two phases, the increased surface energy resulting from particle strain and the decreased volume of the particle. These combine to increase the Gibbs free energy of mixing two phases, as reported for titania nanoparticles.¹⁷² Another way of describing this is that when grain sizes approach the scale of the Debye length, the volume-averaged defect concentration increases which raises the entropy contribution to the Gibbs free energy. This in turn lowers the temperature at which the two phases mix and leads to the possibility of removal of the miscibility gap entirely at room temperature, but only if the crystallites were of extremely small, and probably

impractical dimensions. Owing to the inter-relationship of these nanoscale effects (shorter ion/electron transport lengths, increased surface energy, reduced unit cell volume strain, slightly lower activation energy in the solid-solution regime) it is difficult to determine which of these effects would have the greatest contribution to improving the electrochemical properties of nano-LiFePO₄.

The Mössbauer experiments pinpoint the temperature of formation of the solid solution on heating LiFePO₄/FePO₄ above 400 K, and showed that transition to the solid solution occurs at a much lower temperature for nanocrystallites, by about 80 K compared to the bulk phase. Moreover, the average activation energy for small polaron hopping was found to decrease. The nature of this effect is likely related to reduced strain between the LiFePO₄ and FePO₄ phases.

3.7 Hydrothermal Synthesis and High Temperature Studies of LiMnPO₄

Other lithium phospho-olivines including LiMgPO₄ and LiMnPO₄ could also be synthesized hydrothermally, by using MgSO₄ and MnSO₄•H₂O respectively as a substitute for ferrous ammonium sulfate. An X-ray diffraction pattern and subsequent Rietveld refinement of LiMnPO₄ prepared at 190 °C is shown in Figure 3.22 and a summary of the fit parameters is presented in Table 3.4. As with hydrothermally prepared LiFePO₄, the fit was found to be best when a small quantity of Mn (3%) was placed on the Li site. The lattice parameters for LiMnPO₄ are similar to those from earlier reports of materials made by other synthetic methods. These compounds can be also be synthesized with carbon, using the same additives described previously. As with hydrothermal LiFePO₄, the use of polyacrylic acid also produces nanocrystalline LiMnPO₄, with particles in the 40–80 nm range.

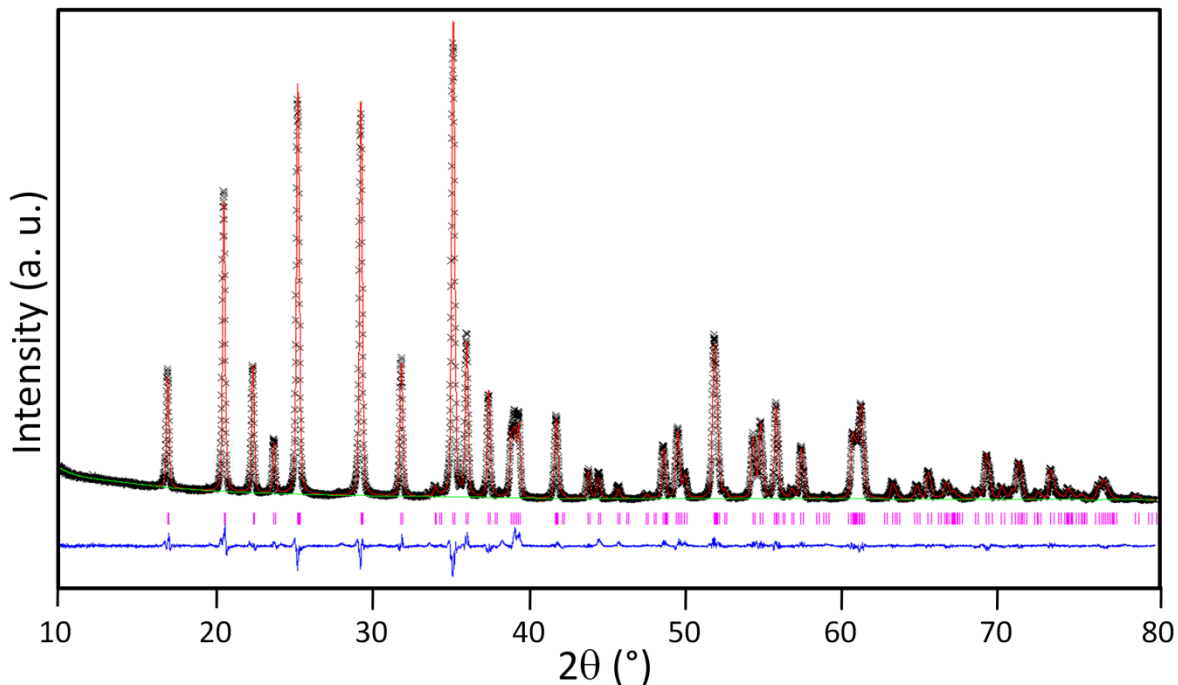


Figure 3.22: Rietveld refinement of hydrothermally-prepared LiMnPO_4 at $190\text{ }^\circ\text{C}$. Experimental pattern shown in black, calculated in red, difference map in blue and phase lines for LiMnPO_4 are shown in magenta. Refinement parameters are shown in Table 3.4.

Table 3.4: Lattice constants and atomic parameters for hydrothermal LiFePO_4 refined from X-ray diffraction powder data. X-ray diffraction agreement factors: $R_{\text{wp}} = 6.73\%$, $R_{\text{p}} = 4.79\%$, $\chi^2 = 6.49$.

LiMnPO ₄					
Space group: Pnma (#62), Orthorhombic					
$M_w = 156.86\text{ g/mol}$					
$a = 10.4430(2)\text{ \AA}$					
$b = 6.09815(6)\text{ \AA}$					
$c = 4.7456(1)\text{ \AA}$					
$V = 302.29(1)\text{ \AA}^3$					
Atom	x/a	y/b	z/c	Occ.	U_{iso}
Li(1)	0	0	0	0.976(1)	0.015
Mn(1)	0	0	0	0.024(1)	0.015
Li(2)	0.2817(2)	1/4	0.9706(2)	0.024(1)	0.007(1)
Mn(2)	0.2817(2)	1/4	0.9706(2)	0.976(1)	0.007(1)
P(1)	0.0932(1)	1/4	0.4096(4)	1.0	0.011(2)
O(1)	0.0944(3)	1/4	0.7385(6)	1.0	0.012(2)
O(2)	0.4535(4)	1/4	0.2169(5)	1.0	0.013(2)
O(3)	0.1605(4)	0.0423(5)	0.2740(6)	1.0	0.015(2)

Note that although nano-triphylite experienced a decrease in unit cell volume, a similar lattice strain on the nano-crystalline LiMnPO_4 seemed to have virtually no effect on the lattice parameters. Although line broadening in the diffraction pattern characteristic of microstrain and small coherence lengths was observed for nano- LiMnPO_4 , little effect on the unit cell volume was noted, unlike that seen for nanoparticles of LiFePO_4 , as outlined in Table 3.3. This is likely due to the oxidative stability of Mn^{2+} relative to that of Fe^{2+} .

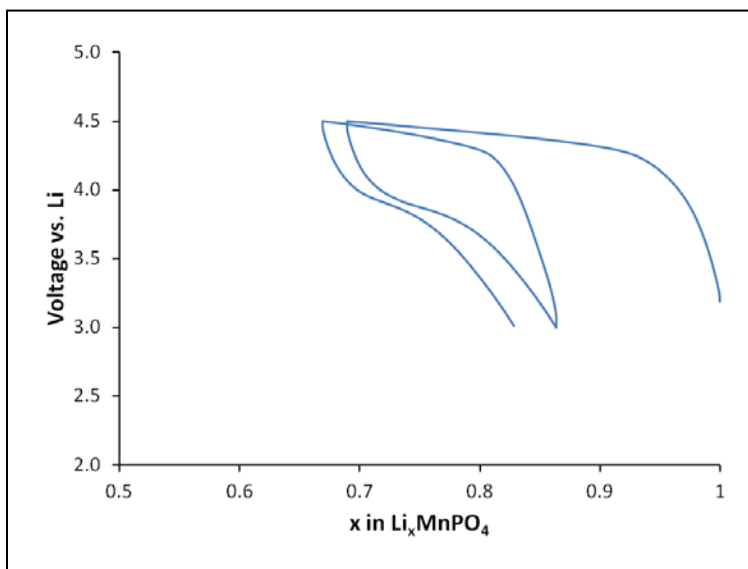


Figure 3.23: Electrochemistry of nano- LiMnPO_4 .

The electrochemistry of hydrothermally prepared LiMnPO_4 powder with polyacrylic acid as a synthetic additive is shown in Figure 3.23. LiMnPO_4 was reported to undergo a two-phase transition on delithiation, similar to that of LiFePO_4 , although the potential for LiMnPO_4 is 0.6 V higher: about 4.1 V *versus* lithium.⁵⁰ Although the LiMnPO_4 particles prepared with polyacrylic acid were nanosized, the high polarization of 0.5 V and poor capacity (only 15% reversible) indicated that there may be poor electrical connection between the insulating particles of active material and the electronically conductive carbon inside the cell.

The intriguing discovery of a high-temperature solid-solution regime in the LiFePO_4 system led us to study the high-temperature properties of partially delithiated LiMnPO_4 . $\text{Li}_{0.5}\text{MnPO}_4$ was prepared by the reaction of LiMnPO_4 with 0.5 eq. NO_2BF_4 . The resultant X-ray diffraction pattern is shown in Figure 3.24. The peaks of LiMnPO_4 (JCPDS #33-0803) are present along with those of purpurite MnPO_4 (JCPDS #37-0478), the manganese-rich oxidized olivine phase. Without the ability to monitor any solid-solution behaviour in the $\text{Li}_{0.5}\text{MnPO}_4$ system spectroscopically, we endeavoured to isolate quenched high-temperature solid-solutions of the manganese olivine. $\text{Li}_{0.5}\text{MnPO}_4$ was heated to 200 °C for 18 hours in both air and argon atmospheres in ceramic crucibles and the samples were quenched by placing the crucibles in cold water. The X-ray diffraction patterns of the quenched samples are shown in Figure 3.24. In both samples, LiMnPO_4 was found to be present, along with $\text{Mn}_2\text{P}_2\text{O}_7$; the peaks corresponding to MnPO_4 were absent, thus we concluded decomposition of the MnPO_4 phase occurred prior to reaching 200 °C.

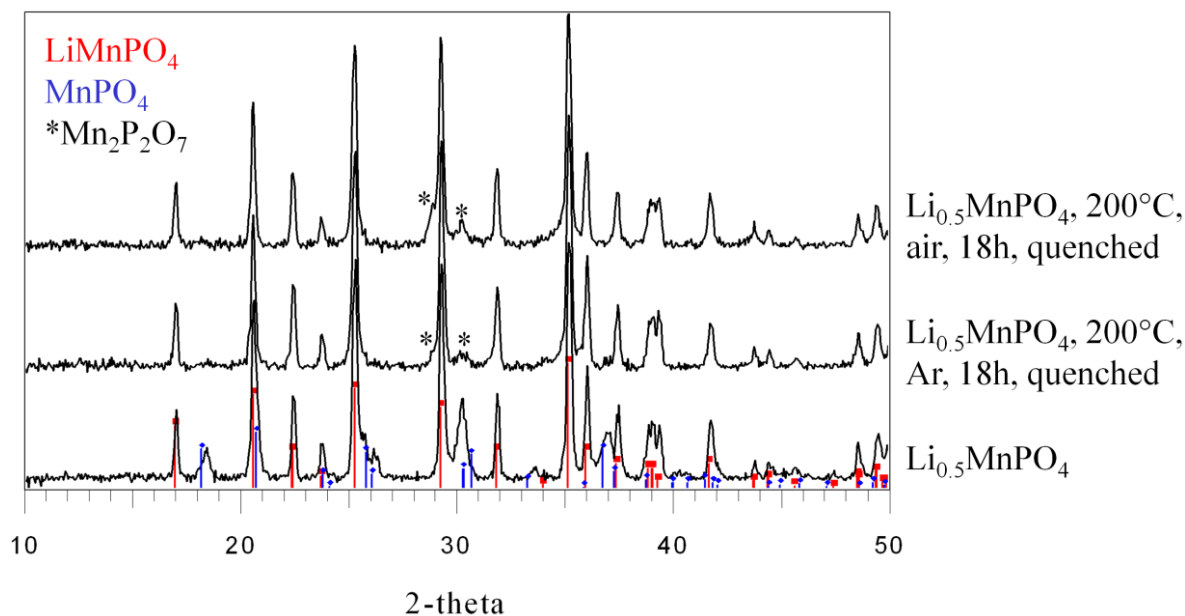


Figure 3.24: X-ray diffraction patterns of $\text{Li}_{0.5}\text{MnPO}_4$ prepared by chemical oxidation of LiMnPO_4 . The $\text{Li}_{0.5}\text{MnPO}_4$ was heated to 200 °C where it decomposed into $\text{Mn}_2\text{P}_2\text{O}_7$.

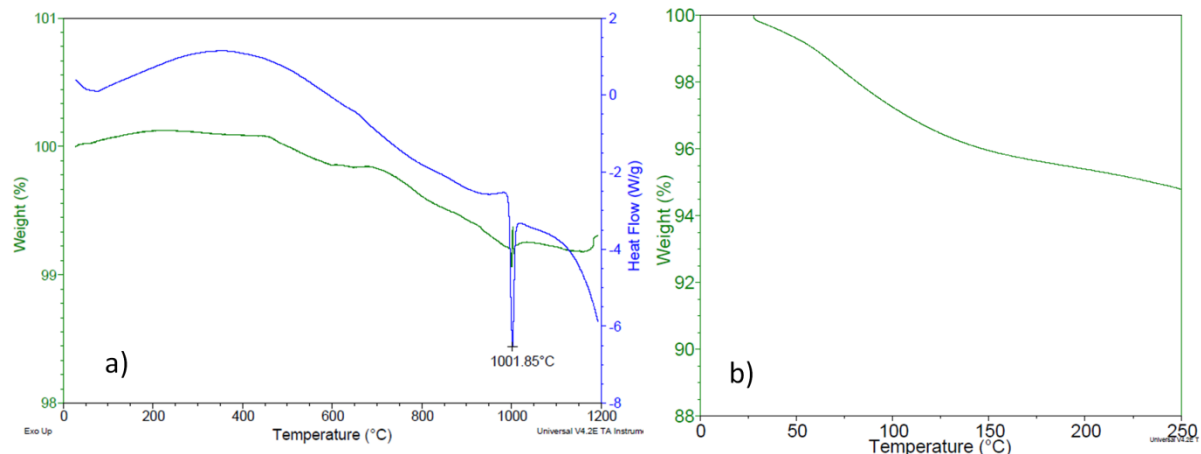


Figure 3.25: a) TGA of LiMnPO₄ and b) Li_{0.5}MnPO₄, both heated in air.

This was confirmed by TGA analysis of both the LiMnPO₄ and Li_{0.5}MnPO₄ samples heated in air; the data are shown in Figure 3.25. Although LiMnPO₄ exhibited nominal mass loss up to its 1000 °C melting point, Li_{0.5}MnPO₄ experienced a mass loss between 75-100 °C of about 4%. This corresponds with the decomposition of MnPO₄ by the following mechanism:



This result is particularly interesting as it highlights the instability of the MnPO₄ which underwent reduction in the presence of both air and argon. The poor temperature stability of MnPO₄ limits the practical application of LiMnPO₄ as a high-temperature battery material.

3.8 Conclusions

LiFePO₄ and LiMnPO₄ crystallize under autogeneous pressure in hydrothermal reactors at temperatures above 120 °C. These reactions could be tailored to produce nanoparticles by the modulation of reaction temperature, concentration of precursors and the addition of organic compounds to act as particle growth inhibitors. Ascorbic acid was found to be a particularly useful organic additive: on top of limiting particle growth, it acted as a reducing agent for iron and decomposed at a low enough temperature to deposit a carbon

coating on the surface of the particles. All of these factors were critical to electrochemical performance of LiFePO_4 . Synthesis of olivines at temperatures below $200\text{ }^\circ\text{C}$ resulted in the formation of antisite defects in the order of about 2-3% which may adversely affect the electrochemical performance. Care must be taken to protect nano- LiFePO_4 from air exposure which resulted in surface oxidation; such precautions are not necessary for LiMnPO_4 , owing to the oxidative stability of Mn^{2+} .

Although LiFePO_4 was found to reversibly intercalate lithium by a two-phase mechanism at room temperature, when heated to temperatures over $220\text{ }^\circ\text{C}$, a solid solution formed as the result of electron delocalization in the lattice, as probed by Mössbauer spectroscopy on partially delithiated LiFePO_4 . The onset of rapid small polaron hopping on the time scale was precisely correlated with the temperature that the lithium ions begin to disorder in the lattice. Furthermore, this onset of this phenomenon was found to be dependent on the particle size: nanoparticles were found to reach this solid-state regime at a temperature 80 K lower than found for bulk particles. This implies that with sufficiently small particles, LiFePO_4 free of disorder and defects may display solid-solution character at room temperature. Solid solutions were not found to be stable at high temperature in the case of partially delithiated LiMnPO_4 as MnPO_4 was found to decompose near $200\text{ }^\circ\text{C}$.

4 Preparation, Electrochemistry and Anion-Induced Solid Solutions in Hydroxyphosphates and Fluorophosphates based on the Tavorite Structure

4.1 Overview of Tavorite-type Compounds

Fluorophosphates are another class of electrode materials under scrutiny as potential lithium battery electrodes. As with the olivines, the iron and manganese compounds of this family were the focus of our work owing to the relative abundance and low environment of iron and manganese compounds. Depending on the framework connectivity, these compounds may be expected to exhibit a high cell potential as a result of both the inductive effect of PO_4^{3-} group and the electron-withdrawing character of the F^- ion. Similar to the olivines, the environmentally benign character of these compounds is confirmed by their presence as natural minerals. Among these are montebrasite (LiAlPO_4OH), amblygonite (LiAlPO_4F) and compositional solid solutions thereof ($\text{LiAlPO}_4(\text{OH})_x\text{F}_{1-x}$),^{68,173–175} all of which are isostructural with another iron-containing natural mineral, tavorite (LiFePO_4OH).¹⁷⁶ It is commonly found lithium-rich pegmatitic deposits in the presence of other iron-containing phosphates such as triphylite (LiFePO_4), heterosite ($(\text{Fe,Mn})\text{PO}_4$), vivianite ($\text{Fe}_3(\text{PO}_4)_2 \cdot 8\text{H}_2\text{O}$), barbosalite ($\text{Fe}_3(\text{PO}_4)_2(\text{OH})_2$) and ferrisicklerite ($\text{Li}_x(\text{Fe,Mn})\text{PO}_4$).^{176,177} It is not clear whether tavorite is formed hydrothermally or formed by weathering of triphylite.

Compounds of this type have the general formula AMTO_4X where $\text{A} = \text{H, Li}$; $\text{M} = \text{Mg, Al, V, Cr, Mn, Fe}$; $\text{T} = \text{P, S, As}$; $\text{X} = \text{OH or F}$. Unlike the olivines or the other fluorophosphates in this thesis, compounds of this class tend to crystallize in lower symmetry

(monoclinic or triclinic) space groups. The structure of these compounds can be generalized as consisting of parallel chains of MO_6 octahedra (or in the case of fluorine-containing compounds, MO_4F_2 octahedra) which are interconnected by corner-shared TO_4 tetrahedra. The resulting framework is very cavernous and as a result, tavorite compounds which contain lithium have been found to be good Li-ion conductors at high temperatures. For example, the ionic conductivity of lithium was measured to be 1.5×10^{-3} S/cm at 520°C in LiMgSO_4F ⁹⁶ and 3×10^{-5} S/cm at 200°C in $\text{LiMnPO}_4(\text{OH})$.⁹⁷

Ionic conductivity is an important property for intercalation electrodes. Up to this point, only one fluorophosphate from this family has been explored as a potential Li-ion battery cathode. LiVPO_4F was first reported in 2003 as a 4.1 V positive electrode material with a theoretical capacity of 155 mAh/g, corresponding to the extraction of one Li.^{44,102,178} Interestingly, it was later shown that LiVPO_4F could also intercalate Li at a potential of about 1.8 V. Since LiVPO_4F was shown to function as both a positive and negative electrode, this led to the report of a $\text{LiVPO}_4\text{F}/\text{LiVPO}_4\text{F}$ symmetric cell with one electrode working on the $\text{V}^{3+} \rightarrow \text{V}^{4+}$ redox couple and the other working on the $\text{V}^{3+} \rightarrow \text{V}^{2+}$ redox couple.¹⁷⁹ We commenced our fluorophosphate study with the synthesis as well as electrochemical and structural study of LiVPO_4F . Electrochemical cycling and *ex-situ* diffraction studies were used to determine the mechanism of Li insertion and extraction for the two electron reaction. The fully lithiated ($\text{Li}_2\text{VPO}_4\text{F}$) and fully oxidized (VPO_4F) structures were characterized by X-ray diffraction and in the case of the former, neutron diffraction was also employed.

Our focus then turned to the synthesis of iron and manganese phosphates based on the tavorite structure. After our first report of LiFePO_4F ,¹⁸⁰ the synthesis and electrochemical properties of LiFePO_4F prepared by ionothermal methods was also reported.¹⁸¹ LiFePO_4F is

a promising positive electrode material with a potential of 2.8 V. LiFePO_4F was synthesized by solid-state and solvothermal methods while hydrothermal methods were used to synthesize $\text{LiFePO}_4(\text{OH})$ and mixed hydroxy/fluorophosphates with the general formula $\text{LiFePO}_4(\text{OH})_{1-x}\text{F}_x$. Characterization of the structures was performed by refinement of powder X-ray diffraction data. Further characterization was carried out by infrared spectroscopy, thermal gravimetric analysis and various electrochemical techniques.

As with the olivines, the manganese compounds would have higher potential than the iron compounds of this class. $\text{LiMnPO}_4(\text{OH})$ and the structurally similar $\text{MnPO}_4 \cdot \text{H}_2\text{O}$ have both been reported,¹⁸² however, LiMnPO_4F has not. We tested the electrochemical properties of both $\text{LiMnPO}_4(\text{OH})$ and $\text{MnPO}_4 \cdot \text{H}_2\text{O}$ and endeavoured to synthesize LiMnPO_4F .

4.2 Synthesis of Tavorite Compounds

LiFePO_4F (solid state): FePO_4 was synthesized by reaction of stoichiometric quantities of Fe_2O_3 and $(\text{NH}_4)_2\text{HPO}_4$ in silicon nitride milling media at 300 rpm for 4 hours. The powder was then calcined in air at 870 °C for 6-10 h. The FePO_4 was then ball milled with LiF and heated at 600 °C for 75 minutes in an argon flow.

LiFePO_4F (solvothermal): In a typical synthesis, 0.500 g $\text{FeF}_3 \cdot 3\text{H}_2\text{O}$ and 0.315 g LiH_2PO_4 were added to 15 ml of ethanol in a polymer-lined hydrothermal bomb. The bomb was stirred at room temperature for 1 hr before the bomb was placed in an oven at 230 °C, where it remained for 3-5 days. The attained product was filtered and washed with a small amount of water and ethanol before being dried under vacuum at 80 °C.

Li_{1+x}FePO₄F: LiFePO₄F was stirred with a stoichiometric amount of LiAlH₄ in tetrahydrofuran in an argon-filled glove box for 44 hours. The product was washed with tetrahydrofuran and dried under ambient conditions.

LiFePO₄(OH): FePO₄•2 H₂O, LiOH•H₂O and Li(CH₃COO)•2 H₂O (1:0.6:0.6 mole ratio) were stirred in 15 ml distilled water for 15 minutes. The solution was transferred to a 23 ml Parr Teflon-lined Parr acid digestion bomb and heated to 160 °C for 16 hours. A bright yellow solid formed under autogeneous pressure and was collected by filtration or centrifugation, washed several times with distilled water and dried overnight in an oven at 100 °C.

LiFePO₄(OH)_{0.4}F_{0.6}: 1.87 g FePO₄•2 H₂O and 0.26 g LiF were stirred in 15 ml distilled water for 15 minutes and the suspension was transferred to a 23 ml Parr reactor. The reactor was heated to 160 °C for 16 hours and cooled naturally to room temperature. The product was filtered and washed with distilled water and acetone. The product was dried overnight in an oven at 100 °C.

LiVPO₄F: As reported by Barker *et. al.*,⁴⁴ stoichiometric amounts of V₂O₅ and NH₄H₂PO₄ were ground with carbon and fired at 800 °C to produce VPO₄/C. Stoichiometric amounts of VPO₄/C and LiF were ground in zirconia milling media and subsequently fired at 700 °C for 2 hours under an Ar atmosphere.

MnPO₄•H₂O: prepared in a similar way to the method previously outlined by Boonchom *et al.*¹⁸³ 5.0 g Mn(NO₃)₂•4H₂O was dissolved in 5 ml of 85% H₃PO₄, after which time 20 ml of ethanol was added. The resulting solution was vigorously stirred for 3 h at 70 °C. The green precipitate was collected by filtration.

LiMnPO₄(OH): LiMnPO₄(OH) was prepared similarly to a method previously described by Aranda *et. al.*¹⁸² Briefly, the precursor MnPO₄•H₂O was ground in a 1:4 molar ratio with LiNO₃ and heated to 200 °C for approximately 2 weeks.

4.3 Diffraction and Electrochemical Studies of LiVPO₄F

Carbon-coated LiVPO₄F was successfully prepared by a solid-state route similar to a previous report. A high-resolution X-ray diffraction pattern, collected at the Advanced Photon Source at Argonne National Labs in Chicago IL, and Rietveld refinement of the data is shown in Figure 4.1 and the refinement results are listed in Table 4.1. LiVPO₄F adopts the tavorite structure and is isostructural with several known fluorophosphate compounds such as LiAlPO₄F⁶⁸ and very similar to the structure of LiFePO₄OH,⁶⁷ which was used for the basis for the refinement, with the H atoms removed. These compounds crystallize in the triclinic space group P-1. Figure 4.2 depicts a graphical representation of the crystal structure derived from the refinement. [V³⁺F₂O₄] octahedra form corner-sharing chains in the (010) direction, where alternate octahedra are tilted. The F-ligands act as the bridging ligands. These chains are connected by corner-sharing phosphate tetrahedra to make a cavernous 3D framework: wide tunnels (>3 Å in diameter) are present along all of the (100), (010) and (001) directions. The refined unit cell volume of 174.31 Å³ is very similar to that reported by Barker and co-workers of 174.35 Å³, even though the choice of the two triclinic cells differed, as evidenced by the difference in angles between the two reported cells.

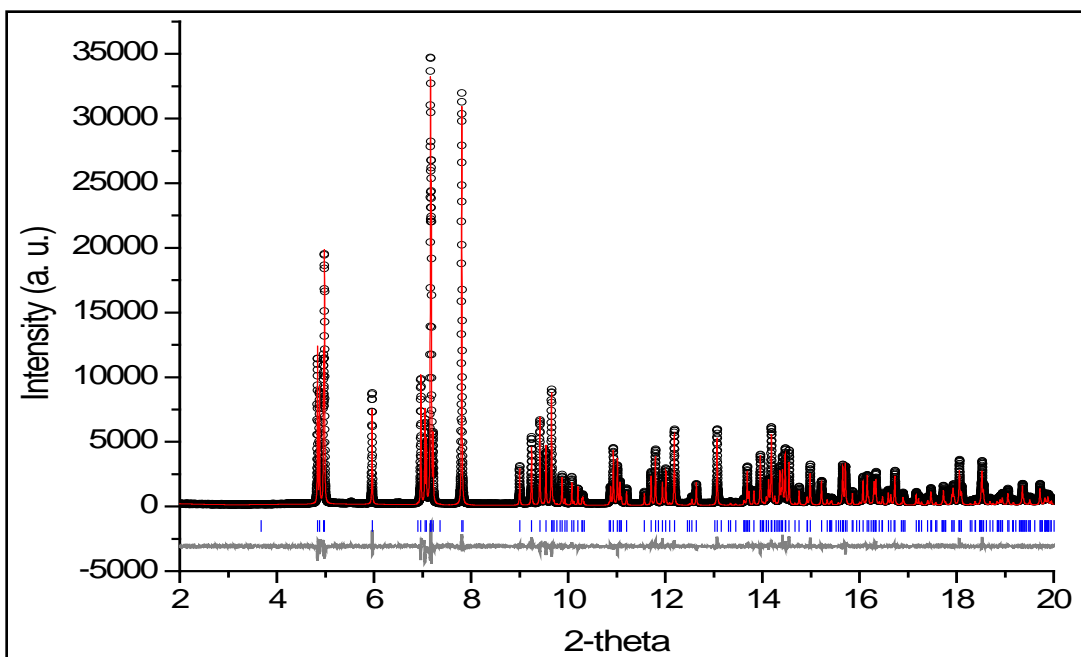


Figure 4.1: Synchrotron X-ray diffraction pattern ($\lambda = 0.4122\text{\AA}$) and Rietveld refinement of LiVPO_4F synthesized by a solid state method. The experimental points are black, the fit is shown in red, the calculated reflections are shown in blue and the difference map is shown in grey. Reprinted with permission from reference ¹⁰³, copyright 2011, American Chemical Society.

Table 4.1: Lattice constants and atomic parameters of LiVPO_4F refined from powder XRD data. Agreement factors: $R_{\text{wp}} = 10.30\%$, $R_{\text{p}} = 7.88\%$, $R_{\text{F}2} = 3.45\%$.

LiVPO_4F						
Space group: P -1 (#2), Triclinic						
$a = 5.30941(1)\text{\AA}$		$\alpha = 112.933(0)^\circ$				
$b = 7.49936(2)\text{\AA}$		$\beta = 81.664(0)^\circ$				
$c = 5.16888(1)\text{\AA}$		$\gamma = 113.125(0)^\circ$				
$V = 174.306(0)\text{\AA}^3$						
Atom	Wych.	x/a	y/b	z/c	Occ.	U_{iso}
Li (1)	$2i$	0.389(2)	0.334(1)	0.659(2)	0.18(1)	0.015
Li (2)	$2i$	0.373(2)	0.236(1)	0.517(2)	0.82(1)	0.015
V (1)	$1a$	0	0	0	1.0	0.0043(3)
V (2)	$1b$	0	1/2	1/2	1.0	0.0059(3)
P (1)	$2i$	-0.6476(2)	-0.2515(2)	0.0719(2)	1.0	0.0070(3)
O (1)	$2i$	0.2109(4)	-0.0936(3)	0.1701(4)	1.0	0.015(2)
O (2)	$2i$	-0.3420(4)	-0.1375(3)	0.1705(4)	1.0	0.016(2)
O (3)	$2i$	-0.7627(4)	-0.4100(3)	0.2163(4)	1.0	0.013(2)
O (4)	$2i$	-0.6695(4)	-0.3597(3)	-0.2503(4)	1.0	0.014(2)
F (1)	$2i$	0.0875(3)	0.2450(2)	0.3585(3)	1.0	0.015(2)

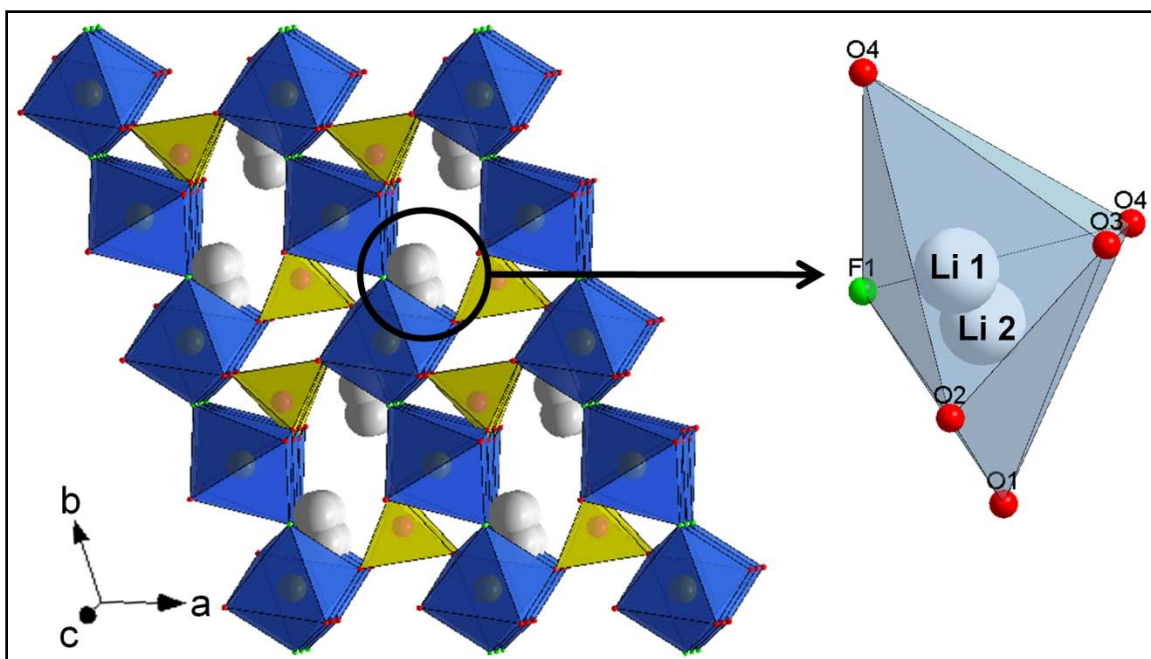


Figure 4.2: Pictorial representation of the structure of LiVPO_4F with a close-up view of the split lithium position. The vanadium octahedra are shown in blue, phosphate tetrahedra are shown in yellow, and the Li atoms are shown in white. Reprinted with permission from reference ¹⁰³, copyright 2011, American Chemical Society.

It has been previously reported that lithium fluorophosphates with the tavorite structure tended to have a low-symmetry octahedral lithium site which results in a split lithium position.¹⁷³ The distribution of lithium over these sites varied based on the method of preparation and the nature of the anion (OH^- vs. F^-) as these factors influenced the geometry of the site itself. The lithium co-ordination in LiVPO_4F is shown in Figure 4.2 and bond distances are summarized in Table 4.2. In LiVPO_4F , the centers of the two Li sites Li1 and Li2 are approximately 0.79 Å apart. The Li1 site has one Li-F bond and two Li-O bonds which are 1.92-2.12 Å in length, all of which are consistent for bond distances with Li in a 4-coordinate environment. Two additional oxygen ligands are 2.29 and 2.43 Å from the Li1 site, thus the Li1 environment may be described as 5-co-ordinate geometry. The final oxygen ligand is greater than 3 Å from Li1. In contrast, the Li2 site may be described as having [5+1] geometry. Li2 has one close F ligand and 4 oxygen ligands at distances varying

Table 4.2: Summary of bond distances for Li environment in LiVPO₄F.

Atom	Ligand	Distance (Å)
Li1	Li2	0.795
	O2	1.919
	O3	1.970
	F1	2.117
	O4'	2.293
	O4	2.428
	O1	3.092
Li2	Li1	0.795
	F1	1.861
	O2	1.983
	O4	2.112
	O3	2.275
	O1	2.323
	O4'	2.881

between 1.98-2.32 Å. A fifth oxygen ligand (O3) is 2.88 Å from Li2. With the difference in co-ordination and bond lengths, it was not surprising to find that the two Li sites were not equally occupied. In our refinement, the occupancy of the Li1 and Li2 sites was found to be 18% and 82% respectively. The higher thermodynamic stability which results from the larger number of ligands in the Li2 site renders it the slightly preferred Li environment. This is not the case in LiFePO₄(OH), where the relative occupancy of the Li1 and Li2 sites in that structure was reported to be 1:1.⁶⁷

Figure 4.3 depicts the full electrochemical curve of LiVPO₄F, starting with discharge (red arrow). At a rate of C/10, 0.85 Li could be intercalated into the material at a potential of 1.8 V (vs. Li/Li⁺). The observed flat plateau of the electrochemical profile in this region implied the reduction of LiVPO₄F to Li₂VPO₄F proceeded *via* a two-phase process.

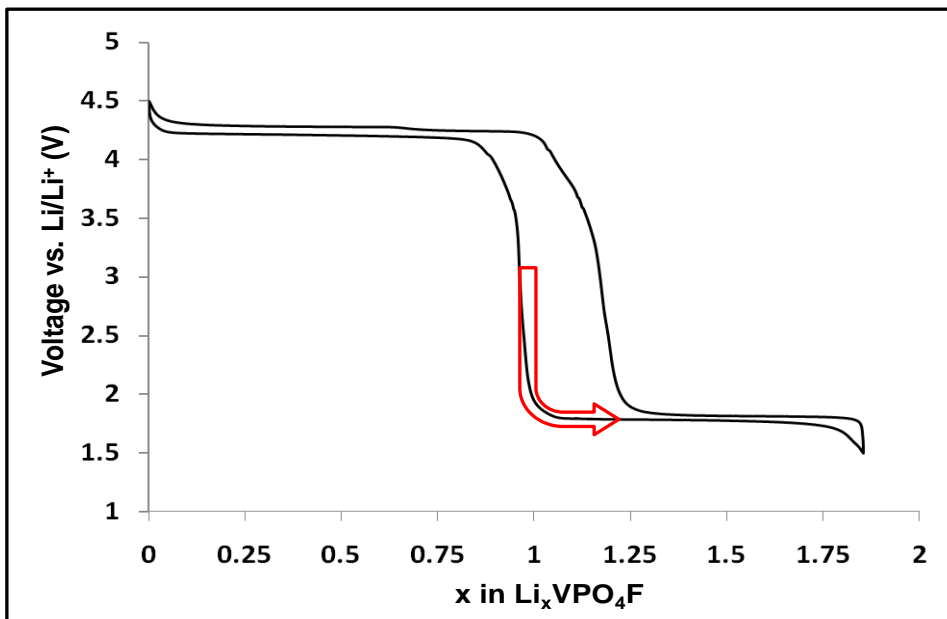


Figure 4.3: Electrochemical curve of $\text{LiVPO}_4\text{F}/\text{C}$ composite cycled vs. Li/Li^+ starting in discharge (as shown by the red arrow). The active material loading was $5 \text{ mg}/\text{cm}^2$ and the cell was cycled at a rate of $\text{C}/10$. Reprinted with permission from reference ¹⁰³, copyright 2011, American Chemical Society.

This is in contrast to the reduction of LiFePO_4F and $\text{LiFePO}_4(\text{OH})$ where approximately half of the electrochemical curve exhibited sloping behavior, as discussed in a later section. Charging the cell back to LiVPO_4F showed the same two-phase behavior. As the re-oxidation of V^{2+} to V^{3+} neared completion, we observed a rise in the voltage up to 4.25 V which occurs between $\text{Li}_{1.25}\text{VPO}_4\text{F}$ and LiVPO_4F unlike the more gradual voltage rise to 4.25 V between $\text{Li}_{1.25}\text{VPO}_4\text{F}$ and $\text{Li}_{0.87}\text{VPO}_4\text{F}$ observed in Barker's study.¹⁷⁹ The oxidation process continued (from V^{3+} to V^{4+}) on two new plateaus (4.25 V vs. Li/Li^+ for $\text{Li}_{1-x}\text{VPO}_4\text{F}$, $0 < x < 0.35$ and 4.3 V vs. Li/Li^+ for $\text{Li}_{1-x}\text{VPO}_4\text{F}$, $0.35 < x < 1.0$) until complete oxidation was achieved. Re-intercalation of the VPO_4F occurred at 4.20 V vs. Li/Li^+ and once 1.0 Li had been intercalated, the potential dropped sharply to 1.8 V where intercalation to $\text{Li}_2\text{VPO}_4\text{F}$ continued.

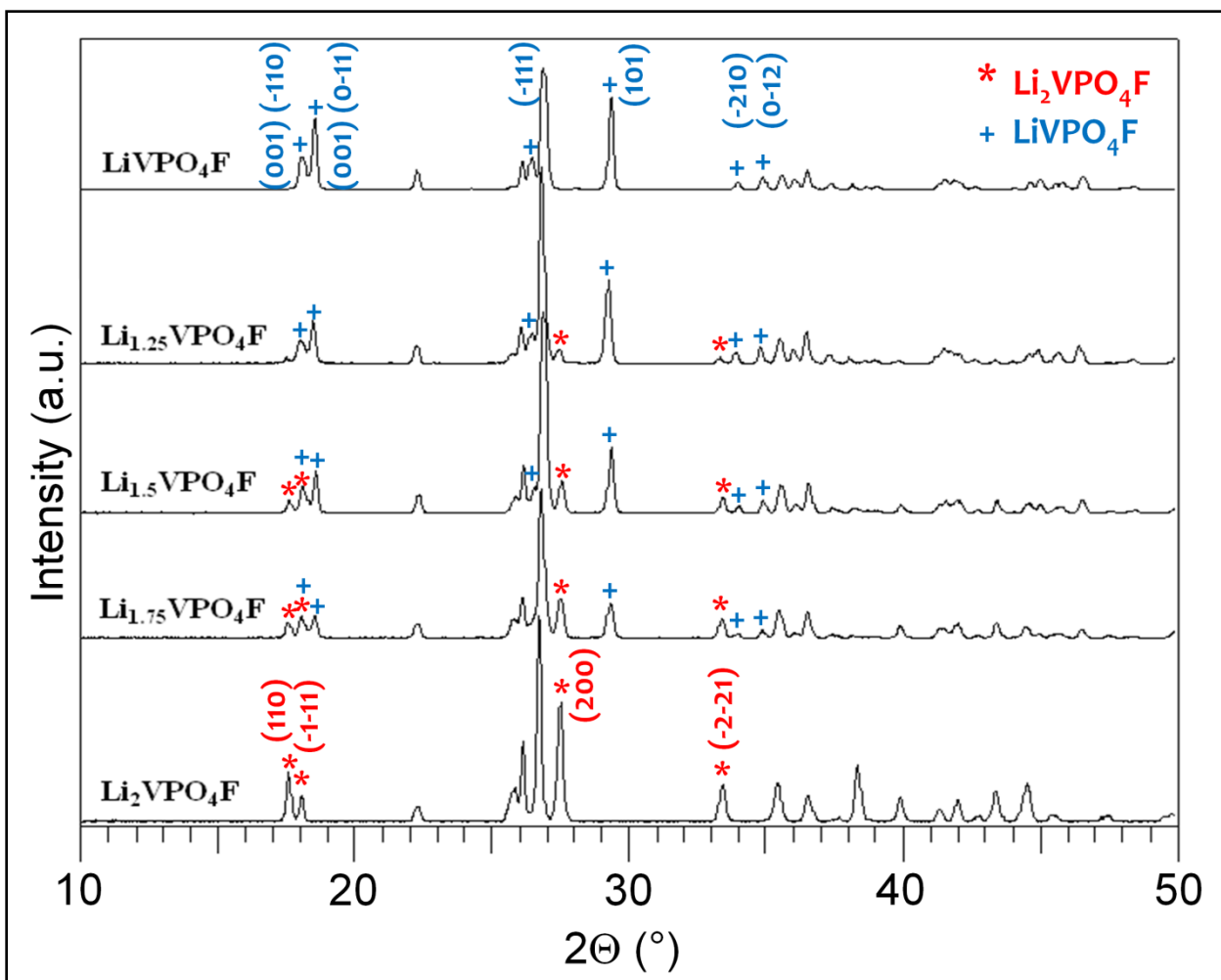


Figure 4.4: X-ray powder diffraction patterns of $\text{Li}_{1-x}\text{VPO}_4\text{F}$, synthesized by the chemical reduction of LiVPO_4F with LiAlH_4 . Two-phase behavior was observed as the quantity of LiVPO_4F decreases and the quantity of $\text{Li}_2\text{VPO}_4\text{F}$ increases with increasing x . Reprinted with permission from reference ¹⁰³, copyright 2011, American Chemical Society.

Compositions of $\text{Li}_{1-x}\text{VPO}_4\text{F}$ ($0 \leq x \leq 1$) by chemical oxidation (with NOBF_4) and $\text{Li}_{1+x}\text{VPO}_4\text{F}$ ($0 \leq x \leq 1$) by chemical reduction (with LiAlH_4) of LiVPO_4F were prepared to verify the two-phase nature of each vanadium redox step observed in the electrochemistry. Indeed, X-ray diffraction also showed this to be the case. Figure 4.4 depicts the evolution of $\text{Li}_{1+x}\text{VPO}_4\text{F}$ from $x = 0$ to $x = 1$ formed upon chemical reduction of LiVPO_4F with LiAlH_4 under Ar atmosphere. Due to the instability of V(II) compounds, the diffraction patterns were collected in a sealed sample holder filled with Ar.

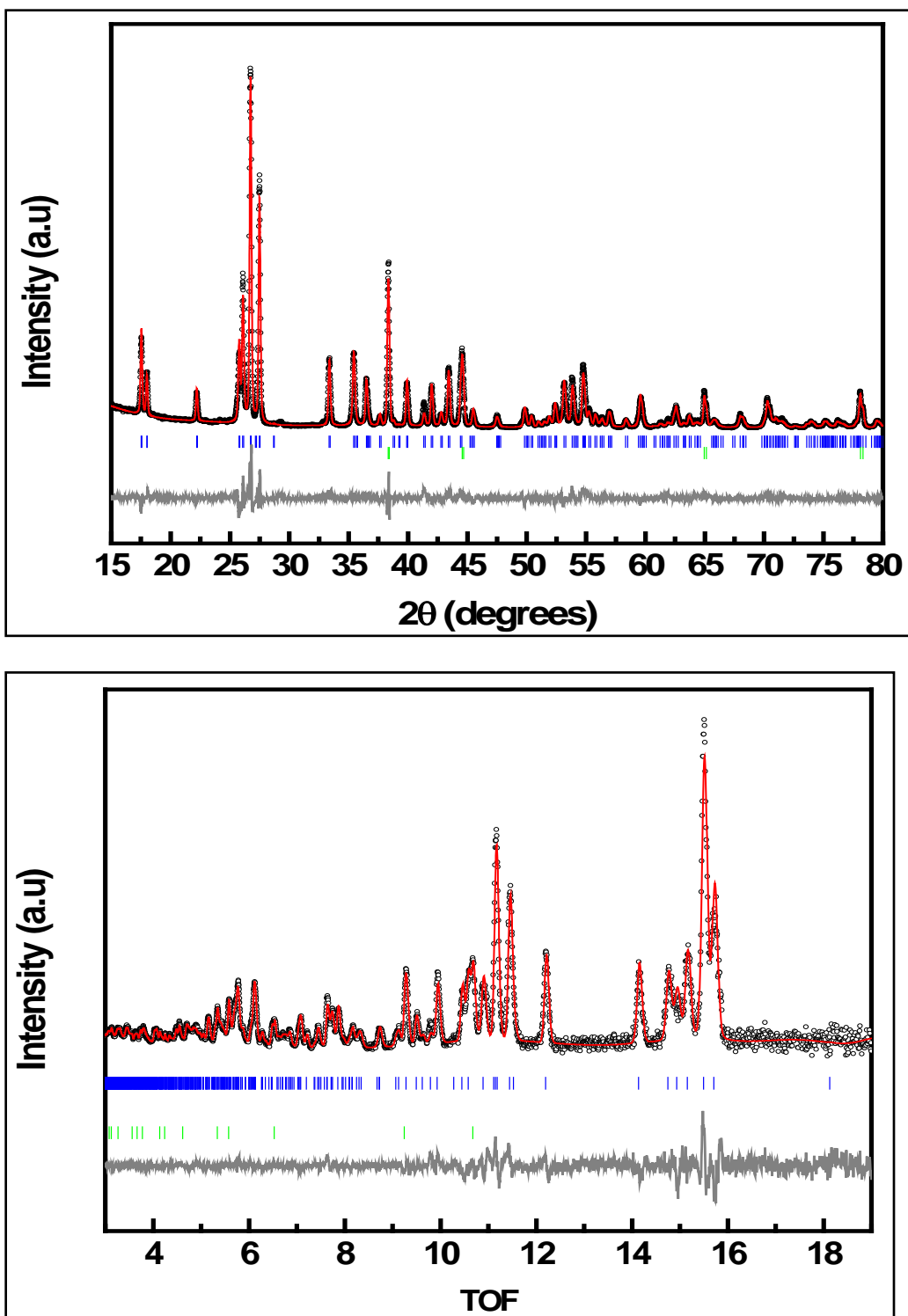


Figure 4.5: X-ray diffraction pattern (top) and neutron diffraction pattern (bottom) combined Rietveld refinement of $\text{Li}_2\text{VPO}_4\text{F}$ synthesized by chemical reduction of LiVPO_4F with LiAlH_4 . For each pattern, the experimental points are black, the fit is shown in red, the calculated reflections of $\text{Li}_2\text{VPO}_4\text{F}$ are shown in blue, calculated reflections of Al are shown in green and the difference map is shown in grey. The lattice parameters and atomic positions are listed in Table 3. Reprinted with permission from reference ¹⁰³, copyright 2011, American Chemical Society.

Table 4.3: Lattice constants and atomic parameters for Li₂VPO₄F refined from combined X-ray and neutron diffraction powder data. X-ray diffraction agreement factors: $R_{wp} = 11.08\%$, $R_p = 8.40\%$, $R_F^2 = 6.79\%$; neutron diffraction agreement factors: $R_{wp} = 4.28\%$, $R_p = 7.93\%$, $R_F^2 = 4.92\%$; combined statistics: $R_{wp} = 9.24\%$, $R_p = 8.40\%$.

Li ₂ VPO ₄ F						
Space group: C 2/c (#15), Monoclinic						
$M_w = 178.79$ g/mol						
$D = 3.171$ g cm ⁻³						
$a = 7.2255(1)$ Å						
$b = 7.9450(1)$ Å						
$c = 7.3075(1)$ Å						
$\beta = 116.771(1)^\circ$						
$V = 374.537(1)$ Å ³						
Atom	Wych.	x/a	y/b	z/c	Occ.	U _{iso}
V(1)	4b	0	1/2	0	1.0	0.0058(1)
P(1)	4e	1/2	0.3563(1)	0.25	1.0	0.0068(1)
O(1)	8f	0.3266(2)	0.4700(1)	0.1069(2)	1.0	0.0095(1)
O(2)	8f	0.0813(3)	0.7447(1)	0.1266(2)	1.0	0.0095(1)
F(1)	4e	0	0.3640(1)	0.25	1.0	0.0088(1)
Li(1)	8f	0.1174(2)	0.1613(1)	0.1597(2)	0.5	0.014(1)
Li(2)	8f	0.1791(2)	0.2177(1)	0.4394(2)	0.5	0.014(1)

Once LiVPO₄F was reduced to Li_{1.25}VPO₄F, a new phase could be observed along with some of the starting LiVPO₄F material in the resultant diffraction pattern. Additional reduction to Li_{1.5}VPO₄F showed further reduction of the signal intensity of LiVPO₄F and increased intensity of the new reduced phase. Subsequent reduction steps showed the same trend: growth of reduced phase at the expense of LiVPO₄F until almost complete intercalation of one equivalent of Li, where the reduced phase was the only vanadium fluorophosphate phase present. Elemental analysis that confirmed a Li:V:P ratio very close to 2:1:1 in the new Li₂VPO₄F phase.

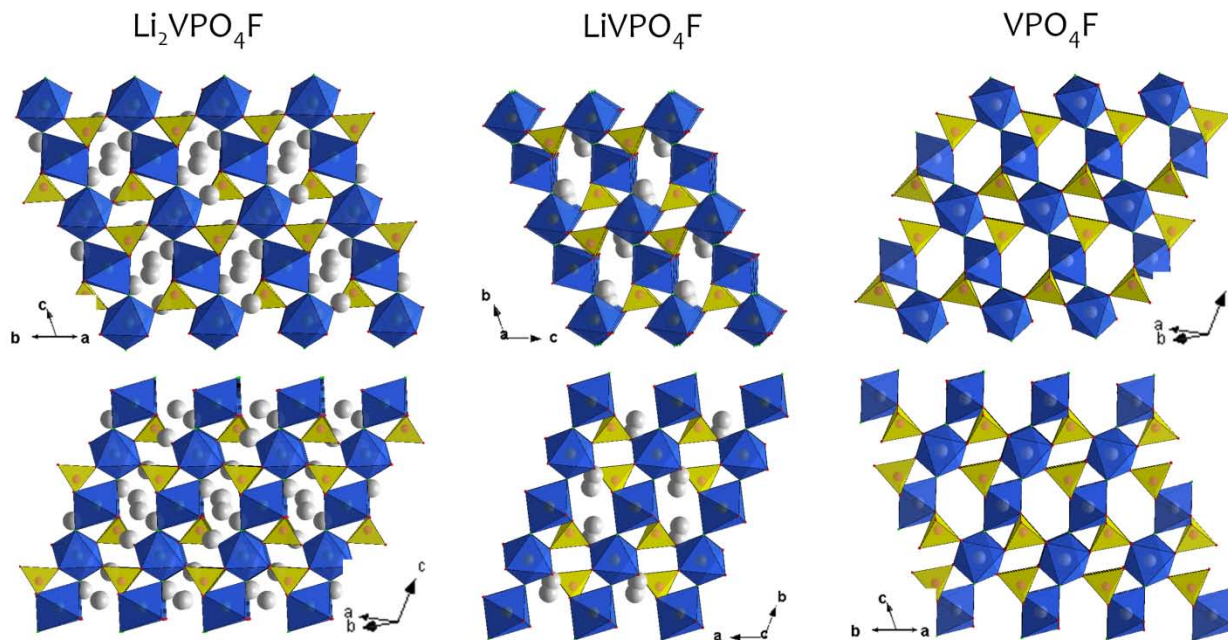


Figure 4.6: Pictorial representation of the structures of VPO_4F , $LiVPO_4F$ and Li_2VPO_4F depicting the chains of corner-shared vanadium octahedra and phosphate tetrahedra common to each structure. The vanadium octahedra are shown in blue, phosphate tetrahedra are shown in yellow and lithium ions are shown in grey. Reprinted with permission from reference ¹⁰³, copyright 2011, American Chemical Society.

Li_2VPO_4F was prepared *ex-situ* by stirring $LiVPO_4F$ with the chemical reducing agent $LiAlH_4$ in an inert atmosphere. Its X-ray diffraction and neutron diffraction patterns are shown in Figure 4.5, along with the results of the combined Rietveld refinement. The fits and resultant lattice parameters/atomic positions are listed in Table 4.3. A comparison of the structures of $LiVPO_4F$ and Li_2VPO_4F (Figure 4.6) makes it clear that although Li_2VPO_4F ($C2/c$) crystallizes in a different space group than $LiVPO_4F$ ($P-1$), Li_2VPO_4F is closely related to the parent phase. The exact same structural motif is present in Li_2VPO_4F , namely one-dimensional chains of VO_4F_2 octahedra which propagate (in the $C2/c$ cell) along the c -axis and which are connected by phosphate tetrahedra to form a fully corner-shared framework. Li ions partially occupy two general sites: Li1 ions reside in octahedral sites along the edges of the (110) tunnels (see Figure 4.6). These sites are nested between pairs of

V octahedra and the Li1 site shares edges with both vanadium sites. This site is quite similar in location to the original split Li position in LiVPO_4F . Although the change in symmetry of the lattice in lithiation makes this difficult to determine from the fractional coordinates, visual comparison of the frameworks shows it clearly (Figure 4.6). The Li ions which reside in the Li2 sites are located at the centre of the (110) tunnels and also sit between pairs of vanadium octahedra. The Li2 ions are face-shared with both vanadium octahedra of the pair, and correspond to the lithium that is inserted on reduction (ie, the new site). The structure of $\text{Li}_2\text{VPO}_4\text{F}$ differs considerably from other $\text{Li}_2\text{MPO}_4\text{F}$ compounds such as $\text{Li}_2\text{FePO}_4\text{F}$ ⁸³ and $\text{Li}_2\text{NiPO}_4\text{F}$,¹⁰⁴ both of which crystallize in orthorhombic space groups, Pbcn and Pnma respectively. The volume change for the transition from LiVPO_4F to $\text{Li}_2\text{VPO}_4\text{F}$ (7.4%) is fairly typical for phosphates, and the lattice mismatch between the two phases is one of the main reasons the electrochemical potential is flat in this region.

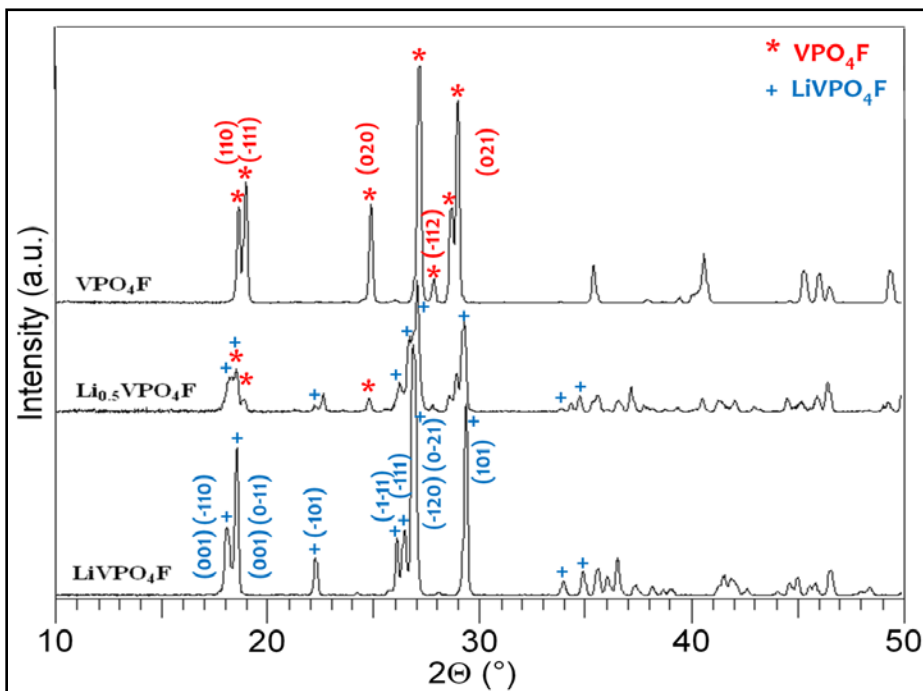


Figure 4.7: X-ray powder diffraction patterns of $\text{Li}_{1-x}\text{VPO}_4\text{F}$, synthesized by the chemical oxidation of LiVPO_4F with NOBF_4 . Two-phase behavior was observed up to the formation of VPO_4F . Reprinted with permission from reference¹⁰³, copyright 2011, American Chemical Society.

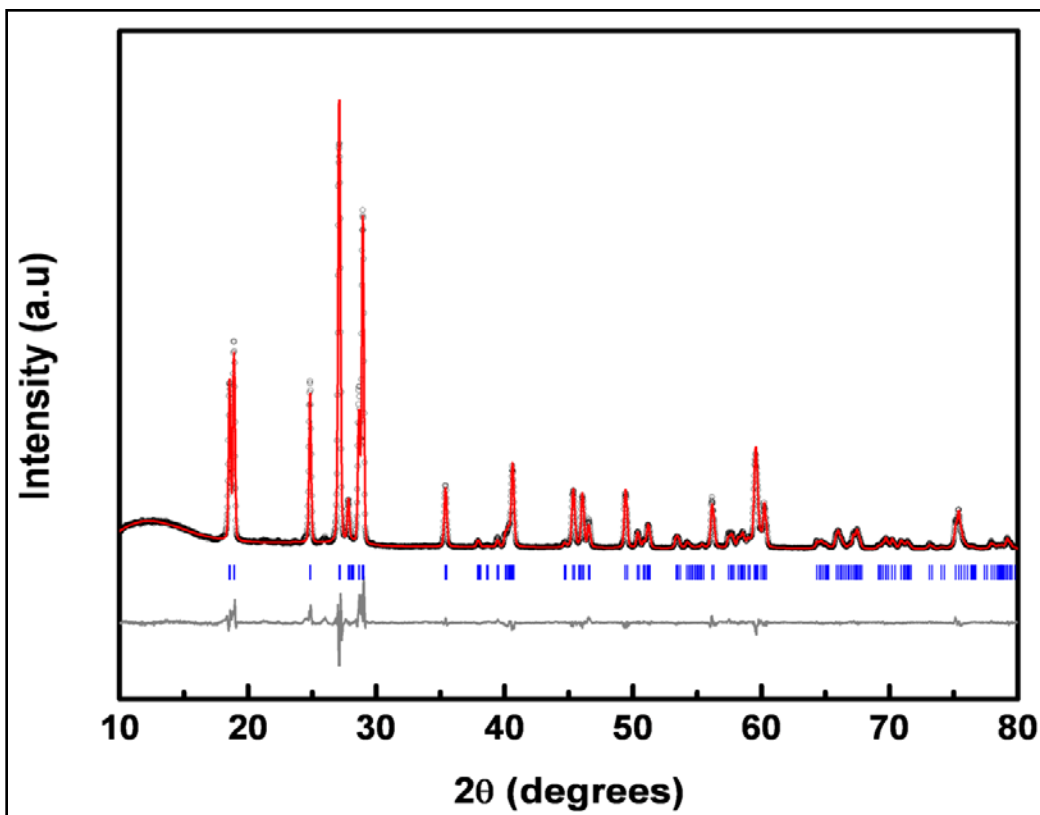


Figure 4.8: X-ray diffraction pattern and Rietveld refinement of VPO_4F synthesized by chemical oxidation of LiVPO_4F . The experimental points are black, the fit is shown in red, the calculated reflections are shown in blue and the difference map is shown in grey. Reprinted with permission from reference ¹⁰³, copyright 2011, American Chemical Society.

Table 4.4: Lattice constants and atomic parameters of VPO_4F refined from powder XRD data. Agreement factors: $R_{\text{wp}} = 8.88\%$, $R_p = 6.80\%$, $R_{F2} = 4.76\%$.

VPO ₄ F						
Space group: C 2/c (#15), Monoclinic						
a = 7.1553(2) Å						
b = 7.1014(1) Å β = 118.089(1)°						
c = 7.1160(2) Å						
V = 319.001(8) Å ³						
Atom	Wych.	x/a	y/b	z/c	Occ.	U _{iso}
V	4d	0.25	-0.25	0	1.0	0.015(1)
P	4e	0.5	0.1245(3)	0.25	1.0	0.012(1)
F	4e	0	-0.1684(5)	-0.25	1.0	0.014(1)
O (1)	8f	0.3309(3)	0.0037(4)	0.0749(4)	1.0	0.012(1)
O (2)	8f	0.3951(3)	0.2479(4)	0.3456(2)	1.0	0.014(1)

Figure 4.7 shows the evolution in the XRD patterns of $\text{Li}_{1-x}\text{VPO}_4\text{F}$ from $x = 0$ to $x = 1$ formed upon chemical oxidation of LiVPO_4F with NOBF_4 under an argon atmosphere. On partial oxidation of LiVPO_4F to $\text{Li}_{0.5}\text{VPO}_4\text{F}$, a mixture of LiVPO_4F and a new phase is apparent in the diffraction pattern. Complete oxidation shows only the presence of this new phase, namely VPO_4F . An X-ray diffraction pattern and subsequent Rietveld refinement on the pure VPO_4F powder sample is shown in Figure 4.8 and the refinement results are summarized in Table 4.4. The structure (Figure 4.6) is also strongly related to LiVPO_4F , and is also isostructural with FeSO_4F which crystallizes in the same C2/c lattice as discussed later. VPO_4F consists of corner-shared chains of VO_4F_2 octahedra interconnected by phosphate groups *via* corner-sharing where the tunnels are obviously free of lithium ions. The volume change for the transition from $\text{LiVPO}_4\text{F} \leftrightarrow \text{VPO}_4\text{F}$ is 8.5%, substantially larger than in $\text{LiFePO}_4 \leftrightarrow \text{FePO}_4$ olivine, for example (6.7%).¹⁴⁶ The large unit cell volume difference is one of the reasons two-phase behavior is observed in this region of the electrochemical curve, yet the two phase electrochemical transition takes place with very low polarization suggestive of high Li-ion mobility and relatively rapid kinetics.

4.4 Synthesis & Electrochemical and *Ex-Situ* X-ray Studies of the Novel Lithium Iron Fluorophosphate LiFePO_4F

LiFePO_4F was prepared by a solid-state method under inert atmosphere which produced a pure single phase material, as opposed to other reports where the sintering environment was reported to be air.¹⁸⁴ Our attempts to crystallize LiFePO_4F in the presence of oxygen at high temperature produced mixtures of $\text{Li}_3\text{Fe}_2(\text{PO}_4)_3$ and Fe_2O_3 . Our novel solvothermal technique reported here also produces pure LiFePO_4F at a much lower

temperature than the solid state or other solution-based methods and without the need to recover expensive ionic liquids. The precursors were dried in an oven at 100 °C and the ethanol was dried over molecular sieves prior to starting the reaction to minimize water and suppress OH⁻ formation in solution. X-ray diffraction patterns and FESEM images of material produced from both synthetic methods are shown in Figure 4.9.

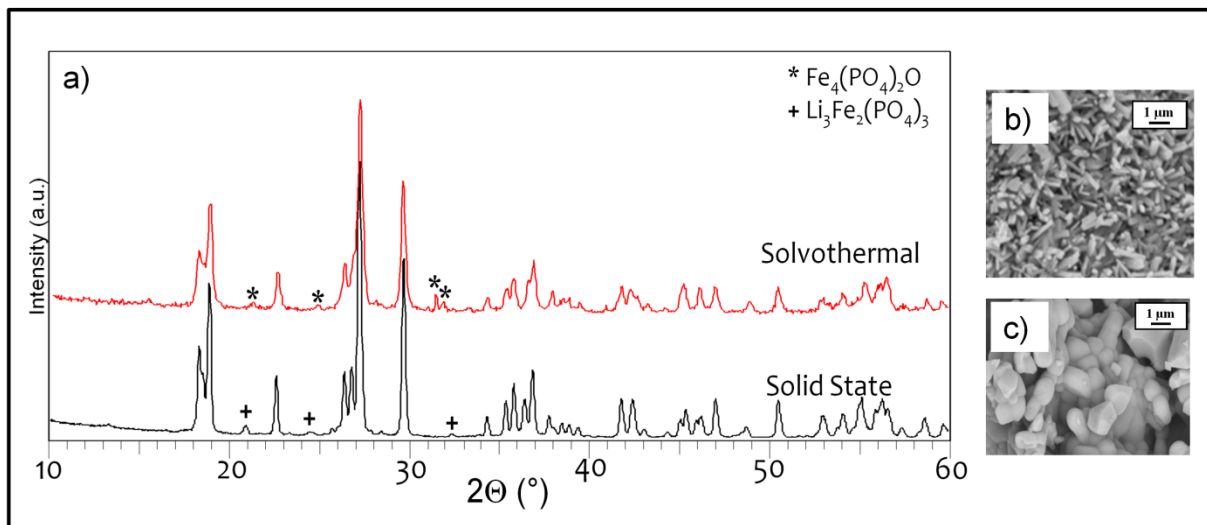


Figure 4.9: a) X-ray diffraction patterns and SEM micrographs of b) LiFePO₄F prepared by our solvothermal method and c) LiFePO₄F prepared by our solid-state method.

We note that pH control in the solvothermal route is critical in order to ensure LiFePO₄F is the main product. The addition of NH₄HF₂ which acts as both a fluorinating agent and a weak acid favored the formation of giniite, Fe₅(PO₄)₄(OH)₃•2H₂O, which precipitates in acidic media.¹⁷⁷ Trace impurities of Fe₄(PO₄)₂O were present in the solvothermally prepared material while most solid-state prepared materials were contaminated with traces of Li₃Fe₂(PO₄)₃. The solid-state prepared material formed agglomerates of large (300-1000 nm) particles typical of carbon-free high-temperature synthesis routes. The solvothermal LiFePO₄F material had a matchstick-like morphology: crystallites exhibited very small dimensions (< 100 nm) in two directions with lengths up to 1 μm.

Table 4.5: Lattice parameters for solid-state and solvothermally prepared iron tavorite phosphates.

Compound	a (Å)	b (Å)	c (Å)	α (°)	β (°)	γ (°)	V (Å ³)
LiFePO ₄ (OH)*	5.3523(1)	7.2851(2)	5.1163(2)	109.287(2)	97.827(2)	106.336(4)	174.83
LiFePO ₄ (OH) _{0.4} F _{0.6} *	5.3227(1)	7.2881(1)	5.1326(1)	108.997(1)	97.818(1)	106.798(1)	174.31
SS-LiFePO ₄ F*	5.3002(2)	7.2601(2)	5.1516(2)	107.880(3)	98.559(3)	107.343(3)	173.67
ST-LiFePO ₄ F [†]	5.301	7.262	5.153	107.95	98.62	107.41	173.58
SS: Solid state; ST: Solvothermal							
[†] : Lattice parameters obtained by indexing; *: Lattice parameters Rietveld refinement							

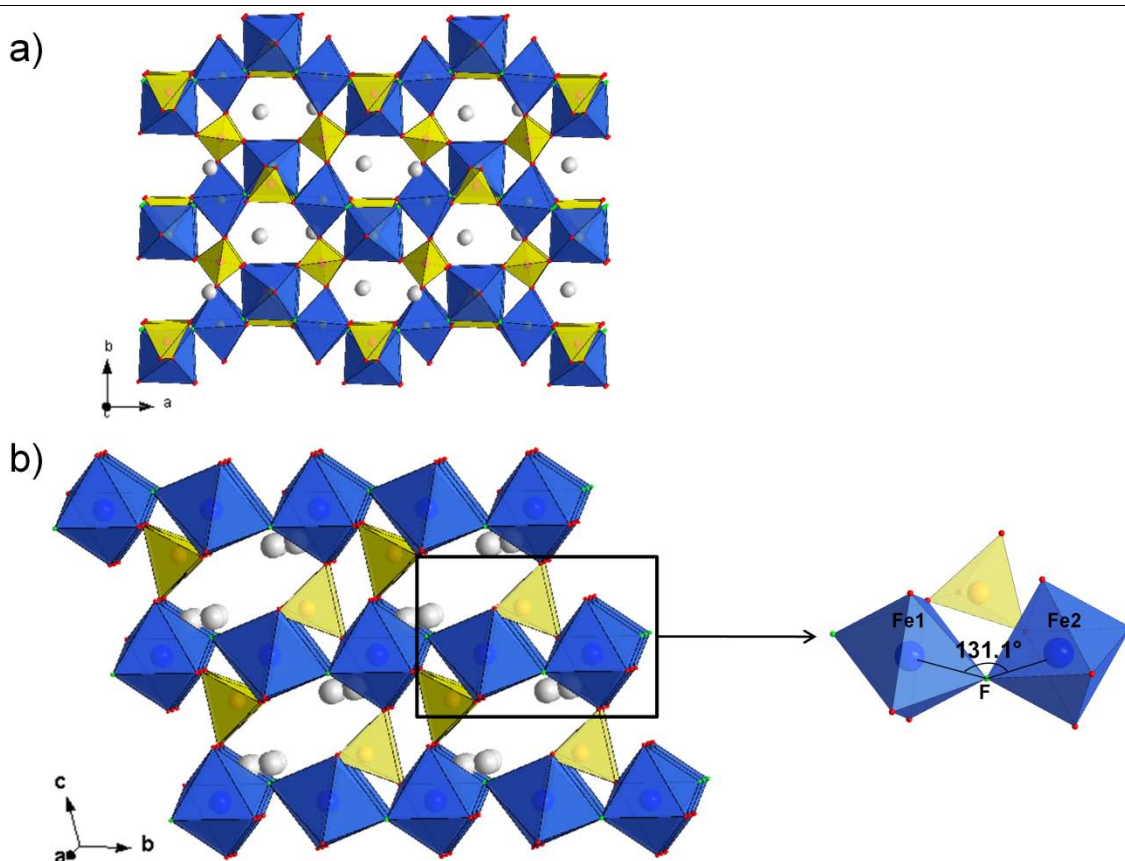


Figure 4.10: Graphical comparison of the KFePO₄F and tavorite (LiFePO₄F) structures; phosphate tetrahedra are depicted in yellow, iron octahedra in blue and alkali metal ions in grey.

The lattice parameters for materials prepared by both methods are given in Table 4.5. The triclinic (P-1) structure of LiFePO₄F is similar to that of other LiM³⁺PO₄(OH,F) compounds reported previously, such as LiAlPO₄(OH) and LiAlPO₄F, but it differs from the structure of KFePO₄F.¹⁸⁵ A polyhedral representation of the two structures is shown in

Figure 4.10. KFePO_4F crystallizes in an orthorhombic space group ($\text{P2}_1\text{nb}$) and is isostructural with $\text{NH}_4\text{FePO}_4\text{F}$.¹⁸⁶ The structure of KFePO_4F is comprised of corner-sharing of alternating *cis*- and *trans*- FeO_4F_2 octahedra which form a zig-zag pattern. These chains are linked by corner-shared phosphate tetrahedra to make a 3-D framework with large tunnels down the *b*-axis and the *c*-axis; potassium ions reside in these channels. LiFePO_4F is comprised of one-dimensional chains of corner-sharing $[\text{FeO}_4\text{F}_2]$ octahedra, with alternate octahedra in the chain slightly tilted. These chains are interconnected by corner-sharing phosphate tetrahedra which effectively limit electron transport to one dimension. The resulting cavities house the Li^+ but afford open pathways for 3-D ion transport.

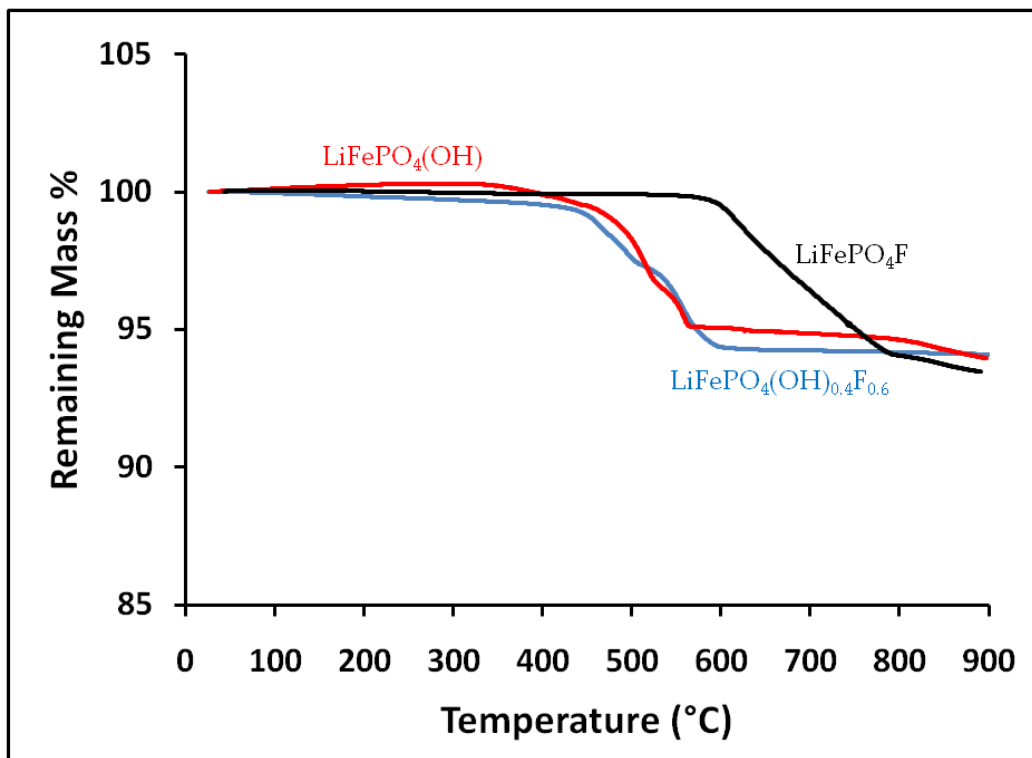
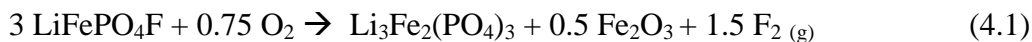


Figure 4.11: Thermal gravimetric analysis of iron phosphate fluorides heated under a nitrogen atmosphere at a rate of $5^\circ\text{C}/\text{min}$.

The thermal stability of LiFePO_4F in a nitrogen atmosphere was tested and the results are shown in Figure 4.11. LiFePO_4F remained stable in a nitrogen atmosphere up to 600°C ,

at which point it decomposed. In the presence of trace quantities of O₂, the decomposition reaction proceeded as follows:



Not surprisingly, these similar to the products found after thermal decomposition of olivine LiFePO₄ performed under oxidizing conditions.⁹⁹ A mass loss of 6.0 % was measured for this process, in good agreement with the calculated value of 6.2 %.

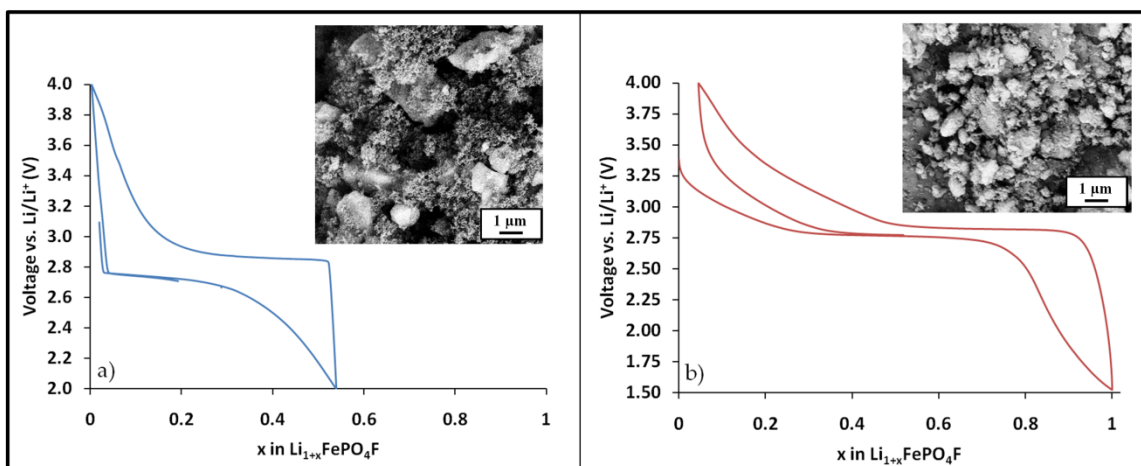


Figure 4.12: Electrochemical data for LiFePO₄F vs. Li/Li⁺ collected in coin cells at a rate of C/50 for a) as-synthesized solid-state LiFePO₄F and b) LiFePO₄F ground in a ball mill for 3 hours. SEM images of prepared electrodes for each material are shown in the insets.

Electrochemical profiles of as-prepared and pulverized samples of LiFePO₄F cycled at a slow rate (C/50) are shown in Figure 4.12. The initial discharge of the as-prepared sample featured a short plateau at 2.75 V followed by a long sloping overcharge (Figure 4.12a). Since the electrode was comprised of rather large particles of LiFePO₄F which were not carbon-coated, the as-prepared material had a low capacity for Li intercalation (0.55 Li) as well as a high polarization (0.25 V). These shortcomings were eradicated by pulverizing the as-synthesized material for 3 hours in a planetary ball mill at a low speed (< 200 rpm). An SEM micrograph of the active material after milling is shown in the inset of Figure 4.12b.

The particle morphology changed significantly from the as-prepared material (see Figure 4.9). After milling, the particles had a spherical shape and ranged in size from 200-400 nm, and the carbon was better dispersed. For this material, the electrochemical profile exhibited a sloping curve up to the insertion of 0.4 Li into the structure, at which point the profile was flat. The plateau was also at 2.75 V vs. Li. The cell reached full capacity (1.0 Li) and the polarization of this cell was much lower (0.10 V) than that of the as-prepared electrode material. Although grinding the carbon-free sample after preparation clearly reduced the primary particle size of the electrode, it is not clear whether the change in profile shape was strictly the result of particle size reduction or whether other factors, such as the change in particle shape or formation of an amorphous iron fluorophosphate phase, were responsible.

Regardless of the method of sample preparation, LiFePO_4F has some degree of a flat voltage plateau at 2.75 V, indicative of a two-phase transition. To verify this, we prepared variable compositions of $\text{Li}_{1+x}\text{FePO}_4\text{F}$ ($0 < x < 1$) by chemical reduction of as-synthesized LiFePO_4F with LiAlH_4 . Powder XRD patterns of these compositions are shown in Figure 4.13; for clarity, the region of 2Θ from $10\text{-}40^\circ$ is highlighted and peaks of interest are indexed. On reduction to $\text{Li}_{1.25}\text{FePO}_4\text{F}$ ($x = 0.25$ Li) a new second phase is barely evident in the diffraction pattern, signaled by the appearance of a very weak reflection at $2\theta = 27.8^\circ$. This peak becomes clearly evident at the composition $\text{Li}_{1.5}\text{FePO}_4\text{F}$. Subsequent reduction indicates continued growth of the new $\text{Li}_2\text{FePO}_4\text{F}$ phase at the expense of LiFePO_4F until complete intercalation of one equivalent of Li results, in accord with the electrochemical data. The stoichiometry of this phase was verified by elemental analysis which confirmed a Li:Fe:P ratio of approximately 2:1:1, and EDX measurements which confirmed a Fe:P:F ratio

of very close to 1:1:1. In short, the existence of a solid solution between $0 < x < 0.3$ is unclear, but for $x > 0.4$, the existence of a two phase regime is unequivocal.

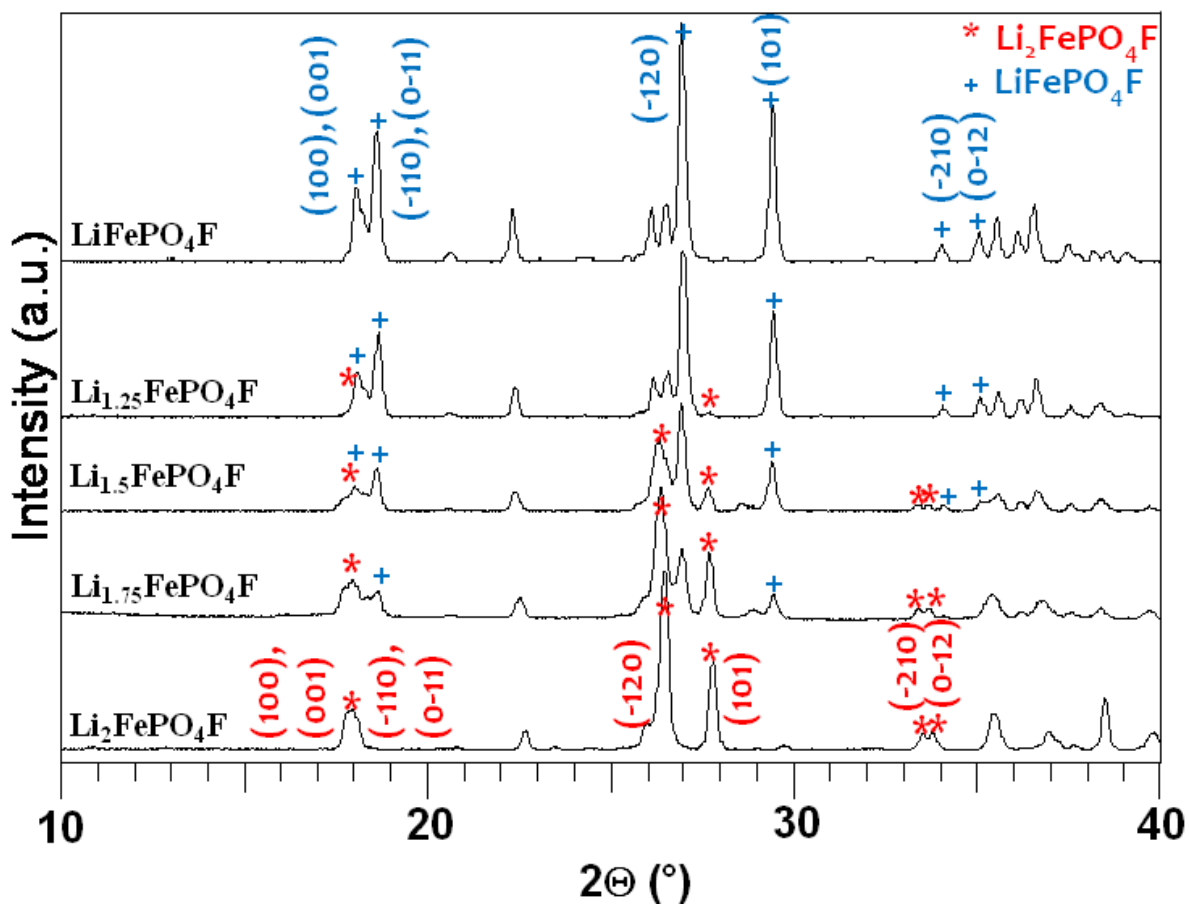


Figure 4.13: XRD patterns of $\text{Li}_{1+x}\text{FePO}_4\text{F}$ compositions prepared by chemical reduction with stoichiometric amounts of LiAlH_4 , showing the two-phase behavior upon LiFePO_4F reduction. Selected peaks of LiFePO_4F are shown with blue crosses and selected peaks of $\text{Li}_2\text{FePO}_4\text{F}$ are shown with red asterisks. Reproduced from reference¹⁰¹ with permission from the Royal Society of Chemistry.

Mössbauer spectroscopy revealed important clues about the lattice symmetry of LiFePO_4F , and especially $\text{Li}_2\text{FePO}_4\text{F}$. The Mössbauer spectrum for as-synthesized LiFePO_4F is shown in Figure 4.14a. The major signal (>90 % of the total measured intensity) was fitted with a single isomer shift (IS) of 0.42(1) mm/s and quadrupole splitting (QS) of 1.15(1) mm/s, consistent with Fe^{3+} in the presence of an octahedral field. Although

there are two crystallographically unique Fe^{3+} sites in LiFePO_4F , the two sites are very similar, with two fluoride and four oxygen ligands of similar bond lengths co-ordinated to both unique Fe atoms, and thus it is difficult to resolve the two sites. The Mössbauer spectrum and fit for the reduced material, $\text{Li}_2\text{FePO}_4\text{F}$ are shown in Figure 4.14b. Two distinct signals are clearly seen in the spectrum: the most prominent has parameters of $\text{IS} = 1.24 \text{ mm/s}$ and $\text{QS} = 2.79 \text{ mm/s}$ and the second signal has Mössbauer parameters of $\text{IS} = 1.22 \text{ mm/s}$ and $\text{QS} = 2.18 \text{ mm/s}$. Together, these two signals make up about 90% of the total signal, which confirms the nearly full reduction of Fe^{3+} to Fe^{2+} in this sample. These two signals are in a ratio of 3:1. This is significant as LiFePO_4F has only two unique Fe sites in the structure.

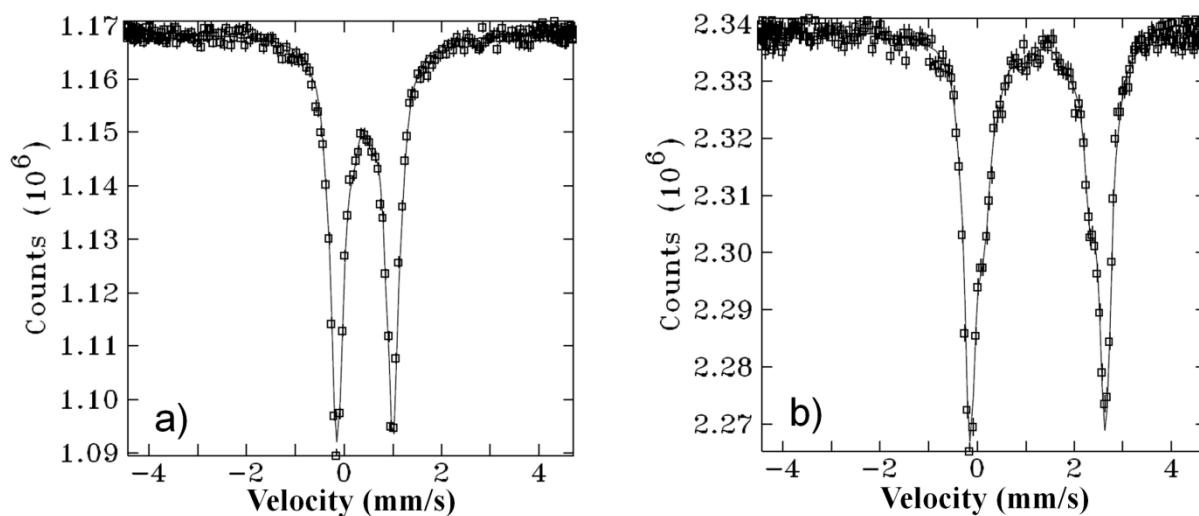


Figure 4.14: Room temperature Mössbauer spectra and fit (solid line) of a) LiFePO_4F and b) $\text{Li}_2\text{FePO}_4\text{F}$, prepared from chemical reduction of LiFePO_4F with LiAlH_4 .

The structure of $\text{Li}_2\text{FePO}_4\text{F}$ was elucidated by a combined Rietveld refinement of powder X-ray diffraction and neutron diffraction patterns. The fitted patterns are shown in Figure 4.15 and the refinement results are presented in Table 4.6. Indexing software indicated the space group for $\text{Li}_2\text{FePO}_4\text{F}$ was P-1, the same as that of LiFePO_4F . The final

refined lattice parameters are similar to those reported previously from a LeBail fit whereupon an 8.0% volume expansion of the LiFePO_4F lattice upon Li intercalation was reported.¹⁸⁰ Owing to the expected similarities in the iron fluorophosphates framework between the pristine and reduced materials, the crystal structure of $\text{LiFePO}_4(\text{OH})$ was used as the basis for the refinement of $\text{Li}_2\text{FePO}_4\text{F}$. The positions of the Fe, P, O and F atoms, along with the lattice parameters, background and line-shape parameters were optimized before Li was introduced into the structure.

Lithium was first introduced into the structure as a split position with two separate sites equally occupied, as in $\text{LiFePO}_4(\text{OH})$.¹⁸⁷ Refinement of these atomic positions resulted in their convergence to one central site (Li1) in $\text{Li}_2\text{FePO}_4\text{F}$. A comparison of the Li1 environments in LiFePO_4F and $\text{Li}_2\text{FePO}_4\text{F}$ is shown in Figure 4.15. The oxygen and fluorine ions which co-ordinate both Li and Fe shift slightly on reduction, owing to the significantly larger radius of the Fe^{2+} ions (78 pm) compared to Fe^{3+} (64 pm).¹⁸⁸ The slight shift in the oxygen and fluorine positions, specifically O1 and O2' in Figure 4.16 results in a new coordination environment for Li1, even though Li1 in $\text{Li}_2\text{FePO}_4\text{F}$ is positioned close to the centroid of the split Li position in the parent LiFePO_4F . Furthermore, the new environment for the Li1 ion is smaller than that in LiFePO_4F ; as a consequence, the new Li position is not split.

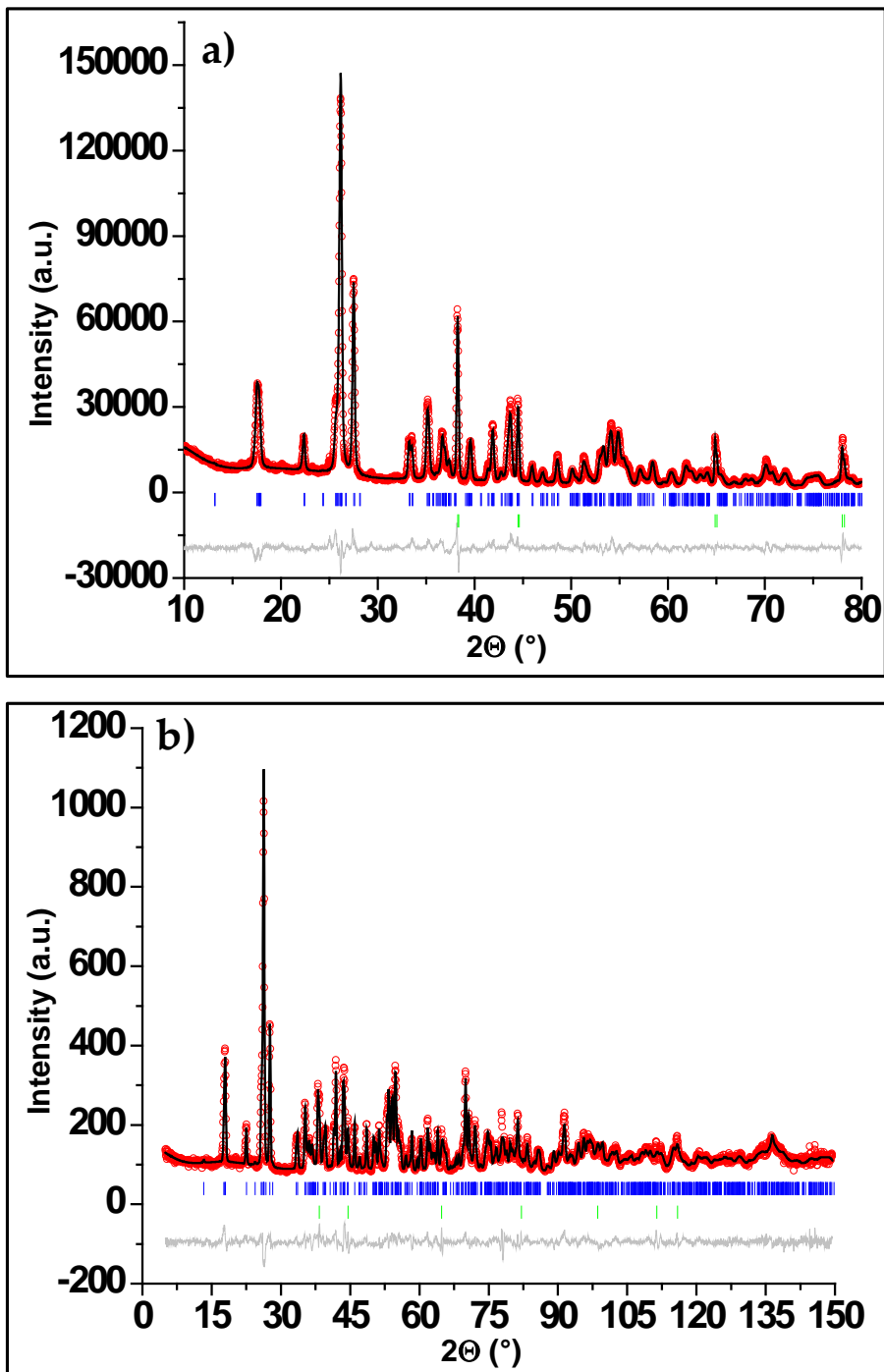


Figure 4.15: Combined Rietveld refinement of X-ray and neutron powder diffraction data from a sample of $\text{Li}_2\text{FePO}_4\text{F}$. The statistical agreement factors for the combined refinement are: $R_{\text{wp}} = 9.45\%$, $R_p = 7.29\%$, $\chi^2 = 45.79$. a) Refined X-ray diffraction pattern with agreement factors of $R_{\text{wp}} = 9.48\%$, $R_p = 7.32\%$, $R_F^2 = 6.87\%$. b) Refined neutron diffraction pattern with agreement factors of $R_{\text{wp}} = 6.40\%$, $R_p = 4.95\%$, $R_F^2 = 6.83\%$. For each pattern, the collected data are in red, the fit is shown in black, the calculated reflections of $\text{Li}_2\text{FePO}_4\text{F}$ are shown in blue, calculated reflections of Al are shown in green and the difference map is shown in grey. A summary of the refined data is given in Table 4.6. Reproduced from reference ¹⁰¹ with permission from the Royal Society of Chemistry.

Table 4.6: Lattice constants and atomic parameters of $\text{Li}_2\text{FePO}_4\text{F}$ determined by a combined refinement of X-ray and neutron powder diffraction data. Agreement factors for neutron diffraction data: $R_{\text{wp}} = 6.40\%$, $R_p = 4.95\%$, $R_F^2 = 6.83\%$. Agreement factors for X-ray diffraction data: $R_{\text{wp}} = 9.48\%$, $R_p = 7.32\%$, $R_F^2 = 6.87\%$. Agreement factors for combined refinement: $R_{\text{wp}} = 9.45\%$, $R_p = 7.29\%$, $\chi^2 = 45.79$

$\text{Li}_2\text{FePO}_4\text{F}$						
Space group: P -1 (#2), Triclinic						
$M_w = 183.70 \text{ g/mol}$						
$D = 3.225 \text{ g cm}^{-3}$						
$a = 5.3736(2) \text{ \AA}$						
$b = 7.4791(2) \text{ \AA}$						
$c = 5.3276(2) \text{ \AA}$						
$\alpha = 108.398(4)^\circ$						
$\beta = 94.615(4)^\circ$						
$\gamma = 108.217(4)^\circ$						
$V = 189.142(8) \text{ \AA}^3$						
Atom	Wych.	x/a	y/b	z/c	Occ.	U_{iso}
Fe (1)	1a	0	0	0	1.0	0.011(2)
Fe (2)	1b	0	1/2	0	1.0	0.008(1)
P	2i	0.6389(9)	0.750(1)	0.348(1)	1.0	0.011(1)
O (1)	2i	0.657(2)	0.866(2)	0.147(2)	1.0	0.015(3)
O (2)	2i	0.335(2)	0.635(1)	0.309(2)	1.0	0.018(3)
O (3)	2i	0.790(2)	0.620(2)	0.304(2)	1.0	0.012(3)
O (4)	2i	0.278(2)	0.097(2)	0.365(2)	1.0	0.017(3)
F	2i	0.888(1)	0.262(2)	0.171(2)	1.0	0.013(2)
Li (1)	2i	0.465(5)	0.679(4)	0.743(5)	1.0	0.015
Li (2)	1g	0	1/2	1/2	1.0	0.015
Li (3)	2i	0.112(5)	0.824(7)	0.521(8)	0.5	0.015

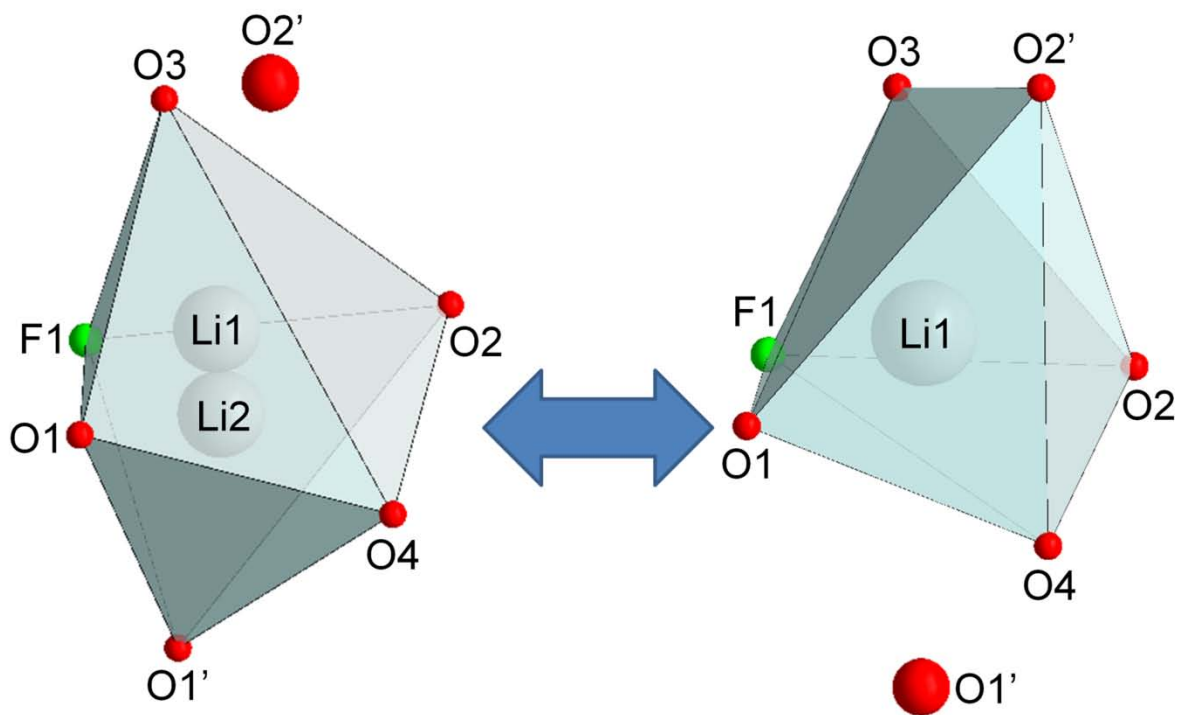


Figure 4.16: Comparison of the Li1 environments in LiFePO₄F (left) and Li₂FePO₄F (right).

Although the iron fluorophosphate framework of Li₂FePO₄F is very similar to that in LiFePO₄F: 1-D chains of corner-shared FeO₄F₂ octahedra connected by PO₄³⁻ tetrahedra, three crystallographically unique Li sites were found in Li₂FePO₄F. A graphical representation of the structure is shown in Figure 4.17a. The two sites where the intercalated Li reside are Li2 and Li3, each of which is occupied by 0.5 Li. Li2 resides between the chains of Fe octahedra on a special position, the 1g site and is coordinated by two fluorine and four oxygen ligands. A previous study of a natural slightly reduced sample of LiFePO₄(OH) showed this site is partially occupied by Fe²⁺ ions.¹⁸⁷ The Li3 site is a general position which is half occupied and octahedrally coordinated by one fluorine and five oxygen ligands.

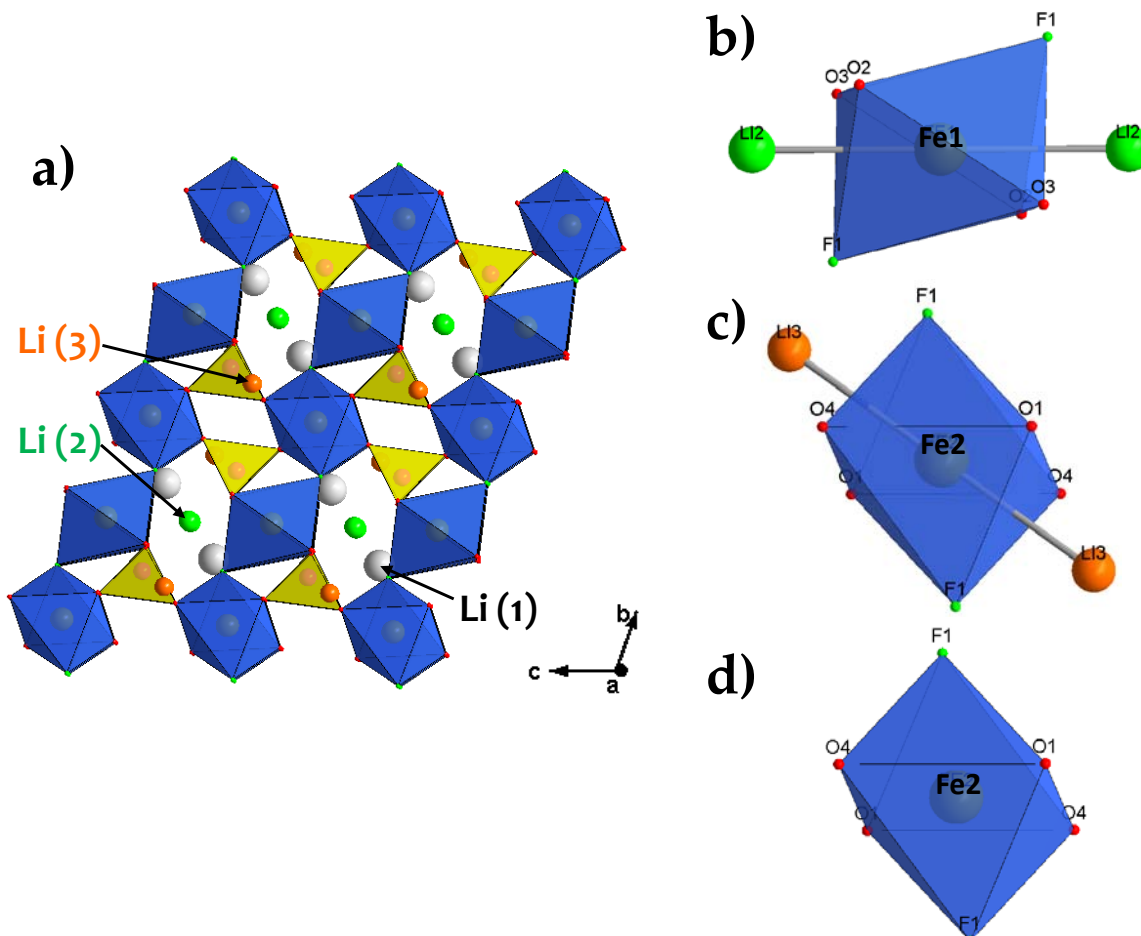


Figure 4.17: a) Graphical representation of the $\text{Li}_2\text{FePO}_4\text{F}$ structure with iron octahedra in blue, phosphate tetrahedra in yellow and lithium ions Li1 in white, Li2 in green and Li3 in orange. Graphical representations of the Fe environments in $\text{Li}_2\text{FePO}_4\text{F}$ are shown for b) Fe1, c) Fe2A and d) Fe2B. Reproduced from reference ¹⁰¹ with permission from the Royal Society of Chemistry.

Table 4.7: Summary of Bond Distances for Each Iron Environment in $\text{Li}_2\text{FePO}_4\text{F}$

<u>Atom</u>	<u>Ligand</u>	<u>Multiplicity</u>	<u>Distance (Å)</u>
Fe1	O2	2x	2.074
	O3	2x	2.137
	F1	2x	2.192
	Li2	2x	2.664
Fe2A	O4	2x	2.125
	O1	2x	2.141
	F1	2x	2.172
	Li3	2x	2.687
Fe2B	O4	2x	2.125
	O1	2x	2.141
	F1	2x	2.172

With the intercalated Li ions occupying these two sites, the Mössbauer results can be put into structural context. Figure 4.17b is a graphical representation of the bonding environment of the Fe1 ion. The Fe-O and Fe-F bond distances range from 2.07 to 2.19 Å (see Table 4.7). Li2 resides between adjacent chains of Fe octahedra and each Fe1 shares triangular faces with two Li2 ions which are 2.66 Å from Fe1. These Li⁺ ions are close enough to the Fe1 site that the Li can be considered part of the Fe bonding environment. Representations of the Fe2 site are shown in Figure 4.17c-d. The Fe-O and Fe-F bonds range from 2.12 to 2.17 Å in length and the Li3 ion is also in close proximity to Fe2 (2.68 Å). If the Li3 site were fully occupied, each Fe2 ion would be face-shared with two Li octahedra, just as the case of the Fe1 site. As the Li3 site is only half occupied, only half of the Fe ions on the Fe2 site will face-share with two Li3 ions (denoted as the Fe2A site, see Figure 4.17c). The remaining Fe2 sites (denoted as Fe2B sites, Figure 4.17d) will not have any cations in the local environment. The similar environments of the Fe1 and Fe2A atoms could not be resolved by Mössbauer spectroscopy and therefore, the ratio of [Fe1+Fe2A] sites to the Fe2B sites in Li₂FePO₄F is 3:1, which is in accord with the Mössbauer data.

Finally, we note that the tavorite-type structure of Li₂FePO₄F prepared by reduction of LiFePO₄F differs greatly from Li₂FePO₄F prepared by ion-exchange of two-dimensional Na₂FePO₄F. The latter contains dimers of face-shared FeO₄F₂ octahedra which are connected by corner sharing in two dimensions to form 2D sheets. The Li ions reside between the layers.

In conclusion, LiFePO₄F demonstrated two-phase behavior in Li cells, although particle size has a significant effect on the capacity. The two-phase nature of LiFePO₄F intercalation was confirmed by chemical reduction of LiFePO₄F where Li_{1+x}FePO₄F

compositions clearly show a mixture of LiFePO_4F and $\text{Li}_2\text{FePO}_4\text{F}$; the overall 8.0% volume expansion of the lattice upon insertion of one Li is a likely origin of the two-phase nature of this compound. The resolved structure of $\text{Li}_2\text{FePO}_4\text{F}$ shows that the corner-shared framework of the “ FePO_4F ” lattice remains intact upon reduction to $\text{Li}_2\text{FePO}_4\text{F}$. The good fits of both the X-ray and neutron powder diffraction patterns produced a robust structural solution for $\text{Li}_2\text{FePO}_4\text{F}$, which was found to have many structural similarities to LiFePO_4F . The structure solution also justified the Mössbauer data. As a result, the structural model of $\text{Li}_2\text{FePO}_4\text{F}$ generated here was a reasonable one. Lithium insertion in the lattice is complex, and occurs in two sites. Occupation of the first appears to occur via a solid solution process (with respect to lithium concentration), whereas occupation of the last site triggers two-phase behavior. The mechanism of lithium intercalation for LiFePO_4F is different than those of the other iron-based iron phosphate favorites, as will be discussed in the upcoming sections.

4.5 The Mechanism of Lithium Insertion into LiFePO_4OH : Preparation of Amorphous $\text{Li}_2\text{FePO}_4\text{OH}$

Three hydrothermal methods of preparation of LiFePO_4OH have been reported in the literature: the first necessitated temperatures above 400°C as well as excessive pressure and long periods of time to crystallize the material;⁶⁷ the second involved the preparation of $\text{Fe}(\text{OH})_2$ in-situ which then reacted with LiCl and P_2O_5 at 170°C under autogeneous pressure for 3 days;⁹⁸ the third involved a reaction between $\text{FePO}_4 \cdot 2\text{H}_2\text{O}$ and lithium acetate at 150°C , also for 3 days.⁹⁹ During the course of our study, another report on LiFePO_4OH was published by Marx *et al.*¹⁸⁹ They noted significant impurities in the previous route and needed to raise the relative quantity of lithium acetate to acquire pure favorite as the product,

after a significantly shorter time (24 hours). In our hydrothermal method, a mixture of lithium hydroxide and lithium acetate reacted with hydrated iron phosphate at 160 °C and the product formed in as little as 16 hours. The hydrothermally prepared yellow powder was collected by filtration. An X-ray powder diffraction pattern of the material and the subsequent Rietveld refinement are shown in Figure 4.18. The crystallographic data obtained from the refinement is summarized in Table 4.8.

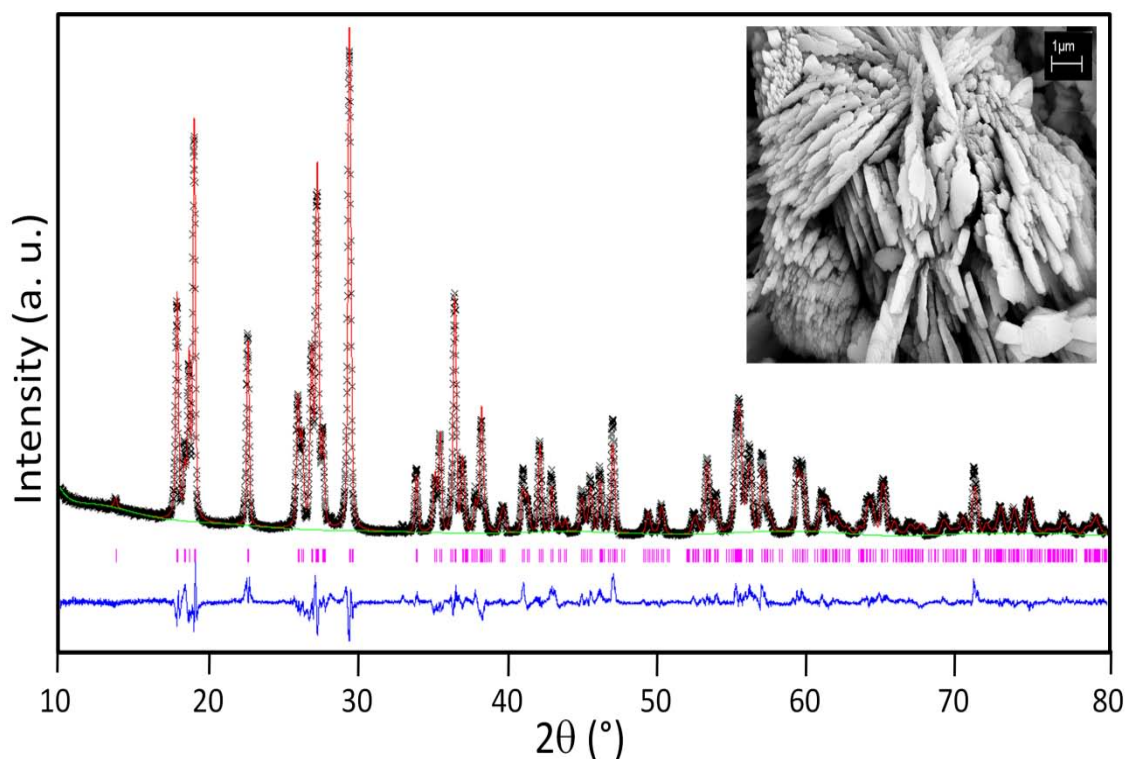


Figure 4.18: Rietveld refinement of X-ray diffraction data from a polycrystalline sample of LiFePO₄OH. The statistical agreement factors for the refinement are: $R_{wp} = 10.93\%$, $R_p = 8.34\%$, $R_F^2 = 9.92\%$, $\chi^2 = 64.10$. The collected data are in black, the fit is shown in red, the calculated reflections of LiFePO₄OH are shown in magenta, and the difference map is shown in blue. A summary of the refined data is given in Table 4.7. Inset: Scanning electron microscope image of the LiFePO₄OH powder.

Table 4.8: Results from the refinement of LiFePO₄OH.

LiFePO ₄ OH						
Space group: P -1 (#2), Triclinic						
a = 5.3523(1) Å		α = 109.287(2)°				
b = 7.2851(2) Å		β = 97.827(2)°				
c = 5.1163(2) Å		γ = 106.336(4)°				
V = 174.825(6) Å ³						
Atom	Wyck.	x/a	y/b	z/c	Occ.	U _{iso}
Fe (1)	1a	0	0	0	1.0	0.009(2)
Fe (2)	1b	0	1/2	0	1.0	0.008(1)
P	2i	0.6316(5)	0.7634(4)	0.3242(5)	1.0	0.009(1)
O (1)	2i	0.6559(8)	0.882(1)	0.102(1)	1.0	0.011(2)
O (2)	2i	0.336(1)	0.669(1)	0.327(1)	1.0	0.010(2)
O (3)	2i	0.951(1)	0.281(1)	0.148(1)	1.0	0.010(2)
O (4)	2i	0.766(1)	0.609(1)	0.271(1)	1.0	0.012(2)
O (5)	2i	0.259(1)	0.047(1)	0.365(1)	1.0	0.013(2)
Li (1)	2i	0.604(8)	0.184(6)	0.256(8)	0.5	0.015
Li (2)	2i	0.627(8)	0.296(6)	0.276(8)	0.5	0.015

LiFePO₄OH¹⁸⁷ was used as the basis for the refinement and the two lithium sites were fixed at half occupancy. The refined lattice parameters were a = 5.3523(1) Å, b = 7.2851(2) Å, c = 5.1163(2) Å, α = 109.287(2)°, β = 97.827(2)°, γ = 106.336(4)° and the unit cell volume was 174.825(6) Å³, in good agreement with the other reports of this compound. No other phases were identified in the pattern, thus the material collected was pure LiFePO₄OH.

A representative scanning electron microscope image of the resultant material is shown in the inset of Figure 4.18. This hydrothermal technique yields micron-sized platelets of pure LiFePO₄(OH), similar to other hydrothermal synthesis methods of similar temperature but longer duration, although reaction time is not a major factor in determination

of particle morphology in the low-temperature hydrothermal preparation of phosphate materials.

LiFePO_4F is essentially isostructural with LiFePO_4OH as the except the hydroxide ions act as bridging ligands. Replacement of F^- with OH^- results in numerous subtle changes to the lattice. By virtue of the fact that the fluoride ion is a single atom anion, its effective radius (133 pm) is slightly smaller than that of the hydroxide ion (137 pm). This narrows the angle between Fe1-B-Fe2 (B = bridging OH or F ligand) from 131.8° in $\text{LiFePO}_4(\text{OH})$ to 131.1° in LiFePO_4F (see Figure 4.10b), which causes the Fe-Fe distance to decrease slightly (from 3.64 Å to 3.63 Å). As a result, OH substitution gives rise to a slight increase in the c lattice parameter but contraction of the other lattice parameters, leading to a small reduction of the overall unit cell volume from 174.8 \AA^3 for $\text{LiFePO}_4(\text{OH})$ to 173.6 \AA^3 for LiFePO_4F .

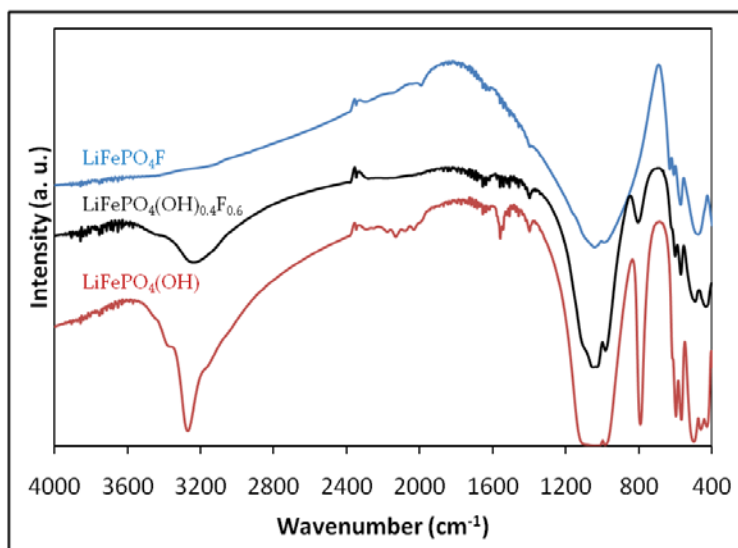


Figure 4.19: Infrared spectroscopy data for LiFePO_4F , $\text{LiFePO}_4(\text{OH})_{0.4}\text{F}_{0.6}$ and LiFePO_4OH .

Infrared spectroscopy was used to verify the presence of hydroxide in the mixed $\text{LiFePO}_4(\text{OH},\text{F})$ compositions. The spectra are shown in Figure 4.19. In the case of $\text{LiFePO}_4(\text{OH})$, the $\nu(\text{O-H})$ stretch is evident as a very strong peak at 3280 cm^{-1} , and a strong

peak at 790 cm^{-1} corresponds to an O-H bending mode.⁶⁸ For LiFePO_4F , there are no peaks in the $3000\text{-}3600\text{ cm}^{-1}$ or $750\text{-}800\text{ cm}^{-1}$ regions of the IR spectrum which indicates that the compound is free of hydroxide and thus fully fluorinated.

Data from the thermal gravimetric analysis of LiFePO_4OH heated under inert atmosphere is shown in Figure 4.11. The sample was stable up to $500\text{ }^\circ\text{C}$ at which point a 5.7% weight loss occurred. X-ray diffraction of the product confirmed the presence of $\text{Li}_3\text{Fe}_2(\text{PO}_4)_3$ at the end of the run, indicating the reaction mechanism for the decomposition of LiFePO_4OH may be similar to that of LiFePO_4F . The lower temperature of decomposition results from the presence of hydroxide in the structure, easily released as water.

Electrochemical results for Li-ion cells based on the other anion end member, $\text{LiFePO}_4(\text{OH})$, are presented in Figure 4.20. As with LiFePO_4F , the $\text{LiFePO}_4(\text{OH})$ cells were prepared by ball-milling the as-prepared material for various lengths of time. The first discharge profiles of cells comprised of as-synthesized $\text{LiFePO}_4(\text{OH})$, as well as material milled for 1-3 hours are shown in Figure 4.20a. Each $\text{LiFePO}_4(\text{OH})$ cell has a flat plateau near 2.3 V, roughly 0.4 V less than that of LiFePO_4F . This difference is the result of the weaker electronegativity of the OH^- ion in $\text{LiFePO}_4(\text{OH})$ which decreases the inductive effect.

Of particular interest is how the electrochemical profiles of $\text{LiFePO}_4(\text{OH})$ differ with milling times: the voltage of the as-prepared sample (2.30 V) is significantly lower than that of the sample milled for 1 hour (2.34 V) or milled for 3 hours (2.35 V). This subtle increase in potential as a result of particle size reduction has also been reported for the olivine LiFePO_4 system.⁹² The discharge capacity is also improved by decreasing the $\text{LiFePO}_4(\text{OH})$ particle size. Full cycling curves and SEM micrographs of the electrode material for the cells

prior to cycling are shown in Figure 4.20b,c. By decreasing the particle size of the as-synthesized material from 1-2 μm to 250-350 nm in dimension after milling for 3 hours, the discharge capacity increased from 0.7 to 0.95 Li, both capacities being greater than those reported recently. Furthermore, subsequent discharge cycles for cells comprised of either as-prepared material or material milled for 3 hours exhibit a plateau at 2.42 V vs. Li.

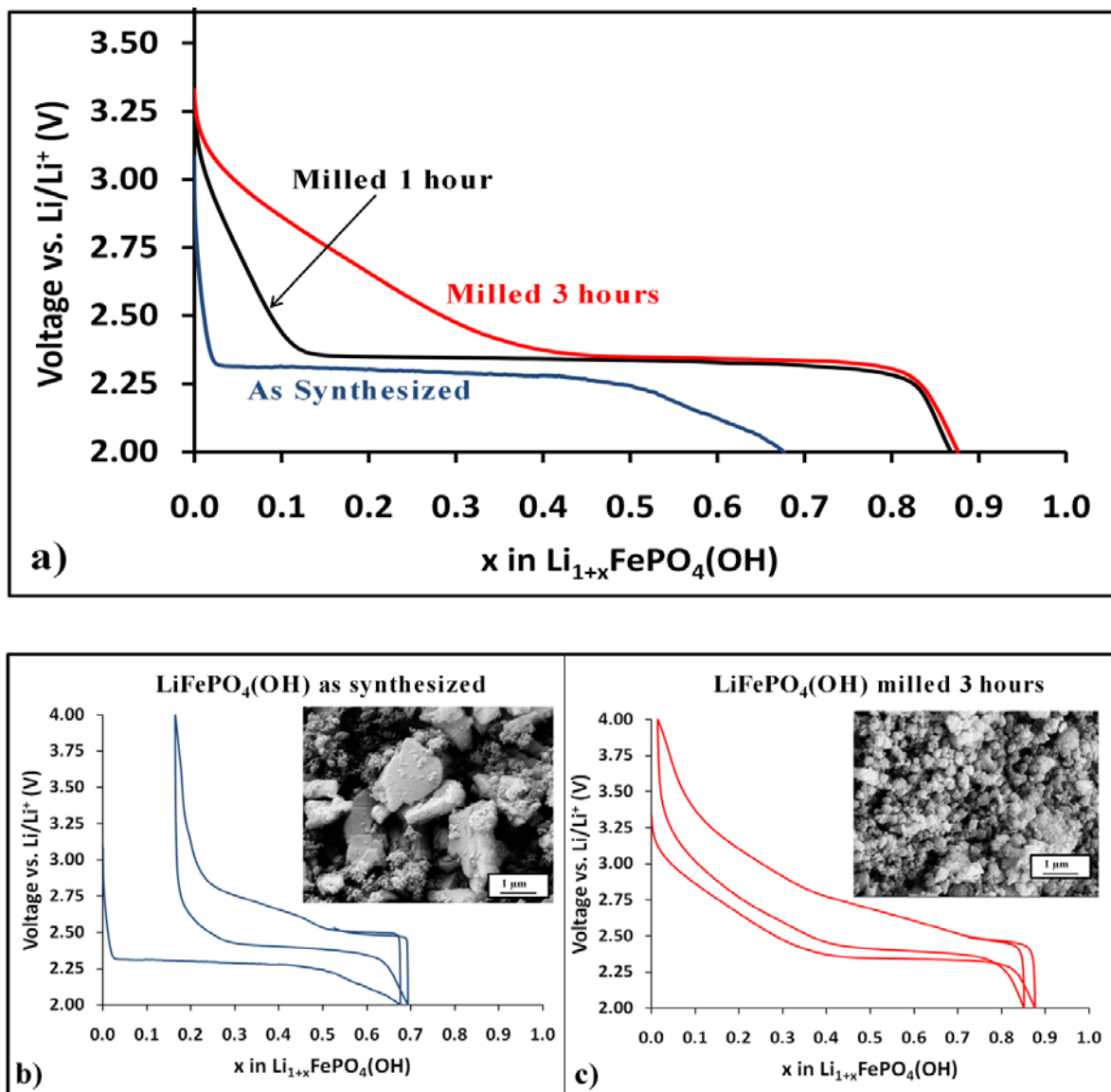


Figure 4.20: Electrochemical data for $\text{LiFePO}_4(\text{OH})$ vs. Li/Li^+ (rate of C/50). a) Initial discharge curves for as-synthesized hydrothermal $\text{LiFePO}_4(\text{OH})$ (blue), $\text{LiFePO}_4(\text{OH})$ ground in a ball mill for 1 hour (black) and $\text{LiFePO}_4(\text{OH})$ ground in a ball mill for 3 hours (red). The first two full cycles and SEM micrographs of cells of the as-prepared and 3 hour milled samples are shown in b) and c) respectively. Reproduced from reference¹⁰¹ with permission from the Royal Society of Chemistry.

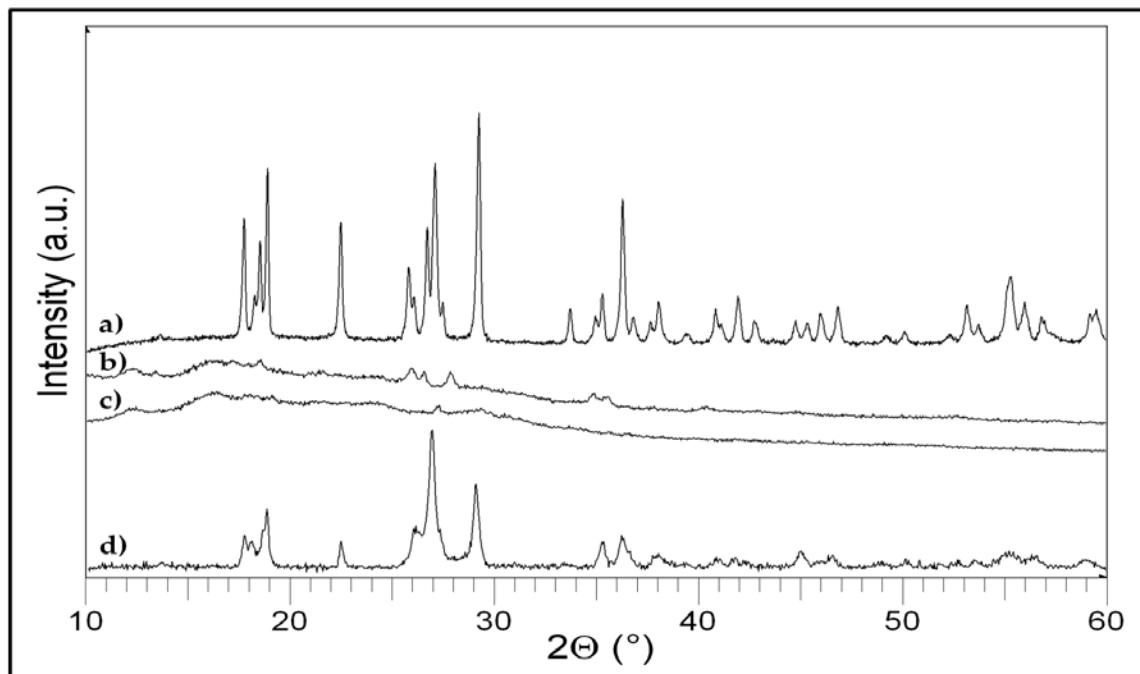


Figure 4.21: X-ray diffraction patterns of a) as-prepared LiFePO_4OH ; b) LiFePO_4OH reduced with n-butyl lithium to make $\text{Li}_2\text{FePO}_4\text{OH}$; c) the chemical oxidation of $\text{Li}_2\text{FePO}_4\text{OH}$ with NO_2BF_4 to make LiFePO_4OH ; d) the material in c) exposed to air for 10 minutes at ambient conditions. Reproduced from reference ¹⁰¹ with permission from the Royal Society of Chemistry.

The origin of this increase in discharge voltage of 0.12 V, seen on the second cycle (see above) was examined by chemical lithiation of $\text{LiFePO}_4(\text{OH})$ with n-butyl lithium to produce $\text{Li}_2\text{FePO}_4(\text{OH})$. The $\text{Li}_2\text{FePO}_4(\text{OH})$ material was black in colour. Powder X-ray diffraction, performed in an air-sensitive holder sealed under argon, revealed no crystalline diffraction peaks, as shown in Figure 4.21.

The amorphous $\text{Li}_2\text{FePO}_4(\text{OH})$ was chemically oxidized with NO_2BF_4 in an attempt to regenerate $\text{LiFePO}_4(\text{OH})$. Again, an X-ray diffraction pattern was collected in a sealed holder under argon, and the pattern is shown in Figure 4.21c. Interestingly, no crystalline diffraction peaks are observed at this stage, although the material partially recrystallizes after exposure to air (figure 4.21d). Based on these results, the electrochemical profile of

LiFePO₄(OH) may be explained: upon initial discharge, crystalline LiFePO₄(OH) undergoes a transformation to an amorphous phase. Once the crystalline to amorphous transition is complete (the end of the first charge cycle), the second (and subsequent) charge and discharge cycles involve the (de)intercalation of lithium from this amorphous phase. Other positive electrode materials have been found to also undergo structural rearrangements to amorphous phases on the first electrochemical cycle, most notably the high-capacity silicate Li₂MnSiO₄.⁶⁰

4.6 Anion Disorder Induced Solid Solution Behaviour in LiFePO₄(OH)_{0.4}F_{0.6}

It has been shown previously that anionic solid solutions LiAlPO₄(OH)_xF_{1-x} which span the entire compositional range between montebrazite (LiAlPO₄OH) and amblygonite (LiAlPO₄F), can be found both in nature and as synthesized materials.^{68,173} This led us to question whether anion compositional disorder could drive lithium compositional solid solution behavior in analogous redox active compounds. A new composition, LiFePO₄(OH)_{0.4}F_{0.6}, was synthesized by introducing a fluoride-containing precursor (LiF) into the hydrothermal reaction used to prepare LiFePO₄OH. The stoichiometry was determined by EDX measurements which revealed a Fe:P:F ratio of approximately 1:1:0.6 which indicates the compound is not fully fluorinated. A Rietveld refinement of the powder XRD pattern is shown in Figure 4.22, and Table 4.9 summarizes the refinement results.

Based on a previous study in which a relationship between the relative occupancies of the sites of the split Li position and the OH/F content of the tavorite compound was established, the Li site was retained as a split site with both Li occupancies fixed at 0.5 for

the purposes of the refinement.¹⁸⁷ The lattice parameters and unit cell volume are intermediate between those of LiFePO_4OH and LiFePO_4F (see Table 4.5). The lack of coherent regions of either end-member in the diffraction pattern confirms the random distribution of OH^- and F^- ions as the bridging ligands between the iron sites and thus an anionic solid solution was formed.

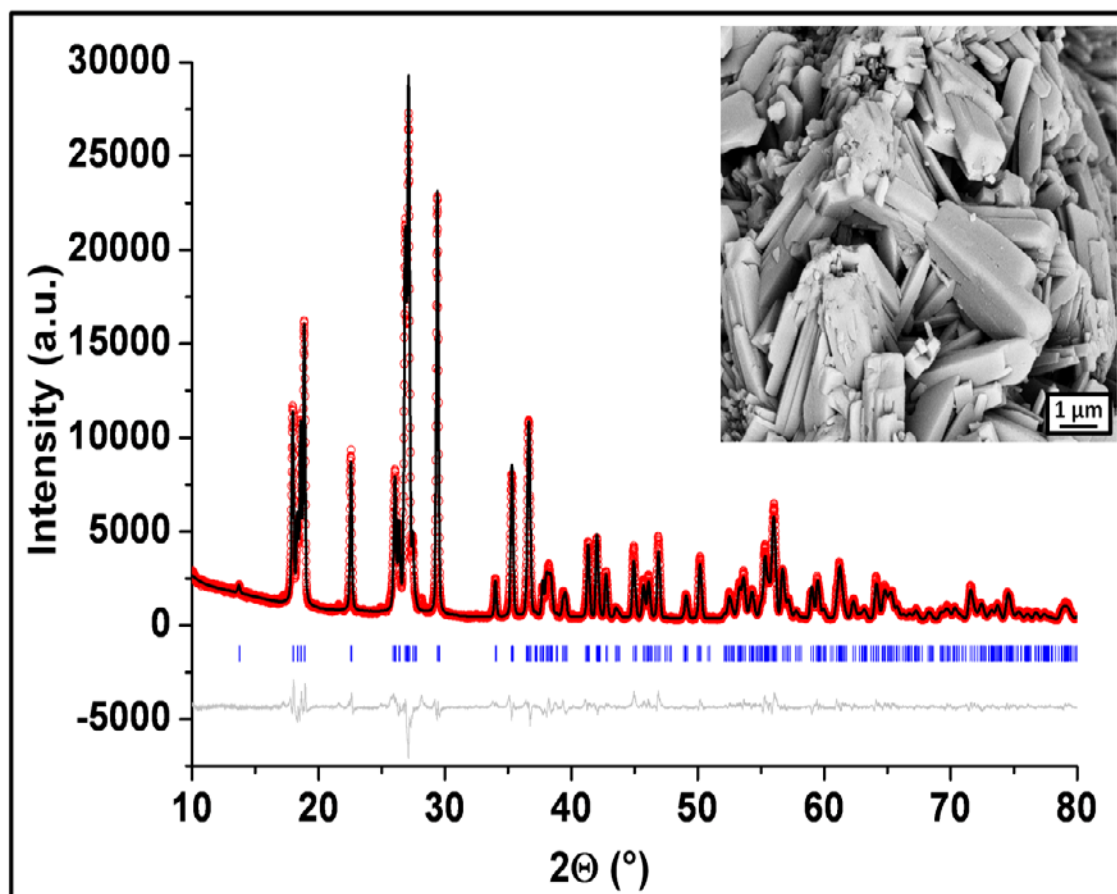


Figure 4.22: Rietveld refinement of XRD data from a sample of hydrothermally prepared $\text{LiFePO}_4\text{F}_{0.6}(\text{OH})_{0.4}$. The statistical agreement factors for the refinement are: $R_{\text{wp}} = 8.51\%$, $R_p = 6.37\%$, $R_F^2 = 7.25\%$. The collected data are in red, the fit is shown in black, the calculated reflections are shown in blue and the difference map is shown in grey. A summary of the refined data is given in Table 4.9. SEM image of the polycrystalline powder shown in inset. Reprinted with permission from reference ¹⁹⁰, copyright 2012, American Chemical Society.

Table 4.9: Lattice constants and atomic parameters of $\text{LiFePO}_4(\text{OH})_{0.4}\text{F}_{0.6}$ refined from powder XRD data.

$\text{LiFePO}_4(\text{OH})_{0.4}\text{F}_{0.6}$						
Space group: P -1 (#2), Triclinic						
$M_w = 175.96 \text{ g/mol}$						
$D = 3.330 \text{ g cm}^{-3}$						
$a = 5.3227(1) \text{ \AA}$						
$b = 7.2881(1) \text{ \AA}$						
$c = 5.1326(1) \text{ \AA}$						
$\alpha = 108.997(1)^\circ$						
$\beta = 97.818(1)^\circ$						
$\gamma = 106.798(1)^\circ$						
$V = 174.308(4) \text{ \AA}^3$						
Atom	Wych.	x/a	y/b	z/c	Occ.	U_{iso}
Li (1)	2i	0.609(8)	0.180(6)	0.254(8)	0.5	0.015
Li (2)	2i	0.631(8)	0.292(6)	0.276(7)	0.5	0.015
Fe (1)	1a	0	0	0	1.0	0.0068(3)
Fe (2)	1b	0	1/2	0	1.0	0.0091(3)
P	2i	0.6377(6)	0.7621(4)	0.3236(5)	1.0	0.014(1)
O (1)	2i	0.661(1)	0.8767(8)	0.116(1)	1.0	0.015(2)
O (2)	2i	0.337(1)	0.6567(7)	0.314(1)	1.0	0.012(2)
O (3)	2i	0.789(1)	0.6074(8)	0.263(1)	1.0	0.013(2)
O (4)	2i	0.245(1)	0.0711(7)	0.365(1)	1.0	0.014(2)
O/F	2i	0.940(1)	0.2700(8)	0.146(1)	1.0	0.011(2)

Infrared spectroscopy was used to verify the presence of hydroxide in the mixed $\text{LiFePO}_4(\text{OH},\text{F})$ composition. The spectrum is shown in Figure 4.19. For $\text{LiFePO}_4(\text{OH})_{0.4}\text{F}_{0.6}$, the intensity of the O-H stretching vibration at 3280 cm^{-1} decreases as a result of partial replacement of hydroxide with fluoride. Also notable is the increased breadth of the O-H stretch as well as a shift to slightly lower wavenumber (to 3230 cm^{-1}).

The intensity of the O-H bend peak at 790 cm^{-1} is also diminished. These phenomena have been observed previously in $\text{LiAlPO}_4(\text{OH})_x\text{F}_y$ compounds and were attributed to local disorder in the structure and variations in bond sum as a result of partial loss of hydrogen moieties available for hydrogen bonding.⁶⁸ The varied O-H environments which result cause a broad and poorly defined peak shape.

Data from the thermal gravimetric analysis of $\text{LiFePO}_4(\text{OH})_{0.4}\text{F}_{0.6}$ heated under inert atmosphere is shown in Figure 4.11. Although the F:OH ratio is greater than 1, the thermal stability of substantial of $\text{LiFePO}_4(\text{OH})_{0.4}\text{F}_{0.6}$ and $\text{LiFePO}_4(\text{OH})$ are similar, owing to a significant quantity of hydroxide present in former. Both were found to decompose around $500\text{ }^\circ\text{C}$. As with the other iron phosphate tavorite, X-ray diffraction of the TGA product confirmed the presence of $\text{Li}_3\text{Fe}_2(\text{PO}_4)_3$ at the end of the run.

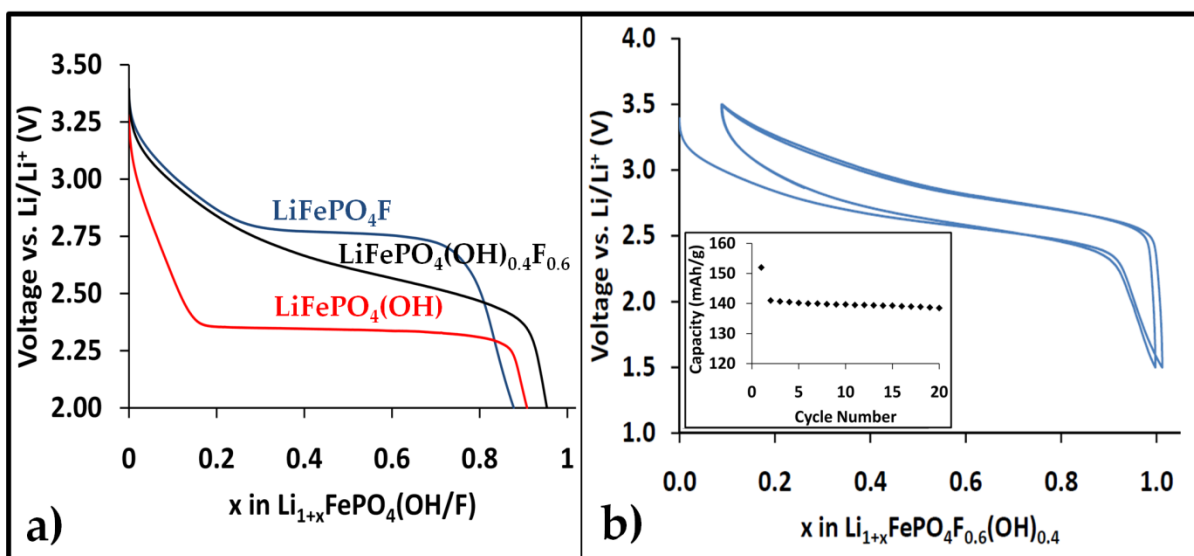


Figure 4.23: a) Voltage profile on first discharge of LiFePO_4F , LiFePO_4OH and $\text{LiFePO}_4\text{F}_{0.6}(\text{OH})_{0.4}$ b) Electrochemical cycling of cells comprised of $\text{LiFePO}_4\text{F}_{0.6}(\text{OH})_{0.4}$ cycled at a rate of C/10. Inset: discharge capacity at a C/10 rate for the first 20 cycles. . Reprinted with permission from reference¹⁹⁰, copyright 2012, American Chemical Society.

Electrochemical data for as-prepared $\text{LiFePO}_4\text{F}_{0.6}(\text{OH})_{0.4}$, cycled vs. Li at a rate of C/10 are presented in Figure 4.23; the profiles of the first discharge cycle for LiFePO_4F , $\text{LiFePO}_4\text{F}_{0.6}(\text{OH})_{0.4}$ and LiFePO_4OH are shown for comparison in 4.23 a and the full cycling profile of $\text{LiFePO}_4\text{F}_{0.6}(\text{OH})_{0.4}$ is shown in Figure 4.23b. Unlike the two end-members of the (OH,F) favorite family that exhibit two-phase plateaus at 2.42 V and 2.75 V respectively, $\text{LiFePO}_4\text{F}_{0.6}(\text{OH})_{0.4}$ exhibits a sloping profile over the entire lithium stoichiometry range on both charge and discharge. This is indicative of solid-solution behavior. On initial discharge, the full capacity (153 mAh/g) is obtained at an average potential of 2.6 V. Successive charge and discharge cycles of the cell result in a sustainable, reversible capacity of 140 mAh/g (see Figure 4.23b inset). The potential and the capacity are stable over long-term cycling, despite the presence of OH^- in the lattice.

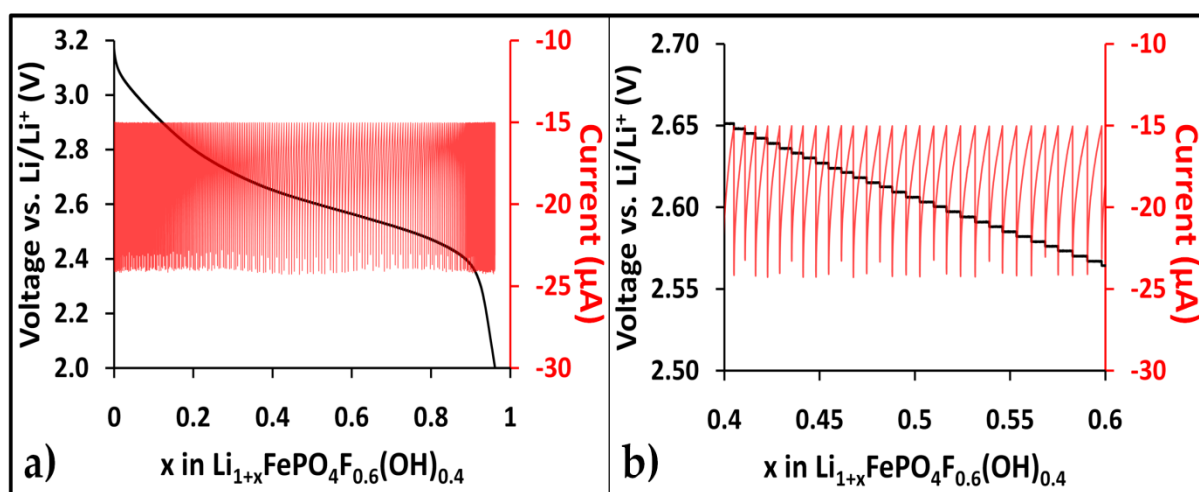


Figure 4.24: a) PITT measurement of the first discharge of $\text{LiFePO}_4\text{F}_{0.6}(\text{OH})_{0.4}$ b) Closeup of the PITT data in the region $\text{Li}_{1+x}\text{FePO}_4\text{F}_{0.6}(\text{OH})_{0.4}$, $0.4 \leq x \leq 0.6$. The electrochemical potential is shown in black and the current response in red. Reprinted with permission from reference ¹⁹⁰, copyright 2012, American Chemical Society.

Potentiostatic intermittment titration (PITT) measurements were also performed on a $\text{LiFePO}_4\text{F}_{0.6}(\text{OH})_{0.4}$ electrochemical cell starting from the fully charged Fe^{3+} state. The voltage was decreased in 6 mV increments and the current at each constant voltage step

measured until it dropped to a C/50 rate, hence the capacity available at finely resolved voltage steps was measured. The resultant electrochemical curve is displayed in Figure 4.24a and a closeup of the central region is shown in Figure 4.24b. As with the constant-current data, the electrochemical potential (shown in black) is in constant decline during discharge. The current response (shown in red) is a rapid exponential decay at each voltage step, confirming the presence of a lithium compositional solid solution. This is in contrast to known two-phase materials such as LiFePO_4 , where PITT measurements reveal characteristic features of a flat voltage curve and a bell-shaped current response.⁹² The observed behavior is the result of two important factors. The first is the substitutional solid solution of the OH^-/F^- site in the lattice such that there is a statistical distribution of each throughout the lattice. In principle, the presence of extended F^- rich or OH^- rich regions in the crystals would lead to a profile comprised of two plateaus, one for each end-member of the substitutional solid solution. The other important factor is the thermodynamics of the tavorite lattice which may favor disorder on the lithium sites: for example, partial solid-solution behavior is apparently exhibited by $\text{Li}_{1+x}\text{FePO}_4\text{F}$ for $0 < x < 0.4$. These two factors operate in concert in $\text{LiFePO}_4\text{F}_{0.6}(\text{OH})_{0.4}$. It is the first polyanion-based positive electrode material to employ anion substitution to yield electrochemically active materials which display solid-solution character.

The solid-solution behavior of $\text{LiFePO}_4\text{F}_{0.6}(\text{OH})_{0.4}$ by chemical reduction was studied by X-ray diffraction: the patterns of $\text{Li}_{1.5}\text{FePO}_4\text{F}_{0.6}(\text{OH})_{0.4}$ and the fully reduced $\text{Li}_2\text{FePO}_4\text{F}_{0.6}(\text{OH})_{0.4}$ compound are compared to the as-prepared sample in Figure 4.25. In the diffraction pattern of $\text{Li}_{1.5}\text{FePO}_4\text{F}_{0.6}(\text{OH})_{0.4}$, the peaks are shifted (compared to the as-prepared sample) by various degrees to higher d-spacings, which indicates this single phase

is an intercalated favorite. This differs from partially reduced LiFePO_4F where the two end-members (LiFePO_4F and $\text{Li}_2\text{FePO}_4\text{F}$) are present. It also differs from LiFePO_4OH where the fully reduced phase ($\text{Li}_2\text{FePO}_4\text{OH}$) was found to be amorphous. Clearly, favorite $\text{Li}_{1.5}\text{FePO}_4\text{F}_{0.6}(\text{OH})_{0.4}$ is single phase owing to the OH^-/F^- anionic disorder. Full reduction to $\text{Li}_2\text{FePO}_4\text{F}_{0.6}(\text{OH})_{0.4}$ shows further shift of the peaks to higher d-spacings. While clearly single-phase, the poor crystallinity of these reduced samples prohibited the indexing of these XRD patterns.

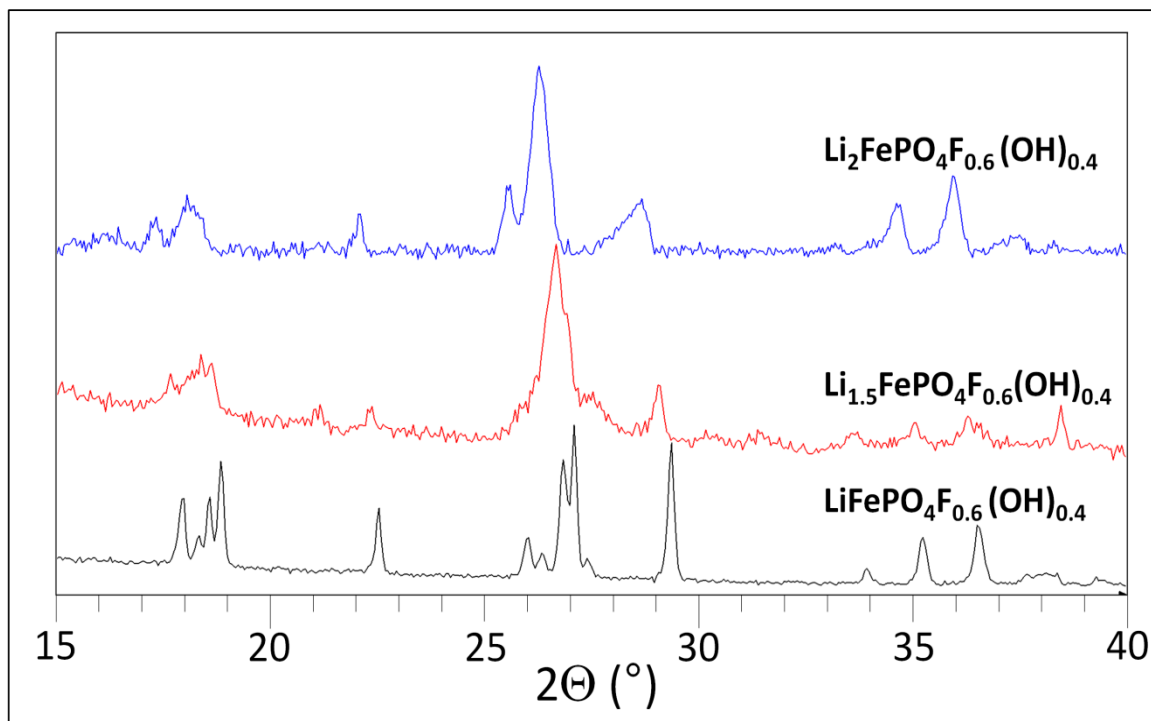


Figure 4.25: X-ray diffraction patterns of $\text{LiFePO}_4(\text{OH})_{0.6}\text{F}_{0.4}$ chemically reduced with LiAlH_4 to produce $\text{Li}_{1.5}\text{FePO}_4(\text{OH})_{0.6}\text{F}_{0.4}$, and $\text{Li}_2\text{FePO}_4(\text{OH})_{0.6}\text{F}_{0.4}$.

The mixed hydroxy-fluorophosphate, $\text{LiFePO}_4\text{F}_{0.6}(\text{OH})_{0.4}$ demonstrated solid-solution behavior in an electrochemical cell over the entire lithium compositional range $\text{Li}_{1+x}\text{FePO}_4\text{F}_{0.6}(\text{OH})_{0.4}$, at an average potential of 2.6 V vs. Li. This phenomenon is driven by a combination of the anion disorder between OH^- and F^- in the lattice and the

thermodynamics of the tavorite framework. These findings should lead to new ways of inducing solid solution behavior in a variety of electrochemically active polyanion compositions, and a better understanding of the forces that drive phase transformations in the materials.

4.7 Synthesis and Electrochemistry of Manganese Phosphate Tavorites

Among many reports of materials with interesting magnetic properties, manganese compounds related to the tavorite structure, AMnXO_4OH ($\text{A} = \text{H}, \text{Li}$; $\text{X} = \text{P}, \text{As}$) were prepared.^{97,182,191} The Mn^{3+} hydrates were prepared by simple solution reactions and the lithium analogues were prepared by a solid state ion exchange around 200 °C with molten lithium nitrate. $\text{MnPO}_4 \cdot \text{H}_2\text{O}$ bears a close resemblance to the tavorite structure while LiMnPO_4OH is isostructural with tavorite. Given that the replacement of iron by manganese results in an increase the electrochemical potential, as is the case with the olivines,¹⁵¹ we these two compounds were synthesized and electrochemical properties were measured. The structure of LiMnPO_4OH was solved in the P-1 space group. We also endeavoured to synthesize the fluorophosphate member of this family, LiMnPO_4F .

Figure 4.26a shows the X-ray diffraction patterns for a sample of as-prepared $\text{MnPO}_4 \cdot \text{H}_2\text{O}$. As can be seen, the experimental pattern matches very closely with the pattern for $\text{MnPO}_4 \cdot \text{H}_2\text{O}$ from the JCPDS database (JCPDS 44-0071). As this compound contains Mn^{3+} octahedrally co-ordinated with oxygen ligands, it exhibits a notable Jahn-Teller distortion: four of the Mn-O bonds at each co-ordination site are short (1.88-1.91 Å) and two are longer (2.28 Å) associated with the d_z^2 orbital of the Mn. In $\text{MnPO}_4 \cdot \text{H}_2\text{O}$, the long Mn-O bonds are those to the water molecules that bridge the octahedra along the 1-D chains of corner-shared octahedra.

A scanning electron micrograph is shown in the inset of Figure 4.26a which shows $\text{MnPO}_4 \cdot \text{H}_2\text{O}$ crystallizes in small platelets roughly 100 x 200 nm. These particles aggregate in solution to form large agglomerates up to 1 μm in dimension. The high-temperature stability of $\text{MnPO}_4 \cdot \text{H}_2\text{O}$ in air was analyzed by TGA and the resultant plot is shown in Figure 4.26b. $\text{MnPO}_4 \cdot \text{H}_2\text{O}$ is stable up to about 400 $^\circ\text{C}$ where it undergoes decomposition to $\text{Mn}_2\text{P}_2\text{O}_7$ by the following reaction:

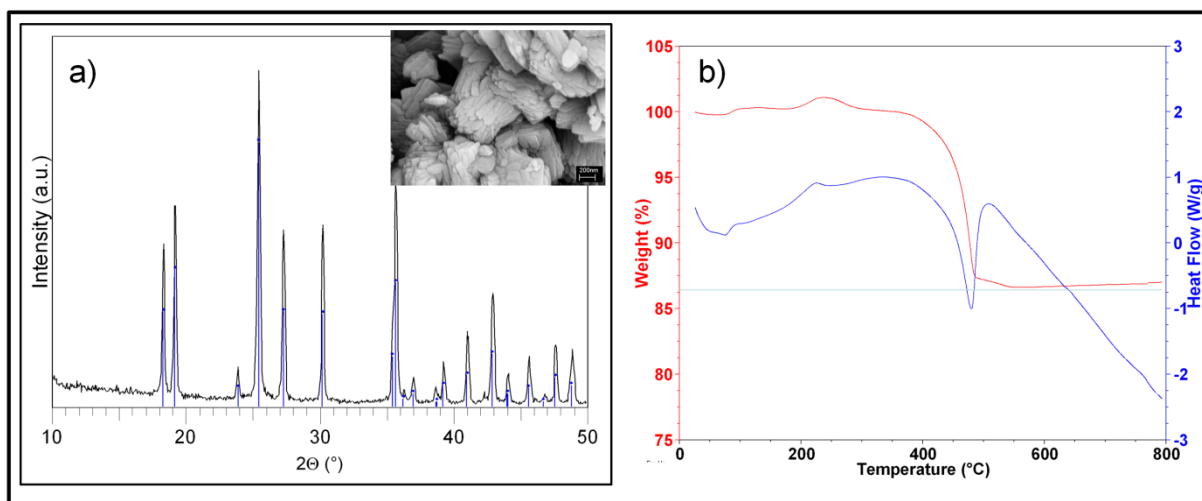


Figure 4.26: a) X-ray diffraction pattern and SEM micrograph (inset) of $\text{MnPO}_4 \cdot \text{H}_2\text{O}$ precipitated from solution. Lines of $\text{MnPO}_4 \cdot \text{H}_2\text{O}$ (JCPDS 44-0071) are shown in blue. b) TGA data for $\text{MnPO}_4 \cdot \text{H}_2\text{O}$ heated under nitrogen.

The theoretical mass loss for the above reaction is 15.5% which is in good accord with the 14.0% mass loss observed in the TGA plot. That $\text{MnPO}_4 \cdot \text{H}_2\text{O}$ releases oxygen and reduces to a Mn^{2+} phosphate in the presence of oxygen underscores the instability of Mn^{3+} phosphate compounds.

The electrochemical performance of $\text{MnPO}_4 \cdot \text{H}_2\text{O}$ in a cell charged and discharged at a rate of C/50 vs. Li/Li^+ is shown in Figure 4.27. On the first discharge, there is a plateau at 3 V however only 0.1 mol Li are intercalated into the $\text{MnPO}_4 \cdot \text{H}_2\text{O}$ structure. Although

roughly the same quantity of lithium was extracted on the first charge cycle, the tiny capacity renders this compound impractical for use in a lithium-ion cell. $\text{MnPO}_4 \cdot \text{H}_2\text{O}$ was also found not to react with the reducing agent LiI, further evidence of the inability of this compound to intercalate lithium ions.

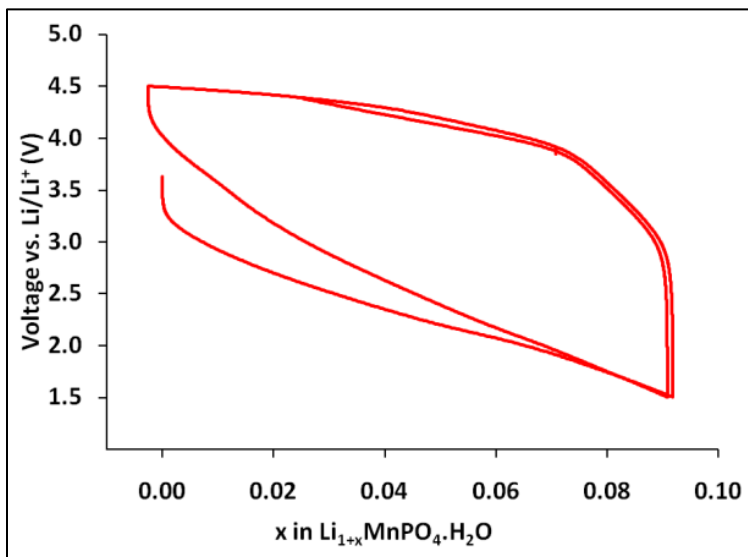


Figure 4.27: Electrochemical data for $\text{MnPO}_4 \cdot \text{H}_2\text{O}$ cycled at a rate of C/50.

LiMnPO_4OH was first synthesized by Aranda and coworkers in 1992 using $\text{MnPO}_4 \cdot \text{H}_2\text{O}$ as a precursor.¹⁸² The $\text{MnPO}_4 \cdot \text{H}_2\text{O}$ was ground with lithium nitrate and heated in an oven at 200 °C for 2 weeks, over which time an ion-exchange reaction (Li^+ for H^+) took place. The crystal structure of the final product, LiMnPO_4OH , was determined to be isostructural with LiAlPO_4OH and LiFePO_4OH but the structure was solved in C-1, a non-standard setting of P-1. We synthesized LiMnPO_4OH using the same method as Aranda and the resultant X-ray diffraction pattern is shown in Figure 4.28. The pattern was then refined in GSAS, where the background, profile coefficients, lattice parameters, atomic positions and atomic displacement parameters were refined. Instead refining the structure in C-1 as previously reported, the structure was refined using LiFePO_4OH (P-1) as the starting point

for the refinement. A graphical representation of the final refinement is also shown in Figure 4.28 and a list of refined structural parameters and statistics is shown in Table 4.10. The compound can be satisfactorily refined by this method and the resultant compound is, as expected, isostructural with LiFePO_4OH . One key distinction in the manganese compound is the presence of a notable Jahn-Teller in the one-dimensional chains of corner-shared MnO_6 octahedra. Four of the Mn-O bonds at each co-ordination site are shorter (1.94-1.99 Å) and two are longer (2.14 Å), the latter associated with unequal energetics of the e_g orbitals which results in an elongation of the d_{z^2} orbital. In LiMnPO_4OH , the orientation of the Jahn-Teller distortion differs from that found in $\text{MnPO}_4\cdot\text{H}_2\text{O}$ such that the long bonds are to oxygens associated with the phosphate groups rather than the Mn- O(H)-Mn bridging direction. This subtle structural feature has a large effect on the electrochemistry of these two compounds.

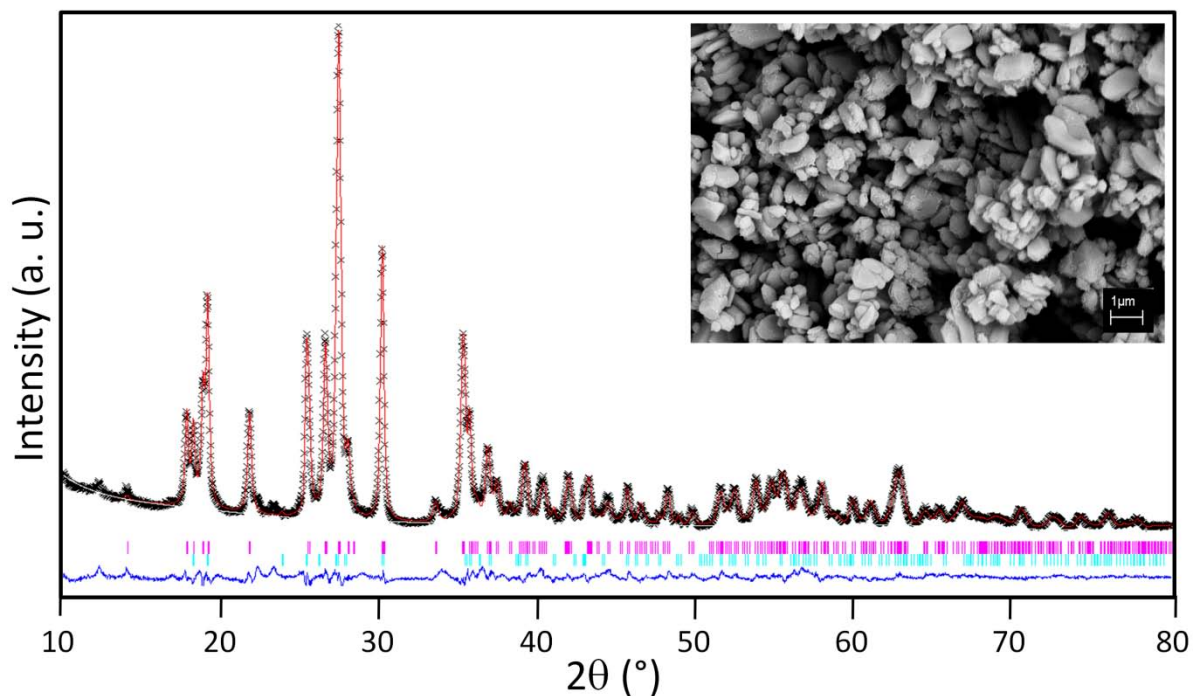


Figure 4.28: Rietveld refinement of XRD data from a sample of LiMnPO_4OH . The statistical agreement factors for the refinement are: $R_{wp} = 6.35\%$, $R_p = 4.62\%$, $R_{F2} = 4.85\%$, $\chi^2 = 11.87$. The collected data are in black, the fit is shown in red, the calculated reflections of LiMnPO_4OH are shown in magenta, those of

$\text{MnPO}_4 \cdot \text{H}_2\text{O}$ in cyan and the difference map is shown in blue. A summary of the refined data is given in Table 4.10. An SEM image of the polycrystalline powder shown in inset.

Table 4.10: Lattice constants and atomic parameters of LiMnPO_4OH refined from powder XRD data.

LiMnPO_4OH						
Space group: P -1 (#2), Triclinic						
a = 5.4505(3) Å		$\alpha = 108.177(4)^\circ$				
b = 7.1142(3) Å		$\beta = 101.252(4)^\circ$				
c = 5.1287(3) Å		$\gamma = 106.274(5)^\circ$				
V = 172.45(1) Å ³						
Atom	Wych.	x/a	y/b	z/c	Occ.	U _{iso}
Li (1)	2i	0.601(6)	0.172(5)	0.230(5)	0.5	0.015
Li (2)	2i	0.622(5)	0.273(5)	0.253(5)	0.5	0.015
Mn (1)	1a	0	0	0	1.0	0.011(1)
Mn (2)	1b	0	½	0	1.0	0.008(1)
P (1)	2i	0.627(1)	0.7583(8)	0.326(1)	1.0	0.012(1)
O (1)	2i	0.635(1)	0.868(1)	0.108(1)	1.0	0.022(2)
O (2)	2i	0.349(1)	0.659(1)	0.300(1)	1.0	0.022(2)
O (3)	2i	0.959(1)	0.870(1)	0.111(1)	1.0	0.018(2)
O (4)	2i	0.772(1)	0.611(1)	0.300(1)	1.0	0.018(2)
O (5)	2i	0.240(1)	0.0660(7)	0.362(1)	1.0	0.020(2)

Electrochemical data for LiMnPO_4OH cycled vs. Li at a rate of C/50 is shown in Figure 4.29. On the initial discharge cycle, 0.25 Li are inserted into the structure of LiMnPO_4OH . There is an initial voltage plateau at 3.1 V which is higher than the initial plateau of LiFePO_4OH by 0.9 V, followed by a gradual decrease in the voltage, possibly indicative of solid-solution behaviour. Upon charging, there is an initial plateau voltage of 3.4 V vs. Li, followed by a gradual increase of the voltage to 4.2 V. Particularly interesting is the capacity on charge: 0.40 Li, 0.15 Li higher than the capacity of the initial discharge which suggests that not only were the initial 0.25 Li de-intercalated but some of the Li in the

as-prepared LiMnPO_4OH were also de-intercalated. This further implies the oxidation of $\text{Mn}^{3+} \rightarrow \text{Mn}^{4+}$ was achieved, which is the first report of a Mn^{4+} phosphate in a lithium-ion cell. Furthermore, this oxidation from Mn^{2+} to Mn^{3+} to Mn^{4+} is reversible: on the subsequent discharge cycle, 0.15 Li were extracted at a potential between 4.2 and 3.2 V, along with an additional 0.20 Li at a potential ranging from 3.2 down to 2.0 V. As electron transport in these materials propagates down the length of the 1-D chains of MnO_6 octahedra, the longer Mn-O-Mn distances of 4.56 Å in $\text{MnPO}_4 \cdot \text{H}_2\text{O}$ hinder electron transport compared to the shorter Mn-O-Mn distances in LiMnPO_4OH of 3.98 Å.

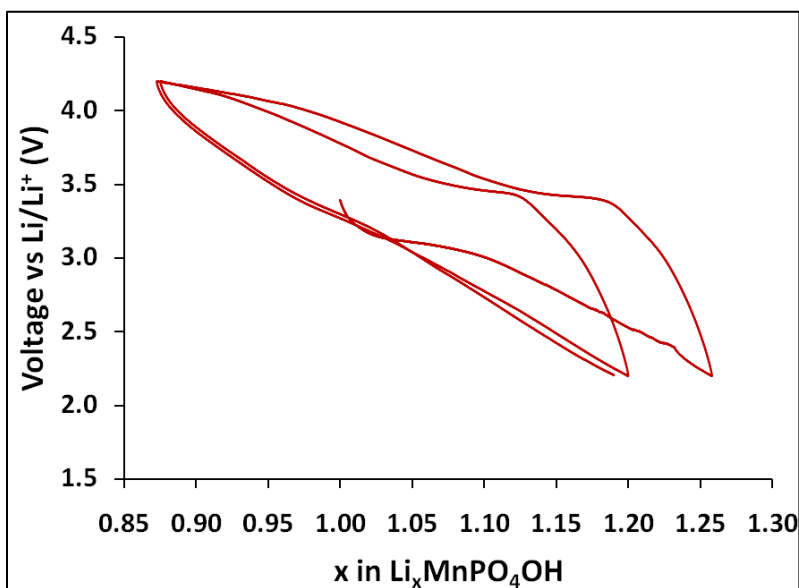


Figure 4.29: Electrochemical results for cycling of LiMnPO_4OH versus Li at a rate of C/50.

The intriguing results for LiMnPO_4OH led us to research the synthesis of LiMnPO_4F which was claimed to have been made by a high-temperature solid-state route with Mn_2O_3 used as the Mn^{3+} precursor. In our trials, the reproduction of this procedure instead produced $\text{Mn}_2\text{P}_2\text{O}_7$ at 800 °C. This result is not surprising, given the temperatures at which the iron tavorites were found to decompose (400-600 °C). As such, we attempted to synthesize LiMnPO_4F using a similar method used to produce $\text{LiMnPO}_4(\text{OH})$: low-temperature heating

of $\text{MnPO}_4 \cdot \text{H}_2\text{O}$, which was ground with LiF. After heating the mixture for two weeks at 200 °C, the same conditions used to produce $\text{LiMnPO}_4(\text{OH})$, no reaction had occurred. The same precursors were heated in a hydrothermal reactor at 190 °C for 2 days and the main product formed was olivine LiMnPO_4 . Unreacted LiF and $\text{MnPO}_4 \cdot \text{H}_2\text{O}$ were also found in the diffraction pattern.

In a separate experiment, the same precursor mixture was heated in ambient conditions to 275 °C for two weeks. There were three products found: unreacted $\text{MnPO}_4 \cdot \text{H}_2\text{O}$, Li_3PO_4 and a phase whose lines matched those of $\text{LiMnPO}_4(\text{OH})$. Analysis of the sample inside a scanning electron microscope equipped with an EDX probe revealed that the total sample was comprised of a Mn:P:F ratio of approximately 1:1:0.05. This insignificant quantity of F indicated the favorite phase formed was in fact $\text{LiMnPO}_4(\text{OH})$ and that fluorine volatilized during the reaction, possibly as HF gas according to the reaction:



We concluded that the hydroxide favorite was formed due to the water present in the lattice of the manganese phosphate precursor. As such, we prepared anhydrous MnPO_4 from the chemical oxidation of LiMnPO_4 . As previously noted, the poor thermal stability of olivine MnPO_4 resulted in a reduction to Mn^{2+} phosphates. In part, this proved to be the case as the compounds which were produced at 200 °C included $\text{Mn}_2\text{P}_2\text{O}_7$ but also the hydration product $\text{MnPO}_4 \cdot \text{H}_2\text{O}$ and unreacted LiF. In an attempt to enhance the fluorine content of the products, MnF_3 was used as a precursor, in a reaction with LiH_2PO_4 in an oven at 200 °C over 7 days. This reaction produced MnF_2 as the only crystalline product.

The prospect of manganese favorites as high potential and high capacity electrodes is very intriguing. These two factors drive the study of $\text{Li}_2\text{MnSiO}_4$, another manganese

compound in which the possibility of two lithium ions may be reversibly extracted exists. The preparation of LiMnPO_4OH is slow, although simple and accomplished at low temperature. Under carefully controlled conditions, the synthesis of the high voltage material LiMnPO_4F may be accomplished, however those conditions have not yet been ascertained.

4.8 Conclusions

Compounds which crystallize in the tavorite structure hold great promise as positive electrode materials for lithium-ion batteries. Environmentally friendly solid state as well as hydro- and solvothermal methods readily produced in vanadium, iron or manganese tavorite-type phosphate phases. Most of these compounds are electrochemically active and reversibly intercalate and deintercalate lithium with a two-phase mechanism as a result of large differences (7-14%) between the unit cell dimensions of the lithiated and delithiated phases. LiFePO_4OH undergoes a crystalline to amorphous transformation on lithium intercalation but the amorphous phase generated after the first charge cycle exhibited reversibility albeit at a different potential.

The most interesting member of this group we synthesized may be the mixed hydroxy-fluorophosphate, $\text{LiFePO}_4\text{F}_{0.6}(\text{OH})_{0.4}$, which demonstrated solid-solution behavior in an electrochemical cell over the entire lithium compositional range $\text{Li}_{1+x}\text{FePO}_4\text{F}_{0.6}(\text{OH})_{0.4}$, at an average potential of 2.6 V vs. Li. This was driven by a combination of the anion disorder between OH^- and F^- in the lattice and the thermodynamics of the tavorite framework. These findings should lead to new ways of inducing solid solution behavior in a variety of electrochemically active polyanion compositions, and a better understanding of the forces that drive phase transformations in the materials.

5 Fluorophosphates of the Composition A_2MPO_4F ($A = Li, Na$; $M = Mg, Mn, Fe, Co, Ni$)

5.1 Background

Continuing from the research on favorite fluorophosphates of the stoichiometry $LiMPO_4F$, we endeavoured to prepare other fluorophosphate compounds of a similar stoichiometry, Li_2MPO_4F ($M = Mn, Fe$). Like the lithium metal silicates (Li_2MSiO_4),^{60,62,66,192–194} these compounds contain two lithium ions per transition metal which offers the possibility of high capacity for lithium extraction provided the transition metal could accommodate the $M^{2+} \rightarrow M^{4+}$ transition when all of the lithium is extracted from the lattice. The first report of a compound from this group was a report on the synthesis and structure of Li_2NiPO_4F which was found to crystallize in the space group $Pnma$ (#62).¹⁰⁴ A schematic depiction of the structure is shown in Figure 5-1. The framework of the structure can be described as linear chains of edge-shared NiO_4F_2 octahedra which propagate down the b -axis. These chains are linked by corner-sharing phosphate tetrahedra. Lithium ions reside in three different interstitial sites, two of which are square-pyramidal while the other is octahedral. A second study on the structure and electrochemical properties of Li_2CoPO_4F was published in 2005 by Okada *et al.*¹⁹⁵ This study showed that Li_2CoPO_4F was isostructural with Li_2NiPO_4F and that the potential for Li^+ extraction from Li_2CoPO_4F had an average value of 4.8 V, slightly higher than that of $LiCoPO_4$ of 4.7 V and out of the stability window for most organic carbonate based electrolytes.

Additional reports of Li_2MPO_4F compounds, most notably Li_2FePO_4F , may be found in patent literature although no structural or electrochemical data was shown. We

endeavored to synthesize both $\text{Li}_2\text{FePO}_4\text{F}$ and $\text{Li}_2\text{MnPO}_4\text{F}$. These two compounds might be expected to exhibit similar potentials to those in the corresponding transition metal olivines, based on the finding that the potential of $\text{Li}_2\text{CoPO}_4\text{F}$ is similar to that of LiCoPO_4 .¹⁹⁵

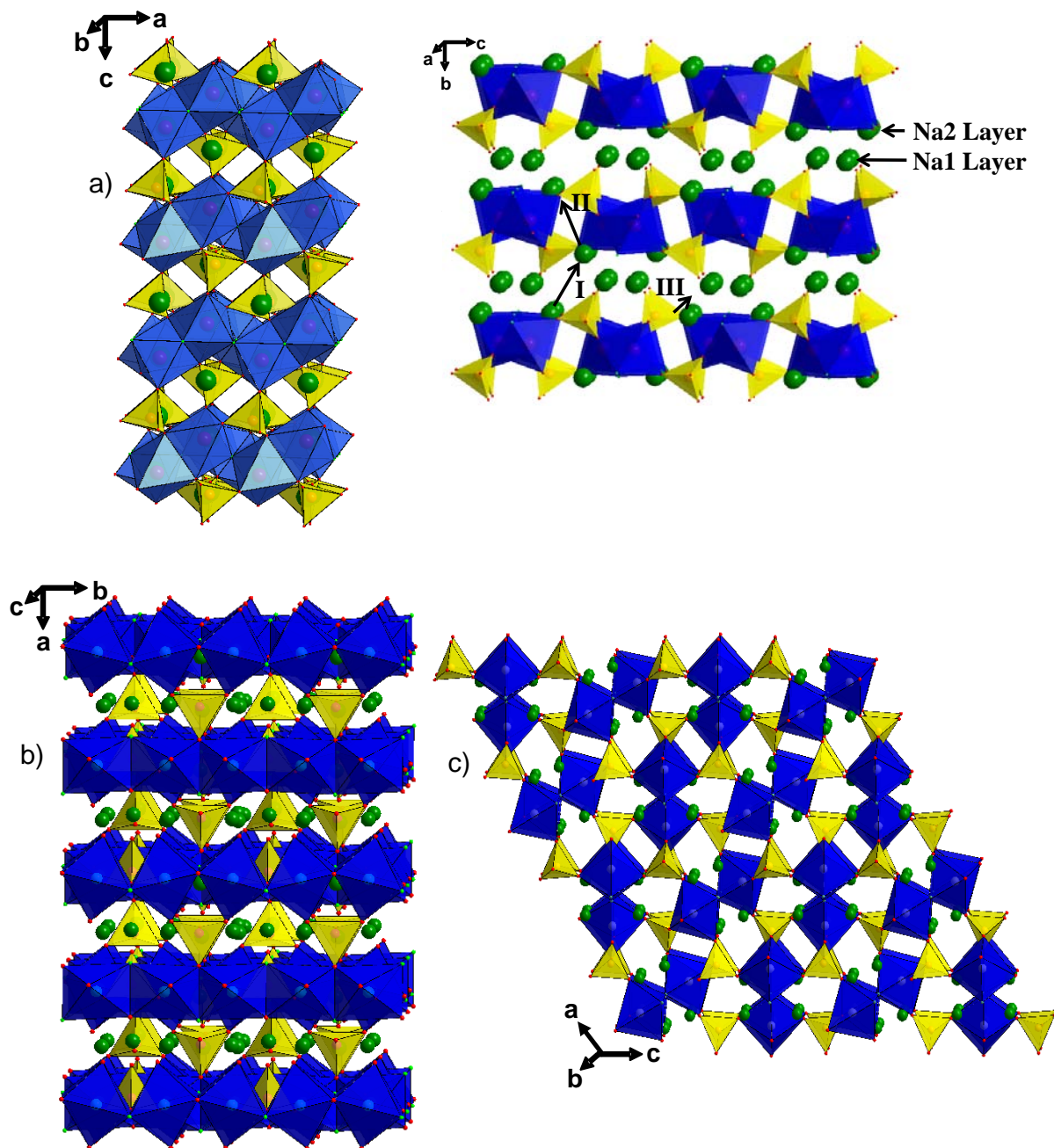


Figure 5.1: The crystal structure of $\text{Na}_2\text{FePO}_4\text{F}$ a) view down b-axis and down a-axis. Ion transport Pathways (I, II and III) are marked. b) The crystal structure of $\text{Li}_2\text{CoPO}_4\text{F}$ and c) the structure of $\text{Na}_2\text{MnPO}_4\text{F}$. The transition metal octahedra are shown in blue, phosphate tetrahedra in yellow and alkali ions in green.

5.2 Synthesis of Li₂MPO₄F Materials

Solid-state Li₂MPO₄F: Following the method of Avignant *et al.*,¹⁰⁴ equimolar amounts of transition metal olivine (LiMnPO₄, LiFePO₄, LiCoPO₄ or LiNiPO₄) synthesized by solid-state routes and lithium fluoride were ground in a mortar and pestle and the powder was pressed into a circular pellet which was heated to 740-900 °C under flowing argon for 1-8 hours.

Solid-state Li₂FePO₄F (alternative route): A mixture of FeC₂O₄•2H₂O, H₂PO₃F, LiNO₃ and Ketjen Black carbon in a 1:1:2:0.2 ratio was ground in a mortar and pestle and pressed into a pellet which was heated to 600 °C for 8 hours under flowing argon.

Solvothermal Li₂FePO₄F: FeF₂, LiH₂PO₄ and Li(CH₃COO)•2H₂O were sealed in a 45 ml Teflon-lined Parr reactor with 30 ml tetraethylene glycol and heated to 220 °C for 48 hours. The solid that formed under the autogeneous pressure of the reactor was filtered, washed three times with acetone and dried at 50 °C unvacuum overnight.

5.3 Li₂MPO₄F Results

We prepared the two previously reported fluorophosphates, Li₂NiPO₄F and Li₂CoPO₄F by a solid-state route and the resultant diffraction patterns are shown in Figure 5.2. These patterns match those in the previous reports, indicating that the syntheses were successful. The peaks of Li₂CoPO₄F are slightly shifted to the left of those in Li₂NiPO₄F owing to the slightly larger ionic radius of Co²⁺ (0.745 Å) compared to Ni²⁺ (0.69 Å).¹⁸⁸

Owing to the popularity of iron and manganese phosphates as electrode materials in Li-ion batteries, we endeavored to synthesize the iron and manganese fluorophosphates with this structure using the same solid-state method. Figure 5.3 shows the diffraction pattern of

the resultant powder from the reaction between LiMnPO_4 and LiF at 800°C . The diffraction pattern showed that LiMnPO_4 and LiF remain and thus, no reaction occurred.

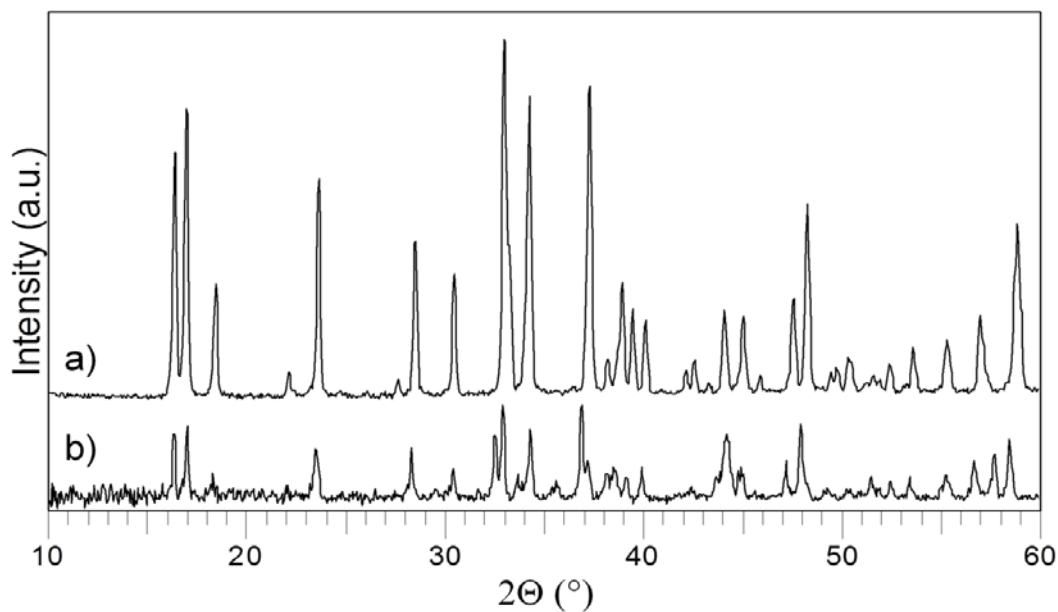


Figure 5.2: Powder X-ray diffraction patterns of a) $\text{Li}_2\text{NiPO}_4\text{F}$ and b) $\text{Li}_2\text{CoPO}_4\text{F}$ prepared by heating the respective transition metal olivine and LiF .

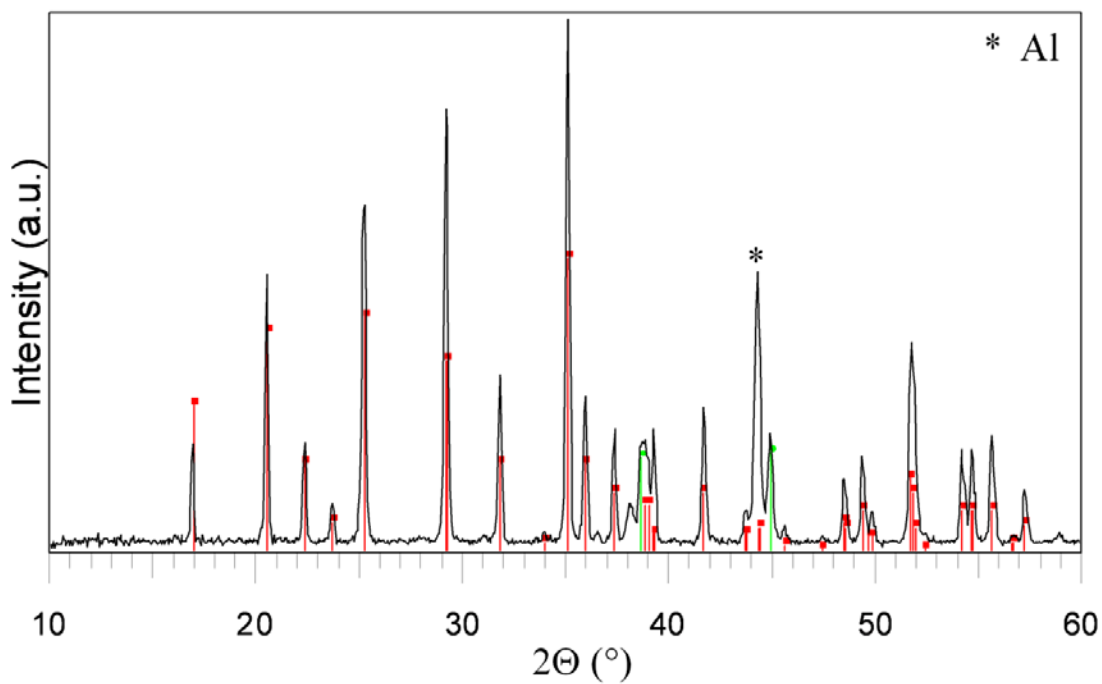


Figure 5.3: X-ray diffraction pattern after treatment of LiMnPO_4 and LiF at 800°C . Peaks of LiMnPO_4 are marked in red, those of LiF in green. Peaks from the Al sample holder marked by (*).

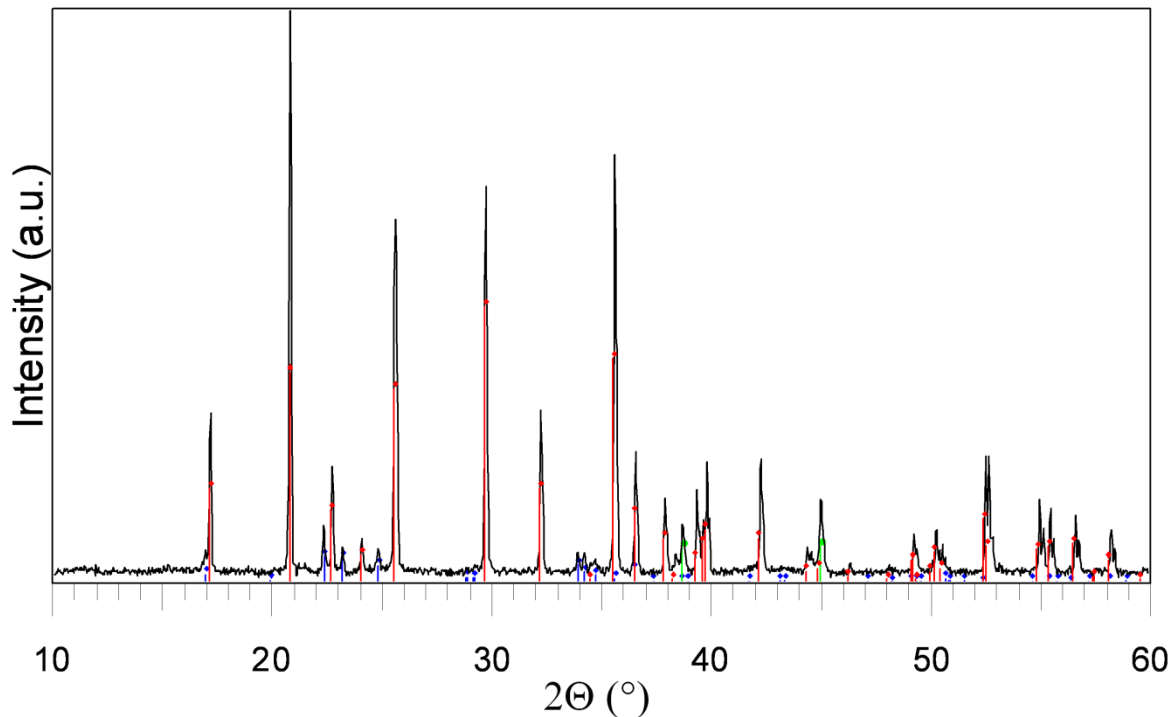


Figure 5.4: X-ray diffraction pattern after treatment of LiFePO₄ and LiF at 750 °C. Peaks of LiFePO₄ are marked in red, LiF in green and Li₃PO₄ in blue.

In the same fashion, carbon-coated LiFePO₄ and LiF were ground and heated to 750°C and the diffraction pattern of the final product is shown in Figure 5.4. Analysis of the product showed the only Fe-containing phase in the final products was the starting material LiFePO₄. Lithium phosphate and unreacted LiF were also found. In order to promote reactivity of the starting reagents, LiFePO₄ and LiF were ground and heated to 900°C for two hours. After this reaction was complete, the products from this synthesis were again found to be LiFePO₄, Li₃PO₄ and LiF. As the iron-containing olivine was found to be an unreactive reagent, an alternative solid-state method was tried based on the following reaction:



This reaction is similar to another reaction reported to make Li₂FePO₄F.¹⁹⁶ Again, this reaction produced LiFePO₄ as the main product and failed to produce any trace of Li₂FePO₄F.

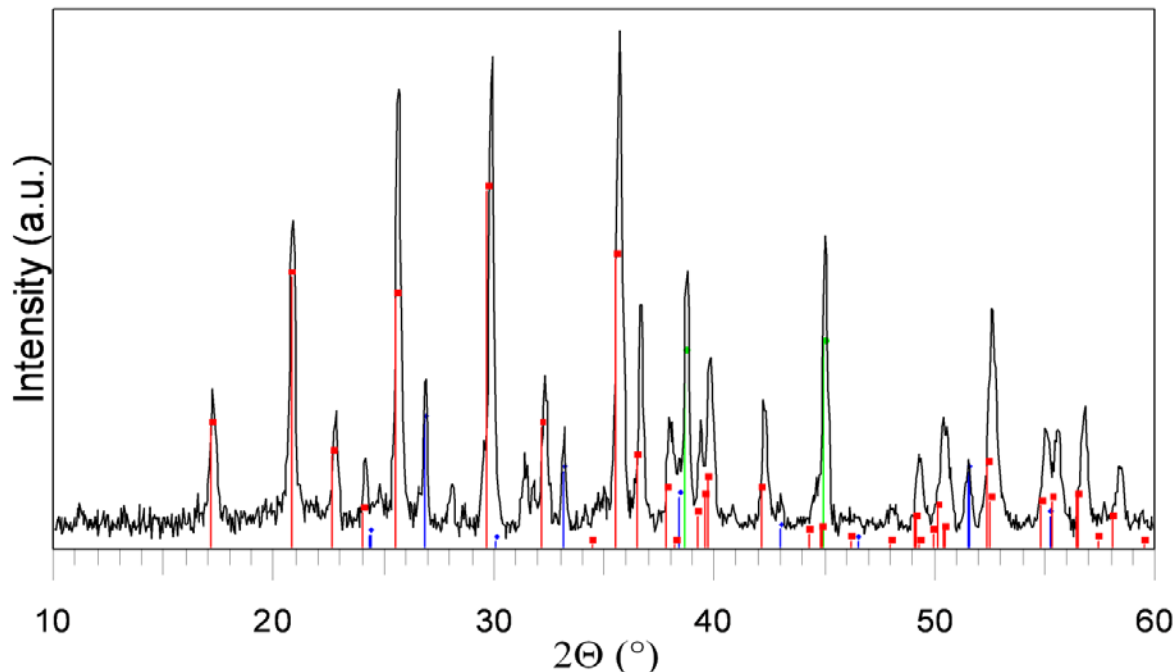


Figure 5.5: X-ray diffraction pattern of the solvothermal reaction of FeF_2 , LiH_2PO_4 and LiOAc . Red lines are LiFePO_4 , green are LiF and blue are unreacted FeF_2 .

Based on the success of the synthesis of Fe^{2+} compounds in glycol media, a solvothermal synthesis route was employed using tetraethylene glycol as the solvent. Glycols are known to act as reducing agents and their use in solvothermal syntheses at temperatures much lower than those typically used for solid-state syntheses provide an ideal environment for the production of products with low thermodynamic stability.¹⁹⁷ Typically, these reactions are done without the addition of strong acids or bases which would decompose the glycol at high temperatures. FeF_2 was chosen as a precursor in order to promote Fe-F bonds in the final product as the transition metal environment in $\text{Li}_2\text{MPO}_4\text{F}$ has two M-F bonds. FeF_2 was mixed with LiH_2PO_4 and $\text{Li}(\text{CH}_3\text{COO})\cdot 2\text{H}_2\text{O}$ and sealed in a Parr reactor at 200°C for 48 hours. The X-ray diffraction pattern of the final product is shown in Figure 5.5. The main phase produced was LiFePO_4 , along with some LiF . The temperature

of the reaction was low enough that not all of the FeF_2 reacted, as evidenced that some FeF_2 was also present in the diffraction pattern at the end of the reaction period.

Clearly, the transition metal olivines can be divided into two classes: those which react with LiF to produce $\text{Li}_2\text{MPO}_4\text{F}$ (LiNiPO_4 and LiCoPO_4) and those which do not react to produce a fluorophosphate (LiFePO_4 and LiMnPO_4). Interestingly, the stability of each olivine does not account for such differences in reactivity: all lithium-containing olivine phosphates have similar Madelung energies (6600-6800 kCal/mol) and when prepared at high temperature, all are perfectly ordered with the Li residing on the M1 site of the olivine.¹⁹⁸ Instead the inability to produce $\text{Li}_2\text{MnPO}_4\text{F}$ and $\text{Li}_2\text{FePO}_4\text{F}$ is related to the symmetry of the Pnma $\text{Li}_2\text{MPO}_4\text{F}$ structure. Pairs of edge-shared octahedra are capped with a phosphate tetrahedron as shown in Figure 5.6a for the M1 site. As can be seen, P2 lies on the mirror plane perpendicular to the b-axis in Pnma and two of the phosphorus ligands (O1) are symmetry related by the same symmetry element.

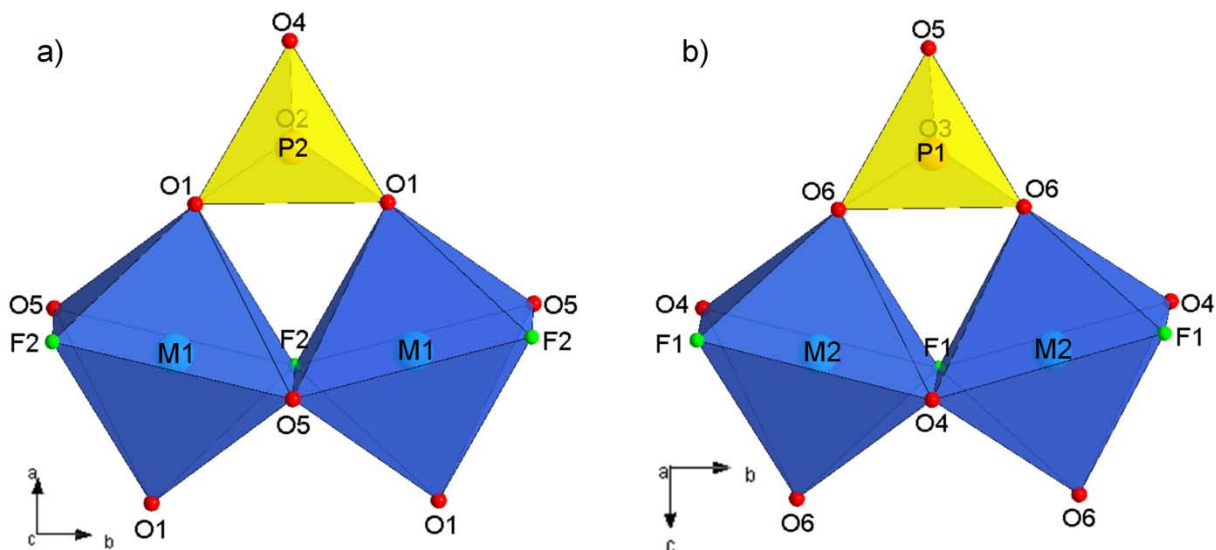


Figure 5.6: Schematic representation of a) the M1-M1 edge-sharing sites and b) the M2-M2 edge-sharing sites in $\text{Li}_2\text{MPO}_4\text{F}$ ($\text{M} = \text{Co}, \text{Ni}$).

Table 5.1: Bond lengths for transition metal sites in Li₂MPO₄F, M = Co, Ni.

Transition Metal Site	Ligand	Bond Length in Li ₂ CoPO ₄ F (Å)	Bond Length in Li ₂ NiPO ₄ F (Å)
M1	O1	1.996	2.011
	O5	2.087	2.070
	F2	2.164	2.081
M2	O6	2.009	2.013
	O4	2.061	2.036
	F1	2.155	2.082

Table 5.2: Lattice parameters for Li₂CoPO₄F and Li₂NiPO₄F.

Li ₂ MPO ₄ F	a (Å)	b (Å)	c (Å)
Li ₂ CoPO ₄ F	10.444	6.381	10.864
Li ₂ NiPO ₄ F	10.473	6.289	10.846

The geometry of the phosphate group (tetrahedral, P-O bond distances 1.5-1.6 Å) essentially fixes the distance between oxygen ligands at roughly 2.5 Å, which in turn limits the size of the metal ion which can reside on the M1 site. The M-O and M-F bond distances for the M1 site are listed in Table 5.1. According to Shannon, a standard Ni²⁺-O²⁻ bond is approximately 2.09 Å and a Ni²⁺-F⁻ bond is close to 2.01 Å. As can be seen from Table 5.1, the Ni1-O5 bonds are standard bond lengths whereas the Ni1-O1 bond is substantially shorter, due to the nature of the fixed position of the O1 ions. To compensate, the Ni1-F2 bond is slightly longer than a typical Ni-F bond. The geometry of the M1 site in Li₂CoPO₄F has the same geometry. A standard high-spin state Co²⁺-O²⁻ bond is 2.14 Å and a Co²⁺-F⁻ bond is close to 2.05 Å. In the case of Li₂CoPO₄F, the Co1-O5 bond is slightly compressed while the Co1-O1 bond is substantially shorter than a typical Co-O bond, and even slightly shorter than that found in Li₂NiPO₄F, even though Co²⁺ is a larger ion than Ni²⁺. In order to compensate, the

Co1-F2 bond is substantially larger than the expected 2.05 Å. It is not clear why the M1-O1 bond is shorter in the case of $\text{Li}_2\text{CoPO}_4\text{F}$ compared with $\text{Li}_2\text{NiPO}_4\text{F}$. Furthermore, the consequence of this fixed-length M1-O1 bond is seen in a comparison of the a-axis lattice parameters of these two compounds (see Table 5.2) as the M1-O1 bond is almost parallel with the a-axis: the slightly shorter M1-O1 bond in $\text{Li}_2\text{CoPO}_4\text{F}$ leads to a slightly shorter a-axis unit cell parameter.

A similar geometry exists for the M2 site in these compounds: pairs of edge-sharing metal octahedra are capped by a phosphate group which sits on a mirror plane. A schematic of the M2 site is shown in Figure 5.6b. In this case, it is the O6 ligand of the metal octahedron which is fixed in place by the phosphate tetrahedraon.

5.4 Sodium-ion and Hybrid Na/Li-ion Cells for Energy Storage

It has been shown that cycling of sodium-containing electrode materials may be performed in a lithium cell, where the negative electrode is lithium and the electrolyte contains a lithium salt,¹⁹⁹ or a “hybrid-ion” with a graphite negative electrode and a lithium salt electrolyte.²⁰⁰ In these systems, lithium was found to be the ion which was intercalated at the negative electrode, not sodium, as sodium does not intercalate into graphite.^{82,201,202} This is not surprising as lithium, present in the electrolyte at concentrations near 1 M, is present at much higher concentrations than the sodium, which is present in mg quantities in the positive electrode. This preliminary study demonstrated the insertion stability of this novel battery configuration where a sodium-containing positive electrode material may be paired with a Li electrolyte and graphite to achieve the high potential electrochemical reactivity of lithium.

The possibility of preparing Na-containing electrodes for Na/Li-ion cells also allows us to tap into the additional structural diversity of sodium compounds: many sodium-containing structure types exist in the literature which are not known to have equivalent lithium analogues. With this in mind, we set about preparation of sodium analogues of the lithium compounds described above. Sodium compounds with similar compositions such as $\text{Na}_2\text{FePO}_4\text{OH}$,²⁰³ $\text{Na}_2\text{MgPO}_4\text{F}$,²⁰⁴ $\text{Na}_2\text{CoPO}_4\text{F}$ ²⁰⁵ and $\text{Na}_2\text{MnPO}_4\text{F}$ ¹⁰⁵ have been reported as single crystal structures, but not as polycrystalline materials. We found solid-state and hydrothermal methods to prepare powders of $\text{Na}_2\text{FePO}_4\text{F}$, $\text{Na}_2\text{CoPO}_4\text{F}$ and $\text{Na}_2\text{MnPO}_4\text{F}$ for the first time. These materials were characterized structurally and cycled them both in lithium cells, with a lithium negative electrode and lithium salt electrolyte and full sodium-ion cells.

5.5 Synthesis of $\text{Na}_2\text{MPO}_4\text{F}$ Compounds

Sol-gel $\text{Na}_2\text{FePO}_4\text{F}$: Stoichiometric amounts of $\text{Fe}(\text{CH}_3\text{COO})_2$, NaCH_3COO , NaF and solid H_3PO_4 were stirred in a solution of dimethoxyethane and the solvent was then evaporated. The homogeneous gel was fired at 300°C under flowing Ar for 2 hours. The powder was subjected to further heating at $525\text{-}625^\circ\text{C}$ for 6 hours.

Solid-State $\text{Na}_2(\text{Fe,Co,Ni})\text{PO}_4\text{F}$: Stoichiometric amounts of $\text{Na}(\text{CH}_3\text{COO})$, NaF and $\text{NH}_4\text{H}_2\text{PO}_4$ (or $\text{Na}_2\text{PO}_3\text{F}$ for carbon-free methods) were ground in ceramic media in a planetary ball mill for 4-6 hours with $\text{Fe}(\text{C}_2\text{O}_4)\cdot 2\text{H}_2\text{O}$, CoCO_3 or NiCO_3 to make compositions of $\text{Na}_2(\text{Fe}_x\text{Co}_y\text{Ni}_z)\text{PO}_4\text{F}$, ($x + y + z = 1$). The samples were then treated at 350°C for 4-6 hours under flowing Ar to decompose the precursors. The powders were then subjected to further milling for 4-6 hours, followed by a final heat treatment at $500\text{-}625^\circ\text{C}$ for 4-6 hours.

Hydrothermal Na₂FePO₄F: Ten milliliters of a 0.30 M solution of H₃PO₄ was added to 10.0 ml of a 0.30 M solution of (NH₄)₂Fe(SO₄)₂, CoCl₂, or MgCl₂. The solution was basified with 0.9 g NaF and 1.2 g NaOH. The mixture was sealed in a 43 ml Teflon-lined Parr reactor and heated to 170-220 °C, where the product formed under autogeneous pressure. The powders were then heated to 500-625 °C for 4-6 hours under an Ar atmosphere.

Solid-State Na₂MnPO₄F: A stoichiometric amount of Mn(CH₃COO)₂•4H₂O and Na₂PO₃F were ball-milled for 6 hours followed by heat treatments at 350 °C and 600 °C under inert atmosphere.

Chemical Oxidation: Microcrystalline pure Na₂FePO₄F was oxidized with stoichiometric amounts of NO₂BF₄ in acetonitrile for 1 h to obtain the desired sodium content. Microcrystalline pure Na₂MnPO₄F was stirred with stoichiometric amounts of NO₂BF₄ in acetonitrile for 15 h.

Ion Exchange: Samples of Na₂FePO₄F were refluxed in acetonitrile with LiBr under a nitrogen atmosphere for 1-24 hours. Samples of Na₂CoPO₄F were mixed with LiBr and placed in a 23 ml Teflon-lined Parr reactor, using ethanol as the solvent. The reactor was heated to 225 °C for 7 h.

5.6 Synthesis and Structure of Na₂FePO₄F

Polycrystalline powders of Na₂FePO₄F could be prepared by solid-state or sol-gel synthesis at high temperatures (500-625 °C) and by a low-temperature hydrothermal route. In the hydrothermal reaction, the reagents were sealed inside a Teflon-lined Parr reactor in alkaline aqueous media and heated to temperatures up to 220 °C under autogenous pressure, similar to the synthesis procedure for LiFePO₄. The X-ray diffraction pattern is shown in Figure 5.7a. The lattice parameters are virtually identical to those of the single crystal. The

Na/P/Fe/F ratio was confirmed to be 2:1:1:1 by elemental dispersive X-ray analysis in the scanning electron microscope. The morphology of the product is shown in the SEM image in Figure 5.7b. The resultant particles are rodlike, typically 75-100 nm in the two thin dimensions and 300-700 nm in the longest dimension. This anisotropic particle shape is not unexpected for a compound which has two long crystallographic axes (b and c) and one short

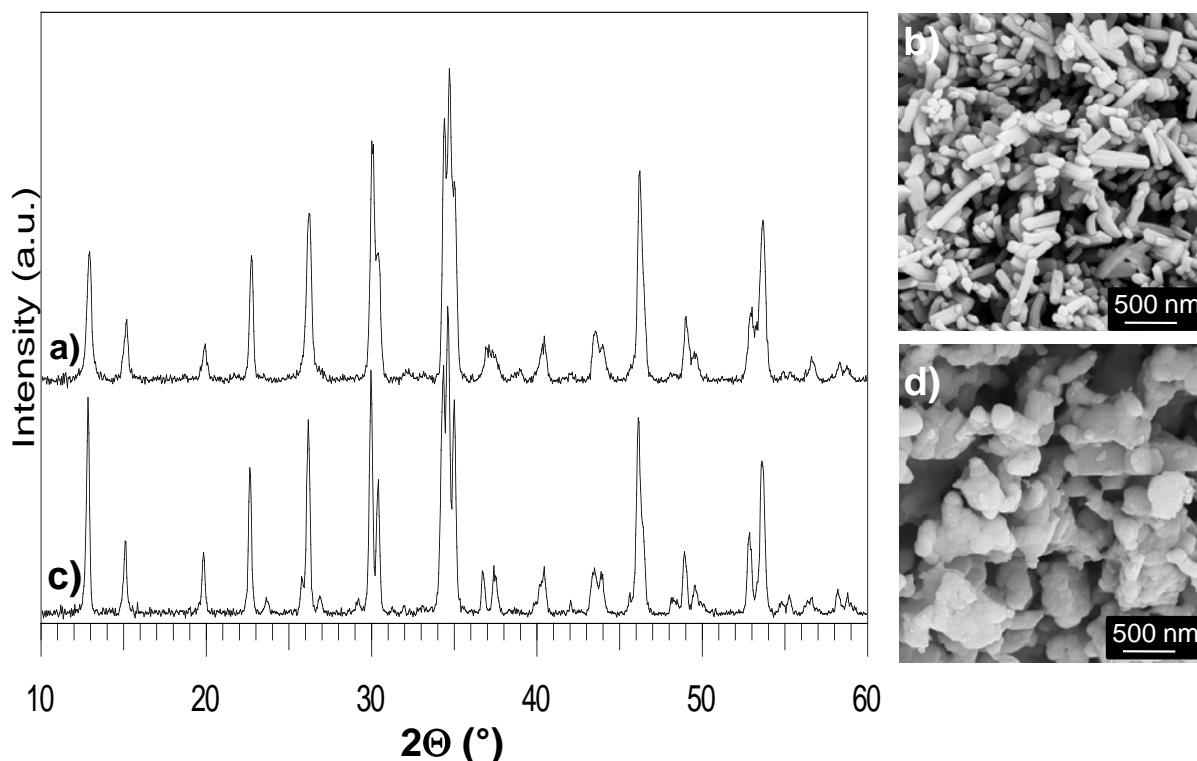


Figure 5.7: Powder diffraction patterns and corresponding SEM micrographs of $\text{Na}_2\text{FePO}_4\text{F}$ a) & b) prepared hydrothermally (lattice parameters: $a = 5.231 \text{ \AA}$, $b = 13.887 \text{ \AA}$, $c = 11.806 \text{ \AA}$); c) & d) prepared by a solid-state route (lattice parameters: $a = 5.218 \text{ \AA}$, $b = 13.854 \text{ \AA}$, $c = 11.779 \text{ \AA}$). Reprinted with permission from reference ⁸⁴, copyright 2010, American Chemical Society.

axis (a). It was also a consequence of the specific nucleation and crystal growth conditions in the hydrothermal bomb, since the sol-gel and solid state routes (see below) provided much more isotropic crystallites. The solid-state route involved the mechanical grinding of solid precursors followed by heat treatment in a furnace under inert atmosphere. The resulting X-ray diffraction pattern is shown in Figure 5.7c. The morphology of $\text{Na}_2\text{FePO}_4\text{F}$ prepared by

the solid-state route using a carbon containing precursor (Fe oxalate) is shown in Figure 5.7d. The sample was comprised of large agglomerates (up to 800 nm) made up of smaller particles about 50-200 nm in size.

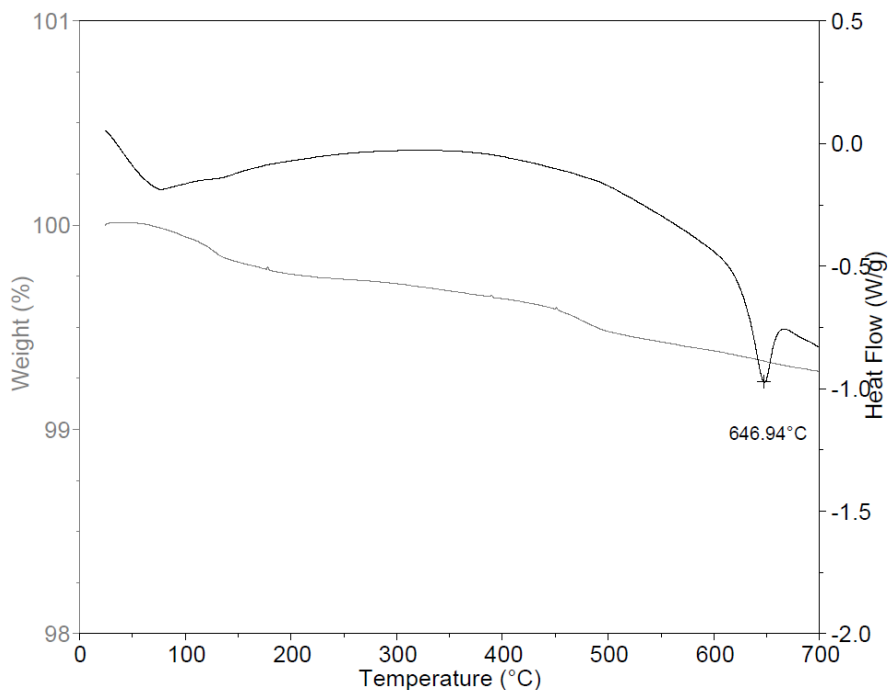


Figure 5.8: TGA curve showing the decomposition point of $\text{Na}_2\text{FePO}_4\text{F}$. Reprinted with permission from reference ⁸⁴, copyright 2010, American Chemical Society.

Approximately 2% carbon was contained within the material based on TGA analysis (performed under flowing air). Thermal gravimetric analysis of a solid-state sample was performed in an inert (nitrogen) atmosphere up to 700 °C, which revealed an endothermic event at 646 °C (Figure 5.8). At this temperature, the compound decomposed and the decomposition products were NaF, Na_3PO_4 , Fe and Fe_3O_4 . In contrast, LiFePO_4 is more thermally robust: carbothermal reduction occurs at a much higher temperature for LiFePO_4 (near 800 °C),²⁰⁶ and hence formation of conductive sp^2 carbon and/or conductive phosphides at high temperature is much more difficult for $\text{Na}_2\text{FePO}_4\text{F}$ than for the olivine. We note that since $\text{Na}_2\text{FePO}_4\text{F}$ decomposes near 650 °C, it would be virtually impossible to

synthesize this compound directly at a temperatures of 700 °C and above, as suggested in patent literature,¹⁹⁶ although high-temperature synthesis methods are possible for LiFePO₄, as a result of the greater thermal stability of the olivine.

Table 5.3: Atomic paramters and unit cell constants for Na₂FePO₄F.

Na₂FePO₄F			
Pbcn (Orthorhombic), Z = 8			
M _w = 215.80 g/mol			
D = 3.365 g cm ⁻³			
a = 5.2200(2) Å			
b = 13.8540(6) Å			
c = 11.7792(5) Å			
V = 851.85(6) Å ³			
Atom	x	y	z
Fe	0.2275(1)	0.0101(1)	0.3261(1)
P	0.2035(1)	0.3810(1)	0.0871(1)
Na (1)	0.2633(1)	0.2446(1)	0.3281(1)
Na (2)	0.2395(1)	0.1249(1)	0.0836(1)
F (1)	0	0.1238(1)	0.25
F (2)	0.5	0.1009(1)	0.25
O (1)	0.2663(2)	0.3882(1)	-0.0396(1)
O (2)	0.2846(2)	0.2837(1)	0.1330(1)
O (3)	-0.0905(2)	0.3948(1)	0.1027(1)
O (4)	0.3398(2)	0.4636(1)	0.1515(1)

Na₂FePO₄F crystallizes in the orthorhombic space group Pbcn. An X-ray diffraction pattern of the material prepared by the solid-state route is shown in Figure 5.7c and the crystal data for Na₂FePO₄F are summarized in Table 5.3. Two different views of the structure are depicted in Figure 5.1a. Each iron center is 6-coordinate, with four oxygen ligands and two fluorine ligands per metal ion. What makes this structure distinct is the connectivity of the 6-coordinate metal centers: Na₂FePO₄F consists of pairs of face-sharing Fe octahedra, each coordinated to four oxygen and two fluorine ions. These Fe₂O₆F₃ bioctahedral units are connected by corner-sharing (via F2) to other pairs of Fe face-shared

octahedra along the *a* direction, as shown in Figure 5.1a. These chains of Fe octahedra are connected through corner-sharing of PO₄³⁻ tetrahedra along the *c* direction.

Table 5.4: Selected bond distances in Na₂FePO₄F.

Atoms	Distance (Å)	Atoms	Distance (Å)
Fe1-O3	2.038	Na1-F1	2.352
Fe1-F2	2.100	Na1-O2	2.364
Fe1-O1	2.120	Na1-O3	2.411
Fe1-O4	2.140	Na1-O1	2.415
Fe1-F1	2.167	Na1-O2	2.464
Fe1-O4	2.183	Na1-F2	2.517
		Na1-O2	2.947
Fe-Fe	2.976		
		Na2-O2	2.288
P1-O2	1.513	Na2-F1	2.325
P1-O1	1.531	Na2-O3	2.383
P1-O4	1.546	Na2-F2	2.408
P1-O3	1.558	Na2-O4	2.409
		Na2-O1	2.531
		Na2-O1	2.804

Bond lengths are given in Table 5.4. The phosphate tetrahedra are very regular with P-O bond distances ranging between 1.51 and 1.56 Å. There are two crystallographically unique sodium sites, Na1 and Na2, as indicated in Figure 5.1a. The Na1 site is surrounded by four oxygen ion (Na-O distances between 2.36 and 2.46 Å) and two fluorine ions. The Na-F bond lengths are 2.35 and 2.52 Å. Note there is an extra neighboring oxygen ion located 2.93 Å from Na1, which makes a small contribution to the valence bond sum of Na1. This [6+1] coordination of the Na1 ion is similar to that seen for sodium in Na₂BeB₂O₅.²⁰⁷ Pairs of face-shared Na1 polyhedra corner-share via bridging fluorine ions (F1) in the *a* direction. The Na2 environment is slightly smaller than that of Na1. The Na2 site has four oxygen ligands with Na-O bonds varying from 2.28 to 2.53 Å and two fluorine ligands, 2.32 and 2.41 Å from Na2. There is also an additional oxygen atom 2.80 Å from Na2. As a

result, Na2 may be classified as having [6+1] coordination, much like Na1. The refined single crystal unit cell parameters for Na₂FePO₄F ($a = 5.2200(2)$ Å, $b = 13.8540(6)$ Å, and $c = 11.7792(5)$ Å) result in a unit cell volume of 851.85 Å³. That the Na₂FePO₄F unit cell is slightly larger than that of Na₂CoPO₄F ($a = 5.2475(9)$ Å, $b = 13.795(2)$ Å, $c = 11.689(2)$ Å, $V = 846.2$ Å³)²⁰⁵ is expected based on the larger ionic radius of Fe²⁺ (78 pm) compared to that of Co²⁺ (74 pm).¹⁸⁸ Although the cobalt coordination site is smaller than that of the iron site, the Na1 and Na2 environments are similar for both compounds.

It is noteworthy that the materials of the same stoichiometry, namely A₂MPO₄F (A = Li, Na; M = Co, Ni, Fe, Mn) crystallize in three different structures as a result of the subtle effects of ion size mediated interactions and magnetic interactions. The structures of the layered Na₂(Fe,Co,Mg)PO₄F, the “stacked” Li₂(Co,Ni)PO₄F, and the 3-D Na₂MnPO₄F are shown in Figure 5.1 respectively. Although location of the transition metal in octahedral sites is common to all three, the connectivity of the octahedra runs the entire gamut from mixed face-shared and corner-shared in Na₂FePO₄F to edge-shared in Li₂CoPO₄F and corner-shared in Na₂MnPO₄F. Considering the structures in which the alkali metals are the same, namely, Na₂FePO₄F *versus* Na₂MnPO₄F, the similar radii of Fe²⁺ (78 pm) compared to Mn²⁺ (83 pm)¹⁸⁸ suggest that the two structures might be more closely related. However, although Fe²⁺, Mg²⁺ and Co²⁺ are clearly stable in a face sharing arrangement, the high spin state of Mn²⁺ (d⁵ high spin), and the slightly larger size appears to result in unfavorable thermodynamics. Thus a different framework is adopted. In the case where the transition metal is the same and alkalis differ, namely, Na₂CoPO₄F *versus* Li₂CoPO₄F, the effects of the alkali prevail. The radius of a Na⁺ ion is 1.3 times than of a Li⁺ ion, and thus we would not expect these two structures (prepared at high temperatures under thermodynamic control)

to be the same. However, as was well established by *chimie douce* concepts long ago, ion exchange of one alkali for another at low temperatures can produce metastable compounds while maintaining the parent structure, such as $\text{Li}_2\text{FePO}_4\text{F}$ or $\text{Li}_2\text{CoPO}_4\text{F}$ with the $\text{Na}_2\text{FePO}_4\text{F}$ structure, as long as the ion interactions are not highly destabilized within the resulting lattice. Full understanding of these considerations could be used to predict framework dimensionality and connectivity of polyanion-based lattices.

5.7 Sodium Electrochemistry and *Ex-situ* Diffraction Study

$\text{Na}_2\text{FePO}_4\text{F}$ prepared by the sol-gel method was cycled in an electrochemical cell against sodium with 1 M NaClO_4 in propylene carbonate as the electrolyte. The solvent was dried over molecular sieves prior to use. The resultant electrochemical curve for cycling at a rate of C/20 is shown in Figure 5.9. On the initial charge, there is a flat plateau at 2.95 V until $\text{Na}_{1.7}\text{FePO}_4\text{F}$ at which point a transition to a second plateau at 3.10 V occurred. This is indicative of 2 two-phase regimes: one from $\text{Na}_2\text{FePO}_4\text{F}$ to an intermediate phase and another two-phase regime between the intermediate and NaFePO_4F . One mole of sodium per formula unit was extracted on the first charge. The first discharge was similar to the first charge: two different flat voltage plateaus were observed, although only 80% of the sodium were reintercalated. On the second charge, the profile exhibited different characteristics. The profile shape was sloped. No flat two-phase regions were observed, nor was the transition at the intermediate composition seen. The second discharge mirrored the first, as two plateaus were observed.

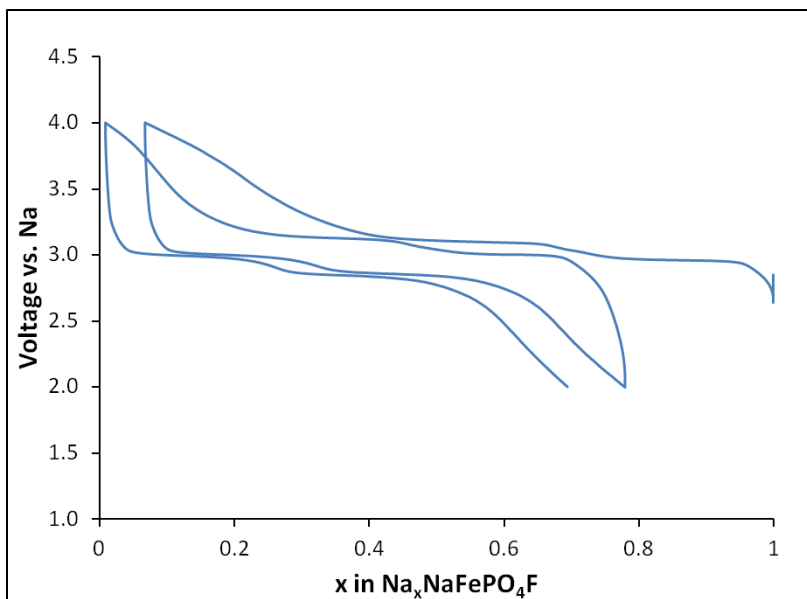


Figure 5.9: The first two cycles of a $\text{Na}_2\text{FePO}_4\text{F}$ composite electrode cycled versus sodium at a rate of $C/20$.

To gain better insight into the reactions happening inside the electrochemical cells, we prepared various compositions of $\text{Na}_{2-x}\text{FePO}_4\text{F}$ by chemical oxidation using NO_2BF_4 in a 1:1 molar ratio, according to the reaction:



The resulting diffraction patterns are shown in Figure 5.10, and lattice parameters are summarized in Table 5.5. The broadened features of some intermediate compositions prevented successful Rietveld refinement of their structures, however, none of the patterns appeared to display a mixture of the two end-members as all could be indexed as single phases. These $\text{Na}_{2-x}\text{FePO}_4\text{F}$ compounds prepared by chemical oxidation appear to have a wide range of nonstoichiometry and share similar structural features and lattice parameters with the parent compound. In the initial steps of oxidation ($\text{Na}_{2-x}\text{FePO}_4\text{F}$, $x < 0.25$), the orthorhombic Pbcn structure was maintained; the a and c lattice parameters contracted while the b lattice parameter increased.

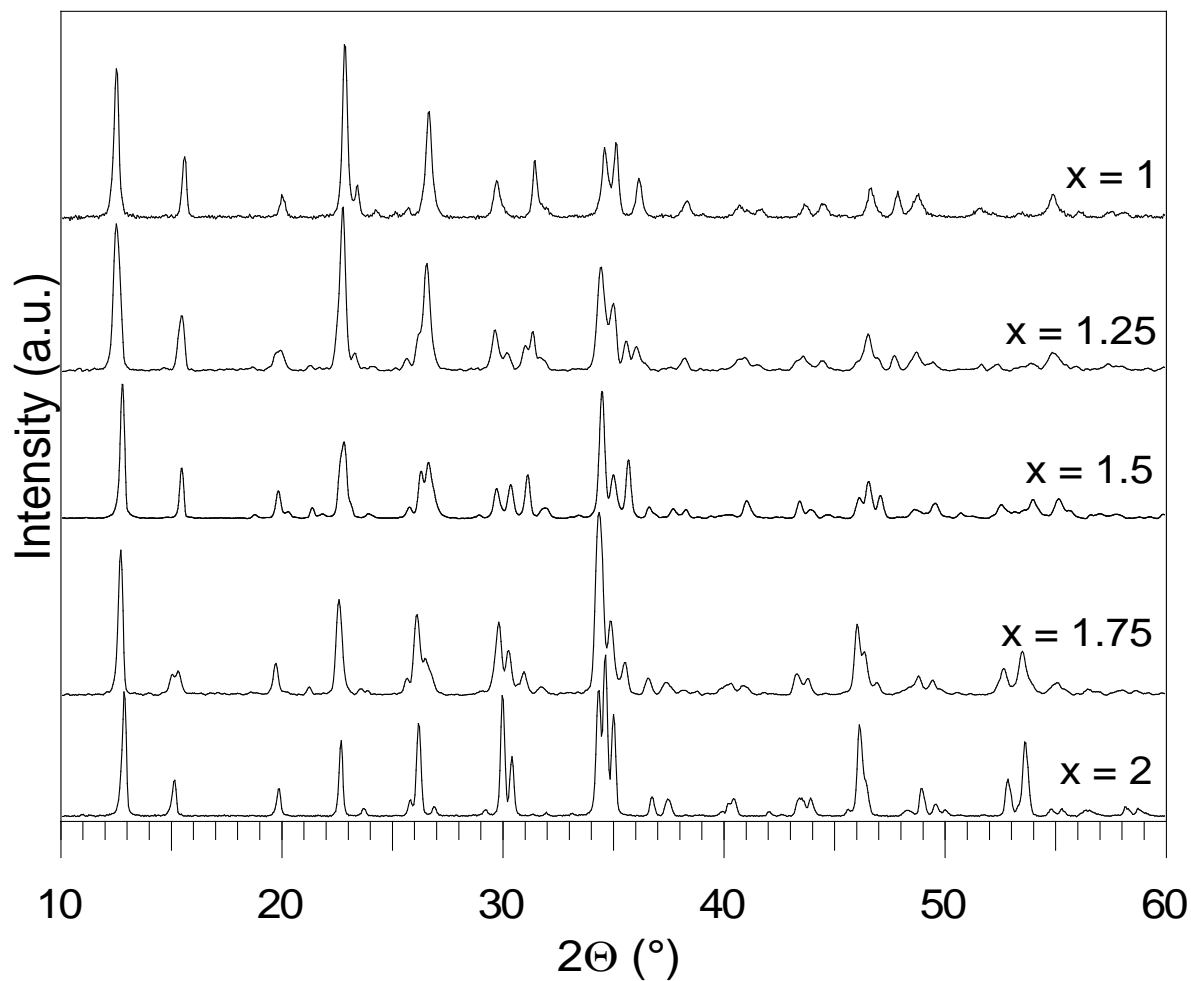


Figure 5.10: X-ray diffraction patterns of $\text{Na}_x\text{FePO}_4\text{F}$ illustrating the solid-solution behavior of the system in the range from $x = 2 \rightarrow 1$. Reprinted with permission from reference ⁸⁴, copyright 2010, American Chemical Society.

Table 5.5: Lattice parameters for sol-gel $\text{Na}_{2-x}\text{FePO}_4\text{F}$ prepared by chemical oxidation of $\text{Na}_2\text{FePO}_4\text{F}$

Compound	Space Group	a (Å)	b (Å)	c (Å)	β (°)	V (Å ³)
$\text{Na}_2\text{FePO}_4\text{F}$	Pbcn	5.2372(5)	13.8587(7)	11.779(1)	90	854.93
$\text{Na}_{1.75}\text{FePO}_4\text{F}$	Pbcn	5.219	13.893	11.602	90	841.23
$\text{Na}_{1.5}\text{FePO}_4\text{F}$	P2/c	13.929(6)	5.200(9)	11.514(7)	91.22(2)	834.03
$\text{Na}_{1.25}\text{FePO}_4\text{F}$	Pbcn	5.204	13.910	11.478	90	830.87
NaFePO_4F	Pbcn	5.1018(7)	14.1224(6)	11.360(1)	90	818.48

Further oxidation resulted in $\text{Na}_{1.5}\text{FePO}_4\text{F}$, which could also be indexed as a single phase with lattice parameters intermediate between the two end members. The diffraction pattern and full pattern refinement is shown in Figure 5.11. Extraction of half of the alkali resulted in a very small distortion in symmetry from the end member orthorhombic Pbcn cells, adopted by both $\text{Na}_2\text{FePO}_4\text{F}$ and NaFePO_4F , to a P2/c monoclinic unit cell with lattice parameters intermediate between the two end-members. Because of the increase of β from 90° to 91.22° , Vegard's law is not precisely obeyed. The distortion in this single phase composition probably results from ordering of the Fe^{2+} and Fe^{3+} ions in the lattice (and/or the Na^+ ions) which would likely occur *via* the formation of mixed oxidation state pairs within the $\text{Na}_2\text{FePO}_4\text{F}$ structure (see Figure 5.1a). The distortion may explain the step in the electrochemical curve on initial charge and each discharge cycle.

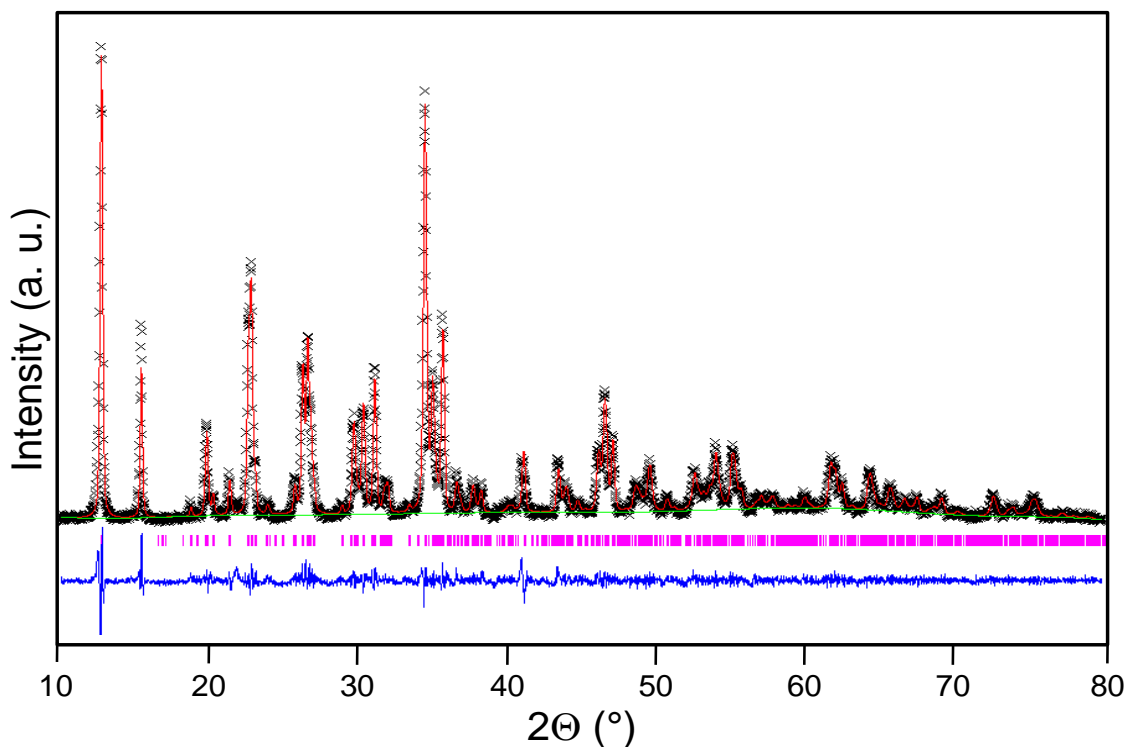


Figure 5.11: LeBail XRD refinement of $\text{Na}_{1.5}\text{FePO}_4\text{F}$ in P2/c, $wRp = 9.07\%$: lattice parameters $a = 13.929(6)$ Å, $b = 5.200(9)$ Å, $c = 11.514(7)$ Å; $\beta = 91.22^\circ$. Reprinted with permission from reference ⁸⁴, copyright 2010, American Chemical Society.

Further oxidation results in the structure reverting back to the orthorhombic $Pbcn$ space group. The lattice parameters of NaFePO_4F show that the unit cell volume of 818.48 \AA^3 is only 4% smaller than that of the parent compound $\text{Na}_2\text{FePO}_4\text{F}$. Overall, there is a clear trend in the lattice parameters: the a and c lattice parameters contract while the b lattice parameter increases. Transition between these two closely related phases results in “solid-solution-like” electrochemical behavior after the first cycle over the redox range that is spanned by $\text{Na}_{2-x}\text{FePO}_4\text{F}$, but it is not well understood.

Oxidation of $\text{Na}_2\text{FePO}_4\text{F}$ to form NaFePO_4F resulted in removal of all of the sodium from the Na2 site, while the Na1 site remains fully occupied. NaFePO_4F may be reduced chemically using alkali metal iodides since the potential of NaFePO_4F is greater than 2.7 V. Reduction with NaI reproduced the parent compound $\text{Na}_2\text{FePO}_4\text{F}$ as expected.

5.8 Electrochemistry and Ion Exchange of $\text{Na}_2\text{FePO}_4\text{F}$ with Lithium

Electrodes comprised of carbon-free hydrothermally prepared $\text{Na}_2\text{FePO}_4\text{F}$ were charged and discharged in a lithium cell with metallic Li as the negative electrode, at a rate of 1 Li in 10 hours (C/10). The first electrochemical cycle is shown in Figure 5.12. The discharge capacity of the first cycle is only 65 mAh/g, roughly half of the theoretical capacity of 135 mAh/g. Similar results were obtained for the material prepared by the solid state route. Nonetheless, the capacity can be dramatically improved by coating the surface with carbon. In the case of LiFePO_4 , this can also result in partial carbothermal reduction at elevated temperatures to form conductive iron phosphocarbides or phosphides such as metallic FeP. In tiny quantities (< 1-3%), these, combined with carbon, may facilitate surface electron transport in LiFePO_4 . However, this is problematic for $\text{Na}_2\text{FePO}_4\text{F}$ owing to the similar temperature of carburization, carbothermal reduction and compound decomposition

as described above. Hydrothermally prepared carbon coated materials were produced by adding organic reagents directly to the hydrothermal reactor that readily decompose

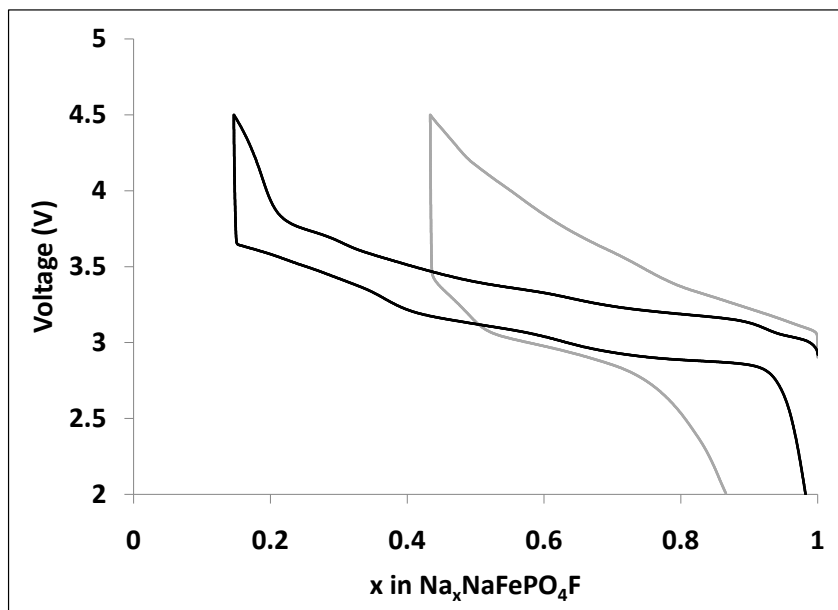


Figure 5.12: Electrochemical curve of $\text{Na}_2\text{FePO}_4\text{F}$ cycled versus Li at a rate of C/10 prepared by a carbon-free hydrothermal technique (grey curve) and by a hydrothermal route containing 2% C (black curve). Reprinted with permission from reference ⁸⁴, copyright 2010, American Chemical Society.

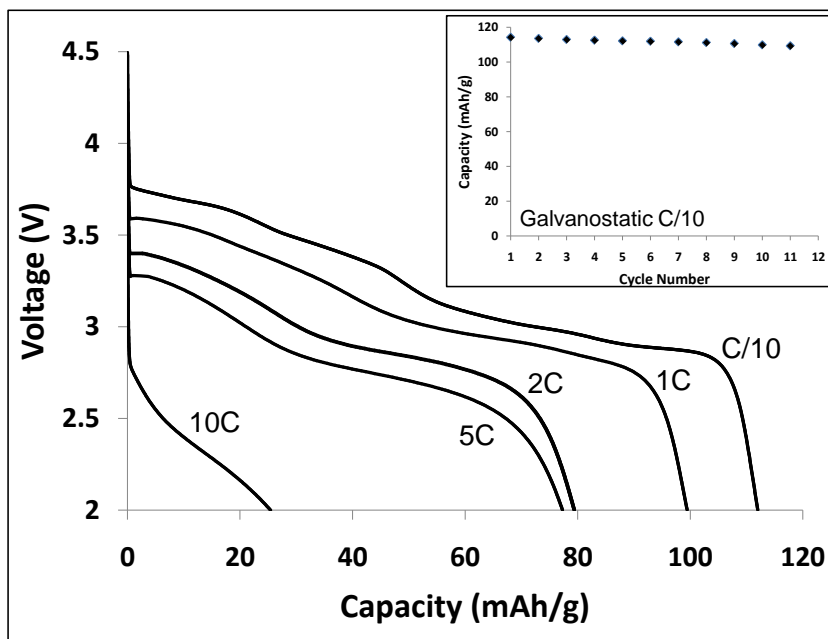


Figure 5.13: Rate performance of carbon-containing hydrothermally prepared $\text{Na}_2\text{FePO}_4\text{F}$ at various discharge rates after charging at a rate of C/10. Inset: Capacity retention data for cycling at C/10. Reprinted with permission from reference ⁸⁴, copyright 2010, American Chemical Society.

and leave a carbonaceous coating on the surface such as sucrose or ascorbic acid. The material was then heat-treated between 550 and 650 °C to carburize the surface coating without inducing carbothermal decomposition. The resultant Na₂FePO₄F contained about 2 wt % carbon.

The first cycle of a cell is shown in Figure 5.12 and initial results of a cell cycled at a C/10 rate at room temperature are shown in the inset of Figure 5.13. The material exhibits a sloping potential in a Li-ion electrolyte with an average potential of 3.3 V (versus Li metal). The voltage is slightly higher than that calculated for this material in a Na-ion cell, but similar to that for Li₂FePO₄F. The reversible capacity of 115 mAh/g is about 85% of the theoretical capacity, and it displays the same stability as the sol-gel derived Na₂FePO₄F (reported previously, for 50 cycles). It shows better rate capability (cells charged at C/10 and discharged at faster rates, Figure 5.13), that is, a capacity of about 80 mAh/g at 5C (discharge in 12 min) was achieved. This is indicative of the benefits a thin carbon coating provides this material. We anticipate substantial improvements in electrochemical properties for smaller particles and improved coatings, which is work in progress.

Transition between these two closely related end-member phases results in “solid-solution-like” electrochemical behavior (when cycled *versus* lithium) over the redox range that is spanned by (LiNa)_{2-x}FePO₄F, and the phase transition from the orthorhombic phase to the monoclinic phase at x = 0.5 is not readily observable in the electrochemical profile of the hydrothermal material in Figure 5.12. Likely, the electrochemical profile is complicated by the Li/Na ion exchange that takes place in the cell at room temperature (see below).

Electrochemical cycling of Na₂FePO₄F versus a Li negative electrode using LiPF₆ electrolyte has been shown to be a method of Na/Li ion exchange. Elemental analysis of the

positive electrode material scraped from multiple cells after cycling at a slow rate (C/10) was performed using EDX, the results of which are shown in Figure 5.14a. Analysis conducted on the positive electrode after the first discharge (Li insertion) revealed that the Na:P ratio is close to 1:1, indicating a chemical formula of (Li,Na)FePO₄F. This indicates that ~1 mol of Na was extracted on the initial charge, followed by the insertion of ~1 mol of Li during the initial discharge. Since Na1 sites are isolated from each other, any deviation from a 1:1 Na:P ratio would imply exchange between the Na1 and Na2 sites. Indeed, this is the case on

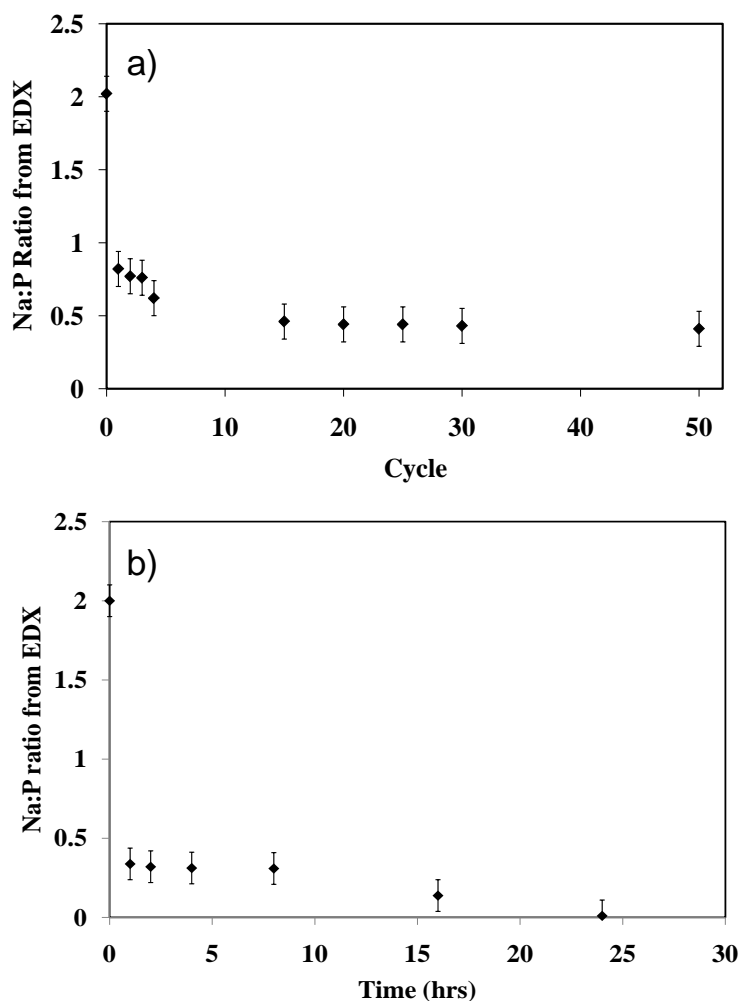


Figure 5.14: Na:P ratios determined by EDX analysis of crystallites in the FESEM. a) Na₂FePO₄F material taken from electrochemical cells cycled versus Li as a function of cycle number; b) Na₂FePO₄F after ion exchange with LiBr in acetonitrile as a function of exchange time. Reprinted with permission from reference ⁸⁴, copyright 2010, American Chemical Society.

prolonged cycling. In a cell halted after five cycles, the Na/Li ratio continued to decline and $\text{Li}_{1.4}\text{Na}_{0.6}\text{FePO}_4\text{F}$ was formed. Although ion exchange between the Na1 and Na2 site occurs, not all of the sodium in the Na1 site exchanged during the course of slow electrochemical cycling: the electrode in a cell after 50 cycles still contained 20% of the original sodium content. Moreover, ion exchange was also observed when a cell based on $\text{Na}_2\text{FePO}_4\text{F}$ versus Li was equilibrated at open circuit voltage (OCV) in $\text{LiPF}_6\text{-EC/DMC}$. At the outset, the cell had an open circuit potential of 2.960 V, but this dropped slowly to 2.905 V after 72 h. The potential remained constant at 2.905 V for another 48 h, at which point the cell was dismantled. The material was scraped from the positive electrode and thoroughly washed. Analysis showed the Na/P ratio was 1:1; thus half of the Na was exchanged for lithium even without cycling the cell.

More forceful conditions of ion exchange, such as solvent reflux with a lithium salt, were necessary to fully convert $\text{Na}_2\text{FePO}_4\text{F}$ into the metastable $\text{Li}_2\text{FePO}_4\text{F}$ phase. Ion exchange of $\text{Na}_2\text{FePO}_4\text{F}$ with Li was performed by refluxing $\text{Na}_2\text{FePO}_4\text{F}$ with LiBr in acetonitrile. Using EDX analysis, the sodium content with respect to reflux time was measured (Figure 5.14b). The exchange proceeds very quickly in the initial stages and after only 1 hour, only 30% of the initial sodium remains. After 24 hours of reflux, the sodium signal is no longer present in the EDX spectrum indicating that the exchange has gone to completion.

A closer look at the sodium layers of the $\text{Na}_2\text{FePO}_4\text{F}$ structure revealed important details about ion exchange *vis a vis* sodium (or lithium) ion mobility. As the oxidized compound NaFePO_4F contains sodium only in the Na1 site, it suggests that Na2 is the more mobile ion. Inspection of the two virtually identical frameworks reveals at least three

potential paths for ion transport (see Figure 5.1a). Pathway I involves displacement primarily in the *b*-direction with small displacements in the *a* and *c* directions. The two Na2 sites are 4.7 Å apart and separated by a large irregularly shaped interstitial site. Pathway II is similar to pathway I in that the primary displacement is also in the *b* direction with small displacements in the *a* and *c* directions. The distance between the two Na2 sites along Pathway II is approximately 4.7 Å, and the two sites are separated by an irregular interstitial site. Pathway III is simply displacement along the *a* axis by one unit cell length (5.22 Å). Pathway III is not a straight pathway however: an iron atom and an oxygen atom (O1) partially obstruct transport (see Figure 5-1a). As a result, ion migration along this pathway may be less probable relative to pathways I and II. The shortest Na2-Na2 distance in the structure is 4.65 Å, but this pathway is obstructed by the two face-sharing Fe atoms. Each Na2 polyhedron shares a face with three Na1 polyhedra, each of which is between 3.25 and 3.32 Å from Na2. This allows exchange of alkali ions between Na1 and Na2. In the case of ion exchange with LiBr in refluxed acetonitrile, the exchange is sufficiently facile to replace all of the Na in the structure with Li.

Although chemical reduction of NaFePO₄F with a sodium-containing reducing agent produced Na₂FePO₄F as expected, reduction with excess LiI results in a composition Li_{1.25}Na_{0.75}FePO₄F, as shown by the 0.6:1 Na:Li ratio obtained from elemental analysis using ICP. A Rietveld refinement of the X-ray diffraction pattern of this sample is shown in Figure 5.15. The atomic positions of sodium and lithium were constrained to be identical while the total occupancy of each alkali cation site was constrained to one. The isotropic thermal parameters for Li and Na were fixed using typical literature values. A summary of the

refinement results is shown in Table 5.6. The stoichiometry attained from the refinement was $\text{Li}_{1.22}\text{Na}_{0.78}\text{FePO}_4\text{F}$, in excellent accord with the chemical analysis.

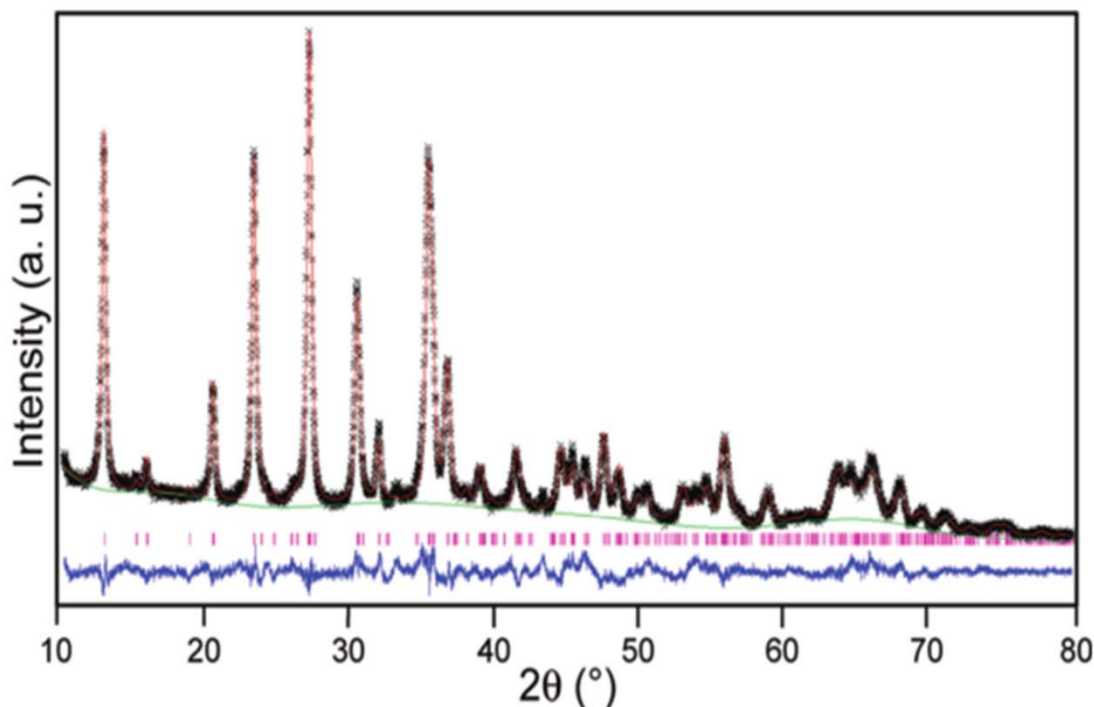


Figure 5.15: Rietveld refinement of $\text{Li}_{1.23}\text{Na}_{0.77}\text{FePO}_4\text{F}$, synthesized from NaFePO_4F reduced with excess LiI in Pbcn, $wRp = 7.69\%$: lattice parameters $a = 5.0327(3)\text{ \AA}$, $b = 13.8590(7)\text{ \AA}$, $c = 11.2081(5)\text{ \AA}$. For each, the fit is shown in red, the calculated reflections are shown in magenta, the background fit is shown in green and the difference map is shown in blue.

The lattice parameters were refined to be $a = 5.0407(3)\text{ \AA}$, $b = 13.8069(9)\text{ \AA}$, $c = 11.2215(5)\text{ \AA}$. As expected, the unit cell volume of this compound (780.98 \AA^3) is significantly less than that of $\text{Na}_2\text{FePO}_4\text{F}$ (854.93 \AA^3), and the sodium occupancy shows that ion scrambling has occurred: approximately 0.2 Na are situated on the Na2 site and only 0.6 Na remain on the Na1 site. Clearly, there is transport of sodium in the lattice from the Na1 site to the previously unoccupied Na2 site. We conclude that not only has LiI reduced NaFePO_4F to $\text{LiNaFePO}_4\text{F}$, but some of the remaining Na has ion exchanged with the excess LiI. This is in accordance with the room-temperature ion-exchange observed for a cell at

OCV (see above). Disordered Na/Li occupation likely contributes to the sloping voltage profile of Na₂FePO₄F cycled *versus* lithium.

Table 5.6: Rietveld refinement results and atomic positions for Li_{1.23}Na_{0.77}FePO₄F synthesized from NaFePO₄F reduced with excess Li.

Li_{1.23}Na_{0.77}FePO₄F					
Wavelength (Å)	1.5405, 1.5443				
Space Group (No.)	Pbcn (60)				
a (Å)	5.0327(3)				
b (Å)	13.8590(7)				
c (Å)	11.2081(5)				
V (Å ³)	781.74(4)				
Z	8				
Fitted Rwp (%)	7.69				
Fitted Rp (%)	5.77				
χ ²	8.022				
R _f (%)	3.76				
Atom	x/a	y/b	z/c	U_{iso}	Occ.
Fe1	0.247(1)	0.0024(4)	0.3295(3)	0.0048(6)	1.0
P1	0.238(2)	0.3747(5)	0.0809(6)	0.012(1)	1.0
Na1	0.325(1)	0.2422(8)	0.3280(6)	0.012(2)	0.530(5)
Li1	0.325(1)	0.2422(8)	0.3280(6)	0.015	0.470(5)
Na2	0.205(2)	0.1375(9)	0.0708(5)	0.012(2)	0.243(6)
Li2	0.205(2)	0.1375(9)	0.0708(5)	0.015	0.737(6)
F1	0	0.133(1)	0.25	0.011(2)	1.0
F2	0.5	0.0683(7)	0.25	0.009(2)	1.0
O1	0.339(3)	0.387(1)	-0.052(1)	0.016(3)	1.0
O2	0.290(3)	0.267(1)	0.110(1)	0.012(2)	1.0
O3	-0.055(2)	0.404(1)	0.073(1)	0.015(3)	1.0
O4	0.370(3)	0.430(1)	0.150(1)	0.018(4)	1.0

5.9 Mössbauer studies of small polaron hopping in Na_{1.5}FePO₄F

Room temperature Mössbauer measurements (Figure 5.16) on materials prepared by a sol-gel route confirm the oxidation state of the iron in the material prepared through this process. In Na₂FePO₄F, there is one dominant signal with an isomer shift (IS) of 1.16 mm/s and a quadrupole splitting (QS) of 2.20 mm/s. These values are typical of Fe⁺² in an

octahedral environment. A small amount, roughly 4 mol % of Fe^{3+} (IS = 0.44 mm/s, QS = 0.48 mm/s, consistent with Fe^{3+} in an octahedral site) was detected in the sample. It is possible that some surface oxidation occurred, or there is a small amount of an amorphous Fe^{3+} impurity. Chemical oxidation results in a decrease in the Fe^{2+} signal intensity that exactly correlates with the increase in the Fe^{3+} signal as expected, up to the formation of $\text{NaFe}^{3+}\text{PO}_4\text{F}$. Further oxidation is made difficult by the inaccessibly high redox couple anticipated for the $\text{Fe}^{3+/4+}$ couple.

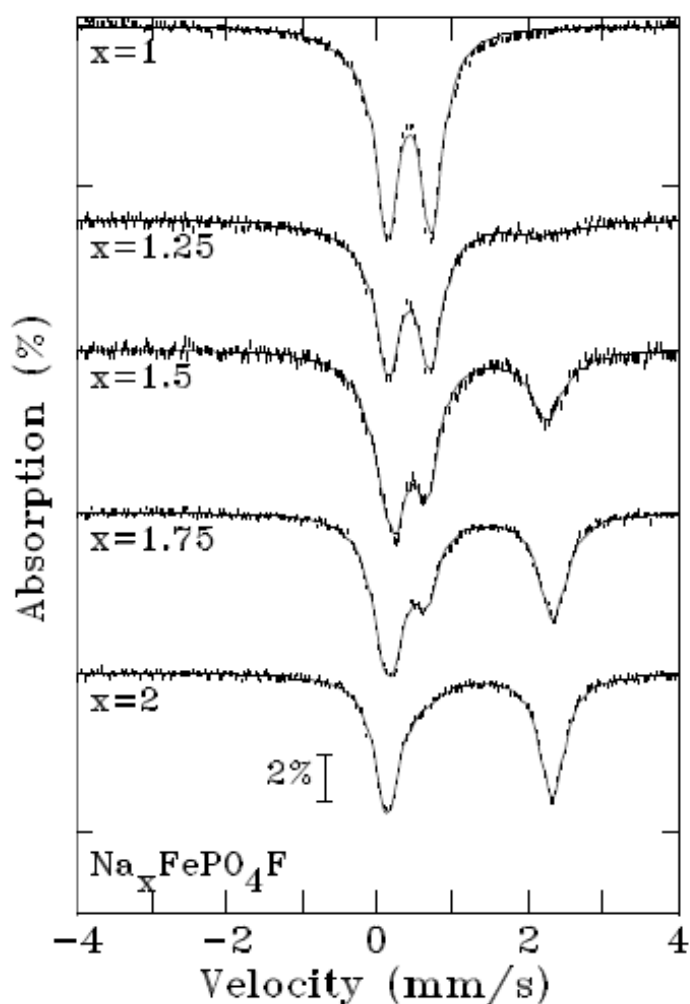


Figure 5.16: Room temperature Mössbauer data of $\text{Na}_2\text{FePO}_4\text{F}$, $\text{Na}_{1.75}\text{FePO}_4\text{F}$, $\text{Na}_{1.5}\text{FePO}_4\text{F}$, $\text{Na}_{1.25}\text{FePO}_4\text{F}$ and NaFePO_4F , prepared by chemical oxidation of $\text{Na}_2\text{FePO}_4\text{F}$. Reprinted with permission from reference ⁸⁴, copyright 2010, American Chemical Society.

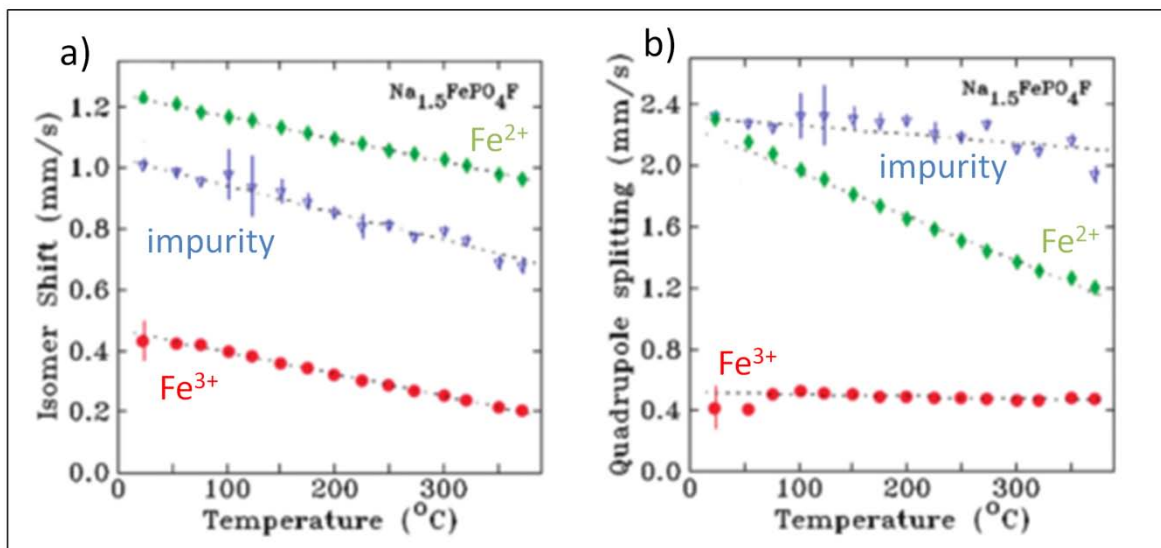


Figure 5.17: Variable temperature Mössbauer data of $\text{Na}_{1.5}\text{FePO}_4\text{F}$ summarizing a) area fraction of each Fe valence in the spectrum and b) isomer shifts at various temperatures.

Temperature-dependent Mössbauer studies were performed on the target compound $\text{Na}_{1.5}\text{FePO}_4\text{F}$ to investigate whether thermally activated small polaron hopping occurs in this mixed $\text{Fe}^{2+}/\text{Fe}^{3+}$ single phase on the Mössbauer time scale (about 10^{-8} s). Analysis of the room-temperature data shows the expected 50:50 ratio of the $\text{Fe}^{2+}/\text{Fe}^{3+}$ components for $\text{Na}_{1.5}\text{FePO}_4\text{F}$. The Fe^{3+} component (IS = 0.43 mm/s, QS = 0.4 mm/s) is identical to that of NaFePO_4F as expected. The Fe^{2+} signal was split into two components: the majority (45%) exhibits typical Fe^{2+} parameters (IS = 1.23 mm/s, QS = 2.31 mm/s). The remaining Fe^{2+} signal (5%; IS = 1.01 mm/s and QS = 2.32 mm/s) was ascribed to surface or defect Fe^{2+} sites that lack full octahedral coordination. The Mössbauer parameters derived from the fitting the $\text{Na}_{1.5}\text{FePO}_4\text{F}$ spectra at the different temperatures up to 373 °C are summarized in Figure 5.17. The standard thermal dependence of the isomer shifts of each of the three components is observed over the entire range of temperatures probed. Furthermore, the relative area of each signal did not change as the sample was heated. Upon cooling the sample back to room temperature the original spectrum was fully recovered.

These are the only components that exist over this temperature range: no new spectral features that would correspond to rapid electron hopping on the Mössbauer time scale emerged at any temperature, unlike the case of the partially olivine LiFePO_4 , as discussed previously. At room temperature, Li^+ ion and electron hopping are a coupled activated process that occurs across the grain boundary between the two phases (LiFePO_4 and FePO_4) which adopt the same space group). At 220 °C, entropy drives the collapse of the phase boundary, and both lithium and electrons disorder within the solid solution lattice. However, $\text{Na}_{1.5}\text{FePO}_4\text{F}$ is a single phase that exhibits a structural distortion to a monoclinic space group compared to its orthorhombic end-members ($\text{Na}_2\text{FePO}_4\text{F}$ and NaFePO_4F). This is likely the result of electron localization in the system to form $\text{Fe}^{2+}/\text{Fe}^{3+}$ sites. Additional energy would be required to remove the distortion and hence average the two sites to $\text{Fe}^{2.5+}$, although the effects of the structural distortion and iron valence ordering do not preclude electron hopping between neighboring $\text{Fe}^{2+}/\text{Fe}^{3+}$ sites which may occur at a slower rate ($< 10^{-8}$ s) than the Mössbauer time scale can measure.

5.10 Synthesis and Electrochemistry of Other $\text{Na}_2\text{MPO}_4\text{F}$ Phases (M = Fe, Co, Ni, Mg, Mn)

In similar fashion to $\text{Na}_2\text{FePO}_4\text{F}$, polycrystalline samples of $\text{Na}_2\text{CoPO}_4\text{F}$ can also be prepared by solid state or hydrothermal routes. According to the Ellingham diagrams detailing carbothermal reduction, Co^{+2} may be reduced to metallic Co at temperatures near 300°C, which is well below that of our solid-state firing temperature. We have observed that $\text{Na}_2\text{CoPO}_4\text{F}$ is very susceptible to carbothermal reduction. All attempts to use carbon-containing precursors for the synthesis, such as cobalt acetate, produced elemental cobalt

which was clearly evident in the diffraction pattern. As such, a carbon-free solid-state method was employed. The diffraction pattern is shown in Figure 5.18a and the corresponding lattice parameters are in Figure 5.19.

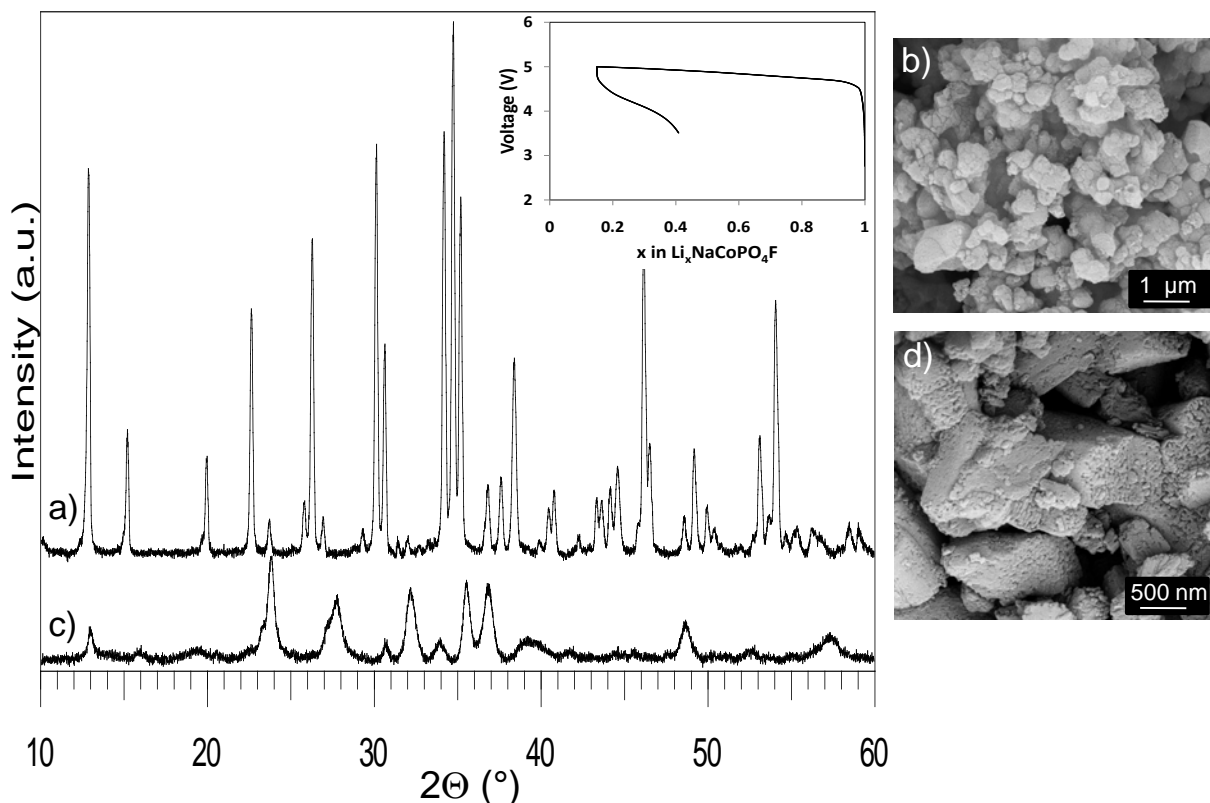


Figure 5.18: Powder diffraction patterns and corresponding SEM micrographs of $\text{Na}_2\text{CoPO}_4\text{F}$ a) & b) prepared by a carbon-free solid-state route c) & d) ion-exchanged for 7 hours. Inset: First electrochemical profile of $\text{Na}_2\text{CoPO}_4\text{F}$ cycled at a rate of C/10. Reprinted with permission from reference ⁸⁴, copyright 2010, American Chemical Society.

Comparison of refined powder X-ray data for $\text{Na}_2\text{CoPO}_4\text{F}$ and $\text{Na}_2\text{FePO}_4\text{F}$ shows that the two Na sites (Na1 and Na2) in both compounds are almost identical. The unit cell volume of 843.1 \AA^3 differs from the original report by Sanz²⁰⁵ by 0.3% and EDX measurements confirms a Na:Co:P:F ratio of 2:1:1:1. The product consists of agglomerated particles which range up to 750 nm in dimension, as seen in the SEM micrograph in Figure 5.18b. A solvent-reflux method of ion exchange of $\text{Na}_2\text{CoPO}_4\text{F}$ was not sufficiently forcing

to produce a complete exchange of Na for Li in the material. Thus a pressurized ion exchange was performed using a solution of LiBr and ethanol which yielded $\text{Li}_2\text{CoPO}_4\text{F}$. The resultant diffraction pattern is shown in Figure 5.18c. The broad diffraction peaks and weak signal to noise ratio clearly indicate the crystallinity of the material has decreased.

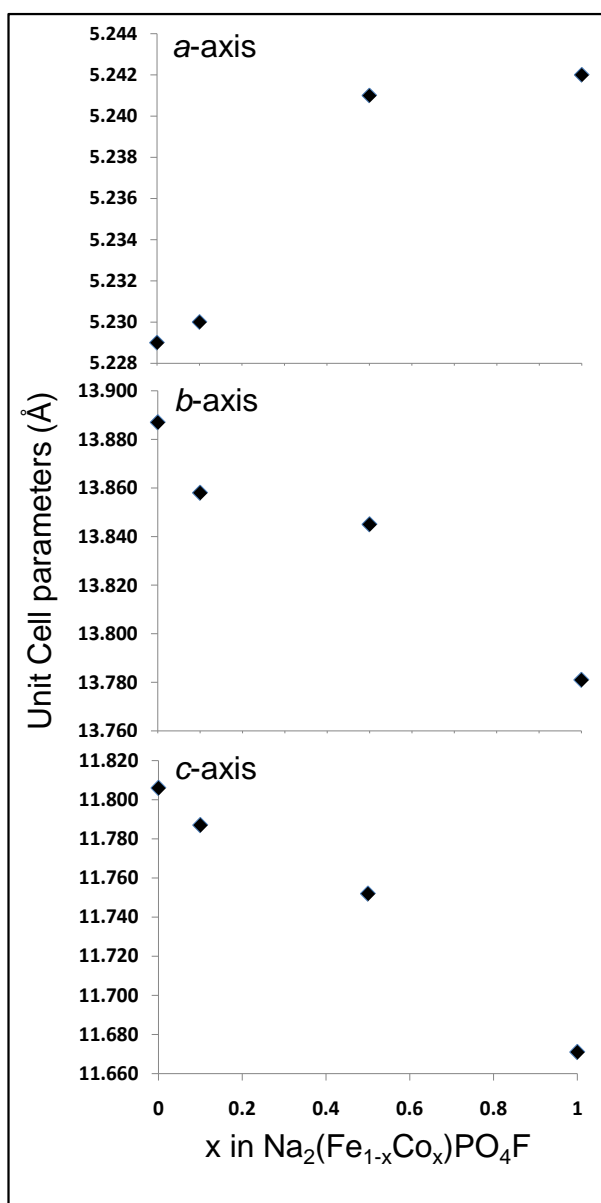


Figure 5.19: Lattice parameters for single-phase solid solution compounds $\text{Na}_2(\text{Fe}_{1-x}\text{Co}_x)\text{PO}_4\text{F}$. Reprinted with permission from reference ⁸⁴, copyright 2010, American Chemical Society.

This was confirmed by an SEM image of the particle surface (Figure 5.18d) where distinct cracking of the particles was observed. The difficulty in ion-exchange indicated a reduced ability for sodium ion transport through the lattice. However, $\text{Na}_2\text{CoPO}_4\text{F}$ has a unit cell volume almost 2% less than that of $\text{Na}_2\text{FePO}_4\text{F}$: this increased crystallographic density may inhibit facile motion of ions.

Comparison of the diffraction patterns from $\text{Na}_2\text{CoPO}_4\text{F}$ and $\text{Li}_2\text{CoPO}_4\text{F}$ produced from ion-exchanged $\text{Na}_2\text{CoPO}_4\text{F}$ clearly show that the ion-exchanged material maintains the structural features of the structure (Fig. 5.1a). But not surprisingly, this form of $\text{Li}_2\text{CoPO}_4\text{F}$ is meta-stable. Heating this compound to 580°C under an Ar flow causes the structure to revert back to the thermodynamically stable form of $\text{Li}_2\text{CoPO}_4\text{F}$: the edge-shared structure described earlier in this chapter. Electrochemical cycling, using Li as a counter electrode was performed at a very slow rate (C/10), with the voltage profile of the first cycle shown in Figure 5.18 (inset). $\text{Na}_2\text{CoPO}_4\text{F}$ exhibits a long sloping first charge profile between 4.7 and 5.0 V, at which point 85% of the capacity was reached. However, the discharge capacity was very low compared to that of the overall capacity as only 25% of the material was discharged. The poor reversible capacity of sodium cobalt fluorophosphate is similar to that reported for LiCoPO_4 .⁵⁴

Although Mg, Co and Fe variants of $\text{Na}_2\text{MPO}_4\text{F}$ are known, $\text{Na}_2\text{NiPO}_4\text{F}$ is not. We synthesised this material by the solid-state route and its diffraction pattern is shown in Figure 5.20. This compound is sensitive to reduction as well, since trace amounts of elemental Ni were found in the diffraction pattern, even with the usage of carbon-free precursors. $\text{Na}_2\text{NiPO}_4\text{F}$ clearly has a similar structure as the aforementioned Mg, Co and Fe sodium fluorophosphates. On indexing the pattern, $\text{Na}_2\text{NiPO}_4\text{F}$ was found to have a unit cell volume

of 823.4 \AA^3 which is 4% smaller than that for $\text{Na}_2\text{FePO}_4\text{F}$ and 1.5% smaller than that for $\text{Na}_2\text{CoPO}_4\text{F}$, owing to the smaller size of the nickel ion compared to the other transition metal ions. An electrochemical cell which contained $\text{Na}_2\text{NiPO}_4\text{F}$ as the positive electrode material did not show any electrochemical activity below 5 V. It is expected that this compound has a $\text{Ni}^{+2}/\text{Ni}^{+3}$ redox couple above 5 V, similar to that of other nickel phosphates such as LiNiPO_4 ²⁰⁸ and $\text{Li}_2\text{NiPO}_4\text{F}$.¹⁹⁵

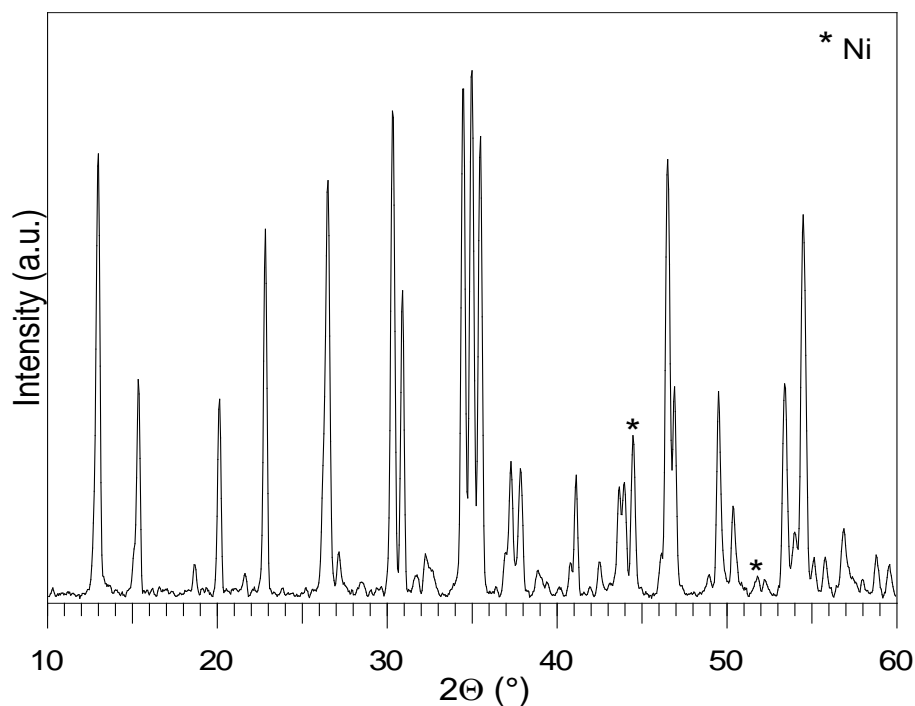


Figure 5.20: X-ray powder diffraction pattern of $\text{Na}_2\text{NiPO}_4\text{F}$, with Ni impurity peaks noted. Reprinted with permission from reference⁸⁴, copyright 2010, American Chemical Society.

Although electrochemical inactivity may be anticipated for $\text{Na}_2\text{NiPO}_4\text{F}$ up to 5 V, surprising was the complete lack of electrochemical activity we observed for carbon-containing $\text{Na}_2\text{MnPO}_4\text{F}$. Although this material is not isostructural with $\text{Na}_2\text{FePO}_4\text{F}$, the structure (Figure 5.1c) suggests that open pathways should be available for Na mobility, most notably in the *b*-direction where Na ions are situated along tunnels within the structure. The material was prepared by a solid-state method similar to that for $\text{Na}_2\text{FePO}_4\text{F}$ which involved

vigorous ball-milling of the precursors for up to 12 hours and produced agglomerates of small particles. The final $\text{Na}_2\text{MnPO}_4\text{F}$ product contained roughly 3% carbon by mass, owing to the use of manganese acetate as a precursor. Despite these efforts, the material did not exhibit any electrochemical activity below 5 V. Furthermore, the solid state prepared $\text{Na}_2\text{MnPO}_4\text{F}$ was also found to resist chemical oxidation: no reaction was observed upon stirring the material with NO_2BF_4 for 15 hours.

Substitutional solid solution compounds of the type $\text{Na}_2(\text{Mg}_w, \text{Fe}_x, \text{Co}_y, \text{Ni}_z)\text{PO}_4\text{F}$, ($w + x + y + z = 1$) could also be directly synthesized hydrothermally or by a solid-state route. Single phase compounds of the solid solution $\text{Na}_2(\text{Fe}_{1-x}\text{Co}_x)\text{PO}_4\text{F}$ are observed by X-ray diffraction and the lattice parameters are summarized in Figure 5.19. The individual lattice parameters follow a clear trend upon substitution of Co for Fe: the a lattice parameter increases while those for b and c decrease. However, these trends are not linear and do not strictly follow Vegard's law. Similar compounds are also known for lithium phospho-olivines: substitutional solid solutions of M2 site ions have been synthesized as lithium-ion battery materials by various solid-state and hydrothermal routes, and remain of particular interest for electrochemical study.^{137,138} Initial electrochemical results for $\text{Na}_2(\text{Fe}_{1-x}\text{Co}_x)\text{PO}_4\text{F}$ compounds cycled up to 5 V vs. Li show two distinct regions of redox potential (near 3.3 V and 4.7 V) but minimal reversibility was demonstrated. Preliminary results for $\text{Na}_2(\text{Fe}_{1-x}\text{Mg}_x)\text{PO}_4\text{F}$ ($x < 0.15$) compounds show electrochemical profiles similar to those for $\text{Na}_2\text{FePO}_4\text{F}$, with only slight performance improvement upon doping with Mg. In the case of $\text{Li}(\text{Fe}_{1-x}\text{Mg}_x)\text{PO}_4$, Mg doping up to 15% has been shown to substantially improve the performance of the olivine.¹⁴⁹ This may be due in part to the lesser unit cell volume difference between the end members, which reduces lattice strain. For example,

$\text{Li}(\text{Fe}_{0.90}\text{Mg}_{0.10})\text{PO}_4$ and $\text{Li}_{0.1}(\text{Fe}_{0.90}\text{Mg}_{0.10})\text{PO}_4$ exhibited a volume difference of only 5.15%, close to that reported for high-rate LiFePO_4 nanocrystallites and much less than for the bulk material, of 6.6%.¹⁴⁹

5.11 Conclusions

The $\text{A}_2\text{MPO}_4\text{F}$ family of compounds crystallize in a diverse array of structures depending on the identity of the alkali metal and transition metal in the structure. While the lithium variants of the cobalt and nickel fluorophosphate may be easily prepared, the iron and manganese variants were unable to be prepared over the course of this study. However, we were able to prepare all sodium compounds of this group, including the previously unreported $\text{Na}_2\text{FePO}_4\text{F}$ and $\text{Na}_2\text{NiPO}_4\text{F}$, both of which are isostructural with NaCoPO_4F which crystallizes in the space group Pbcn. The diffraction data confirms the unique structural features of the structure, including the [6+1] octahedral geometry of both Na sites in the lattice and the face-sharing dimers of iron atoms. Both $\text{Na}_2\text{FePO}_4\text{F}$ and the isostructural $\text{Na}_2\text{CoPO}_4\text{F}$ can be synthesized a variety of methods, including sol-gel, hydrothermal and high temperature solid-state routes. Furthermore, electrochemically active substitutional solid solutions of the form $\text{Na}_2(\text{Mg}_w\text{Fe}_x\text{Co}_y\text{Ni}_z)\text{PO}_4\text{F}$, ($w + x + y + z = 1$) may also be prepared.

$\text{Na}_2\text{FePO}_4\text{F}$ is a promising energy storage material which can be reversibly cycled in an electrochemical cell with lithium as the counter electrode at rates up to 5C. Ion exchange of $\text{Na}_2\text{FePO}_4\text{F}$ and this series of compounds is accomplished by several methods including by reflux with a Li salt, and in a Li cell by electrochemical exchange, or by simple equilibration at OCV. The propensity of these sodium fluorophosphates to undergo ion exchange demonstrates the high mobility of the alkali ions in the lattice.

6 Final Conclusions and Future Directions

There have been exciting developments in new positive electrode materials for energy storage in the last decade. Although layered, spinel, and nanostructured lithium metal oxides still remain amongst the most viable materials, polyanionic compounds have emerged as highly suitable candidates, including LiFePO_4 and its olivine analogues such as LiMnPO_4 which are starting to make a practical mark. Promising electrochemical properties including excellent cycling stability, low synthetic cost, improved safety characteristics, and low environmental impact are factors which have driven research interest in these compounds although polyanionic compounds brings to the forefront the importance of nanoscale synthesis methods and particle engineering to mitigate these materials' shortcomings, namely poor electronic conductivity. Low-temperature synthesis routes for preparation of these materials are desirable as they are not energy intensive and produce nanocrystalline powders. Nanocrystalline LiFePO_4 materials exhibit enhanced solid solution behavior possibly as the result of reduced lattice strain on the lattice upon deintercalation. This resulted in superior electrochemical properties compared to electrodes prepared from larger bulk materials, as demonstrated in the case of hydrothermally prepared LiFePO_4 . These developments in the scientific community have helped lead to the commercialization of this material.

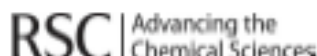
Fluorophosphates and hydroxyphosphates of iron, vanadium and manganese based on the tavorite structure are a promising new class of materials. Although the fluorophosphates in this group have the highest potentials, the OH-containing phosphates of this group demonstrated diverse electrochemical characteristics. Most intriguing of these was the mixed hydroxy-fluorophosphate $\text{LiFePO}_4(\text{OH})_{0.4}\text{F}_{0.6}$ which demonstrated solid-solution behaviour as a result of anion mixing, a concept to be explored for other polyanionic frameworks.

More recently, orthosilicates of the Li_2MSiO_4 ($\text{M} = \text{Mn, Fe, Co}$) family have garnered interest. The promise held by the Li_2MSiO_4 system is that, in principle, extraction of two lithium ions per transition metal is possible for a two electron redox process (operation of the $\text{M}^{2+} \rightarrow \text{M}^{3+}$ and $\text{M}^{3+} \rightarrow \text{M}^{4+}$ redox couples) for both $\text{M} = \text{Mn}$ and Fe with organic electrolyte systems. With the realization of full extraction of lithium from the silicates, high gravimetric capacities in excess of 300 mAh/g would be obtained, well in excess of most other intercalation systems in which one lithium at most can be extracted. While such high-capacity materials are highly sought after, the low electronic conductivity of the silicates combined with the large volume change of the lattice upon extraction of two Li per formula unit and oxidation of the transition metal from $\text{M}^{2+} \rightarrow \text{M}^{4+}$, one might expect lithium (de)intercalation kinetics to be hindered. Two-electron redox materials exist in the family of favorite compounds, namely LiVPO_4F and LiMnPO_4OH . These compounds are not ideal, as the $\text{M}^{3+} \rightarrow \text{M}^{2+}$ redox potential of LiVPO_4F is very low (1.75 V vs. Li/Li^+) compared to the $\text{M}^{4+} \rightarrow \text{M}^{3+}$ (at 4.25 V vs. Li/Li^+). LiMnPO_4OH exhibits poor thermal stability and is easily reduced to LiMnPO_4 , thus coating this material with conductive carbon is difficult.

Owing to concerns over lithium cost and availability, sodium and sodium-ion batteries have begun to emerge as promising candidates for both portable and stationary energy storage. While molten Na cells based on Na/S and Na/ NiCl_2 are available for commercial use, ambient-temperature sodium-ion cells are a growing field. Many positive electrode materials reported thus far have been analogues of various Li-ion battery materials such as the layered oxides, NaSICON compounds and olivines. Negative electrode materials thus far have also followed this trend: carbons and titanium dioxide have also been reported as Na-ion intercalation compounds. Based on rate and cycling data, open and layered

structures which are better able to accommodate the large Na^+ ions have proved to hold the most promise of the intercalation compounds. The successful development of $\text{Na}_2\text{FePO}_4\text{F}$, both for use in lithium and sodium-ion cells demonstrates the value in the difficult task of preparing previously unreported materials. New structures and framework types based on sodium which were not previously known as lithium compounds are critical for advancement of the Na-ion battery field.

Permissions



Royal Society of Chemistry
Thomas Graham House
Science Park
Milton Road
Cambridge
CB4 0WF

Tel: +44 (0)1223 420 066
Fax: +44 (0)1223 423 623
Email: contracts-copyright@rsc.org

www.rsc.org

Acknowledgements to be used by RSC authors

Authors of RSC books and journal articles can reproduce material (for example a figure) from the RSC publication in a non-RSC publication, including theses, without formally requesting permission providing that the correct acknowledgement is given to the RSC publication. This permission extends to reproduction of large portions of text or the whole article or book chapter when being reproduced in a thesis.

The acknowledgement to be used depends on the RSC publication in which the material was published and the form of the acknowledgements is as follows:

- For material being reproduced from an article in *New Journal of Chemistry* the acknowledgement should be in the form:
 - [Original citation] - Reproduced by permission of The Royal Society of Chemistry (RSC) on behalf of the Centre National de la Recherche Scientifique (CNRS) and the RSC
- For material being reproduced from an article *Photochemical & Photobiological Sciences* the acknowledgement should be in the form:
 - [Original citation] - Reproduced by permission of The Royal Society of Chemistry (RSC) on behalf of the European Society for Photobiology, the European Photochemistry Association, and RSC
- For material being reproduced from an article in *Physical Chemistry Chemical Physics* the acknowledgement should be in the form:
 - [Original citation] - Reproduced by permission of the PCCP Owner Societies
- For material reproduced from books and any other journal the acknowledgement should be in the form:
 - [Original citation] - Reproduced by permission of The Royal Society of Chemistry

The acknowledgement should also include a hyperlink to the article on the RSC website.

The form of the acknowledgement is also specified in the RSC agreement/licence signed by the corresponding author.

Except in cases of republication in a thesis, this express permission does not cover the reproduction of large portions of text from the RSC publication or reproduction of the whole article or book chapter.

A publisher of a non-RSC publication can use this document as proof that permission is granted to use the material in the non-RSC publication.



RightsLink®



ACS Publications Title: Small Polaron Hopping in Li_xFePO₄ Solid Solutions: Coupled Lithium-Ion and Electron Mobility
Author: Brian Ellis,[†], Laura K. Perry,[‡], Dominic H. Ryan,[‡] and, and L. F. Nazar^{*,†}
Publication: Journal of the American Chemical Society
Publisher: American Chemical Society
Date: Sep 1, 2006
Copyright © 2006, American Chemical Society

PERMISSION/LICENSE IS GRANTED FOR YOUR ORDER AT NO CHARGE

This type of permission/license, instead of the standard Terms & Conditions, is sent to you because no fee is being charged for your order. Please note the following:

- Permission is granted for your request in both print and electronic formats, and translations.
- If figures and/or tables were requested, they may be adapted or used in part.
- Please print this page for your records and send a copy of it to your publisher/graduate school.
- Appropriate credit for the requested material should be given as follows: "Reprinted (adapted) with permission from (COMPLETE REFERENCE CITATION). Copyright (YEAR) American Chemical Society." Insert appropriate information in place of the capitalized words.
- One-time permission is granted only for the use specified in your request. No additional uses are granted (such as derivative works or other editions). For any other uses, please submit a new request.

If credit is given to another source for the material you requested, permission must be obtained from that source.



RightsLink®



ACS Publications Title: Structure and Electrochemistry of Two-Electron Redox Couples in Lithium Metal Fluorophosphates Based on the Tavorite Structure
Author: Brian L. Ellis, T. N. Ramesh, Linda J.M. Davis, Gillian R. Goward, and Linda F. Nazar
Publication: Chemistry of Materials
Publisher: American Chemical Society
Date: Dec 1, 2011
Copyright © 2011, American Chemical Society

PERMISSION/LICENSE IS GRANTED FOR YOUR ORDER AT NO CHARGE

This type of permission/license, instead of the standard Terms & Conditions, is sent to you because no fee is being charged for your order. Please note the following:

- Permission is granted for your request in both print and electronic formats, and translations.
- If figures and/or tables were requested, they may be adapted or used in part.
- Please print this page for your records and send a copy of it to your publisher/graduate school.
- Appropriate credit for the requested material should be given as follows: "Reprinted (adapted) with permission from (COMPLETE REFERENCE CITATION). Copyright (YEAR) American Chemical Society." Insert appropriate information in place of the capitalized words.
- One-time permission is granted only for the use specified in your request. No additional uses are granted (such as derivative works or other editions). For any other uses, please submit a new request.

If credit is given to another source for the material you requested, permission must be obtained from that source.



RightsLink®



ACS Publications Title:

High quality. High impact.

Anion-Induced Solid Solution
Electrochemical Behavior in Iron
Tavorite Phosphates

Author: Brian L. Ellis and Linda F. Nazar

Publication: Chemistry of Materials

Publisher: American Chemical Society

Date: Mar 1, 2012

Copyright © 2012, American Chemical Society

PERMISSION/LICENSE IS GRANTED FOR YOUR ORDER AT NO CHARGE

This type of permission/license, instead of the standard Terms & Conditions, is sent to you because no fee is being charged for your order. Please note the following:

- Permission is granted for your request in both print and electronic formats, and translations.
- If figures and/or tables were requested, they may be adapted or used in part.
- Please print this page for your records and send a copy of it to your publisher/graduate school.
- Appropriate credit for the requested material should be given as follows: "Reprinted (adapted) with permission from (COMPLETE REFERENCE CITATION). Copyright (YEAR) American Chemical Society." Insert appropriate information in place of the capitalized words.
- One-time permission is granted only for the use specified in your request. No additional uses are granted (such as derivative works or other editions). For any other uses, please submit a new request.

If credit is given to another source for the material you requested, permission must be obtained from that source.



RightsLink®



Title: A multifunctional 3.5V
iron-based phosphate cathode
for rechargeable batteries

Author: B. L. Ellis, W. R. M. Makahnouk,
Y. Makimura, K. Toghill, L. F.
Nazar

Publication: Nature Materials

Publisher: Nature Publishing Group

Date: Sep 9, 2007

Copyright © 2007, Rights Managed by Nature
Publishing Group

Author Request

If you are the author of this content (or his/her designated agent) please read the following. If you are not the author of this content, please click the Back button and select an alternative [Requestor Type](#) to obtain a quick price or to place an order.

Ownership of copyright in the article remains with the Authors, and provided that, when reproducing the Contribution or extracts from it, the Authors acknowledge first and reference publication in the Journal, the Authors retain the following non-exclusive rights:

- To reproduce the Contribution in whole or in part in any printed volume (book or thesis) of which they are the author(s).
- They and any academic institution where they work at the time may reproduce the Contribution for the purpose of course teaching.
- To reuse figures or tables created by them and contained in the Contribution in other works created by them.
- To post a copy of the Contribution as accepted for publication after peer review (in Word or Text format) on the Author's own web site, or the Author's institutional repository, or the Author's funding body's archive, six months after publication of the printed or online edition of the Journal, provided that they also link to the Journal article on NPG's web site (eg through the DOI).



RightsLink®



Title: Crystal Structure and Electrochemical Properties of A₂MPO₄F Fluorophosphates (A = Na, Li; M = Fe, Mn, Co, Ni)[†]

Author: Brian L. Ellis, W. R. Michael Makahnouk, W. N. Rowan-Weetaluktuk, D. H. Ryan, and Linda F. Nazar

Publication: Chemistry of Materials

Publisher: American Chemical Society

Date: Feb 1, 2010

Copyright © 2010, American Chemical Society

PERMISSION/LICENSE IS GRANTED FOR YOUR ORDER AT NO CHARGE

This type of permission/license, instead of the standard Terms & Conditions, is sent to you because no fee is being charged for your order. Please note the following:

- Permission is granted for your request in both print and electronic formats, and translations.
- If figures and/or tables were requested, they may be adapted or used in part.
- Please print this page for your records and send a copy of it to your publisher/graduate school.
- Appropriate credit for the requested material should be given as follows: "Reprinted (adapted) with permission from (COMPLETE REFERENCE CITATION). Copyright (YEAR) American Chemical Society." Insert appropriate information in place of the capitalized words.
- One-time permission is granted only for the use specified in your request. No additional uses are granted (such as derivative works or other editions). For any other uses, please submit a new request.

If credit is given to another source for the material you requested, permission must be obtained from that source.

References

- (1) Tarascon, J. M.; Armand, M. *Nature* **2001**, *414*, 359.
- (2) Armand, M.; Tarascon, J.-M. *Nature* **2008**, *451*, 652.
- (3) Scholey, N. *Ele. Comm. Eng.* **1995**, 93.
- (4) Anani, A.; Visintin, A.; Petrov, K.; Srinivasan, S.; Reilly, J. J.; Johnson, J. R.; Schwarz, R. B.; Desch, P. B. *J. Power Sour.* **1994**, *47*, 261.
- (5) Whittingham, M. S. US 4009052 **1977**.
- (6) Whittingham, M. S. *Science* **1976**, *192*, 1126.
- (7) Whittingham, M. S. *J. Electrochem. Soc.* **1976**, *123*, 315.
- (8) Besenhard, J. O.; Schollhorn, R. *J. Power Sour.* **1976**, *1*, 267.
- (9) Murphy, D. W.; Christian, P. A.; DiSalvo, F. J.; Carides, J. N. *J. Electrochem. Soc.* **1979**, *126*, 497.
- (10) Schollhorn, R.; Klein-Reesink, F.; Reimold, R. *J. Chem. Soc. Chem. Comm.* **1979**, 398.
- (11) Bonino, F.; Selvaggi, A.; Scrosati, B. *Sol. Stat. Ion.* **1988**, 28-30, 853.
- (12) Orsini, F.; Du Pasquier, A.; Beaudouin, B.; Tarascon, J. M.; Trentin, M.; Langenhuizen, N.; De Beer, E.; Notten, P. *J. Power Sour.* **1999**, 81-82, 918.
- (13) Fauteux, D.; Koksang, R. *J. Appl. Electrochem.* **1993**, *23*, 1.
- (14) Mizushima, K.; Jones, P. C.; Wiseman, P. J.; Goodenough, J. B. *Mat. Res. Bull.* **1980**, *15*, 783.
- (15) Takayuki, Y.; Kato, H.; Anzai, M. US Patent 5053297 **1991**.
- (16) Mohri, M.; Yanagisawa, N.; Tajima, Y.; Tanaka, H.; Mitate, T.; Nakajima, S.; Yoshida, M.; Yoshimoto, Y.; Suzuki, T.; Wada, H. *J. Power Sour.* **1989**, *26*, 545.
- (17) Ohzuku, T.; Ueda, A.; Nagayama, M.; Iwakoshi, Y.; Komori, H. *Electrochim. Acta* **1993**, *38*, 1159.
- (18) Reimers, J. N.; Dahn, J. R. *J. Electrochem. Soc.* **1992**, *139*, 2091.

- (19) Tukamoto, H.; West, A. R. *J. Electrochem. Soc.* **1997**, *144*, 3164.
- (20) Reimers, J. N.; Dahn, J. R.; Von Sacken, U. *J. Electrochem. Soc.* **1993**, *140*, 2752.
- (21) Yazami, R.; Lebrun, N.; Bonneau, M.; Molteni, M. *J. Power Sour.* **1995**, *54*, 389.
- (22) Nohma, T.; Kurokawa, H.; Uehara, M.; Takahashi, M.; Nishio, K. *J. Power Sour.* **1995**, 522.
- (23) Barker, J.; Pynenburg, R.; Koksang, R.; Saidi, M. Y. *Electrochim. Acta* **1996**, *41*, 2481.
- (24) Gupta, R.; Manthiram, A. *J. Sol. Stat. Chem.* **1996**, *121*, 483.
- (25) Ohzuku, T.; Makimura, Y. *Chem. Lett.* **2001**, *2*, 744.
- (26) Lu, Z.; MacNeil, D. D.; Dahn, J. R. *Electrochem. Solid-State Lett.* **2001**, *4*, A191.
- (27) Van der Ven, a.; Ceder, G. *Electrochem. Comm.* **2004**, *6*, 1045.
- (28) Venkatraman, S.; Choi, J.; Manthiram, A. *Electrochem. Comm.* **2004**, *6*, 832.
- (29) Ammundsen, B.; Paulsen, J. *Adv. Mater.* **2001**, *13*, 943.
- (30) Ohzuku, T.; Makimura, Y. *Chem. Lett.* **2001**, 642.
- (31) Lu, Z.; MacNeil, D. D.; Dahn, J. R. *Electrochem. Solid-State Lett.* **2001**, *4*, A200.
- (32) Yin, S.-C.; Rho, Y.-H.; Swainson, I.; Nazar, L. F. *Chem. Mater.* **2006**, *18*, 1901.
- (33) Reale, P.; Privitera, D.; Panero, S.; Scrosati, B. *Sol. Stat. Ion.* **2007**, *178*, 1390.
- (34) Whitfield, P.; Davidson, I.; Cranswick, L.; Swainson, I.; Stephens, P. *Sol. Stat. Ion.* **2005**, *176*, 463.
- (35) Tarascon, J. M.; Guyomard, D.; Baker, G. L. *J. Power Sour.* **1993**, *44*, 689.
- (36) Huang, H.; Vincent, C. A.; Bruce, P. G. *J. Electrochem. Soc.* **1999**, *146*, 3649.
- (37) Thackeray, M. M. *Electrochem. Solid-State Lett.* **1999**, *1*, 7.
- (38) Jang, D. H.; Shin, Y. J.; Oh, S. M. *J. Electrochem. Soc.* **1996**, *143*, 2204.
- (39) Deng, B.; Nakamura, H.; Yoshio, M. *Electrochem. Solid-State Lett.* **2005**, *8*, A171.

- (40) Pahdi, A. K.; Nanjundaswamy, K. S.; Masquelier, C.; Okada, S.; Goodenough, J. B. *J. Electrochem. Soc.* **1997**, *144*, 1609.
- (41) Kerr, T. A.; Gaubicher, J.; Nazar, L. F. *Electrochem. Solid-State Lett.* **2000**, *3*, 460.
- (42) Barker, J.; Saidi, M. Y.; Swoyer, J. L. *Journal of The Electrochemical Society* **2004**, *151*, A796.
- (43) Gaubicher, J.; Wurm, C.; Goward, G.; Masquelier, C.; Nazar, L. *Chem. Mater.* **2000**, *12*, 3240.
- (44) Barker, J.; Saidi, M. Y.; Swoyer, J. L. *J. Electrochem. Soc.* **2003**, *150*, A1394.
- (45) Ado, K.; Tabuchi, M.; Kobayashi, H.; Kageyama, H.; Nakamura, O.; Inaba, Y.; Kanno, R.; Takagi, M.; Takeda, Y. *J. Electrochem. Soc.* **1997**, *144*, L177.
- (46) Nanjundaswamy, K.; Pahdi, A. K.; Goodenough, J. B.; Okada, S.; Ohtsuka, H.; Arai, H.; Yamaki, J. *Sol. Stat. Ion.* **1996**, *92*, 1.
- (47) Padhi, A. K.; Nanjundaswamy, K. S.; Masquelier, C.; Goodenough, J. B. *J. Electrochem. Soc.* **1997**, *144*, 2581.
- (48) Prosini, P. P.; Lisi, M.; Scaccia, S.; Carewska, M.; Cardellini, F.; Pasquali, M. *J. Electrochem. Soc.* **2002**, *149*, A297.
- (49) Masquelier, C.; Reale, P.; Wurm, C.; Morcrette, M.; Dupont, L.; Larcher, D. *J. Electrochem. Soc.* **2002**, *149*, A1037.
- (50) Pahdi, A. K.; Nanjundaswamy, K. S.; Goodenough, J. B. *J. Electrochem. Soc.* **1997**, *144*, 1188.
- (51) Delacourt, C.; Poizot, P.; Morcrette, M.; Tarascon, J.-M.; Masquelier, C. *Chem. Mater.* **2004**, *16*, 93.
- (52) Drezen, T.; Kwon, N.-H.; Bowen, P.; Teerlinck, I.; Isono, M.; Exnar, I. *J. Power Sources* **2007**, *174*, 949.
- (53) Kim, T.; Kim, D.; Ryu, H.; Moon, J.; Lee, J.; Boo, S.; Kim, J. *J. Phys. Chem. Sol.* **2007**, *68*, 1203.
- (54) Bramnik, N.; Bramnik, K.; Buhrmester, T.; Baehtz, C.; Ehrenberg, H.; Fuess, H. *J. Sol. Stat. Electrochem.* **2004**, *8*, 558.
- (55) Bramnik, N. N.; Nikolowski, K.; Baehtz, C.; Bramnik, K. G.; Ehrenberg, H. *Chem. Mater.* **2007**, *19*, 908.

- (56) Bramnik, N. N.; Nikolowski, K.; Trots, D. M.; Ehrenberg, H. *Electrochem. Solid-State Lett.* **2008**, *11*, A89.
- (57) Nyten, A.; Abouimrane, A.; Armand, M.; Gustafsson, T.; Thomas, J. O. *Electrochem. Comm.* **2005**, *7*, 156.
- (58) Zaghbi, K.; Ait Salah, a.; Ravet, N.; Mauger, a.; Gendron, F.; Julien, C. M. *Journal of Power Sources* **2006**, *160*, 1381–1386.
- (59) Dominko, R.; Bele, M.; Gaberscek, M.; Meden, A.; Remskar, M.; Jamnik, J. *Electrochem. Comm.* **2006**, *8*, 217.
- (60) Dominko, R. *J. Power Sources* **2008**, *184*, 462.
- (61) Lyness, C.; Delobel, B.; Armstrong, A. R.; Bruce, P. G. *Chem. Comm.* **2007**, 4890.
- (62) Kokalj, A.; Dominko, R.; Mali, G.; Meden, A.; Gaberscek, M.; Jamnik, J. *Chem. Mater.* **2007**, *19*, 3633.
- (63) Armstrong, A. R.; Kuganathan, N.; Islam, M. S.; Bruce, P. G. *J. Am. Chem. Soc.* **2011**, *133*, 13031.
- (64) Dominko, R.; Conte, D. E.; Hanzel, D.; Gaberscek, M.; Jamnik, J. *J. Power Sources* **2008**, *178*, 842.
- (65) Arroyo-de Dompablo, M. E.; Armand, M.; Tarascon, J. M.; Amador, U. *Electrochem. Comm.* **2006**, *8*, 1292.
- (66) Muraliganth, T.; Stroukoff, K. R.; Manthiram, A. *Chem. Mater.* **2010**, *22*, 5754.
- (67) Pizarro-Sanz, J.; Dance, J.; Villeneuve, G.; Arriortua-Marcaida, M. *Mater. Lett.* **1994**, *18*, 327.
- (68) Groat, L. A.; Raudsepp, M.; Hawrorn, F. C.; Ercit, T. S.; Sherriff, L.; Hartman, J. S. *Amer. Miner.* **1990**, *75*, 992.
- (69) Risacher, F.; Fritz, B. *Aqu. Geochem.* **2009**, *15*, 123.
- (70) Yaksic, A.; Tilton, J. E. *Resour. Policy* **2009**, *34*, 185.
- (71) Yao, Y. Y.; Kummer, J. T. *J. Inorg. Nucl. Chem.* **1967**, *29*, 2453.
- (72) Kummer, J. T.; Weber, N. Battery having a molten alkali metal anode and molten sulfur cathode **1968**.
- (73) Dunn, B.; Breiter, M. W.; Park, D. S. *J. Appl. Electrochem.* **1981**, *11*, 103.

- (74) Oshima, T.; Kajita, M. *Int. J. Appl. Cer. Tech.* **2004**, *1*, 269.
- (75) Van Zyl, A. *Sol. Stat. Ion.* **1996**, 86-88, 883.
- (76) Sudworth, J. L. *J. Power Sour.* **2001**, *100*, 149.
- (77) Xiong, H.; Slater, M. D.; Balasubramanian, M.; Johnson, C. S.; Rajh, T. *J. Phys. Chem. Lett.* **2011**, *2*, 2560–2565.
- (78) Senguttuvan, P.; Palacín, M. R. *Chem. Mater.* **2011**, *23*, 4109.
- (79) Berthelot, R.; Carlier, D.; Delmas, C. *Nat. Mater.* **2011**, *10*, 74.
- (80) Patoux, S.; Rouse, G.; Leriche, J.; Masquelier, C. *Chem. Mater.* **2003**, *3*, 2084.
- (81) Stevens, D. A.; Dahn, J. R. *J. Electrochem. Soc.* **2000**, *147*, 1271.
- (82) Stevens, D. A.; Dahn, J. R. *J. Electrochem. Soc.* **2001**, *148*, A803.
- (83) Ellis, B. L.; Makahnouk, W. R. M.; Makimura, Y.; Toghil, K.; Nazar, L. F. *Nat. Mater.* **2007**, *6*, 749.
- (84) Ellis, B. L.; Makahnouk, W. R. M.; Rowan-Weetaluktuk, W. N.; Ryan, D. H.; Nazar, L. F. *Chem. Mater.* **2010**, *22*, 1059.
- (85) Ozawa, K. *Sol. Stat. Ion.* **1994**, *69*, 212.
- (86) Chung, S.-Y.; Bloking, J. T.; Chiang, Y.-M. *Nat. Mater.* **2002**, *1*, 123.
- (87) Herle, P. S.; Ellis, B.; Coombs, N.; Nazar, L. F. *Nat. Mater.* **2004**, *3*, 147.
- (88) Delacourt, C.; Poizot, P.; Tarascon, J.-M.; Masquelier, C. *Nat. Mater.* **2005**, *4*, 254.
- (89) Dodd, J. L.; Yazami, R.; Fultz, B. *Electrochem. Solid-State Lett.* **2006**, *9*, A151.
- (90) Dodd, J. L.; Halevy, I.; Fultz, B. *J. Phys. Chem. C* **2007**, *111*, 1563.
- (91) Yamada, A.; Koizumi, H.; Sonoyama, N.; Kanno, R. *Electrochem. Solid-State Lett.* **2005**, *8*, A409.
- (92) Meethong, N.; Huang, H.-Y. S.; Carter, W. C.; Chiang, Y.-M. *Electrochem. Solid-State Lett.* **2007**, *10*, A134.
- (93) Ellis, B.; Perry, L. K.; Ryan, D. H.; Nazar, L. F. *J. Am. Chem. Soc.* **2006**, *128*, 11416.

- (94) Ellis, B.; Kan, W. H.; Makahnouk, W. R. M.; Nazar, L. F. *J. Mater. Chem.* **2007**, *17*, 3248.
- (95) Badi, S.-P.; Wagemaker, M.; Ellis, B. L.; Singh, D. P.; Borghols, W. J. H.; Kan, W. H.; Ryan, D. H.; Mulder, F. M.; Nazar, L. F. *J. Mater. Chem.* **2011**, *21*, 10085.
- (96) Sebastian, L.; Gopalakrishnan, J.; Piffard, Y. *J. Mater. Chem.* **2002**, *12*, 374.
- (97) Aranda, M. A. G.; Bruque, S.; Attfield, J. P. *Sol. Stat. Ion.* **1993**, *65*, 407.
- (98) Yang, S.; Zavalij, P. Y.; Stanley Whittingham, M. *Electrochem. Comm.* **2001**, *3*, 505.
- (99) Yang, S.; Song, Y.; Zavalij, P. Y.; Whittingham, M. S. *Electrochem. Comm.* **2002**, *4*, 239.
- (100) Ellis, B. L.; Nazar, L. F. *Chem. Mater.* **2012**, *24*, 966.
- (101) Ellis, B. L.; Ramesh, T. N.; Rowan-Weetaluktuk, W. N.; Ryan, D. H.; Nazar, L. F. *J. Mater. Chem.* **2012**, *22*, 4759.
- (102) Barker, J.; Gover, R. K. B.; Burns, P.; Bryan, A.; Saidi, M. Y.; Swoyer, J. L. *J. Power Sour.* **2005**, *146*, 516.
- (103) Ellis, B. L.; Ramesh, T. N.; Davis, L. J. M.; Goward, G. R.; Nazar, L. F. *Chem. Mater.* **2011**, *23*, 5138.
- (104) Dutreilh, M.; Chevalier, C.; El-Ghozzi, M.; Avignand, D.; Montel, J. M. *J. Sol. Stat. Chem.* **1999**, *142*, 1.
- (105) Yakubovich, O. V.; Karimova, O. V.; Melnikov, O. K. *Acta Cryst. C* **1997**, *53*, 395.
- (106) Toby, B. H. *J. Appl. Cryst.* **2001**, *34*, 210.
- (107) Larson, A. C.; Von Dreele, R. B. *Los Alamos National Laboratory Report LAUR 86-748* **2004**.
- (108) Jansen, E.; Schäfer, W.; Will, G. *J. Appl. Cryst.* **1994**, *27*, 492.
- (109) Koltypin, M.; Aurbach, D.; Nazar, L.; Ellis, B. *J. Power Sour.* **2007**, *174*, 1241.
- (110) Artioli, G.; Rinaldi, R.; Wilson, C. C.; Zanazzi, P. F. *Amer. Miner.* **1995**, *80*, 197.
- (111) Islam, M. S.; Driscoll, D. J.; Fisher, C. a. J.; Slater, P. R. *Chem. Mater.* **2005**, *17*, 5085.
- (112) Morgan, D.; Van der Ven, A.; Ceder, G. *Electrochem. Solid-State Lett.* **2004**, *7*, A30.

- (113) Li, J.; Yao, W.; Martin, S.; Vaknin, D. *Sol. Stat. Ion.* **2008**, *179*, 2016.
- (114) Nishimura, S.; Kobayashi, G.; Ohoyama, K.; Kanno, R.; Yashima, M.; Yamada, A. *Nat. Mater.* **2008**, *7*, 707.
- (115) Amin, R.; Balaya, P.; Maier, J. *Electrochem. Solid-State Lett.* **2007**, *10*, A13.
- (116) Wagemaker, M.; Ellis, B. L.; Lützenkirchen-Hecht, D.; Mulder, F. M.; Nazar, L. F. *Chem. Mater.* **2008**, *20*, 6313.
- (117) Maier, J.; Amin, R. *J. Electrochem. Soc.* **2008**, *155*, A339.
- (118) Meethong, N.; Kao, Y.-H.; Speakman, S. a.; Chiang, Y.-M. *Adv. Funct. Mat.* **2009**, *19*, 1060.
- (119) Fisher, C. A.; Hart Prieto, V. M.; Islam, M. S. *Chem. Mater.* **2008**, *20*, 5907.
- (120) Gibot, P.; Casas-Cabanas, M.; Laffont, L.; Levasseur, S.; Carlach, P.; Hamelet, S.; Tarascon, J.-M.; Masquelier, C. *Nat. Mater.* **2008**, *7*, 741.
- (121) Chen, G.; Song, X.; Richardson, T. J. *J. Electrochem. Soc.* **2007**, *154*, A627.
- (122) Malik, R.; Burch, D.; Bazant, M.; Ceder, G. *Nano Lett.* **2010**, *10*, 4123.
- (123) Gaberscek, M.; Dominko, R.; Jamnik, J. *Electrochem. Comm.* **2007**, *9*, 2778.
- (124) Meethong, N.; Huang, H.-Y. S.; Speakman, S. a.; Carter, W. C.; Chiang, Y.-M. *Adv. Funct. Mat.* **2007**, *17*, 1115.
- (125) Dominko, R.; Bele, M.; Gaberscek, M.; Remskar, M.; Hanzel, D.; Pejovnik, S.; Jamnik, J. *J. Electrochem. Soc.* **2005**, *152*, A607.
- (126) Ding, Y.; Jiang, Y.; Xu, F.; Yin, J.; Ren, H.; Zhuo, Q.; Long, Z.; Zhang, P. *Electrochem. Comm.* **2010**, *12*, 10.
- (127) Doherty, C. M.; Caruso, R. a.; Drummond, C. J. *Ener. & Env. Sci.* **2010**, *3*, 813.
- (128) Oh, S. W.; Myung, S.-T.; Oh, S.-M.; Oh, K. H.; Amine, K.; Scrosati, B.; Sun, Y.-K. *Adv. Mater.* **2010**, *22*, 4842.
- (129) Fisher, C. a. J.; Islam, M. S. *Journal of Materials Chemistry* **2008**, *18*, 1209.
- (130) Huang, Y.-H.; Goodenough, J. B. *Chem. Mater.* **2008**, *20*, 7237.
- (131) Maccario, M.; Croguennec, L.; Weill, F.; Lecras, F.; Delmas, C. *Sol. Stat. Ion.* **2008**, *179*, 2383.

- (132) Wang, Y.; Wang, Y.; Hosono, E.; Wang, K.; Zhou, H. *Angew. Chem. Int. Ed.* **2008**, *47*, 7461.
- (133) Muraliganth, T.; Murugan, A. V.; Manthiram, A. *J. Mater. Chem.* **2008**, *18*, 5661.
- (134) Delacourt, C.; Wurm, C.; Laffont, L.; Leriche, J.; Masquelier, C. *Sol. Stat. Ion.* **2006**, *177*, 333.
- (135) Goni, A.; Lezama, L.; Pujana, A.; Arriortua, M. I.; Rojo, T. *Int. J. Inorg. Mater.* **2001**, *3*, 937.
- (136) Goni, A.; Lezama, L.; Arriortua, M. I.; Barberis, G. E.; Rojo, T. *J. Mater. Chem.* **2000**, *10*, 423.
- (137) Yamada, A.; Chung, S.-C. *J. Electrochem. Soc.* **2001**, *148*, A960.
- (138) Yamada, A.; Kudo, Y.; Liu, K.-Y. *J. Electrochem. Soc.* **2001**, *148*, A1153.
- (139) Srinivasan, V.; Newman, J. *J. Electrochem. Soc.* **2004**, *151*, A1517.
- (140) Yamada, A.; Koizumi, H.; Nishimura, S.-I.; Sonoyama, N.; Kanno, R.; Yonemura, M.; Nakamura, T.; Kobayashi, Y. *Nat. Mater.* **2006**, *5*, 357.
- (141) Martin, J. F.; Yamada, A.; Kobayashi, G.; Nishimura, S.; Kanno, R.; Guyomard, D.; Dupré, N. *Electrochem. Solid-State Lett.* **2008**, *11*, A12.
- (142) Kobayashi, G.; Nishimura, S.; Park, M.-S.; Kanno, R.; Yashima, M.; Ida, T.; Yamada, A. *Adv. Funct. Mat.* **2009**, *19*, 395.
- (143) Delacourt, C.; Rodríguez-Carvajal, J.; Schmitt, B.; Tarascon, J.-M.; Masquelier, C. *Sol. Stat. Sci.* **2005**, *7*, 1506.
- (144) Kim, D.-H.; Kim, J. *Electrochem. Solid-State Lett.* **2006**, *9*, A439.
- (145) Yamada, a.; Chung, S. C.; Hinokuma, K. *J. Electrochem. Soc.* **2001**, *148*, A224.
- (146) Andersson, A. S.; Kalska, B.; Haggstrom, L.; Thomas, J. O. *Sol. Stat. Ion.* **2000**, *130*, 41.
- (147) Takahashi, M. *Sol. Stat. Ion.* **2002**, *148*, 283.
- (148) Chen, Z.; Dahn, J. R. *J. Electrochem. Soc.* **2002**, *149*, A1184.
- (149) Barker, J.; Saidi, M. Y.; Swoyer, J. L. *Electrochem. Solid-State Lett.* **2003**, *6*, A53.

- (150) Doeff, M. M.; Wilcox, J. D.; Yu, R.; Aumentado, A.; Marcinek, M.; Kostecky, R. *J. Solid State Electrochem.* **2007**, *12*, 995.
- (151) Delacourt, C.; Laffont, L.; Bouchet, R.; Wurm, C.; Leriche, J.-B.; Morcrette, M.; Tarascon, J.-M.; Masquelier, C. *J. Electrochem. Soc.* **2005**, *152*, A913.
- (152) Kim, D. H.; Im, J. S.; Kang, J. W.; Kim, E. J.; Ahn, H. Y.; Kim, J. *J. Nanosci. Nanotech.* **2007**, *7*, 3949.
- (153) Wang, D.; Buqa, H.; Crouzet, M.; Deghenghi, G.; Drezen, T.; Exnar, I.; Kwon, N.-H.; Miners, J. H.; Poletto, L.; Grätzel, M. *J. Power Sources* **2009**, *189*, 624.
- (154) Barpanda, P.; Recham, N.; Djellab, K.; Boulineau, A.; Armand, M.; Tarascon, J.-M. *ECS Trans.* **2010**, *25*, 1.
- (155) Recham, N.; Dupont, L.; Courty, M.; Djellab, K.; Larcher, D.; Armand, M.; Tarascon, J.-M. *Chem. Mater.* **2009**, *21*, 1096.
- (156) Kanamura, K.; Koizumi, S.; Dokko, K. *Journal of Materials Science* **2007**, *43*, 2138–2142.
- (157) Chen, J.; Whittingham, M. *Electrochem. Comm.* **2006**, *8*, 855.
- (158) Burba, C. M.; Frech, R. *J. Electrochem. Soc.* **2004**, *151*, A1032.
- (159) Burba, C. M.; Frech, R. *Spectrochim. acta A: Molecul. Biomolecul. Spec.* **2006**, *65*, 44.
- (160) Chen, G.; Song, X.; Richardson, T. J. *Electrochem. Solid-State Lett.* **2006**, *9*, A295.
- (161) Liao, X.-Z.; Ma, Z.-F.; Wang, L.; Zhang, X.-M.; Jiang, Y.; He, Y.-S. *Electrochem. Solid-State Lett.* **2004**, *7*, A522.
- (162) Singh, C.; Shaffer, M. S. P.; Windle, A. H. *Carbon* **2003**, *41*, 359.
- (163) Endo, M.; Kim, Y. A.; Fukai, Y.; Hayashi, T.; Terrones, M.; Terrones, H.; Dresselhaus, M. S. *Appl. Phys. Lett.* **2001**, *79*, 1531.
- (164) Rho, Y.-H.; Nazar, L. F.; Perry, L.; Ryan, D. *Journal of The Electrochemical Society* **2007**, *154*, A283.
- (165) Vassiliou, J. K.; Mehrotra, V.; Russell, M. W.; Giannelis, E. P.; McMichael, R. D.; Shull, R. D.; Ziolo, R. F. *J. Appl. Phys.* **1993**, *73*, 5109.
- (166) Lopes, I.; El Hassan, N.; Guerba, H.; Wallez, G.; Davidson, A. *Chem. Mater.* **2006**, *18*, 5826.

- (167) Tsunekawa, S.; Ito, S.; Y., K. *Appl. Phys. Lett.* **2004**, *85*, 3845.
- (168) Stevens, R.; Dodd, J. L.; Kresch, M. G.; Yazami, R.; Fultz, B.; Ellis, B.; Nazar, L. F. *J. Phys. Chem. B* **2006**, *110*, 22732.
- (169) Song, C. J.; Mullen, J. G. *Phys. Rev. B: Condens. Matter Mater. Phys.* **1976**, *14*, 2761.
- (170) Maxisch, T.; Zhou, F.; Ceder, G. *Phys. Rev. B* **2006**, *73*, 104301–1.
- (171) Marcus, R. A. *Pure Appl. Chem.* **1977**, *69*, 13.
- (172) Wagemaker, M.; Borghols, W. J. H.; Mulder, F. M. *J. Am. Chem. Soc.* **2007**, *129*, 4323.
- (173) Groat, L. A.; Chakoumakos, B. C.; Brouwer, D. H.; Hoffman, C. M.; Fyfe, C. A.; Morell, H.; Schultz, A. J. *Amer. Miner.* **2003**, *88*, 195.
- (174) Fransolet, A.-M.; Tarte, P. *Amer. Miner.* **1977**, *62*, 559.
- (175) Cerna, I.; Cerny, P.; Ferguson, R. B. *Amer. Miner.* **1973**, *58*, 291.
- (176) Lindberg, M. L.; Pecora, W. T. *Amer. Miner.* **1953**, *40*, 952.
- (177) Rouzies, D.; Varloud, J.; Millet, J.-M. M. M. *J. Chem. Soc. Faraday Trans.* **1994**, *90*, 3335.
- (178) Barker, J.; Saidi, M. Y.; Swoyer, J. L. *J. Electrochem. Soc.* **2004**, *151*, A1670.
- (179) Barker, J.; Gover, R. K. B.; Burns, P.; Bryan, A. *Electrochem. Solid-State Lett.* **2005**, *8*, A285.
- (180) Ramesh, T. N.; Lee, K. T.; Ellis, B. L.; Nazar, L. F. *Electrochem. Solid-State Lett.* **2010**, *13*, A43.
- (181) Recham, N.; Chotard, J.-N.; Jumas, J.-C.; Laffont, L.; Armand, M.; Tarascon, J.-M. *Chem. Mater.* **2010**, *22*, 1142.
- (182) Aranda, M. a. G.; Bruque, S.; Attfield, J. P. *Angew. Chem. Int. Ed.* **1992**, *31*, 1090.
- (183) Boonchom, B.; Baitahe, R.; Joungmunkong, Z.; Vittayakorn, N. *Powder Tech.* **2010**, *203*, 310.
- (184) Barker, J.; Saidi, M. Y.; Swoyer, J. L. Lithium Metal Phosphate Materials and Preparation Thereof. **2005**, US 6,855,462 B2.

- (185) Belokovena, E. L.; Yakubovich, O. V.; Tsirel'son, V. G.; Urusov, V. S. *Izv. Akad. Nauk. SSR Neorg. Mater.* **1990**, *26*, 595.
- (186) Loiseau, T.; Calage, Y.; Lacorre, P.; Ferey, G. *J. Sol. Stat. Chem.* **1994**, *111*, 390.
- (187) Yakubovich, O. V.; Urusov, V. S. *Geokhimiya* **1997**, *7*, 720.
- (188) Shannon, R. D. *Acta Cryst. A* **1976**, *A32*, 751.
- (189) Marx, N.; Croguennec, L.; Carlier, D.; Wattiaux, A.; Cras, F. Le; Suard, E.; Delmas, C. *Dalton transactions (Cambridge, England : 2003)* **2010**, 39.
- (190) Ellis, B. L.; Nazar, L. F. *Chem. Mater.* **2012**, *24*, 966.
- (191) Aranda, M. a. G.; Bruque, S.; Attfield, J. P.; Palacio, F.; Von Dreele, R. B. *Journal of Solid State Chemistry* **1997**, *132*, 202–212.
- (192) Aravindan, V.; Karthikeyan, K.; Amaresh, S.; Lee, Y. S. *Electrochemical and Solid-State Letters* **2011**, *14*, A33.
- (193) Boulineau, A.; Sirisopanaporn, C.; Dominko, R.; Armstrong, A. R.; Bruce, P. G.; Masquelier, C. *Dalton Trans.* **2010**, 39, 6310.
- (194) Arroyo y de Dompablo, M. E.; Amador, U.; Gallardo-Amores, J. M.; Morán, E.; Ehrenberg, H.; Dupont, L.; Dominko, R. *J. Power Sour.* **2009**, *189*, 638.
- (195) Okada, S.; Ueno, M.; Uebou, Y.; Yamaki, J. *J. Power Sour.* **2005**, *146*, 565.
- (196) Barker, J.; Saidi, M. Y.; Swoyer, J. L. Method for Making Phosphate Based Electrode Active Materials. **2008**, US 2008/0241043 A1.
- (197) Chen, X.; Wang, X.; Wang, Z.; Wan, J.; Liu, J.; Qian, Y. *Nanotech.* **2004**, *15*, 1685.
- (198) Alberti, A.; Vezzalini, G. *Zeit. Kristall.* **1978**, *147*, 167.
- (199) Barker, J.; Saidi, M. Y.; Swoyer, J. L. *Electrochem. Solid-State Lett.* **2003**, *6*, A1.
- (200) Barker, J.; Gover, R. K. B.; Burns, P.; Bryan, a. J. *Electrochem. Solid-State Lett.* **2006**, *9*, A190.
- (201) Asher, R. C. *J. Inorg. Nucl. Chem.* **1959**, *10*, 238.
- (202) Ge, P.; Fouletier, M. *Sol. Stat. Ion.* **1988**, *30*, 1172.
- (203) Sokolova, E.; Hawthorne, F. C. *Can. Miner.* **2001**, *39*, 1275.

- (204) Swafford, S.; Holt, E. M. *Solid State Sci.* **2002**, *4*, 807.
- (205) Sanz, F.; Parada, C.; Ruíz-Valero, C. *J. Mater. Chem.* **2001**, *11*, 208.
- (206) Ellis, B.; Subramanya Herle, P.; Rho, Y.-H.; Nazar, L. F.; Dunlap, R.; Perry, L. K.; Ryan, D. H. *Faraday Discussions* **2007**, *134*, 119.
- (207) Li, W.; Ye, N. *Acta Cryst. E* **2007**, *E63*, i160.
- (208) Wolfenstine, J.; Allen, J. J. *Power Sour.* **2005**, *142*, 389.